6-28-2022 2:00 PM

Probing the Inner Structure of Active Galactic Nuclei Through Reverberation Mapping

Viraja Chandrashekhar Khatu, *The University of Western Ontario*

Supervisor: Gallagher, Sarah C., *The University of Western Ontario*

A thesis submitted in partial fulfillment of the requirements for the Doctor of Philosophy degree in Astronomy

Abstract

In the centres of massive galaxies, active galactic nuclei (AGN) are supermassive black holes, surrounded by an accretion disk of ionized gas, that release tremendous energy in the form of electromagnetic radiation. Because AGN are unresolved through telescopes, we employ reverberation mapping (RM) to study their structure. RM capitalizes on the fact that AGN are variable – the continuum emission from the accretion disk varies, and surrounding gas (in the broad-line region, BLR) responds to those variations with a positive time lag. RM translates the measured time lag into a size of the BLR. Combined with gas velocities (measured from the width of broad emission lines in AGN spectra), RM yields dynamically measured black hole masses, essential for understanding *How supermassive black holes grow over cosmic time?*

We conducted a detailed RM study of a highly accreting AGN, Markarian 142, for the first time with the Gemini North and Lijiang Observatories, with simultaneous ultraviolet (UV) continuum and spectroscopic BLR observations. We determined an Hβ lag of 8.58 days relative to the UV continuum. Deriving UV lags is important as UV emission more closely tracks the ionizing continuum that dominates the energetics of the BLR than the optical continuum.

Constraining black hole masses in RM is difficult, partly due to uncertainties on emission-line widths. Higher-resolution and high signal-to-noise spectra allow separation of blended lines that originate in different regions of the BLR. In the particular case of Markarian 142, we determined that unresolved narrow lines and flexible narrow-line flux ratios result in excess flux attributed to the narrow-line component of the complex Hβ line, broadening the apparent widths measured for these broad lines. We further present recommendations on methodology for line-width measurements in narrow-line AGN to extract more accurate values.

RM studies have improved over time with larger sample sizes that span a broader diversity of the AGN population. To successfully implement large-scale variability campaigns, optimized survey designs are required to maximize science returns. We illustrated the use of such a survey simulation pipeline to optimize AGN RM surveys with a next-generation UV telescope, CASTOR.

Keywords: Active, galaxies, black holes, accretion, variability, spectra, telescopes, surveys, simulation

Summary for Lay Audience

Residing at the centres of massive galaxies, active galactic nuclei (AGN) are supermassive black holes (millions to billions of solar masses) surrounded by a disk of gas orbiting the central black hole. Gas accreting onto the black hole releases tremendous energy in different forms of light which makes these objects extremely luminous. However, AGN are a thousand times smaller than their host galaxies and hence cannot be mapped with telescopes.

To study AGN, we rely on reverberation mapping that takes advantage of the varying light output in these systems to probe their sizes. The light from the disk illuminates and is absorbed by nearby gas (in the broad-line region, BLR) and re-emitted with a time lag. Reverberation mapping converts time lag into distance (size of the BLR). Using BLR size and gas velocities from broad emission lines in AGN spectra (light from different energies spread on a detector), we can calculate black hole masses in AGN. Studying black holes in a large number of AGN over a wide range of cosmic times is important to understand how supermassive black holes grow over time.

Although AGN have been studied for decades, the structure of AGN that grow very quickly is poorly understood. In our first project, we focused on one such object – Markarian 142. We derived the time lag of the BLR response to the ultraviolet (UV) light from the disk using simultaneous observations from four telescopes on the ground and in space.

To accurately calculate black holes masses in AGN, we need higher-resolution and high signal-to-noise spectra that allow us to separate blended emission lines. This deblending is critical to reliably measure BLR gas velocities. In our second project, we investigated how low spectral resolution affects measurements of narrower broad lines in AGN spectra.

Considering the increasing scale of surveys that aim to measure many AGN black hole masses, it is important that we optimize large-scale surveys with next-generation facilities to maximize science outcomes. In our third project, we illustrated the use of a survey computer simulation pipeline to optimally design variability surveys with a proposed, Canadian-flagship UV telescope, CASTOR.

Co-Authorship Statement

Chapter 2 ::

This project is a work of collaboration as described below.

I led the proposal for spectroscopic observations with the Gemini North Telescope (Gemini) with support from my supervisor Sarah Gallagher and coauthors Edward Cackett, Jian-Min Wang, Chen Hu, and Patrick Hall. Members of the Super-Eddington Accreting Massive Black Holes (SEAMBH) collaboration led the spectroscopic campaign with the Lijiang Telescope (LJT), Edward Cackett led the X-ray campaign with the *Neil Gehrels Swift Observatory* (*Swift*), and Rick Edelson led the observing campaign with the Las Cumbres Observatory (LCO) that included the *g*-band photometric data.

I reduced and calibrated the Gemini data using the Gemini `IRAF` software. I developed various scripts in `Python` to correct undesirable features in the Gemini spectra. Sofia Pasquini contributed in reducing the data during early stages of the process. Members of the SEAMBH collaboration reduced and calibrated the LJT spectra that were then provided by Chen Hu. The *Swift*/*UVW2* and the LCO/*g* continuum light curves were provided by Edward Cackett.

I performed the complete analysis with three different types of software. I modelled the Gemini and LJT spectra in `PrepSpec` for relative flux calibration. Keith Horne provided tremendous support through the installation and use of `PrepSpec`. He also offered valuable insights in interpreting `PrepSpec` modelling results and gaining a comprehensive understanding of analyzing data for reverberation-mapping studies. I modelled the continuum and emission lines in the Gemini and LJT spectra in `Sherpa` to measure physical properties of the Hβ, [O III], and He I lines. Keith Horne and Chen Hu offered useful suggestions during spectral fitting. Chen Hu also provided the template model for fitting Fe II emission in the spectra. In `PyROA`, I inter-calibrated the 5100 Å continuum light curves from Gemini and LJT spectra to generate a single light curve. I repeated the inter-calibration to generate a single light curve for the broad Hβ line as well. I performed cross-correlation analysis with the continuum and Hβ emission-line light curves with `PyROA` to measure ultraviolet and optical time lags for Hβ. Keith Horne provided his support while using the `PyROA` software.

I carried out the black hole mass and luminosity calculations. I interpreted the results using insights from Keith Horne and Sarah Gallagher. I generated all figures and tables. I led the writing of this Chapter incorporating comments from Sarah Gallagher and Keith Horne.

==========

Chapter 3 ::

This project is a work of collaboration as described below.

I measured physical properties of the Hβ, [O III], and He I emission lines in the Mrk 142 spectra taken with the Gemini and LJT telescopes at higher and lower resolution, respectively, to conduct a detailed correlation analysis between the measurements. Keith Horne offered his insights while interpreting the correlations. I performed all calculations, and discussed references from the literature relevant to the presented analysis. Sarah Gallagher provided her advice and perspectives on the broader context of the project. From discussions with Sarah

Gallagher, I presented recommendations on line-measurement methods.

I generated all figures including the decision-making tree of recommendations. I led the writing of this entire Chapter adding comments from Sarah Gallagher.

==========

Chapter 4 ::

This project is a work of collaboration as described below.

I constructed the Active Galactic Nuclei (AGN) Survey Simulation pipeline (under development) including all its modules. While building the module to generate source distribution of AGN, coauthors Aaron Sigut, Patrick Côté, and Christopher Willott provided valuable suggestions. Patrick Côté provided (1) three filter functions of the *Cosmological Advanced Survey Telescope for Optical and ultraviolet Research* (CASTOR) used for generating the K correction, and (2) tables of photometric signal-to-noise ratios used for generating the observed continuum light curves.

I generated illustrations of how the AGN Survey Simulation Pipeline can be used to design large-scale AGN variability surveys with advice and direction from Sarah Gallagher. I generated all figures and led the writing of this Chapter inputting comments from Sarah Gallagher.

==========

Epigraph

"There's something in the very small minutia of life that tells us something about the big, big picture that we see every day all over the place, and so I think the more specific and creative and revelatory you are in the micro, the more powerful the macro will be."

– *Philip Seymour Hoffman*

Dedication

For the deprived children of our planet who hope and strive to emerge against all odds!

Acknowledgements

It has been an incredible journey of discovery through all my graduate years. I feel that professional training, exciting travel experiences, and connections with a huge number of people have shaped me tremendously, both as a researcher and an individual.

I would like to first thank my supervisor, Sarah Gallagher for her phenomenal support, incredible insights, and timely directions. Sarah has been a guide and a mentor, who always encouraged me to explore in different dimensions. I thank my advisory committee members, Peter Brown and Martin Houde, for their support and directions throughout my graduate years. I thank Jan Cami, who has tremendously shaped my outreach experience. I would like to deeply thank Keith Horne for the long and stimulating discussions over Zoom. Keith's support was vital to convene a major part of this research. I thank Edward Cackett for his support and being so welcoming during my research visit to Wayne State University. I would also like to thank Chen Hu and Patrick Côté for supporting me through various stages of my research. I thank Gordon Richards and Girish Kulkarni for their advice and support for part of this research. I thank Kim Venn, my supervisor for the New Technologies for Canadian Observatories (NTCO) program for her support during my internships. I would also like to thank my NTCO internship supervisors, Marie Lemoine-Busserolle, Andrew Stephens, Stephen Se, and Ahmed Sigiuk for giving me the opportunity to learn from their experiences. I also thank the communities of the The National Research Council's Herzberg Astronomy and Astrophysics (HAA) for being incredibly welcoming, supportive, and engaging during my visiting term at HAA. I thank Donald Terndrup and Karen Leighly, my collaborators from my Master's project who trained me in using two software tools that I applied for my PhD research. I would also like to thank John Lester, my first Astronomy professor, who has been a guide and a friend since my undergraduate years.

I thank the staff at in the Department of Physics and Astronomy at Western for their support. I also thank my friends and office mates for always being there to share their stories, listen to mine, and talk through both tough and happy times. And as they say, last but not the least, my family – my Mommy, my Dad, and my little sister – thanks a zillion for your commendable support and patience throughout my graduate journey.

We acknowledge the support of the Natural Sciences and Engineering Research Council of Canada (NSERC), Discovery Grants. Viraja C. Khatu acknowledges the support of the Ontario Graduate Scholarships. This research was undertaken with the financial support of the Canadian Space Agency. The research of Viraja C. Khatu was partially supported by the New Technologies for Canadian Observatories, an NSERC CREATE program.

This research was based on observations obtained at the Gemini Observatory (processed using the Gemini IRAF package), which is managed by the Association of Universities for Research in Astronomy (AURA) under a cooperative agreement with the National Science Foundation on behalf of the Gemini Observatory partnership: the National Science Foundation (United States), National Research Council (Canada), Agencia Nacional de Investigación y Desarrollo (Chile), Ministerio de Ciencia, Tecnología e Innovación (Argentina), Ministério da Ciência, Tecnologia, Inovações e Comunicações (Brazil), and Korea Astronomy and Space Science Institute (Republic of Korea). This work was enabled by observations made from the Gemini North telescope, located within the Maunakea Science Reserve and adjacent to the summit of Maunakea. We are grateful for the privilege of observing the Universe from

a place that is unique in both its astronomical quality and its cultural significance. Viraja C. Khatu acknowledges the support of Joel Roediger and the Gemini Observatory staff during the planning of observations and data reduction for part of this research.

This research used observations from the Lijiang 2.4 m Telescope funded by the Chinese Academy of Sciences (CAS) and the People's Government of Yunnan Province. Viraja C. Khatu acknowledges the support of the Super-Eddington Accreting Massive Black Holes (SEAMBH) collaboration for providing the reduced and calibrated data taken with the Lijiang Telescope. This research also used observations from the *Neil Gehrels Swift Observatory* and the Las Cumbres Observatory that were provided by Edward Cackett.

Contents

List of Figures

List of Tables

List of Appendices

List of Abbreviations, Symbols, and Nomenclature

Symbol/Notation/Abbreviation	Description
$M_\bullet$	Mass of black hole
$M_\odot$	Mass of our Sun
G	Gravitational constant
$R_\bullet$	Radius of black hole
$E_{\rm acc}$	Accretion energy
c	Speed of light
λ	Wavelength
$\lambda_{\rm rest}$	Rest wavelength
$\lambda_{\rm obs}$	Observed wavelength
$\lambda_{\rm emit}$	Emitted wavelength
ν	Frequency
$\nu_{\rm rest}$	Rest frequency
$\nu_{\rm obs}$	Observed frequency
$\nu_{\rm emit}$	Emitted frequency
$E_{\rm acc}$	Accretion energy
η	Accretion efficiency
L	Luminosity
$L_{\rm Edd}$	Eddington luminosity
$\dot{M}$	Mass accretion rate
$\dot{M}_{\rm Edd}$	Eddington mass accretion rate
$M_{\rm V}$	Absolute magnitude in the visible band (typically, green colour in the optical)
F	Flux
F_λ	Flux density – flux per unit wavelength
F_ν	Flux density – flux per unit frequency
$m_{\rm p}$	Mass of a proton
$\sigma_{\rm T}$	Thompson scattering cross section
n	Particle density of gas
Φ	Ionizing photon flux
U	Ionization parameter
z	Redshift
$\alpha_{\rm ox}$	Optical-to-X-ray spectral index
$t_{\rm rest}$	Time in rest frame
$t_{\rm obs}$	Time in observed frame
$H_{\rm disk}$	Scale height of the accretion disk
$R_{\rm disk}$	Radius of the accretion disk
$M_{\rm i}$	Absolute magnitude in the i band
$\Delta m_{\rm obs}$	Observed variability magnitude
Δm_∞	Long-term variability amplitude
$\Delta t_{\rm obs}$	Observing cadence

List of Abbreviations, Symbols, and Nomenclature (cont'd)

Symbol/Notation/Abbreviation	Description
$\tau_{\rm damping}$	Characteristic damping timescale
τ	Time lag
BLR	Broad-line region
R (or) $R_{\rm BLR}$	Radius of the broad-line region
ΔV	Velocity width
$V_{\rm orb}$	Orbital velocity of gas
LOS	Line of sight
$V_{\rm LOS}$	Line-of-sight velocity
θ	Angle between an observer's line of sight and the broad-line region
$F_{\rm CCF}$	Cross-correlation function
$F_{\rm ACF}$	Auto-correlation function
$C(t)$	Continuum light curve at specific times (t)
$L(t)$	Emission-line light curve at specific times (t)
ψ	Transfer function
$\bar{L}(t)$	Background line emission at specific times (t)
FWHM	Full width at half maximum
f	Dimensionless factor in the black hole mass equation that accounts for the geometry, kinematics, and orientation of the broad-line region
$F_{\rm var}$	Fractional variability
H_0	Hubble constant
Ω_Λ	Density of dark energy
$\Omega_{\rm M}$	Density of mass (including ordinary mass and dark matter)
RMS	Root-mean-square
RMSx	Residual root-mean-square
σ	Standard deviation
σ_*	Stellar velocity dispersion
$\sigma_{\rm line}$	Line dispersion
$\sigma_{\rm RMSx}$	Deviation in the residual root-mean-square
χ^2	Chi-squared statistic
χ^2_ν	Reduced chi-squared statistic, where ν stands for degrees of freedom
BIC	Bayesian Information Criterion
ΔBIC	Change in the Bayesian Information Criterion
$\Delta\log {\rm P}$	Change in relative probability
$E(B-V)$	Degree of reddening
$r_{\rm Spearman}$	Spearman correlation coefficient

List of Abbreviations, Symbols, and Nomenclature (cont'd)

Symbol/Notation/Abbreviation	Description
$R_{\mathrm{Fe\ II}}$	Ratio of equivalent width of Fe II in the region from 4434 Å to 4684 Å to that of the broad Hβ λ4861 line
K	Colour correction (also known as K-correction)
$\phi(M)$	Active galactic nuclei luminosity function as a function of absolute magnitude (M)
ϕ_*	Amplitude of the active galactic nuclei luminosity function
M_*	Absolute break magnitude of the active galactic nuclei luminosity function
m_{UV}	Apparent magnitude in the UV band
M_{UV}	Absolute magnitude in the UV band
AGN	Active galactic nuclei
$\mathrm{N_{AGN}}$	Number of active galactic nuclei
SMBH	Supermassive black hole
BLR	Broad-line region
NLR	Narrow-line region
BAL	Broad absorption line
SED	Spectral Energy Distribution
UV	Ultraviolet
IR	Infrared
LOC	Locally optimally emitting cloud
RM	Reverberation mapping
FOV	Field of view
S/N	Signal-to-noise
NLS1	Narrow-Line Seyfert 1
RA	Right Ascension
Dec	Declination
MJD	Modified Julian Date
HJD	Heliocentric Julian Date
UT	Universal Time
SPCALF	SpectroPhotometric CALibration Flag
SPCALG	SpectroPhotometric CALibration Grade
1D	One-dimensional
2D	Two-dimensional
EW	Equivalent width
VP	Virial product
PSF	Point spread function
ROA	Running optimal average
SDSS	Sloan Digital Sky Survey

List of Abbreviations, Symbols, and Nomenclature (cont'd)

Symbol/Notation/Abbreviation	Description
SDSS-RM	Sloan Digital Sky Survey Reverberation Mapping
RMID	Reverberation-Mapping Identifier
SEAMBH	Super-Eddington Accreting Massive Black Holes
STORM	Space Telescope and Optical Reverberation Mapping
OzDES	Australian Dark Energy Survey
NGC	New General Catalogue
PG	Palomar Green
CTS	Calan-Tololo Survey
Mrk 142	Markarian 142 (AGN name)
I Zw 1	I Zwicky 1 (AGN name)
NuSTAR	*Nuclear Spectroscopic Telescope Array*
Swift	*Neil Gehrels Swift Observatory*
LCO	Las Cumbres Observatory
Gemini	Gemini North Telescope
LJT	Lijiang Telescope
CASTOR	*Cosmological Advanced Survey Telescope for Optical and ultraviolet Research*
GMOS	Gemini Multi-Object Spectrograph
GCAL	Gemini Facility Calibration Unit
P.I.	Principal Investigator
FITS	Flexible Image Transport System
PS	PostScript
DRW	Damped random walk
MEM	Maximum Entropy Method
IRAF	Image Reduction and Analysis Facility
PyRAF	Image Reduction and Analysis Facility with Python wrapper
CIAO	Coronagraphic Imager with Adaptive Optics
ICCF	Interpolated Cross-Correlation Function
JAVELIN	Just Another Vehicle for Estimating Lags In Nuclei
PyROA	Python-based Running Optimal Average
CSA	Canadian Space Agency

Chapter 1

Introduction

1.1 Active Galactic Nuclei

Every massive galaxy in the Universe hosts a supermassive black hole[1] (SMBH) at its centre (e.g., Silk & Rees 1998; Magorrian et al. 1998) that is on the order of 10^7–10^{10} $M_\odot$ (Ferrarese & Ford 2005), where $M_\odot$ is the mass of our Sun. In some galaxies, these SMBHs are in a phase where they grow through accretion of matter surrounding them. The accretion mechanism results in the formation of a disk-like structure of ionized gas around SMBHs, now referred to as active galactic nuclei (AGN). In AGN, the accretion of matter onto the SMBH releases gravitational potential energy outward in the form of electromagnetic radiation. This radiation is emitted over a large fraction of the electromagnetic spectrum from $\log \nu$[Hz] $\sim$ 8 (where ν stands for frequency given in the units of Hertz [Hz]) in the radio to 18 in the X-ray, where the typical luminosity range is 10^{43}–10^{48} erg s^{-1} (Peterson 1993). Although the central continuum source (SMBH+accretion disk) is only a few light days[2] in size (Peterson 1993), the light from it can outshine the light from its entire host galaxy by a factor of 100 or more (Peterson 1997). The tremendous amount of radiated energy can drive outflows of gas at high speeds (thousands to several tens of thousands of kilometre per second [km s^{-1}]) away from the central source (Weymann et al. 1991).

The gravitational potential energy released due to the accretion of matter ($E_{\rm acc}$) is given by:

$$E_{\rm acc} = \frac{G\, M_\bullet\, M}{R_\bullet}\ [\rm erg] \tag{1.1}$$

where G is the universal gravitational constant, $M_\bullet$ is the mass of the SMBH, M is the mass of the accreting matter, and $R_\bullet$ is the radius of the SMBH. Here, the ratio $M_\bullet/R_\bullet$ is defined as the compactness of the SMBH - the larger the ratio, the more the gravitational energy released from accretion. The radius of the SMBH ($R_\bullet$) is also called the Schwarzschild radius, given by $R_\bullet \equiv G\, M_\bullet/c^2$, where c ($\approx 3 \times 10^5$ km s^{-1}) is the speed of light. If the ratio $M_\bullet/R_\bullet$ is fixed, the luminosity (L) of an AGN directly depends on the rate of accretion of matter ($\dot{M}$), and the equation for L is:

[1] A black hole is a region where matter is squeezed into a very small volume of space, giving rise to strong gravity that even light cannot escape.

[2] 1 light day $\approx 2.54 \times 10^{15}$ centimetre (cm)

$$L = \frac{\eta\, G\, M_\bullet\, \dot{M}}{R_\bullet}\ [\mathrm{erg\ s^{-1}}] \tag{1.2}$$

Substituting the definition of $R_\bullet$ in Equation 1.2, the equation for L can be written as:

$$L = \eta\, \dot{M}\, c^2\ [\mathrm{erg\ s^{-1}}] \tag{1.3}$$

In Equations 1.2 and 1.3, η is a dimensionless parameter that gives the *efficiency* of the accretion process, that is, the efficiency at which the rest mass energy, c^2 for unit mass, of the accreted material is converted into radiation. Empirically, it is difficult to constrain η although ~0.1 is the value commonly found in the literature (e.g., Murray et al. 1995).

At a critical point, termed as the Eddington limit, the outward radiation pressure and inward gravitational pull balance each other. The corresponding luminosity is called the Eddington luminosity (L_{Edd}) given by:

$$\begin{aligned} L_{\mathrm{Edd}} &= \frac{4\,\pi\, G\, m_{\mathrm{p}}\, c\, M_\bullet}{\sigma_{\mathrm{T}}} \\ &\cong 1.3 \times 10^{38}\ (M_\bullet/M_\odot)\ [\mathrm{erg\ s^{-1}}] \end{aligned} \tag{1.4}$$

where m_{p} is the mass of a proton and σ_{T} is the Thomson scattering[3] cross-section for interacting particles. Consequently, we can determine an Eddington accretion rate ($\dot{M}_{\mathrm{Edd}}$), obtained from setting L in Equation 1.3 equal to L_{Edd} as follows:

$$\dot{M}_{\mathrm{Edd}} = \frac{4\,\pi\, G\, M_\bullet\, m_{\mathrm{p}}}{\eta\, c\, \sigma_{\mathrm{T}}} \tag{1.5}$$

(typically expressed in $M_\odot$/year). Most AGN in the nearby Universe accrete in the sub-Eddington limit. However, Eddington accretion assumes spherical symmetry. Therefore, for objects with asymmetrical geometry such as a disk in AGN, it is possible to surpass the limiting $\dot{M}_{\mathrm{Edd}}$ and grow at a very high rate. Such highly accreting AGN likely evolved during the phase of rapid black hole growth at high redshifts (in the early history of the Universe). Cosmological redshift (or simply, redshift [z]) is defined as follows:

$$z = \frac{\lambda_{\mathrm{obs}} - \lambda_{\mathrm{emit}}}{\lambda_{\mathrm{emit}}} \tag{1.6}$$

where λ_{emit} is the emitted wavelength at the location of an AGN and λ_{obs} is the observed wavelength on the Earth. As the Universe is expanding, the wavelength (λ) of the light emitted at the AGN location is stretched on its way to the Earth and hence is observed at longer (redder) wavelengths here. The difference between λ_{emit} and λ_{obs} depends on the redshift, or equivalently, how far away the AGN is from the Earth. The farther away the AGN, the more the λ_{obs}

[3]Thomson scattering is the process in which electromagnetic radiation is scattered by free charged particles such that the frequency of the scattered radiation and the kinetic energy of the charged particles do not change after scattering.

is redshifted. Because AGN are very luminous objects, they can be detected over a wide range of redshifts, $0 < z \lesssim 7.6$. Wang et al. (2021) reported the highest redshift AGN detected to date at $z = 7.642$.

The most luminous AGN are called *quasars* with $L_{\rm quasar} \gtrsim 10^{46}$ erg s^{-1} and $M_\bullet \gtrsim 10^8\ M_\odot$ (Peterson 1997). Discovered in some of the first radio surveys in the late 1950s (e.g., Schmidt 1963; Netzer 2013), quasars were initially thought to be a different class of luminous star-like objects due to their physical appearance. Thus, they were initially known as "quasi-stellar radio sources", later shortened to "quasars"[4] and the less luminous class of AGN referred to as Seyferts (Seyfert 1943) with a separating absolute magnitude limit of $M_{\rm V} = -23$ (Netzer 2013). The term "quasars" is now used generically to refer to all luminous AGN exhibiting broad lines.

1.2 Spectral Energy Distribution of Quasars

Some of the first studies of quasars were aimed at studying the emission and absorption lines in their spectra along with their radio and optical properties (see Schmidt 1969, and references therein). The power output from an object distributed over a range of frequencies is termed as the spectral energy distribution (SED). Since quasars emit over a broad range from radio to X-ray frequencies, their SED plots and features therein are important to understand (1) how the energy output in a given frequency range contributes to the net energy distribution, and (2) the different physical processes responsible for the observed energy in different frequency regimes. Quasars can be classified as radio-quiet or radio-loud based on their power output at radio wavelengths - the radio-quiet quasars have ≈100 times lower power output at radio wavelengths as compared to their radio-loud counterparts (Peterson 1997). The difference between these two classes is attributed to the presence of radio jets and lobes in radio-loud quasars that are not present in their radio-quiet counterparts (e.g., Wilson & Colbert 1995). Figure 1.1 shows typical quasar SEDs for both radio-loud and radio-quiet types. The SEDs show that in quasars, significant power is generated from infrared (IR) to X-ray frequencies.

A successful quasar model must be able to satisfactorily explain the features in a quasar SED with particular energy generation processes. Richards et al. (2006) discussed the mid-IR and optical properties of quasar mean SEDs and derived physical parameters useful to describe them. The important features in a quasar SED are labelled in Figure 1.1. In general, within a constrained spectral range in the SED, the quasar continuum can be modelled with a power law (Netzer 2013) as follows:

$$F_\nu \propto \nu^\alpha \ [\text{erg s}^{-1}\ \text{cm}^{-2}\ \text{Hz}^{-1}] \tag{1.7}$$

where F_ν is the monochromatic flux density (flux per unit frequency), ν is frequency in Hz, and α is the frequency spectral index. Typically, α for type 1 quasars (see Section 1.3) has a value of ≅-0.44±0.1 (e.g., Vanden Berk et al. 2001) in the spectral range ∼1300 Å[5] to 5000 Å. This indicates that the power output from a quasar increases at higher frequencies (or equivalently, bluer wavelengths). This is also evident in Figure 1.1.

[4]The term "quasar" was coined by Chiu (1964).

[5]1 Angstrom (Å) = 10^{-10} metre (m)

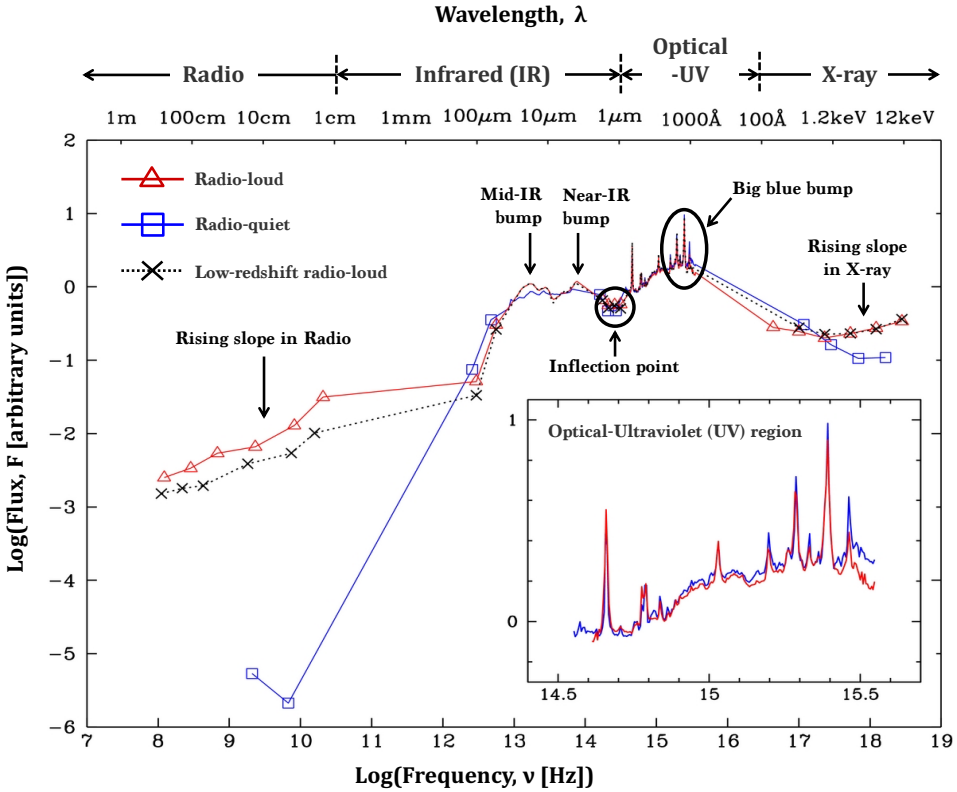

Figure 1.1: Median spectral energy distribution (SED) in the rest frame compiled for 58 radio-loud (open triangles in red) and 27 radio-quiet (open squares in blue) quasars. The median SED for low-redshift (nearby Universe) radio-loud quasars is explicitly shown as a black dotted line with crosses. The inset shows a zoom-in of the optical-UV region. All SEDs are normalized with respect to the 4215 Å point (where 1 Angstrom [Å] = 10^{-10} metre [m]). The approximate point of inflection separating the infrared (IR) and optical-ultraviolet (UV) regions is marked with a black circle. Other important features are also labelled (see explanation in Section 1.2). This figure is taken from Shang et al. (2011) and annotated here.

The most widely accepted quasar model is of a centrally located SMBH cocooned in a hot corona, which is an electron plasma and positive ions, surrounded by a geometrically thin and optically thick accretion disk (Longair 1994). Figure 1.2 shows a schematic of the quasar model. The X-ray emission comes primarily from the hot corona, where the accretion disk photons are inverse Compton-scattered[6] by the high-energy electrons surrounding the central SMBH. In radio-loud quasars, an additional feature at energies greater than 1.2 keV[7] is the rising slope of the X-ray emission that likely comes from relativistic jets in those quasars when the photons from the accretion disk are inverse Compton-scattered by the relativistic plasma in the jets. This feature in the X-ray cannot be modelled by the usual power-law behaviour of the

[6]Inverse Compton scattering is the process in which a lower-energy photon encounters a particle travelling at relativistic speed and gains energy to convert into a higher-energy photon.

[7]1 kiloelectron volt (keV) $\approx 1.6 \times 10^{-16}$ Joule

SED in the ultraviolet (UV) through IR (Elvis et al. 1994). A similar rising slope exists in the radio for radio-loud quasars. This feature also belongs most likely to the jets in these objects as they interact with the interstellar medium[8] at larger physical scales.

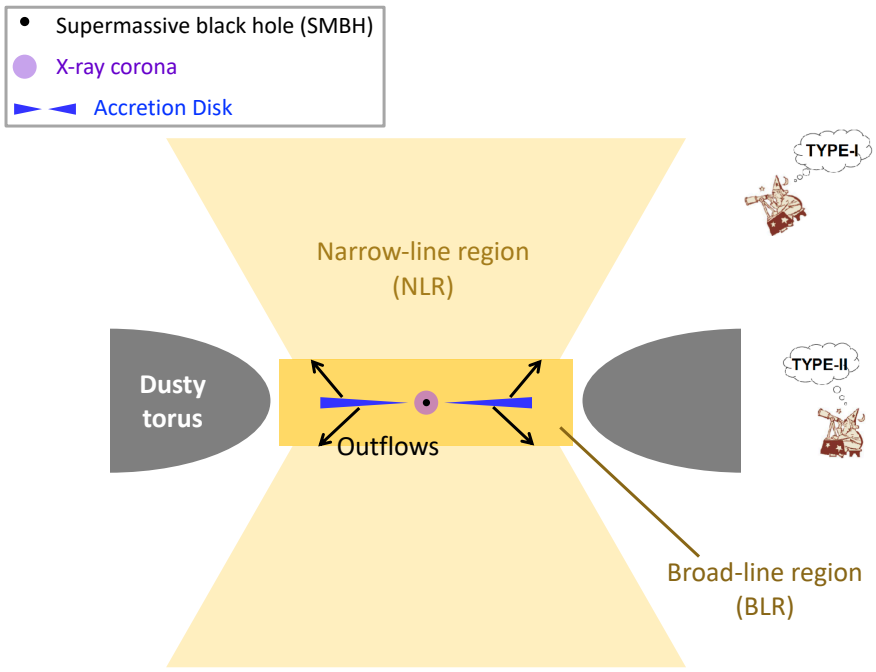

Figure 1.2: Sketch shows the structure of an active galactic nucleus. The supermassive black hole (SMBH) is represented with a black filled circle surrounded by the X-ray corona indicated with a purple filled circle. The accretion disk is shown in blue. Gas outflows launched from the accretion disk are represented with black arrows (see text in Section 1.3 for details). The broad-line region (BLR) is shaded in dark yellow. Emission lines originate at the base of the BLR (see text in Section 1.3 for details). The extended, biconical narrow-line region (NLR) is shaded in faint yellow, indicating lower particle density than in the BLR (see text in Section 1.3 for details). The grey shaded regions represent the dusty torus. The two cartoon observers depict different viewing angles to the central source (SMBH+accretion disk) that lead to the classification of AGN as type 1 or 2 objects. The cartoon observers in the figure were taken from `http://www.claudioricci.eu/AGN_UM.htm`. This figure is not to scale.

The big bump at ≈1000 Å in the UV is called the big blue bump. In the centre of a quasar, the matter orbiting around the SMBH loses angular momentum and falls into the black hole. The gravitational potential energy released in this process is converted into thermal energy, which is then radiated away from the accretion disk (Shakura & Sunyaev 1973). The temperature in this part of the accretion disk is on the order of 10^4 Kelvin. This inner disk emission directly appears in a quasar SED as the big blue bump, which is approximated with a multi-temperature blackbody curve that shows peak emission at $\approx 10^{15}$ Hz.

[8]Interstellar medium is the diffuse medium of gas and dust that fills the space in between the stars in a galaxy.

The smaller bump at ∼3–5 μm[9] in the near-IR is labelled the "Near-IR bump". This radiation is thought to emerge from the inner part of a torus-like structure surrounding the accretion disk. The radius of this region is defined by the dust sublimation radius at temperatures of ∼1500 Kelvin, inside which graphite dust grains sublimate (Barvainis 1990). Previous studies have found silicate emission and absorption features at ∼10 μm that confirm the presence of silicate dust in this region (e.g., Siebenmorgen et al. 2005). The bulk of power in the IR is observed coming from the region of ∼10–20 μm, labelled the "Mid-IR bump", which is well explained by the disk+wind hypothesis by Hönig & Kishimoto (2017).

One way of interpreting the contributions from different spectral regimes is by considering the slope of the ionizing SED. Tananbaum et al. (1979) correlated the optical luminosities of quasars with their X-ray luminosities by introducing the optical-to-X-ray spectral index, $\alpha_{\rm ox}$. The definition of this original term was slightly modified by Just et al. (2007) as follows:

$$\alpha_{\rm ox} = \frac{\log(F_{\nu\ [2\ \rm keV]}/F_{\nu\ [2500\ \text{Å}]})}{\log(\nu_{2\ \rm keV}/\nu_{2500\ \text{Å}})} \tag{1.8}$$

where $F_{\nu\ [2\ \rm keV]}$ and $F_{\nu\ [2500\ \text{Å}]}$ are the monochromatic flux densities at 2 keV and 2500 Å, respectively, in the rest frame. The spectral index basically represents the slope of the ionizing SED. A less negative $\alpha_{\rm ox}$ signifies a harder ionizing SED, where some soft X-rays ionize the gas surrounding the SMBH slightly more than in the case of a quasar with a softer ionizing SED, corresponding to a more negative $\alpha_{\rm ox}$ (steeper optical-to-X-ray slope).

1.3 Basics of Quasar Spectra

The main features in a quasar optical-UV spectrum are the continuum emission from the accretion disk and emission and absorption lines observed in both high- and low-ionization electronic transitions. Transitions that have high probabilities of occurrence in high particle density environments are called *permitted transitions*, which generate broad and narrow lines (e.g., Balmer lines such as Hβ λ4861, Hδ λ4102, He I λ5877; C IV λ1549; Mg II λ2799) observed in quasar spectra. In the regions of low particle densities, the observed transitions are those with extremely low probabilities of occurrence, called *forbidden transitions*. In such environments, the average time between particle collisions is large, and hence electrons in a metastable excited state can remain there for a reasonably long time before decaying to a lower energy state and emitting a photon. At low particle densities, where the de-excitation occurs radiatively resulting in forbidden emission lines, the line intensities are directly proportional to n^2, where n is the number density of particles. Forbidden transitions generate only narrow lines (e.g., [Ne III] λ3968; [O III] $\lambda\lambda$4960, 5008) in quasar spectra.

The emission and absorption lines can have narrow velocity widths of hundreds of km s^{-1} or they can be broad with velocity widths equal to several thousand km s^{-1} (e.g., Charlton & Churchill 2000). In the standard quasar model, the broad and narrow lines arise in two physically separate regions that vary in spatial scale. They are:

1. The *Broad Line Region* (BLR): This is a spatially unresolved region within ∼1 pc[10] of

[9] 1 micrometre (μm) 10^{-6} metre (m)

[10] 1 parsec (pc) $\approx 3.086 \times 10^{18}$ cm

the central SMBH (see Figure 1.2). Calculations from flux ratios of broad emission lines observed in quasar spectra yield 10^4 Kelvin as the average temperature of the gas in this region and $\simeq 10^9$ cm^{-3} as the upper limits on electron densities (Netzer 2013; Krolik 1999). The broad lines observed with velocity widths of several thousand km s^{-1} originate in this region. Such large widths of the broad lines and the temperature of the gas in this region imply that in addition to the thermal motions of the gas, the lines undergo Doppler broadening as the gas orbits around the SMBH.

2. The *Narrow Line Region* (NLR): This is an extended region surrounding the BLR and has a spatial scale of $\geqslant$100 pc from the central SMBH (see Figure 1.2). The temperatures and densities in this region are different from those in the BLR. The gas here is at much lower electron densities of $\approx 10^2$–10^4 cm^{-3} (Netzer 2013). The narrow emission lines arise in this region. Since this region has a much larger spatial extent, it forms a link between the BLR and the interstellar medium of the host galaxy.

Physics of the broad and narrow lines are mainly dominated by photoionization[11] of the gas by the continuum radiation from the central source. This process is required to produce some high-ionization lines for which collisional ionization[12] alone is not sufficient. Line production via photoionization depends upon several parameters such as the shape of the ionizing continuum, the particle density and composition of the gas, and the distance between the central source and the emitting gas. An important parameter to consider in this context is the ionizing photon flux (Φ) which is the number of ionizing photons incident, per unit area per unit time, on the side of the gas facing the central source. This, combined with the particle density of the gas, defines the ionization parameter (U) as follows:

$$U \equiv \frac{\Phi}{n\,c} \text{ (dimensionless)} \tag{1.9}$$

Line production in the broad line region can be modelled by the locally optimally emitting cloud (LOC) paradigm. A range of the parameters on the right-hand side of Equation 1.9 are fed into quasar photoionization models to simulate how photoionization is responsible for producing the line features in quasar spectra. These models employ combinations of the required parameters while accounting for the processes operating in the region of gas (modelled as gas clouds) to predict an observed quasar spectrum. It carefully considers the density and ionization parameter space of a gas cloud. For example, a cloud too close to the central source will be over-ionized, whereas the one far away from the source might not be ionized enough to produce a specific transition line; highly dense gas can suppress certain emission lines. Thus, an emission line is primarily produced in the LOC, where the density and ionization conditions are optimum for the production of that line (e.g., Baldwin et al. 1995; Krolik 1999).

Many theoretical models predict gas outflows originating from the accretion disk, $\sim 10^{16}$ cm from the central engine (e.g., Murray et al. 1995; Proga et al. 2000). These originate as a result of line driving when the radiation pressure from the central source transfers considerable

[11] Photoionization is the process in which electromagnetic radiation interacts with matter and dissociates it into electrically charged particles.

[12] Collisional ionization is the process by which ionization occurs due to collisions of particles with each other causing an increase in the temperature of the matter.

momentum to the gas in the disk (Proga et al. 2000). Here, the presence of shielding gas (X-ray absorbing gas) in the region close to the central SMBH (Murray et al. 1995) plays a key role as it shields the gas in the disk and does not allow it to become over-ionized due to X-rays from the central source. This enables the UV radiation to accelerate the gas away from the centre. Figure 1.3 shows the schematic of a quasar model containing the central SMBH surrounded by an accretion disk. Broad emission lines are generated at the base of the UV line-driven outflows. The purple shaded regions on either sides of the SMBH indicate the shielding gas that absorbs high-energy X-ray radiation thus helping the more energetic UV outflows to be radiatively driven from the disk. Less energetic dust-driven winds emerge from the outer layers of the accretion disk where dust can survive.

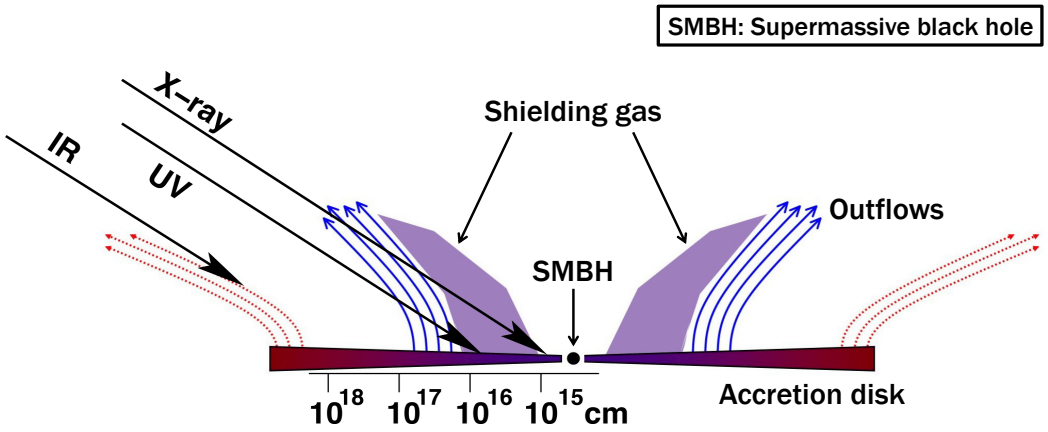

Figure 1.3: Schematic view of a quasar model with its components labelled. The colour gradient of the accretion disk goes from violet indicating high-energy radiation in the X-ray, close to the supermassive black hole (SMBH), to dark red indicating less energetic emission in the IR. The shielding gas is indicated with purple shaded regions close to the SMBH. The UV outflows emerging in the inner accretion disk are indicated with blue arrows and the IR outflows in the outer parts of the disk are indicated with red arrows. The X-ray, UV, and IR lines of sight through the outflows are shown with black arrows. This image is taken from Gallagher & Everett (2007) and annotated here.

A quasar spectrum is rich in features highlighting the different components: accretion disk, emission lines, and absorption lines. Figure 1.4 shows the composite spectrum of Sloan Digital Sky Survey (SDSS) quasars. This spectrum is corrected for cosmological redshifting, which is done simply by rearranging Equation 1.6 and solving for $\lambda_{\rm emit}$ as follows:

$$\lambda_{\rm emit} = \frac{\lambda_{\rm obs}}{1+z} \tag{1.10}$$

The spectrum in Figure 1.4 is thus in the rest wavelength ($\lambda_{\rm rest}$) space.

To study the Doppler line-of-sight (LOS) velocities ($V_{\rm LOS}$) of the emission and absorption features, a quasar spectrum can be shifted from the wavelength or frequency frame to the velocity frame. If the gas is flowing toward (blueshifted) or away (redshifted) from the observer

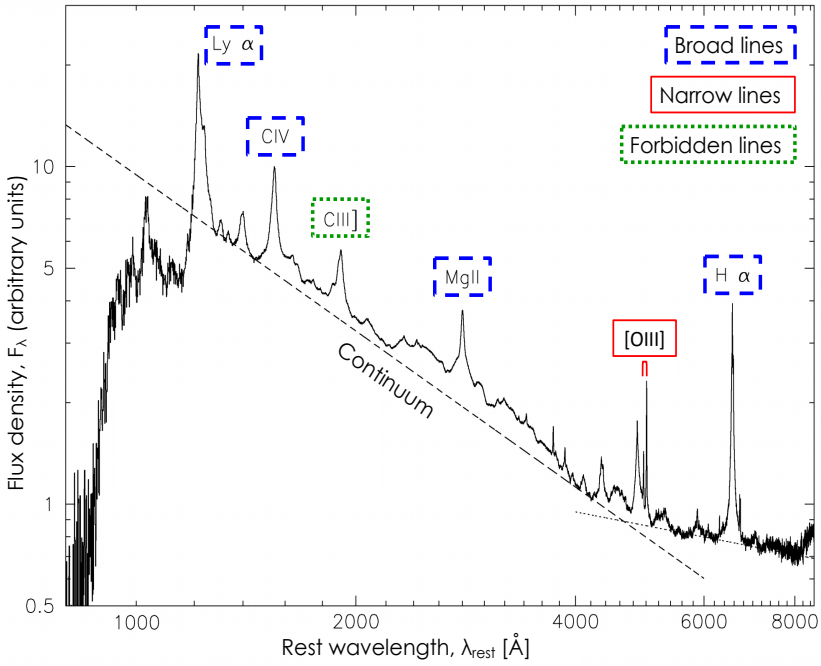

Figure 1.4: Rest-frame composite spectrum (solid line in black) of 2204 quasars from the Sloan Digital Sky Survey (SDSS) catalogue. Power-law fits to the quasar accretion disk continuum are indicated with black dashed and dotted lines. Labels for permitted transitions observed in broad and narrow emission features are enclosed in blue dashed boxes. The label for [O III] $\lambda\lambda 4960, 5008$ forbidden transition is marked with a red solid box around it. The C III] $\lambda 1909$ semi-forbidden transition label is enclosed in a green dotted box. This figure is taken from Vanden Berk et al. (2001) and annotated here.

at very high velocities comparable to the speed of light, relativistic effects must be taken into consideration, and Equation 1.11 must be used to solve for $V_{\rm LOS}$.

$$\nu_{\rm obs} = \nu_{\rm emit} \sqrt{\frac{1 + \frac{V_{\rm LOS}}{c}}{1 - \frac{V_{\rm LOS}}{c}}} \tag{1.11}$$

where $\nu_{\rm emit}$ and $\nu_{\rm obs}$ are the emitted and observed frequencies. For low-velocity gas, the Doppler equation simplifies to:

$$\nu_{\rm obs} = \nu_{\rm emit} \frac{V_{\rm LOS}}{c} \tag{1.12}$$

Cosmological time dilation (or simply, time dilation) is another effect that must be taken into account for high-redshift objects. At higher redshifts, time appears to pass slower and thus takes longer to reach the Earth. An observer will record this dilated time ($t_{\rm obs}$) given by Equation 1.13.

$$t_{\rm obs} = \frac{t_{\rm rest}}{\sqrt{1 - \frac{V_{\rm LOS}^2}{c^2}}} \tag{1.13}$$

where $t_{\rm rest}$ is the time in the rest frame of the object. Gas with $V_{\rm LOS} = 0$ is located in the same frame of reference as the object and is said to be at the systemic redshift, where $\lambda_{\rm obs}$ ($\nu_{\rm obs}$) equals $\lambda_{\rm rest}$ ($\nu_{\rm rest}$[13]) and $t_{\rm obs}$ equals $t_{\rm rest}$.

1.4 Super-Eddington AGN

While typical AGN at low redshifts accrete below the sub-Eddington limit, a subset of the AGN population has high accretion rates well above the Eddington limit (see $L_{\rm Edd}$ in Section 1.1). These highly accreting objects, called the Super-Eddington AGN, likely evolved during cosmic noon (z = 1–3), an era in the history of the Universe that witnessed rapid black hole growth (Brandt & Alexander 2010; Shen et al. 2020).

Super-Eddington AGN are characteristically different than their sub-Eddington counterparts. The sub-Eddington class of AGN are defined by accretion rates a few percent of the Eddington limit and possess a thin-disk structure (Shakura & Sunyaev 1973). However, when mass accretion rates in AGN exceed the Eddington limit, radiation pressure is expected to dominate, consequently inflating the inner disk vertically. The resultant puffed disk is called a 'slim' disk with a scale height, $H_{\rm disk} \leq R_{\rm disk}$, where $R_{\rm disk}$ is the radius of the disk (e.g., Abramowicz et al. 1988). Figure 1.5, panel *a* displays a schematic of a puffed disk structure. The $H_{\rm disk}$–$R_{\rm disk}$ relation in Figure 1.5, panel *b* shows that the size of these disks is estimated at 10^4 gravitational radii (or Schwarzschild radii). The gas in a slim disk follows sub-Keplerian rotation and transonic speeds. The fast radial flow causes photons in the inner disk to get trapped in the accreting matter, into the black hole.

Previous studies have attempted to explain the structure of super-Eddington AGN. Jaroszyński et al. (1980) proposed a funnel model for such systems. They suggested that the inner disk edges of highly accreting objects are close to their bound orbit around the black hole that decreases the disk efficiency of converting mass into radiation. Radiation then flows outward through a funnel along the rotational axis that forms due to a puffed inner disk. In the photon-trapping region, the scale height of the disk increases significantly, thus casting a shadow on the outer disk (e.g., Wang et al. 2014a). Alternatively, Begelman (2002) proposed that the disks in super-Eddington AGN may become inhomogeneous at scales much smaller than the disk scale height due to the development of "photon-bubble instability" – a scenario where gas loops non-linearly between overdense and underdense regions in radiation pressure-driven atmosphere. Even though many models exist to explain the disks in highly accreting AGN, observational studies of these objects are less common.

Empirically, highly accreting AGN exhibit distinct features when compared to the sub-Eddington AGN. The Narrow-Line Seyfert 1 (NLS1) objects are observed to have high accretion rates. Recent studies such as the Super-Eddington Accreting Massive Black Holes (SEAMBH) campaign have been studying the physical properties of identified NLS1 candidates through both photometry and spectroscopy (e.g., Du et al. 2014, 2016a,b, 2018; Hu et al.

[13] $\nu_{\rm rest}$: Rest frequency

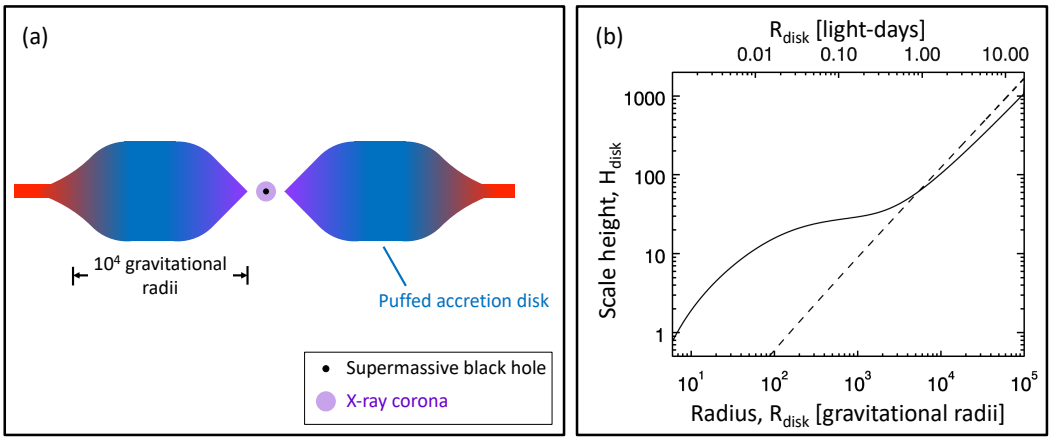

Figure 1.5: Panel *a*: Edge-on schematic of the inner regions of an AGN with a puffed accretion disk, a.k.a. a 'slim disk'. The central supermassive black hole (black filled circle) is surrounded by the X-ray corona (purple filled circle). In this kind of structure, the outer disk may be shielded from the X-ray corona and therefore exhibit a different pattern of correlated X-ray/UV-optical continuum variability compared to a thin disk. Panel *b*: The expected scale height ($H_{\rm disk}$) as a function of radius ($R_{\rm disk}$) for a slim-disk model for a super-Eddington AGN, Markarian 142 (solid line), compared to a Shakura & Sunyaev (1973) thin disk (dashed line). The structure of the slim disk shows a significant hump within ~4000 gravitational radii, where gravitational radius has the same definition as the Schwarzschild radius (model data from Wang et al. 2014a). In AGN with compact X-ray coronae, this hump will prevent the optical emitting region of the disk from receiving direct X-ray radiation close to the central black hole.

2015). From these observations, Du et al. (2016b) showed that the BLR structure in highly accreting AGN is significantly different than the structure in AGN with lower Eddington values. That is, at a given luminosity super-Eddington AGN tend to have smaller BLRs than the (more typical) sub-Eddington population. Du et al. (2018) also discuss about the mass accretion rate as a possible factor affecting the sizes of the BLRs in high accretion-rate AGN. The studies on super-Eddington AGN thus far clearly highlight that this subset of AGN is distinct than the more typical population. Considering the findings by the SEAMBH group and a lack of observational studies of super-Eddington AGN, further research is required to develop a better understanding of their disk and BLR structures.

1.5 Quasar Variability

Quasars are variable on timescales from several days to weeks or years (e.g, Peterson et al. 1982). The observed variability is attributed to the complexity of the quasar phenomenon within the small size scales of the BLR, where the accretion disk generates a time-variable continuum that then ionizes and heats up the nearby gas producing broad emission lines. In response to the varying continuum, the fluxes of the broad emission lines vary as well, but with a time lag (see Section 1.6.2) equal to the light travel time between the accretion disk and the

BLR. Thus, variability in quasars can arise both due to the variations in the continuum emission from the accretion disk and the BLR gas.

Some of the first studies of low-luminosity quasars (e.g., Clavel et al. 1991; Peterson et al. 1991; Dietrich et al. 1993) established two important findings about AGN variability. They are:

1. The continuum variations from the shortest wavelengths (≈1350Å) to the longest wavelengths (≈5100Å), occur in phase with the amplitude of variations decreasing from the shortest to the longest wavelengths. This suggested that the variability amplitude had a wavelength dependence.

2. The highest ionization emission lines (e.g., He II λ1640, Lyα λ1215, C IV λ1549) respond more rapidly to any changes in the continuum flux indicating an origin closer to the black hole, whereas the lowest ionization lines (e.g., Hβ λ4861, C III] λ1909) have the largest time lags indicating that the gas originated further out in the accretion disk (see Section 1.6.3 for further details). This difference signified that the BLR is a region with radial ionization stratification.

Quasar variability studies use the observed characteristics of the continuum variability to understand the parameters that produce it (e.g., Trèvese et al. 2001, and references therein). To quantify quasar continuum variability, a common approach is structure-function analysis (e.g., Collier & Peterson 2001), where structure function is defined as the root-mean-square (RMS) change in the magnitude value for a quasar ($\Delta m_{\rm obs}$) as a function of the time difference between measurements ($\Delta t_{\rm obs}$). Typically, structure-function analysis is carried out in both the observer's frame of reference as well as the rest frame of the quasar since the former is useful to distinguish quasars from other objects (e.g., transients) based on the variability timescales involved and the latter is vital to build physical interpretations of quasars. More recently, variability studies of quasars have introduced a modelling technique called damped random walk (DRW) that characterizes variability in quasar light curves using two parameters, the amplitude from structure-function analysis (the amplitude of long-term variations in the light curve) and the characteristic damping timescale for variations (the timescale when the light-curve variations return to the mean). These parameters can then be correlated to physical properties of quasars.

MacLeod et al. (2010) studied quasar variability in a spectroscopically confirmed sample of quasars in SDSS Stripe 82[14] and confirmed well known variability trends with luminosity and redshift as illustrated in Figure 1.6. Panel *a* shows that the amplitude of long-term variability in the sample of quasars anti-correlates with luminosity (where the *i*-band absolute magnitude $M_{\rm i}$ is used as a proxy for luminosity) since the quasars with smaller $M_{\rm i}$ values have lower amplitudes of variability. This shows that more luminous quasars are less variable. The horizontal dashed lines of constant variability in the panel *a* indicate no dependence on redshift, and the correlation is corrected for the dependence on rest wavelength. Panel *b* shows a marginal anti-correlation of the characteristic damping timescale with luminosity since the quasars with smaller *i*-band magnitudes have smaller damping timescales. The correlation is again corrected for the dependence on the rest wavelength. Here, the characteristic damping timescale does show some correlation with redshift - the quasars at higher redshifts have smaller damping

[14]Stripe 82 is a region of the sky observed repeatedly in one of the SDSS surveys. See Abazajian et al. (2009).

timescales. The results depicted in Figure 1.6 thus restate the luminosity-redshift dependence of quasars - the high-redshift quasars are more luminous with lower variability amplitudes and therefore smaller characteristic damping timescales than the low-redshift quasars.

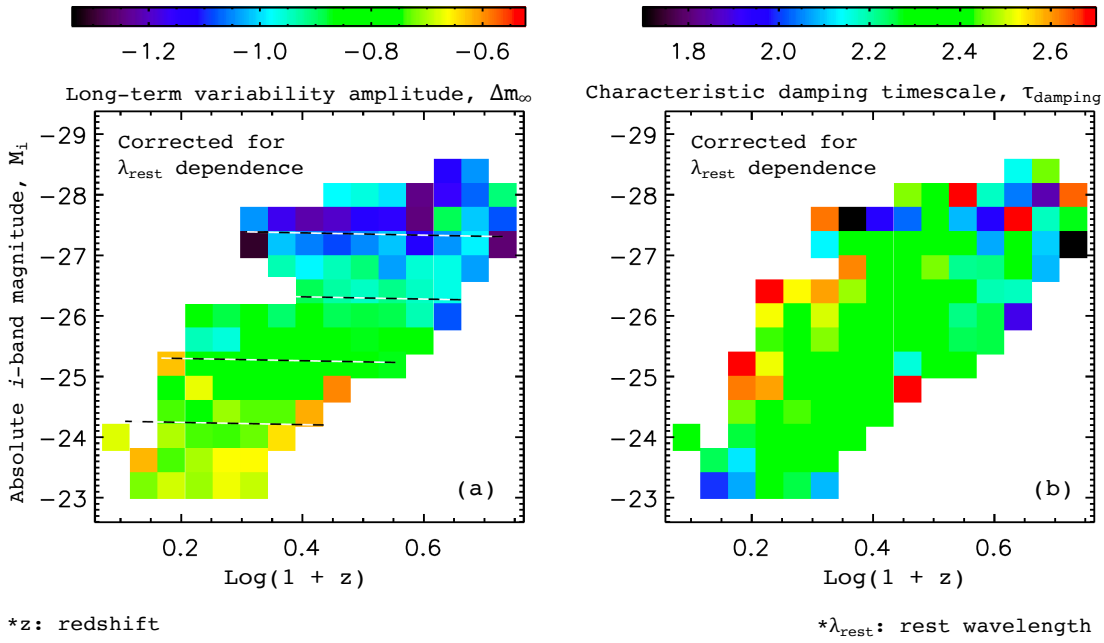

Figure 1.6: Observed variability amplitude ($\Delta m_{\rm obs}$) from structure-function analysis (panel *a*) and the characteristic damping timescale ($\tau_{\rm damping}$) of variability (panel *b*) colour-coded in both panels (with the colour bar displayed above the upper X-axis) on a grid of $M_{\rm i}$–log $(1+z)$, where $M_{\rm i}$ is the absolute magnitude in the *i*-band (centred at ≈7625Å) and z is the redshift, for a selected sample of the SDSS Stripe 82 quasars. The black dashed lines in the left panel indicate lines of constant variability. Both the plots are corrected for the dependence on rest wavelength ($\lambda_{\rm rest}$). This figure is taken from MacLeod et al. (2010) and annotated here.

1.6 Reverberation Mapping

Many quasar variability studies apply a powerful tool called *reverberation mapping* (RM; e.g., Blandford & McKee 1982; Peterson 1993; Cackett et al. 2021) that can make use of the continuum variability in quasars and corresponding response of the emission lines with a time lag to infer the structure and understand the kinematics in the BLR. Thus, the RM technique uses time resolution to study the structure and geometry of the inner environment of quasars, which otherwise remains unresolved at observable angular scales (on the order of μarcseconds[15]).

[15] 1 arcsecond $\approx 4.848 \times 10^{-6}$ radians

1.6.1 Underlying Assumptions

There are a few basic assumptions made in RM studies. They are:

1. The continuum emission originates in a single, central source that emits isotropically: The continuum emission in a quasar originates in the accretion disk and is therefore not isotropic (owing to the shape of the disk). However, there is a relatively narrow range of quasar viewing angles which provide a view of the continuum and the BLR. Therefore, the central source in a quasar can be assumed to emit isotropically. This source is confined to a region of size $\sim 10^{13}$–10^{14} cm and is much smaller than the size scale of the BLR, which is $\sim 10^{18}$ cm (Murray et al. 1995; Peterson 2009). Therefore, the assumption of a single, central continuum source is reasonable.

2. The photons from the continuum source and the emission-line region can freely propagate at the speed of light in the BLR volume, and the light travel time in the region is the most important timescale in this context: The light travel time across the BLR volume is on the order of several days to weeks (Peterson 1993). This is the timescale of continuum variations observed in quasars. In comparison, the other timescales to consider are: 1. *The Recombination time*, defined as the time taken by gas in the BLR to reprocess the ionizing continuum photons into emission-line photons; and 2. *The Dynamical time*, defined as the time taken by a gas element in the vicinity to cross the BLR. In the BLR, particle densities are quite high, $\sim 10^9$ cm^{-3}, resulting in recombination times far less than an hour (Peterson 1993). Thus, the recombination timescale is much smaller than the continuum variability timescale which is critical to be able to detect the emission-line responses to continuum variations. The dynamical time, on the other hand, is usually up to several years for these systems (Peterson 1993). This is much larger than both the recombination and the continuum variability timescales and therefore indicates that there are no global changes in the system throughout the period of the RM experiment.

3. There exists a simple relationship between the observed continuum and the ionizing continuum in the BLR that produces the emission lines: The quasar continuum appears to follow a power-law behaviour. However, the functional form of the ionizing continuum that produces the emission lines is not well known. Because it is difficult to measure the ionizing continuum, the observed continuum closest to the emission lines is used as a proxy for the ionizing continuum although there are some uncertainties associated with that assumption.

1.6.2 Geometry of the BLR

Despite the various assumptions in reverberation mapping, its application does not require any specific geometry of the BLR. However, it is worth considering a simple configuration of the BLR to better understand how the BLR gas responds to variations in the central source continuum.

As described in Peterson (1993), it is useful to consider the BLR as a thin spherical shell of gas with a single continuum source located at the centre. The distance measured from the central source to the spherical shell is given as the radius of the shell, R. In this arrangement,

in general, the spherical shell absorbs the continuum emission and re-radiates it in the form of emission lines. Now, imagine that an increase in the continuum emission occurs due to a sudden outburst of energy in the central source (termed "a δ-function outburst" in Peterson 1993). This radiated energy pulse expands away from the central source as a spherical shell travelling at light speed. At some point, the expanding energy pulse will encounter the spherical gas shell, and this time is equal to the one-way light travel time between the source and the spherical gas shell, R/c. The gas shell then absorbs the radiation and rapidly reprocesses it into emission lines. In this scenario, an observer at the central continuum source will record the response of the emission lines after the energy pulse returns from the gas shell to the source in time, $2R/c$. This is now the two-way light travel time between the observer at the centre and the gas shell. In reality, however, the observer is not at the central source, but located far away from the system. For this observer, the geometry is more complicated as the points on a spherical gas shell are no longer at the same distance. As a result, the time taken by those points to respond to the changes in the continuum flux will be spread out in time. A useful definition to visualize the emission-line response in this context is of an isodelay surface - the locus of all points that respond at the same time lag (or time delay), τ as seen by an observer (Peterson 1993). For an observer located on the central continuum source, isodelay surfaces are concentric spherical shells centred on the continuum source, whereas an observer very far away from the source will see the isodelay surfaces as concentric paraboloids enveloped around the LOS. Figure 1.7 shows the isodelay surfaces of the BLR (assumed to be a thin spherical shell) seen as projected paraboloids by a distant observer in the direction of the red arrow. A sudden continuum outburst in the central source produces the ionizing photons. When these photons reach the BLR shell, they are reprocessed and emitted by the BLR.

From Figure 1.7, it is evident that the gas in the BLR that is close to the distant observer (the near side), along the LOS between the observer and the continuum source, will appear to respond to any continuum changes more rapidly than the gas behind the continuum source (the far side). This response time is termed as the time lag (see Section 1.5), which is measured for different emission lines in quasar spectra. The equation for τ is:

$$\tau = \frac{R}{c}\,(1 + \cos\theta) \tag{1.14}$$

(Peterson 1993), where θ is the angle measured from an observer's LOS to a point in BLR. Thus, $\cos\theta$ is 1 when $\theta = 0^\circ$ for gas on the farthest side of the BLR, resulting in the largest time lag of $2R/c$; for the gas right in front of the continuum source, $\theta = 180^\circ$ and $\cos\theta$ is -1 resulting in the smallest time lag of 0.

1.6.3 The Transfer Equation

One-dimensional Transfer Function and Cross-Correlation Analyses

The emission-line response of the BLR system to a continuum change at a given τ, can be described by a "transfer function" (see Blandford & McKee 1982; Peterson 1993) given by $\psi(\tau)$. In the simplest reprocessing model, the emission-line response is taken to be linearly proportional to the central continuum emission with the transfer function giving the proportionality constant. The total response of the BLR is then a convolution between the continuum

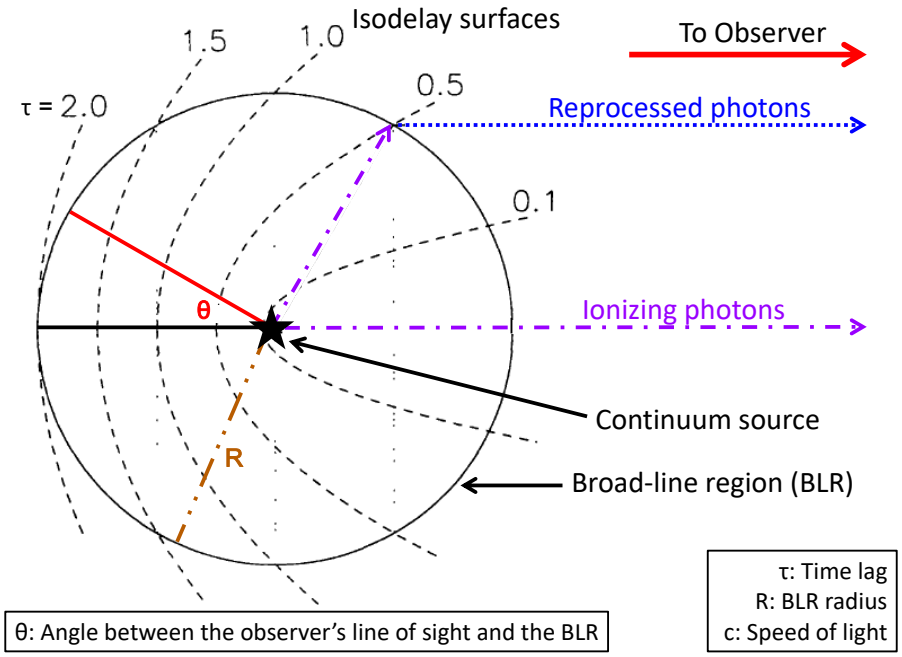

Figure 1.7: Schematic of a thin, spherical broad-line region (BLR) shell with isodelay surfaces marked with black dashed lines, wrapped around the line of sight (LOS) of a distant observer located in the direction of the red solid arrow. The central continuum source is represented with a black star at the centre of the shell. The purple dotted-dashed arrow indicates the ionizing photons emerging directly from the continuum source, and the reprocessed photons are indicated with the blue dotted arrow. The location of the gas on the BLR shell is given by the red solid line at an angle θ from the black solid line (parallel to the LOS of the distant observer). This figure is modified from Horne (1999).

variations of the source and the transfer function that can be embedded in what is called the "transfer equation" (see Blandford & McKee 1982; Peterson 1993) as follows:

$$L(t) = \int_{-\infty}^{\infty} \psi(\tau)\, C(t-\tau)\, \mathrm{d}\tau \tag{1.15}$$

where $L(t)$ is the emission-line light curve and $C(t)$ is the continuum light curve at specific times, t. A light curve is a plot of brightness vs. time for a given object. It signifies how the brightness of an object changes with time over the course of observations. Since gas in different regions of the BLR responds with different time lags, the net emission-line light curve, $L(t)$, at the observer's location is integrated over all time lags.

The goal of reverberation mapping is to solve the integral in Equation 1.15 for $\psi(\tau)$ using the observables, $L(t)$ and $C(t-\tau)$ at specific times, t, and deduce the geometry of the BLR. With a large enough number of data points in quasar light curves, Equation 1.15 can be directly solved for $\psi(\tau)$ through cross-correlation analyses (see Peterson 1993; White & Peterson 1994). In this process, the emission-line light curve is cross-correlated with the continuum light curve and the cross-correlation function ($F_{\mathrm{CCF}}(\tau)$) is given as:

$$F_{\rm CCF}(\tau) = \int_{-\infty}^{\infty} L(t)\, C(t-\tau)\, {\rm d}t \tag{1.16}$$

However, $L(t)$ is also a convolution between $\psi(\tau)$ and $C(t)$ (see Equation 1.15) and hence by substituting Equation 1.15 into Equation 1.16, we can write $F_{\rm CCF}(\tau)$ as follows:

$$F_{\rm CCF}(\tau) = \int_{-\infty}^{\infty} C(t-\tau) \int_{-\infty}^{\infty} \psi(\tau')\, C(t-\tau')\, {\rm d}\tau'\, {\rm d}t \tag{1.17}$$

In order to interpret the right hand side of Equation 1.17, it is useful to define the auto-correlation function ($F_{\rm ACF}(\tau)$) as follows:

$$F_{\rm ACF}(\tau) = \int_{-\infty}^{\infty} C(t)\, C(t-\tau)\, {\rm d}t \tag{1.18}$$

(Peterson 1993). The auto-correlation function describes a convolution of the continuum light curve with itself and is therefore expected to peak at the τ value of 0 days. If the order of integration in Equation 1.17 is now reversed, $F_{\rm CCF}(\tau)$ can be written as:

$$F_{\rm CCF}(\tau) = \int_{-\infty}^{\infty} \psi(\tau')\, F_{\rm ACF}(\tau-\tau')\, {\rm d}\tau' \tag{1.19}$$

(Penston 1991; Peterson 1993), where $F_{\rm CCF}(\tau)$ is now a cross-correlation between $\psi(\tau)$ and the $F_{\rm ACF}$ at $(\tau - \tau')$. The time-shift between the continuum and the emission-line light curves at which this cross-correlation is maximized is defined as the time lag of a particular emission line with respect to the continuum. This technique of cross-correlation analysis has been applied in several studies of local AGN to measure time lags for different emission lines (e.g., Denney et al. 2010; Edelson et al. 2015; Fausnaugh et al. 2016). Since the continuum variations occur rapidly (e.g., of order days), $F_{\rm ACF}$ usually has a sharp peak which yields a sharp peak for $F_{\rm CCF}$ fairly close to where the $\psi(\tau)$ distribution peaks; however, slow changes in the continuum cause the $F_{\rm ACF}$ peak to broaden, resulting in the $F_{\rm CCF}$ peak closer to the centroid of the $\psi(\tau)$ distribution (Horne 1999). Thus, the precision of RM time lags depend on the characteristics of the continuum emission described by $F_{\rm ACF}$ as well as how the BLR responds to the continuum changes as given by $\psi(\tau)$.

Figure 1.8 shows comparison plots from the cross-correlation analyses for two quasars – one where the peak τ is clearly evident (*Left* panel) and other where the no τ is identifiable – from the Sloan Digital Sky Survey Reverberation Mapping (SDSS-RM) project (see Section 1.8.1 for more information). Here, the cross-correlation is performed between the 5100 Å continuum and the Mg II emission-line light curves (*Top* panels). In the *Middle* panels for both quasars, the difference in the nature of their $F_{\rm ACF}$ is clearly evident. The quasar with Reverberation-Mapping Identifier, RMID = 229 shows a narrower $F_{\rm ACF}$ peak and thus an $F_{\rm CCF}$ curve that gives a clear result for τ. In contrast, the quasar with RMID = 589 shows a smeared $F_{\rm CCF}$ profile without an obvious $F_{\rm CCF}$ peak. In both cases, τ for the Mg II line is given by the centroid of the $F_{\rm CCF}$ curve. The centroid value gives a more robust measurement of τ than simply the peak value of the $F_{\rm CCF}$ curve. The 1σ uncertainties in the lag measurements are indicated with blue dashed vertical lines.

Although most RM applications assume a transfer function (e.g., a top-hat function), some methods have been used in the past to determine it. Blandford & McKee (1982) attempted

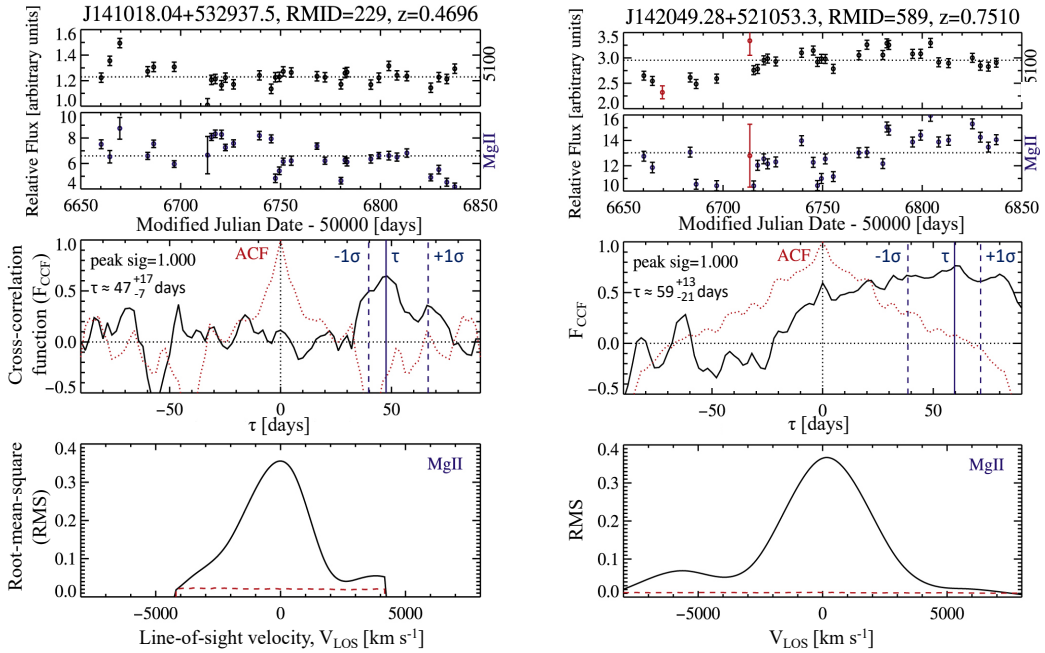

Figure 1.8: Continuum emission at 5100 Å and the Mg II emission-line light curves in the *Top* panels; cross-correlation function ($F_{\rm CCF}$) and auto-correlation function ($F_{\rm ACF}$) in the *Middle* panels; and model root-mean-square (RMS) line-velocity profile of Mg II in the *Bottom* panels from the cross-correlation analyses performed for two of the targets of the Sloan Digital Sky Survey Reverberation Mapping (SDSS-RM) project, J141018.04+532937.5 (*Left* panel) and J142049.28+521053.3 (*Right* panel). The Reverberation-Mapping Identifiers (RMIDs) are the index values assigned for the quasars in the SDSS-RM catalogue. In the *Top* panels, bad epochs are indicated in red. In the *Middle* panels, the black solid curve represents $F_{\rm CCF}$, the red dotted curve represents $F_{\rm ACF}$, the time lag (τ) measured is indicated with a blue solid vertical line, and the 1σ uncertainties in the time lag measurements are marked with blue dashed vertical lines. In the *Bottom* panels, the RMS flux errors for the emission line are represented with red dashed lines. These figures are taken from Shen et al. (2016) and annotated here.

to compute $\psi(\tau)$ using a Fourier Transform method (e.g., Maoz et al. 1991). However, the irregular sampling of data points from actual observations provides less reliable results by this method. Another complication to the problem is that the relationship between the central source continuum and the ionizing continuum is not trivial. For example, as the radiation from the central source photo-ionizes the surrounding gas, the radiation itself can get inverse Compton-scattered by the gas at the same time (see Section 1.2). This can complicate the energy transfer processes in the region. As well, the emission-line response to the ionizing continuum emission is possibly non-linear. Furthermore, there may be additional sources of light (e.g., starlight or narrow emission lines) that add to the observed total spectrum, but are not considered in Equation 1.15. Horne et al. (1991) described the Maximum Entropy Method (MEM) to compute the transfer function that takes into account such complications in addition to the practical limitations of noisy and incomplete data sets (see also Krolik et al. 1991). In

MEM, the predicted continuum and emission-line light curves evaluated at the times closest to the actual observations are fit to the data and a maximum entropy "image" is recovered. This image is a union of the three sub-images representing the functions, $\psi(\tau)$, $C(t)$, and $\bar{L}(t)$, where $C(t)$ is the continuum light curve split into rapidly fluctuating variations and background continuum (generally a constant), and $\bar{L}(t)$ is the background line emission gradually varying with time. Entropy of a given image pixel measures the deviation of the pixel value from the default value supplied as input, and when the two values are equal to each other, entropy maximizes. The total entropy of the image is the sum of the entropies of the three sub-images representing $\psi(\tau)$, $C(t)$, and $\bar{L}(t)$.

Two-dimensional Transfer Function and Velocity-Delay Maps of the BLR

In addition to the time dimension, studying the response of the BLR as a function of $V_{\rm LOS}$ of the gas in the region can offer much more information about the velocity field of the BLR (and thus the spatial structure) along with its coarse geometry. The $V_{\rm LOS}$ is simply the Doppler shift (see Section 1.3) measured for the gas moving in the BLR. Writing in terms of the angle θ (see Equation 1.14), $V_{\rm LOS}$ becomes:

$$V_{\rm LOS} = -V_{\rm orb}\ \sin\theta \tag{1.20}$$

(assuming Keplerian motion; Peterson 2009), where $V_{\rm orb}$ is the orbital speed of the gas orbiting in the BLR. The goal of reverberation mapping is now shifted to solving a "two-dimensional transfer function", $\psi(V, \tau)$, in the following equation:

$$L(V,t) = \int_{-\infty}^{\infty} \psi(V,\tau)\ C(t-\tau)\ \mathrm{d}\tau \tag{1.21}$$

(Peterson 1993), where $L(v, t)$ is the velocity-dependent response of the emission line to the continuum changes.

1.6.4 Velocity Delay Maps

One of the ways of visualizing the BLR picture in $V_{\rm LOS}$–τ space is to consider it as a circulating disk of gas with a configuration that is described as a collection of concentric co-planar cylindrical annuli centred on the continuum source (Horne 1999). Figure 1.9, panel *a* shows this disk flow with two concentric annuli. Here, the observer located to the far left sees emission from the gas indicated with an open circle as blueshifted and emission from the gas indicated with a filled circle as redshifted along the LOS. The gas in the inner annulus, closer the SMBH, orbits at higher speed than the gas rotating in the outer annulus. Thus, $V_{\rm orb}$ decreases from the inner to the outer annuli. Translating this behaviour of $V_{\rm orb}$ into $V_{\rm LOS}$ using Equation 1.20, the largest values of $V_{\rm orb}$ give the maximum possible range in $V_{\rm LOS}$, while the smallest values of $V_{\rm orb}$ span the narrowest range in $V_{\rm LOS}$. Moreover, the gas orbiting closer to the central source and on the near side will have a smaller range of lower time delay values as compared to the gas farther away from the source and on the far side (see Section 1.6.2). Thus, the inner annulus in Figure 1.9, panel *a* maps to the squashed ellipse (along the time-delay axis) in panel *b*, whereas the outer annulus maps to the stretched one.

Figure 1.9, panel *b* is called a velocity-delay map. Here, it represents a Keplerian system of orbits, where $V_{\rm orb}(R) \propto R^{-1/2}$, depicting a tapering response with increasing time delays. In this system, since gas is orbiting the SMBH, it will have the same time delay on the blue and the red side of the disk. Therefore, the velocity-delay map obtained is symmetric about the systemic velocity. The approximate locations of the blueshifted and redshifted circles on the outer annulus in Figure 1.9, panel *a* are indicated in panel *b*. It should be noted that the negative axis of $V_{\rm LOS}$ showing negative values of $V_{\rm orb}$ is only a sign convention to signify that the gas is blueshifted along the LOS of the observer. Accordingly, positive values of $V_{\rm orb}$ imply that gas is redshifted.

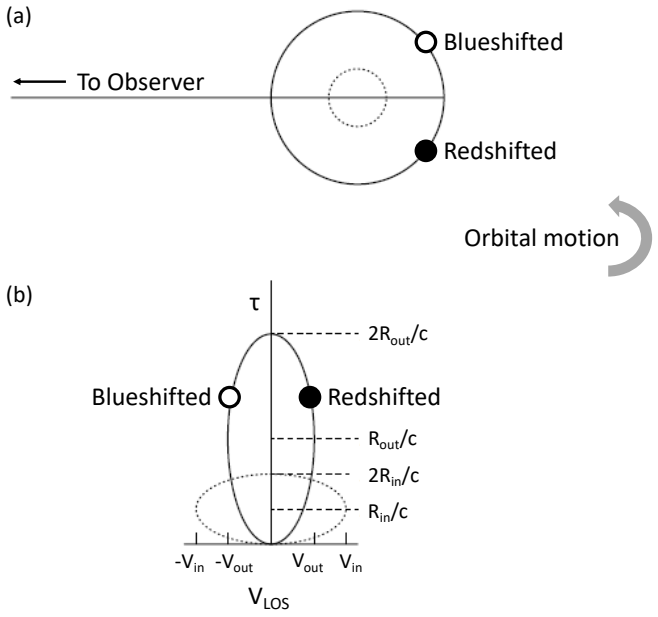

Figure 1.9: Sketches show the broad-line region (BLR) mapped in a two-dimensional space of time lag (τ) vs. line-of-sight (LOS) velocity ($V_{\rm LOS}$). Panel *a*: BLR modelled as two concentric cylindrical annuli centred on the central source. Panel *b*: Velocity-delay map of the BLR geometry in panel *a*. The inner and outer annuli in panel *a* map to the squashed and stretched ellipses (along the time-delay axis), respectively. The one-way and two-way light travel times (defined in Section 1.6.2) across the BLR for both the annuli are marked with dashed horizontal lines. In both figures, the orbital motion of the BLR gas around the central black hole is in the anti-clockwise direction indicated with the grey arrow. A distant observer to the far left of the figures sees the open circle blueshifted and the filled circle redshifted along the LOS. This figure is taken from Peterson & Horne (2004) and annotated here.

Velocity-delay maps can not only trace circular motions of the gas around the SMBH, but also convey information about any red-blue asymmetries generated by inflowing or outflowing gas along the radial direction in the BLR. For example, inflowing gas on the near side (where τ is small) will appear to be redshifted ($V_{\rm LOS} > 0$) and on the far side (where τ is large) will be blueshifted ($V_{\rm LOS} < 0$). On a velocity-delay map, this inflowing gas will therefore span

the space of smaller time delays on the red side and larger time delays on the blue side. In contrast, the signature of outflowing gas on a velocity-delay map will be larger time delays on the red side and smaller time delays on the blue side since it will produce an exactly opposite red-blue asymmetry as compared to the inflowing gas. Gas in simple Keplerian motion around the SMBH will not give rise to any asymmetries in the velocity-delay space. Figure 1.10, taken from Horne et al. (2004), represents the theoretical velocity-delay map (panel *b*) as well as the one recovered (panel *c*) from simulated quasar spectra for a single UV emission line, C IV λ1549 in the case of a spiral density wave in the C IV BLR gas.

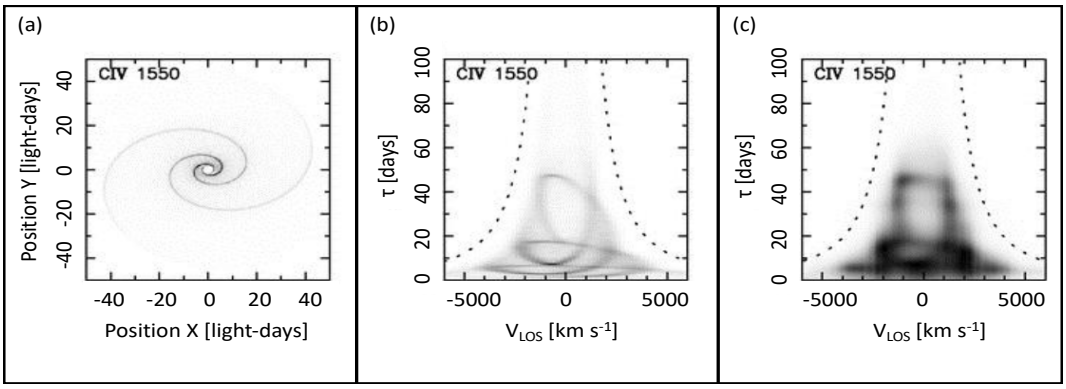

Figure 1.10: Theoretical and recovered (from simulated spectra) velocity-delay maps of the C IV λ1549 line in the UV. Panel *a*: Sky view of the broad-line region (BLR) model, which is a Keplerian disk with elliptical orbits (eccentricity of 0.3) having inclination of 45°, and two trailing spiral arm structures. Panel *b*: Theoretical velocity-delay map of C IV. Panel *c*: Recovered velocity-delay map of C IV. The two dotted curves in the panels *b* and *c* indicate the boundaries of the accretion disk. This figure is taken from Horne et al. (2004).

To study the BLR structure and kinematics using velocity-delay maps, we first need determine the requirements to extract the structure of gas flow in the BLR. Horne et al. (2004) constructed the theoretical velocity-delay map in Figure 1.10 by modelling the BLR as an elliptical Keplerian disk comprised of 10^5 discrete gas clouds in circular motions around a black hole of mass $3 \times 10^7 M_{\odot}$. The plane of the Keplerian orbits was kept inclined at 45° to the LOS, and a "twist" was given to the orbits to generate a trailing spiral arm pattern in the disk. The physical conditions in the disk were modelled with a power law similar to the one defined in Kaspi & Netzer (1999) where both the number density and the column density (defined as the number of particles per unit area in a column of gas along the LOS to the quasar) of gas decrease outward in the radial direction. Consequently, the ionization parameter (see definition in Section 1.3) was also a function of the radial distance, decreasing with increasing radius. Employing the photoionization model used in Kaspi & Netzer (1999) and references therein, Horne et al. (2004) determined the inward and outward emission for the BLR clouds. The outputs of the photoionization models were then used to first obtain the time lags for the C IV line and then trace the theoretical velocity-delay structure in the BLR. The velocity-delay map for C IV was constructed the recovered from simulated data using the MEM technique (see Section 1.6.3). The variations in the ionizing radiation incident on the gas clouds were modelled

as a random walk in time having a power spectrum, $P(\nu) \propto \nu^{-1}$. The UV and optical continuum variations were assumed to be linearly proportional to the ionizing radiation. However, the UV and optical continua arising due to reprocessing of the high-energy X-ray photons by the accretion disk were ignored by assuming that the reprocessed continua exhibit time delays much smaller than those shown by the reprocessed emission lines. Horne et al. (2004) designed the synthetic spectra using the spectral range, resolution, and wavelength-dependent sensitivity defined for the *Kronos* spectrometers (Polidan & Peterson 2001). They incorporated random uncertainties based on photon-counting statistics, assuming an exposure time of 3600 seconds for every observation and systematic errors of 1%. The time resolution was taken to be 0.2 days, and the total duration of the experiment was taken to be 200 days. The recovered velocity-delay map (Figure 1.10, panel *c*) is blurred as compared to the theoretical one in panel *b* because of the finite time resolution adopted while mapping the velocity-delay structure although the spiral arms in the recovered map can still be identified. A wide range of velocities at smaller time delays for the C IV line indicates line emission primarily originating closer to the SMBH. The blueshifted gas (with negative velocities) at larger time delays shows some C IV line-emitting gas inflowing on the far side of the BLR. While the asymmetric gas flow is clearly visible in the theoretical velocity-delay map, again the low time resolution of the simulated data makes it difficult to identify this asymmetry in the recovered map.

In addition to velocity-delay maps for individual emission lines, responses of several emission lines in the BLR can be superimposed on one another to generate a composite velocity-delay map similar to Figure 1.11, taken from Horne et al. (2004). This map traces the velocity-delay space of the emission lines, Lyα λ1215, C IV λ1549, and He II λ1640, for the same BLR model described for Figure 1.11. The gas detected in C IV line emission spans the widest range in velocities at the smallest time lags measured which indicates that the gas originates closer to the SMBH. The He II gas appears to be blueshifted at smaller time delays indicating outflowing gas located on the near side of the BLR, but tightly confined in the region close to the SMBH. The Lyα line-emitting gas is significantly blueshifted at larger time delays which indicates inflowing gas on the far side of the BLR. The asymmetry in the figure highlights the different locations in the BLR where the three emission lines arise and thus traces the varying ionization levels in the regions where the lines are found.

The construction of Figure 1.11 from simulated data in Horne et al. (2004) signifies that it is possible to probe the complex structure of the quasar emission-line region using multiple emission lines to trace different regions of the region. Recent studies have employed the RM technique to determine time lags and recover the velocity-delay maps mainly for the Balmer lines (e.g., Bentz et al. 2010a; Grier et al. 2013a), and further used the recovered maps to suggest the possible geometries of the BLR in those quasars. Pancoast et al. (2014) described a direct way of obtaining the velocity-delay maps. This method uses a light curve for the quasar continuum flux and a pre-defined BLR geometry with a given set of physical conditions to model the emission-line light-curve behaviour with time. The BLR geometry is defined by a physical distribution of point particles that considers their radial distance from the central SMBH, an (unknown) opening angle, inclination of the accretion disk, and other parameters contributing to non-axisymmetric effects in the region. The BLR dynamics are set by assuming the central SMBH mass and a velocity distribution of the particles depending on their positions in the region. The velocity distribution incorporates radial and tangential velocities centred around circular orbits, radial escape velocities for inflowing or outflowing gas, or a combination

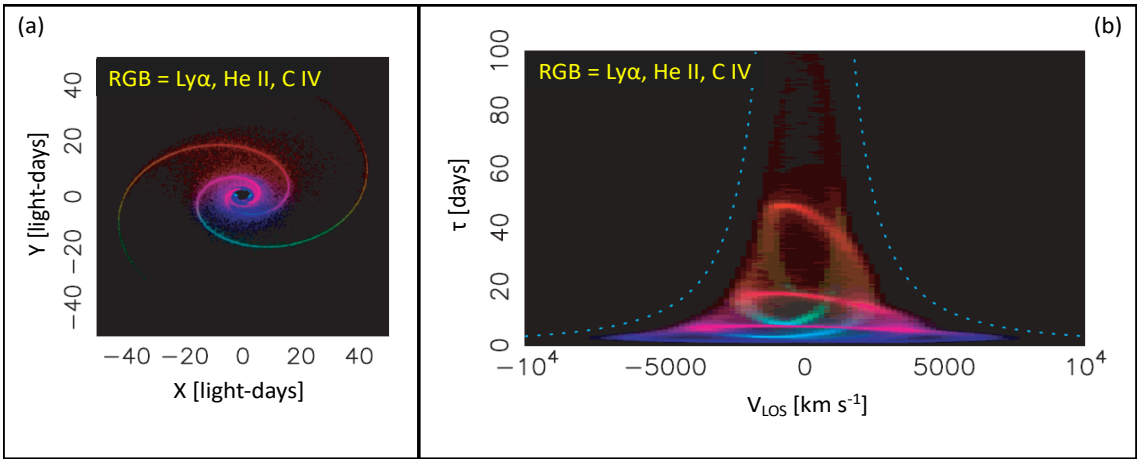

Figure 1.11: Sky view (panel *a*) and velocity-delay map (panel *b*) of the three UV emission lines, Lyα λ1215 (in red), C IV λ1549 (in blue), and He II λ1640 (in green), in the broad-line region (BLR) modelled as a Keplerian disk with elliptical orbits (eccentricity of 0.3) viewed from an inclination of 45°, and two trailing spiral arms. In the sky view of the BLR, the black hole is located at the centre and has a mass on the order of 10^7 $M_\odot$. In the velocity-delay map, the two dotted curves indicate the boundaries of the accretion disk. This figure is taken from Horne et al. (2004) and annotated here.

of both. The AGN continuum flux model uses Gaussian processes to interpolate between data points at different times. The simulated emission-line profiles can then be compared to the observed ones and the continuum flux + BLR model parameters that best describe the observed line profiles can be inferred. This method followed by Pancoast et al. (2014) gives an alternate way of determining the quasar black hole masses.

1.7 AGN Scaling Relations

The RM tool allows us to measure time lags in AGN accurately and precisely. This is important as it gives a direct handle on the size of the BLR and hence the SMBH mass (see Equation 1.22). Improved measurements of these quantities are essential to constrain the scaling relations described below for AGN.

The two fundamental correlations that have been found for AGN are:

1. The velocity width (ΔV) of the emission line in consideration is inversely proportional to the time lag measured for the line; thus, $\Delta V \propto \tau^{-1/2}$. This correlation has been studied in several cases of AGN for which multiple time lags have been measured. The correlation is a natural consequence of a BLR composed of gas in virial motion (e.g., Peterson et al. 2004; Bentz et al. 2010b).

2. There is a correlation between the luminosity of AGN and the size of the BLR which is given as $R_{\rm BLR} \propto L^\beta$, where $\beta \sim 0.5$ (e.g., Kaspi et al. 2005; Bentz et al. 2009a). This

R–L relationship has been well calibrated empirically using the Hβ line in the rest-frame optical for a number of low-redshift AGN.

The first of the above two correlations, signifying virial motion, can be used to compute the masses of central SMBH in AGN using the equation:

$$M_\bullet = f \frac{R_{\rm BLR}\ \Delta V^2}{G} \tag{1.22}$$

where $R_{\rm BLR}$ is simply $c\tau$ (see Section 1.6.2) as light travels across the BLR, ΔV is typically given by the full width at half maximum (FWHM) of the emission line used, and f is a dimensionless factor of the order unity that accounts for any underlying assumptions about the BLR geometry, kinematics, and orientation of the BLR. This factor is particularly difficult to obtain for individual AGN. Ferrarese & Merritt (2000) and Ferrarese & Ford (2005) derived scaling relations for the SMBH mass and the velocity dispersion of galaxy stellar bulges (σ_*) as $M_\bullet \propto \sigma_*^{4.8\pm0.5}$ in the case of quiescent galaxies. Ferrarese et al. (2001) found an $M_\bullet$–σ_* correlation to hold for 6 local active galaxies for which reverberation-mapped black hole masses were previously determined. They verified that the reverberation-mapped black hole masses for the 6 AGN were in good agreement with those obtained from the $M_\bullet$–σ_* relationship for quiescent galaxies. This suggests that there exists a $M_\bullet$–σ_* relationship for AGN that is similar to the one for quiescent galaxies. Nevertheless, it will take large number of AGN with SMBH mass measurements through RM to derive a robust $M_\bullet$–σ_* relation for them. Although it is difficult to calculate the f factor for individual AGN, most RM studies determine a mean f by calculating virial products ($VP = M_\bullet/f$) for AGN samples (e.g. Park et al. 2012; Grier et al. 2013b). Pancoast et al. (2014) illustrated how a forward modelling technique through direct black hole mass measurements (see description in Section 1.6.3) can be used to evaluate the f factor. They evaluated the f factors individually for their sample of 5 local AGN using the two correlations, $M_\bullet$–σ_* and $M_\bullet$–$\Delta V_{\rm FWHM}$ (for the Hβ emission line). The dispersion in the distribution of f obtained from the $M_\bullet$–σ_* correlation was $\log_{10} f_\sigma = 0.75 \pm 0.40$ and that from the $M_\bullet$–$\Delta V_{\rm FWHM}$ correlation was $\log_{10} f_\sigma = 0.77 \pm 0.38$. These values agree to within 10% of the $\log_{10} f_\sigma$ of 0.71 from Park et al. (2012). Extending the direct modelling approach by Pancoast et al. (2014) to determine f values for large AGN sample size will put better constraints on f whose uncertainty is one of the major uncertainties in determining the reverberation-mapped black hole masses.

1.8 Observational Requirements

The exploratory science that can be studied through AGN RM campaigns requires data of very high quality to be able to trace the geometry and velocity structure of the BLR. The success of an RM experiment depends on the following observational parameters (Horne et al. 2004; Cackett et al. 2021).

1. High time resolution: Since AGN vary irregularly and on short timescales, the time interval between two consecutive continuum photon measurements should be carefully considered. This cadence directly affects the cross-correlation analysis performed to

trace the velocity-delay structure of the BLR. The higher the cadence, the better the resolution of the velocity-delay map.

2. Long duration: It is essential to take observations for a long duration to give enough time for emission lines to respond to the changes in the source continuum emission. As a rule of thumb (Press 1978) in time-series analysis, the duration of an observational program should be at least three times longer than the maximum timescale of the data to be analyzed. Thus, to capture the longest response time of ≈20 days (for Hβ in low-redshift AGN), the duration of observations should be $\gtrsim$60 days (Horne et al. 2004). It is important to note that the time duration of an observational experiment will differ depending on the emission line, whose response is to be probed.

3. High spectral resolution: Although broad lines in AGN spectra have velocity widths on the order of several thousand km s^{-1}, they are frequently blended with narrow lines, which do not change on short timescales but must be removed from the analysis. Therefore, medium to high spectral resolution is necessary to study the details of the velocity structure of emission lines in AGN spectra. The typical spectral resolution set for observations is hundreds of km s^{-1}, equal to the velocity widths of narrow emission lines in quasar spectra.

4. High homogeneity and high signal-to-noise (S/N): Low-amplitude variations of the continuum flux and consequently the emission lines necessitate high S/N light curves. This requirement along with optimal integration times ensures construction of high-quality velocity-delay maps to study the BLR.

5. High-quality spectrophotometry: High accuracy in flux calibration is essential in RM studies to capture the subtle flux variations from one epoch to the other. Typically, this is achieved by observing the calibration star in the same slit as the target.

Given the complex nature of flux variations in AGN, it is certainly not trivial to achieve the high standards of observational requirements in designing reverberation mapping projects. Despite the complications involved, more ambitious observational campaigns can yield high-fidelity velocity-delay maps of the BLR through reverberation mapping as demonstrated by Horne et al. (2004).

1.8.1 Reverberation Mapping Studies

Early RM campaigns focused mainly on the low-luminosity Seyfert galaxies. NGC 4151 and NGC 5548 are two of the widely studied Seyferts. Keck et al. (2015) used long exposure *Nuclear Spectroscopic Telescope Array* (NuSTAR) and *Suzaku* X-ray observations of NGC 4151 to study the nature of its compact central source. They suggested that variations in the reflection from the inner accretion disk are responsible for the spectral variability observed in NGC 4151. NGC 5548 is another object that has been studied for over two decades. One of the recent RM campaigns for this object is the Space Telescope and Optical Reverberation Mapping (STORM) project, a six-month long, multi-wavelength spectroscopic study of NGC 5548 (De Rosa et al. 2015). The significant improvement in this campaign was the high time resolution of the concurrent X-ray data obtained. The target was observed in the X-ray about twice

every day for ∼4 months; UV/optical spectra were taken approximately daily. The reverberation mapping in the UV and optical of the accretion disk in NGC 5548 are consistent with the continuum being reprocessed by the BLR gas such that the trend for time lag with wavelength is given by $\tau \propto \lambda^{4/3}$ (Edelson et al. 2015; Fausnaugh et al. 2016).

One of the most recent developments in RM studies include the SDSS-RM project, the optical RM experiment carried out for a large flux-limited sample of 849 broad-line quasars in the redshift range $0.1 < z < 4.5$ with the SDSS-III Baryon Oscillation Spectroscopic Survey spectrograph (Shen et al. 2015). The primary goal of the experiment is to study the UV broad lines and measure their time lags relative to the continuum changes in the quasar sample. The significant improvement in this project was that it surveyed a large sample of quasars over a wide redshift range. The spectroscopic cadence used was $\Delta t \sim 4$ days for more than 30 epochs and the photometric cadence was ∼2 days. Grier et al. (2017) described the procedure they followed to obtain the time lag measurements and subsequently Hβ-based black holes masses for 44 quasars from the first six months of the SDSS-RM project. More recently published black hole mass measurements using the C IV and Mg II lines depict the extent of their sample to redshifts of ∼2.9 (see references in Table 1.1).

RM studies of AGN are summarized in Table 1.1.

Table 1.1: Active Galactic Nuclei (AGN) Reverberation Mapping (RM) Studies (1978-2022)

Survey	AGN Name(s)/Number	Duration	Cadence	Spectral Region
International Ultraviolet Explorer Observations[c]	2 Seyfert 1s, 1 quasar	···	···	UV[a], Optical
Lick Survey of Broad-line Galaxies[d]	9 Seyfert 1s	···	···	Optical
Ohio State University Spectroscopic Monitoring Program[e]	27 Seyfert 1s, 6 Seyfert 2s	14 months	···	Optical
Wise Observatory AGN Monitoring Program[f]	27 Seyfert 1s, 3 quasars	7 months	∼3–4 days	Optical
Lovers of Active Galaxies Collaboration[g]	1302-102 1217+023 NGC 3516	5 months	∼5–10 days ∼1–18 days ∼4–5 days	Optical
International AGN Watch Consortium[h]	NGC 5548, NGC 3783	8 months	4 days (UV)	UV, Optical
Reverberation Mapping of High-Luminosity Quasars[i]	6 quasars	6 years	∼15 days	Optical, IR[b]
Super-Eddington Accreting Massive Black Holes[j] (SEAMBH)	25 Narrow-Line Seyfert 1s	Ongoing	Variable	Optical
Reverberation Mapping of Luminous Quasars at High z[k]	17 quasars	10 years	∼1 year	Optical, IR
Mg II Time Delay in CTS C30.10 with the Southern African Large Telescope[l]	CTS C30.10	6 years	Variable	Optical
C IV Black Hole Mass Measurements with the Australian Dark Energy Survey (OzDES)[m]	2 quasars	Multi-year	Variable	Optical, IR
Space Telescope and Optical Reverberation Mapping[n] (STORM)	NGC 5548	6 months	1 day	UV, Optical
Lick AGN Monitoring Project 2016[o]	21 Seyfert 1s	13 months	3.5 days	Optical
Sloan Digital Sky Survey Reverberation Mapping[p] (SDSS-RM)	124 AGN	Ongoing	4 days	Optical, IR

Continuation of Table 1.1

[a] UV: Ultraviolet
[b] IR: Infrared
[c] Boksenberg et al. (1978); Penston et al. (1981); Perola et al. (1982); Ulrich et al. (1984)
[d] Osterbrock et al. (1978); Osterbrock (1978)
[e] Peterson et al. (1982)
[f] E.g., Maoz (1990); Maoz et al. (1991); Netzer et al. (1990); Maoz et al. (1991)
[g] Jackson et al. (1992); Wanders et al. (1993)
[h] Clavel et al. (1991); Peterson et al. (1991); Dietrich et al. (1993); Maoz et al. (1993); Romanishin et al. (1995)
[i] Kaspi et al. (2007)
[j] Du et al. (2014); Wang et al. (2014b); Hu et al. (2015); Du et al. (2015, 2016a,b, 2018)
[k] Lira et al. (2018)
[l] Czerny et al. (2019)
[m] Hoormann et al. (2019)
[n] De Rosa et al. (2015); Edelson et al. (2015); Fausnaugh et al. (2016); Goad et al. (2016); Pei et al. (2017); Mathur et al. (2017); Horne et al. (2021)
[o] U et al. (2022)
[p] Shen et al. (2015); Sun et al. (2015); Denney et al. (2016); Shen et al. (2016); Grier et al. (2017); Li et al. (2017); Grier et al. (2019); Homayouni et al. (2019, 2020); Fonseca Alvarez et al. (2020); Dalla Bontà et al. (2020); Homayouni et al. (2022)

RM surveys are continually growing in scale as well as the types of AGN being surveyed. Keeping this in mind, it is vital that the next-generation AGN mapping studies consider optimizing survey designs to maximize the science returns from large-scale projects.

1.9 Motivation

Though AGN have been studied for decades, we still do not completely understand the physics behind their accretion mechanism, e.g., accretion in super-Eddington AGN. Super-Eddington AGN likely have a different accretion-disk structure than their sub-Eddington counterparts. While many theoretical studies suggest a "slim"-disk structure for super-Eddington AGN, it lacks sufficient observational evidence. The Super-Eddington Accreting Massive Black Holes (SEAMBH) collaboration that started in 2012 has studied ~25 high accretion-rate AGN to date, and the results are exciting (Du et al. 2014; Hu et al. 2015; Wang et al. 2014b; Du et al. 2016a,b, 2018). The smaller Hβ BLR in these objects as compared to the sub-Eddington AGN at same luminosities is likely indicative of their distinct disk structure. Assuming a slim-disk model for super-Eddington AGN, Wang et al. (2014a) explain how self-shadowing effects in the inner regions of the slim disks can cause the Hβ ionization front to shrink, thus resulting in small measured BLR sizes. With velocity-resolved RM, Du et al. (2016a) found inflows as well as outflows in a handful of SEAMBH objects. However, a clear picture of their BLRs and its effects on the observed emission lines is still unknown. Additionally, the sample size is small, and more observational studies are required to understand both the accretion disk and the BLR in these highly accreting AGN systems.

RM provides the best handle on black hole masses in all but the most nearby AGN. The main challenges of RM are observational and are outlined in the next sentences. As outlined in Section 1.8, a successful application of the RM technique requires high-resolution data, high cadence, high quality of spectrophotometry and photometry, and high S/N. These high standards are critical for accurate and precise measurements of time lags and emission-line profiles, and consequently of black hole masses. For example, measuring emission lines can be particularly challenging with low-resolution data. Ideally, RM requires that the resolution is high enough that the narrow lines are resolved in the spectra. Although this can be less concerning for objects with considerably broad emission lines $\geq$4000 km s^{-1}, it can have severe effects (e.g., line blending) while measuring narrower line profiles, e.g., in Narrow-Line Seyfert 1s, where Hβ lines are much narrower than in their broad-line counterparts. As we expand the application of RM to diverse populations of AGN, it is important to carefully consider how the quality of data as well as our adopted measuring techniques affect the measured quantities.

RM studies have made significant progress since their early years. While early RM studies targeted the low-redshift AGN, recent campaigns such as SDSS-RM have taken further steps by not only increasing the number of reverberation-mapped AGN but also spanning the high-redshift regime. However, different lines are used to probe different redshift regimes. Hβ has been commonly used for surveying low-redshift objects, whereas C IV is used at high redshifts. An important point to note here is that the low- and high-redshift AGN occupy completely different regions of parameter space given their luminosity, the shape of their ionizing SED, and the properties of their host galaxies. Therefore, it is essential to obtain more high quality data in a uniformly sampled luminosity-redshift parameter space for accurately measuring black

hole masses. For successfully conducting more ambitious RM surveys, optimizing survey designs is vital. Optimally planned observing campaigns will allow in maximizing their science outcomes.

Chapter 2

Reverberation Mapping of a Highly Accreting Active Galactic Nucleus, Markarian 142

This work will be submitted as an article to the Astrophysical Journal.

2.1 Introduction

Accretion onto supermassive black holes through an accretion disk of ionized gas powers active galactic nuclei (AGN) at the centres of massive galaxies. AGN accreting at typical rates (a few percent of the Eddington limit) have a geometrically thin but optically thick disk – the 'thin-disk' model (Shakura & Sunyaev 1973). However, theoretical models predict a notably different structure for the AGN with high accretion rates significantly above the Eddington limit – super-Eddington AGN (e.g., Abramowicz et al. 1988). The occurrence of such AGN is likely higher during the peak era of supermassive black hole growth during cosmic noon (z = 1–3; Brandt & Alexander 2010; Shen et al. 2020). Understanding the structure of the accretion system in high-Eddington AGN remains an open issue in accretion physics.

Although models exist for slim-disk systems, observational tests of the structure of the accretion flow in super-Eddington AGN are rare. At high accretion rates, radiation pressure is expected to dominate causing the inner disk to inflate vertically – now called a 'slim' (rather than thin) disk – with a scale height, $H_{\rm disk} \leq R_{\rm disk}$, where $R_{\rm disk}$ is the disk radius (e.g., Abramowicz et al. 1988). Photons are trapped in the fast-flowing matter, eventually falling into the black hole. Given that not all photons escape, the disks in super-Eddington AGN are underluminous relative to the accretion rates as compared to thin disks (Jaroszyński et al. 1980). Begelman (2002) proposed an alternative scenario where the "photon-bubble instability" principle can cause the disks in super-Eddington AGN to become inhomogeneous at scales much smaller than the disk scale height.

Reverberation mapping (RM; Blandford & McKee 1982; Peterson 1993; Cackett et al. 2021) provides a way to observationally study the slim-disk model and broad-line region (BLR) in super-Eddington AGN. RM takes advantage of the observed continuum variability of AGN on many time scales (from several days to weeks and years; e.g, Peterson et al. 1982). The

accretion-disk emission illuminates the BLR on larger scales, and sets the ionization structure and thus the location of the gas generating the broad emission lines (e.g., Hβ). An increase in continuum emission from the accretion disk results in an increase in broad emission-line flux after a time lag (τ) set by the light travel time between the continuum-emitting region and the BLR (Peterson 2014). RM converts this time lag into a spatial distance, the size of the BLR. Thus, applying RM to high-accretion rate AGN gives an observational method to test the structure of the accretion flow and BLR in these systems, and place super-Eddington AGN on the radius-luminosity (R–L) relationship for AGN (Kaspi et al. 2005; Bentz et al. 2013).

The Narrow-Line Seyfert 1 (NLS1) class of AGN are considered to have high accretion rates displaying narrow broad emission lines (e.g., the Hβ line with a full width at half maximum, FWHM $\lesssim$ 2000 km s^{-1}), strong Fe II emission lines, and weak [O III] lines (e.g., Osterbrock & Pogge 1987; Boroson & Green 1992; Boller et al. 1996; Véron-Cetty et al. 2001) in their spectra. The Super-Eddington Accreting Massive Black Holes (SEAMBH) campaign has been performing photometric and spectroscopic monitoring over the past nine years of high accretion-rate AGN that display spectral characteristics of NLS1s (e.g., Du et al. 2014; Wang et al. 2014b; Hu et al. 2015; Du et al. 2015, 2016a,b, 2018). Du et al. (2016b) showed that the BLRs in super-Eddington AGN are smaller than those with sub-Eddington accretion rates. In the context of the slim-disk model, the smaller BLR sizes can be explained as a consequence of the increased scale height of the inner accretion disk that shields the BLR from the central ionizing flux. Hβ, a marker of the hydrogen ionization front in the BLR, can thus exist at smaller radii than in thin accretion-disk systems.

As the most promising SEAMBH object – a bright target with an extremely super-Eddington accretion rate (Eddington ratio[1] $\sim$ 45; Du et al. 2016b) and a well measured Hβ lag – Markarian 142 (Mrk 142 or PG 1022+519, RA[2] = 156.380327°, Dec[3] = 51.676352°, z = 0.045) is the target of our study to probe the structure of its BLR. In the 2012 SEAMBH campaign, Mrk 142 was highly variable with a fractional variability amplitude of $F_{\rm var}$ = 8.1% at 5100 Å over a few months. Its variable nature makes it amenable to RM studies of both accretion-disk structure (from X-ray/ultraviolet [UV]/optical continuum time-lag studies) and the BLR structure (from continuum-emission line time lags). Accretion-disk RM applies the same principle as BLR RM to the inner and outer regions of the accretion disk to determine its size and temperature profile (Cackett et al. 2007). The more energetic X-ray/UV radiation from the inner disk illuminates the disk at larger radii where the optical photons are generated. Therefore, the lower-energy emission will respond with a positive time lag to changes in the high energy radiation giving rise to correlated continuum light curves. Mrk 142 has a total Hβ time lag with respect to the 5100 Å continuum emission of $7.9^{+1.2}_{-1.1}$ days and a black hole mass of $\log(M_\bullet/M_\odot) = 6.59^{+0.07}_{-0.07}$ (Du et al. 2015, 2016b).

In this chapter, we present Mrk 142 time-lag measurements from two ground-based, optical spectroscopic RM campaigns of Mrk 142 concurrent with the photometric monitoring of the target with the *Neil Gehrels Swift Observatory* (*Swift*) in a UV band and the Las Cumbres Observatory (LCO) in an optical band. With our joint campaign, we performed, for the first time, simultaneous measurements of the inner accretion disk and BLR size in a super-Eddington

[1]Eddington ratio is defined as the ratio of the accretion rate of an AGN to its Eddington mass accretion rate.
[2]RA: Right Ascension
[3]Dec: Declination

AGN. This paper is organized as follows. In Section 2.2, we provide details of the observations, and in Section 2.3, we explain the process of data reduction. In Section 2.4, we describe our spectral modelling followed by light-curve analysis in Section 2.5. In Section 2.6, we outline and discuss our results in the context of previous studies. Finally, Section 2.7 provides closing remarks. Throughout this work, we use the standard cosmology with H_0[4] = 67 km s^{-1} Mpc^{-1}, Ω_Λ[5] = 0.68, and Ω_M[6] = 0.32 (Planck Collaboration et al. 2014).

2.2 Observations

We obtained concurrent observations of Mrk 142 with multiple telescopes to perform RM analysis of the accretion disk and BLR simultaneously. Figure 2.1 showing the continuum light curves of Mrk 142 highlights the simultaneous coverage with different telescopes.

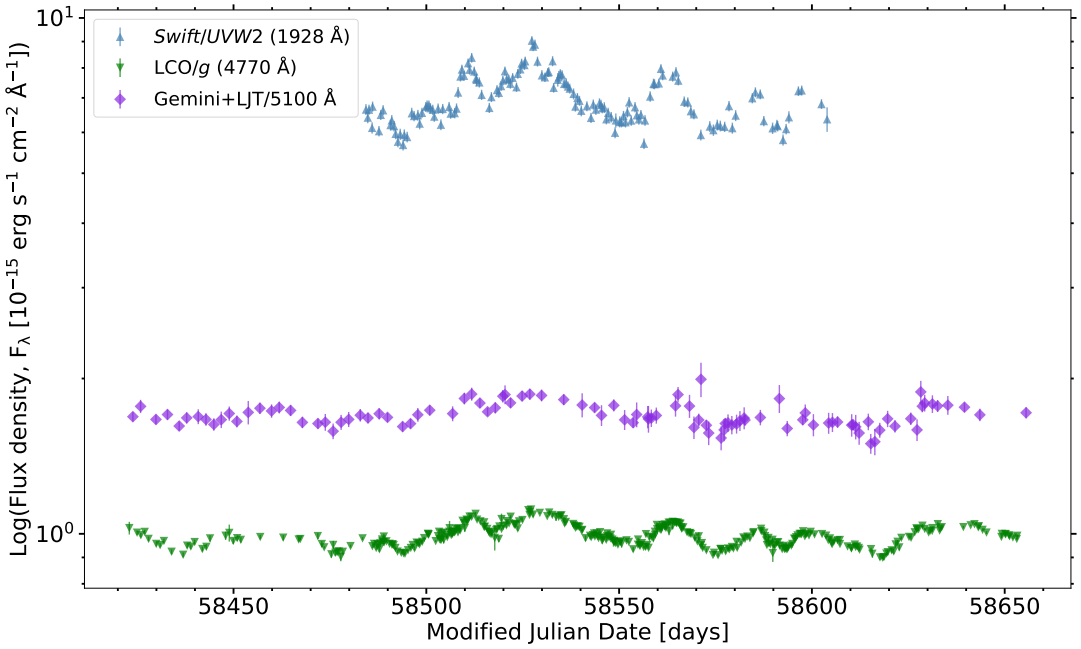

Figure 2.1: Markarian 142 (Mrk 142) continuum light curves – in the *UVW2* band with the *Neil Gehrels Swift Observatory* (*Swift*; blue upright triangles) and the *g* band with the Las Cumbres Observatory (LCO; green flipped triangles) from photometric observations, and at 5100 Å (purple diamonds) inter-calibrated from the spectroscopic observations with the Gemini North Telescope (Gemini) and the Lijiang Telescope (LJT). The 5100 Å inter-calibrated light curve displays the combined spectroscopic coverage over 102 epochs. We performed the inter-calibration with a `Python`-based Running Optimal Average (`PyROA`; Donnan et al. 2021) technique (see introduction to `PyROA` in Section 2.5.1).

[4] H_0: Hubble constant
[5] Ω_Λ: Density of dark energy
[6] Ω_M: Mass density (including ordinary mass and dark matter)

2.2.1 Gemini North Telescope

We obtained new observations of Mrk 142 long-slit spectra taken with the Gemini Multi-Object Spectrograph (GMOS; Hook et al. 2004) on the 8.1-m Gemini North Telescope (Gemini) on Maunakea, Hawai'i with 33 epochs from February 6 through June 1, 2019 under the Queue observing program GN-2019A-Q-121 (P.I.: V. C. Khatu). These are concurrent with the Mrk 142 photometric data from the *Swift* telescope comprising 180 epochs of 1-kilosecond exposures at X-ray, UV, and optical wavelengths from January 1 through April 30, 2019 (P.I.: E. Cackett) as well as with the photometric g-band data from LCO (P.I.: R. Edelson). The *Swift* observations had a twice-daily cadence until March 19, and the cadence was increased to daily from March 20 onward. We required observations from Gemini in early 2019 with considerable overlap with the *Swift* campaign to allow, for the first time, simultaneous measurements of the UV-emitting accretion disk and the BLR of a super-Eddington AGN. The cadence of the Gemini observations was set to *one* day. We obtained data for only two, sparsely separated epochs in February during the beginning of the observing period due to weather interruptions. However, observations were more frequent in March and May, and the daily cadence was achieved in the first week of April.

The spectra were taken with the GMOS-North Hamamatsu detector and a single grating, B600 with two different slits, 0.75″ (narrow slit) and 5.00″ (wide slit), in the two-target acquisition mode, where Mrk 142 and a comparison star were observed in the same slit. The GMOS-North Hamamatsu detector comprises three ∼2048×4176 chips (full detector size of 6278×4176 pixels, mosaiced) arranged in a row with pixel size of 0.0807″ pixel with two chip gaps 4.88″ wide. The choice of the grating was made to obtain the broad emission line of interest, Hβ λ4861, in the spectra. The narrow 0.75″ slit was selected to obtain the spectral resolution of ∼1125 (narrow-slit data) required to study the velocity structure of Hβ. Accuracy in spectrophotometric calibration is a key for RM studies, and therefore, we used the wide slit at a resolution of ∼170 (wide-slit data) to correct for slit losses due to the narrow slit. To satisfy this calibration requirement, Mrk 142 and a comparison star for flux calibration (hereafter, calibration star) were placed simultaneously in the same slit. We achieved this for all observations by fixing the position angle of the slits at 155.20° East of North such that Mrk 142 appeared at the centre of the slit. The selected calibration star (RA = 10:25:36.369, Dec = +51:38:52.18) has a well-calibrated spectrum and was used for previous LJT campaigns. Flatfield images were taken for every object (science target and calibration star) with the Gemini Facility Calibration Unit (GCAL) in the sequence FLAT–OBJECT–OBJECT–FLAT with both slits. The on-target exposures were 90 s long. We also took daytime arc lamp spectra with the CuAr lamp, again, for both slits. Binning of 1 in the spectral (X) direction and 2 in the spatial (Y) direction (1×2) was used for all data except for the wide-slit arc lamp spectra, which used the binning of 1×1. A summary of the GMOS-North science observations is provided in Table 2.1. The object spectra from all epochs except the narrow-slit spectra from epoch 30 were assigned a Pass ("P") flag.

Table 2.1: Summary of Markarian 142 (Mrk 142) Observations with the Gemini Multi-Object Spectrograph (GMOS) from February to June 2019

Epoch	UT[a] Date	MJD[b] Start Time		Airmass	
	(YYYY-MM-DD)	0.75″ slit	5.00″ slit	0.75″ slit	5.00″ slit
1	2019-02-06	58520.412	58520.418	1.275	1.258
		58520.414	58520.420	1.270	1.254
2	2019-02-26	58540.415	58540.421	1.181	1.178
		58540.417	58540.423	1.180	1.177
3	2019-03-03	58545.433	58545.439	1.178	1.181
		58545.435	58545.441	1.178	1.182
4	2019-03-09	58551.430	58551.437	1.187	1.193
		58551.432	58551.438	1.188	1.194
5	2019-03-12	58554.550	58554.557	1.679	1.734
		58554.552	58554.558	1.693	1.750
6	2019-03-15	58557.427	58557.433	1.200	1.209
		58557.428	58557.442	1.202	1.225
7	2019-03-16	58558.355	58558.362	1.189	1.184
		58558.357	58558.363	1.188	1.183
8	2019-03-23	58565.281	58565.287	1.299	1.280
		58565.283	58565.289	1.293	1.276
9	2019-03-26	58568.254	58568.260	1.365	1.341
		58568.256	58568.262	1.359	1.335
10	2019-03-27	58569.410	58569.416	1.225	1.237
		58569.411	58569.418	1.228	1.241
11[c]	2019-03-29	58571.233[c]	58571.239	1.424	1.394
		58571.235[d]	58571.241	1.416	1.387
12	2019-03-31	58573.233	58573.239	1.398	1.370
		58573.235	58573.241	1.390	1.364
13	2019-04-03	58576.457	58576.463	1.451	1.486
		58576.459	58576.465	1.460	1.496
14	2019-04-04	58577.234	58577.240	1.350	1.327
		58577.235	58577.241	1.343	1.321
15	2019-04-05	58578.241	58578.248	1.312	1.292
		58578.243	58578.249	1.306	1.287
16	2019-04-06	58579.236	58579.242	1.322	1.302
		58579.237	58579.243	1.317	1.297
17	2019-04-07	58580.461	58580.467	1.543	1.585
		58580.463	58580.469	1.554	1.597
18	2019-04-08	58581.331	58581.337	1.177	1.179
		58581.333	58581.339	1.177	1.180
19	2019-04-09	58582.432	58582.438	1.408	1.439
		58582.434	58582.440	1.416	1.447

Continuation of Table 2.1

20	2019-04-25	58598.274	58598.280	1.175	1.176
		58598.276	58598.282	1.175	1.176
21	2019-04-27	58600.391	58600.397[c]	1.447	1.481
		58600.392	58600.398	1.456	1.491
22	2019-05-01	58604.338	58604.344[c]	1.282	1.300
		58604.340	58604.346	1.286	1.305
23	2019-05-02	58605.327	58605.333	1.259	1.275
		58605.329	58605.335	1.263	1.280
24	2019-05-07	58610.317	58610.323	1.267	1.285
		58610.318	58610.324	1.272	1.289
25	2019-05-08	58611.361	58611.367	1.450	1.485
		58611.363[c]	58611.369[c]	1.459	1.494
26	2019-05-09	58612.246	58612.253	1.177	1.179
		58612.248	58612.254	1.177	1.180
27	2019-05-12	58615.269	58615.275	1.201	1.209
		58615.270	58615.276	1.203	1.212
28	2019-05-13	58616.320[e]	58616.326	1.329	1.353
		58616.322	58616.328	1.335	1.359
29	2019-05-24	58627.266	58627.272	1.256	1.272
		58627.267	58627.273	1.260	1.276
30	2019-05-25	58628.242[f]	58628.248	1.213	1.223
		58628.243[f]	58628.249	1.216	1.227
31	2019-05-26	58629.251	58629.257	1.235	1.249
		58629.253	58629.259	1.239	1.252
32	2019-05-28	58631.251	58631.257	1.246	1.261
		58631.252	58631.258	1.250	1.265
33	2019-06-01	58635.255	58635.262	1.287	1.307
		58635.257	58635.263	1.292	1.312

Continuation of Table 2.1

[a] UT: Universal Time dates
[b] MJD: Modified Julian Date at the start of the observations for individual exposures.
[c] Science spectrum assigned SPCALF (see *Notes* below)=0.
[d] Science spectrum calibrated with the narrow-slit standard star spectrum from exposure 1 and hence assigned SPCALG (see *Notes* below)=B.
[e] The narrow-slit science spectrum from exposure 1 likely had a calibration issue and hence was not used for further analysis (see Appendix A for details).
[f] Science spectrum assigned DQF (see *Notes* below)=U.

Observations were done with the GMOS-North Hamamatsu detector in the two-target acquisition mode (Mrk 142 and a comparison star in the same slit) positioning the slit at 155.20° East of North, with the B600 grating (covering the broad Hβ emission line at ~4862Å) and two slits, 0.75″ (narrow slit) and 5.00″ (wide slit). Two exposures were taken with every grating/slit combination, each 90 seconds long. A Data Quality Flag (DQF) of "P" or "U" that stands for Pass or Usable was assigned to all data at the time of observing. Unless stated otherwise, all science spectra were assigned a DQF of "P". SpectroPhotometric CALibration Flag (SPCALF) indicates whether the science spectra were calibrated ("1") or not calibrated ("0") during spectral reduction (see Section 2.3.1 for more details). SpectroPhotometric CALibration Grade (SPCALG) indicates the grade assigned to the spectrophotometric calibration based on the epoch and exposure of the calibration star spectrum used for calibrating the science spectra (see Section 2.3.1 for more details). All science spectra were assigned an SPCALF of 1 and an SPCALG of "A" unless indicated otherwise.

2.2.2 Lijiang Telescope

To complement the short observing period of 33 epochs with Gemini, we incorporated supporting observations of Mrk 142 for our study. We observed Mrk 142 with the Yunnan Faint Object Spectrograph and Camera on the Lijiang 2.4-m Telescope (LJT; Wang et al. 2019) in the two-target acquisition mode with the same calibration star as used for the Gemini observations. We followed the same observing procedure as for previous SEAMBH campaigns (e.g., Du et al. 2014, 2015). We obtained long-slit spectra of the target at 69 epochs from November 1, 2018 through June 21, 2019, simultaneous with the *Swift*, LCO, and Gemini observing campaigns.

Table 2.2.2 provides a summary of the overlapping photometric and spectroscopic programs.

2.3 Spectral Reduction

2.3.1 Gemini Spectral Reduction

The spectral reduction process for all Gemini epochs included four stages (in the order of appearance below) with the Gemini Image Reduction and Analysis Facility[7] (Gemini `IRAF`)

[7]Gemini `IRAF` is an external package that makes use of `IRAF` (a software system used for the reduction and analysis of astronomical data, created and supported by the National Optical Astronomy Observatory in Tucson,

Table 2.2: Summary of Overlapping Photometric and Spectroscopic Observations of Mrk 142

Filter/Line	Observatory	Date Range (MJD[a])	Number of Epochs	Cadence
UVW2 [1928 Å][b]	*Swift*	58484.349–58603.941	149	~twice-daily
g [4770 Å][b]	LCO	58422.973–58653.260	361	~2 days
Hβ λ4861[c]	Gemini	58520.414–58635.257	33	~3.6 days
Hβ λ4861[c]	LJT	58423.899–58655.549	69	~3.4 days

[a] Modified Julian Date
[b] Photometry
[c] Spectroscopy

reduction package: (1) baseline calibrations with GCAL flats, two-dimensional (2D) arc lamp spectra, and bias frames; (2) cleaning of 2D spectra followed by the wavelength calibration and extraction of one-dimensional (1D) science and calibration-star spectra (in the same slit); (3) preparing 1D spectra for analysis with `PrepSpec` (see introduction to `PrepSpec` in Section 2.4.1); and (4) flux calibration of the 1D science spectra. For each epoch, we first sorted the data in lists of bias frames, GCAL flats, arc lamp spectra, and object spectra for both the narrow and the wide slits. We then used the the same reduction script with different parameter settings for processing the data taken with the two slits.

Baseline Calibrations

Baseline calibrations comprised creating a masterbias image, generating a dispersion solution with the narrow-slit arc lamp spectra, and constructing masterflat images with both the narrow- and wide-slit flatfield images. For individual observing nights, we used bias frames with the binning of 1×2 and a full-frame readout from the Gemini Observatory Archive (`https://archive.gemini.edu`). We applied an overscan noise correction to all bias images, for a given night, before combining them into a masterbias image. We then reduced the narrow-slit arc-lamp spectra with bias subtraction turned off and used them to generate 2D dispersion solutions with the task `gswavelength`. Generating dispersion solutions was a two-step process – fitting the 1D wavelength solution in the spectral direction and fitting any distortions in the spatial direction. The reference wavelengths for the arc-lamp spectra were used from the Gemini `IRAF` package. Because the re-binned, wide-slit arc-lamp spectra – binned from 1×1 to 1×2 to match the binning of the corresponding GCAL flats and object spectra – were unable to provide a non-distorted wide-slit dispersion solution, we used the narrow-slit solution to wavelength calibrate the wide-slit data. For a given epoch, we combined the two GCAL flats (including a quantum efficiency correction for each) taken with the two slits to create a masterflat corrected for the uneven illumination along the GMOS detector in the long-slit mode.

Arizona). See more at `https://www.gemini.edu/sciops/data-and-results/processing-software/description`.

Cleaning, Wavelength Calibration, and Extraction

We corrected the 2D object spectra affected by cosmic-ray hits and performed their wavelength calibration to then extract the 1D science and calibration-star spectra. With the task `gscrrej`, we first selected a fixed square region surrounding the cosmic-ray affected pixels above a specified threshold and then replaced them with interpolated values from local noise levels. However, this method did not correct for all cosmic rays. We applied an additional correction to the affected pixels that remained uncorrected in the next stage of the reduction process. We applied the derived narrow-slit dispersion solutions to both the narrow- and the wide-slit object spectra.

For a given epoch, we extracted 1D science and calibration-star spectra separately from individual exposures with the task `gsextract`. We selected a considerable swath of background for subtraction from both sides of each trace during the extraction process. The subtraction of bright skylines from the extracted 1D spectra resulted in some sharp spikes in the spectra owing to residual noise. We applied additional correction to remove the sharp features in the 1D spectra in the next stage of reduction.

A few of the extracted science and calibration-star spectra showed flat regions (zero flux values) on the shorter-wavelength (or blue) end (~3355 Å to ~4325 Å) that do not match the true shape of the continuum, while some spectra showed bump-like features. The flat regions were a consequence of the slit position angle not aligned along the parallactic angle, whereas the bump-like features likely resulted from the flat-fielding process, where a higher order spline was used to create the masterflat to appropriately trace detector sensitivity near the chip-gap regions and avoid discontinuities in the calibrated spectra near the chip edges. We corrected the spectra containing flat blue ends or bumpy features individually before attempting flux calibration.

Additional Corrections to 1D Spectra – Preparing Data for `PrepSpec`

To prepare the spectra for PrepSpec, it was important that each spectrum have no gaps. Before the flux calibration stage, we trimmed the blue end of the spectra shorter than ~4325 Å in the rest frame because they were very noisy and not required for the purposes of this study. We further processed the 1D spectra for: (1) flat blue ends (due to the slit position angle) or bump-like features (from the flat-fielding process) appearing in some spectra; and (2) spectral regions affected by artefacts from cosmic-ray removal and sky subtraction as well as chip gaps with no flux. This additional processing was important for the initial stage of modelling spectra with `PrepSpec`, the software tool that corrects spectra for relative calibration differences (see Section 2.4.1 for details).

We developed a script to correct flat and bump-like regions in the 1D spectra in `Python`[8] v3.6.5. A spline function fit to a reference spectrum modelled the true shape of the affected region. We then modelled the flux over the affected pixels assuming a Gaussian distribution of data points with standard deviation equal to the measured standard deviation at the same location in the reference spectrum. The reference spectrum used for recovery was typically the spectrum from another exposure taken on the same night (see Appendix A for exceptions).

[8] Visit `https://www.python.org/` for full documentation on `Python`.

To correct for spectral regions affected by artefacts and chip-gaps, we developed another `Python` script to replace the regions with affected data points by local median values or interpolated and simulated data. In a given window of affected points: (1) if the number of pixels was <5, the algorithm replaced every data point by the median value of a range of 5 pixels on either side of that point with the noise equal to the local median noise; and (2) if the number of pixels was ≥5, the algorithm first linearly interpolated across the affected region and then replaced the interpolated points with simulated data assuming a Gaussian distribution with a standard deviation equal to twice the noise in the interpolated data. The uncertainties for the corrected pixel regions were assigned to be twice as much as the standard deviation of the unaffected individual pixel values in the region.

We used the wide-slit science and calibration-star spectra to correct for the wavelength-dependent slit losses in the narrow-slit spectra with a `PyRAF` (`IRAF` with `Python` wrapper) script. We employed the `IRAF` task `curfit` to fit a spline function to the ratios of the narrow-slit to the reference spectra. We used a single reference spectrum: the mean of the bright, wide-slit spectra. Finally, we updated the starting pixel value of the wavelength scale in the FITS[9] file headers of the slit-loss corrected spectra to generate the appropriate wavelength grid for the trimmed spectra.

The `Python` scripts for performing the above corrections to prepare spectra for `PrepSpec` analysis will be made publicly available on `GitHub`[10] (Khatu et al., in prep.).

Flux Calibration

The flux calibration process included two steps – fitting a sensitivity curve of the detector response to the flux standard with `gsstandard`, and applying the sensitivity solution to the science spectra with the task `gscalibrate`. For flux calibration, we used the calibration star captured in the same slit as the science target except for a handful of spectra for which we used the star from another exposure of the same epoch (see Appendix A for details). Accordingly, we assigned a SpectroPhotometric CALibration Flag (SPCALF) of 1 (0) for calibrated (non-calibrated) science spectra (stated in Table 2.1). Based on the epoch and exposure of the standard star spectrum used for calibration, we further assigned a SpectroPhotometric CALibration Grade (SPCALG; see Table 2.1) to the science spectra as follows.

- SPCALG "A": Science spectrum calibrated with the standard star spectrum from the same exposure.
- SPCALG "B": Science spectrum calibrated with the standard star spectrum from the same epoch but different exposure.

Appendix A outlines special cases of spectral reduction that were treated separately.

The LJT spectra were reduced by members of the SEAMBH collaboration.

[9]FITS stands for Flexible Image Transport System.

[10]See Appendix B for a brief summary of the `GitHub` repository.

2.3.2 Comparison Between Gemini and LJT Spectra

Gemini spectra from 33 epochs and LJT spectra from 69 epochs provided 102 epochs of Mrk 142 spectral observations overlapping with the *Swift* and LCO photometric campaigns. A mean spectrum allows us to visualize spectral features in high signal-to-noise (S/N) from the combined observations, while a root-mean-square (RMS) spectrum signifies the variability in the spectral features. Figure 2.2 displays the mean and RMS of the Gemini (*Top*) and LJT (*Bottom*) spectra at rest wavelengths ($\lambda_{\rm rest}$). The higher-resolution Gemini mean spectrum shows sharper emission-line profiles (Hβ, [O III], and He I) as compared to the LJT mean. At lower resolution, LJT spectra are affected by instrumental broadening which results in the narrow emission lines, e.g., [O III], appearing broader than in the Gemini mean. The instrumental broadening effect also blurs the Fe II emission (shaded in faint blue) and the coronal lines (high-ionization forbidden transitions shaded in brown) in the LJT mean spectrum. In contrast to the Gemini mean, the Fe II features at ~4925 Å and ~5030 Å in the LJT mean appear blended with the Hβ wings on the longer-wavelength (red) side and [O III] λ5008, respectively. The RMS of the Gemini spectra shows a noisy region blueward of 4750 Å likely dominated by calibration noise. It is worth noting, however, that the finer wavelength sampling of the Gemini spectra (owing to the narrow-slit observations) makes that region appear even noisier. On the other hand, the region towards the blue end of the LJT RMS spectrum shows clear evidence of variability in the He II λ4687 line although it is heavily contaminated with Fe II in the surrounding region. Variability in Hβ is revealed by both the Gemini and the LJT RMS spectra. Although no variability in He I is evident from the Gemini RMS, the LJT RMS shows a weak signature of variability in broad He I. A very low, broad wave appears from ~5250 Å to ~5450 Å and from ~5650 Å to ~5950 Å in the LJT RMS spectrum likely resulting from calibration. The GMOS chip gap region in the Gemini spectrum extends from ~5350 Å to ~5410 Å, which also appears as a low bump in the RMS spectrum.

2.4 Spectral Analysis

To measure the Hβ and He I emission lines in the calibrated spectra, we first corrected any discrepancies in the calibrations of the Gemini and LJT spectra, independently, with `PrepSpec` and then modelled their spectral features with `Sherpa`. For `PrepSpec` modelling of Gemini spectra, we used the spectral region from ~4430 Å to ~6300 Å. For LJT spectra, we kept the spectral region from ~3390 Å to ~6300 Å.

2.4.1 `PrepSpec` Modelling

We independently modelled the 64 narrow-slit Gemini spectra and the 69 LJT spectra with `PrepSpec`[11] (developer: K. Horne) to correct for any relative deviations in the calibrated wavelength and flux scales. `PrepSpec` models spectra by fitting the continuum and emission lines with a composite model through an iterative process. We included the following model components for fitting the Mrk 142 spectra: (1) [A]verage spectrum (specified by "A") – mean of the input spectra; (2) [C]ontinuum – variations in the continuum emission from the accretion disk

[11] See Appendix C for documentation of `PrepSpec` and the current version of the software.

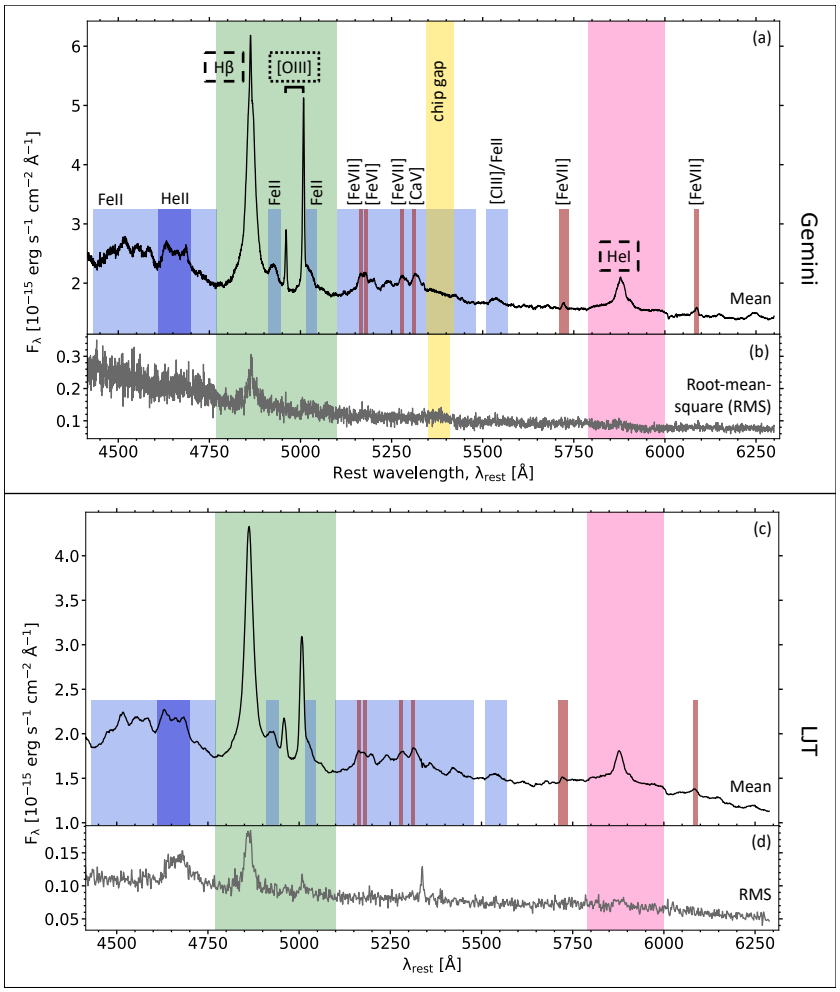

Figure 2.2: Rest-frame mean (black; panels *a* and *c*) and root-mean-square (RMS; grey; panels *b* and *d*) of Mrk 142 Gemini (*Top*; velocity resolution of ∼270 km s^{-1}) and LJT (*Bottom*; velocity resolution of ∼500 km s^{-1}) spectra highlighting the *Regions of Interest* – Hβ λ4861 and [O III] $\lambda\lambda$4960, 5008 (region shaded in green), and He I λ5877 (region shaded in pink). Labels enclosed in dashed (dotted) boxes indicate broad (narrow) lines. The Gemini mean spectrum shows sharp Fe II features (shaded in faint blue), which appear blended with the red wings of Hβ and [O III] λ5008 (blue shaded bars) in the LJT mean. Owing to the high signal-to-noise of the Gemini spectra, the peculiar shape of the He I λ5877 line is clearly evident. The high-ionization coronal lines (shaded in brown) also appear sharp in contrast to the LJT spectrum, as a result. The LJT RMS spectrum shows clear variability in He II (shaded in blue). Both RMS spectra indicate variability in the broad Hβ. However, no significant variability is evident in He I over the timescale of Gemini+LJT observations. The yellow-shaded region in the Gemini spectra indicates the GMOS chip gap from ∼5350 Å to ∼5410 Å.

modelled as a polynomial defined by log λ with time-dependent coefficients; (3) [W]avelength jitter – inter-spectra shifts in the wavelength scales; (4) [F]lux jitter – time-dependent photometric corrections to minimize the scatter of narrow emission-line fluxes relative to their

median; and (4) [B]road-line variations – variability in the broad emission-line features. Modelling emission lines in PrepSpec takes into account the velocity window half-widths of the broad as well as the narrow lines, whose initial values were set to 3000 km s^{-1} and 500 km s^{-1}, respectively. We set the broad Hβ λ4861 and He I λ5877 as variable lines for Gemini spectra, and Hγ λ4342, He II λ4687, Hβ, and He I λ5877 as variable for LJT spectra. The software uses the I Zwicky 1 (I Zw 1) template model (Véron-Cetty et al. 2001) to fit Fe II emission in the mean spectrum. PrepSpec is not designed to handle gaps in spectra or extremely large flux values, e.g., from cosmic-ray hits. Therefore, chip gaps and artefacts from cosmic-ray correction or sky subtraction in the Gemini spectra were replaced by median or simulated data (see Section 2.3.1 for details) during spectral reduction.

In the PrepSpec modelling stage, we first corrected the Gemini and LJT spectra for pixel shifts relative to the [O III] λ5008 line and then modelled the spectra with a composite model. We observed small pixel shifts (<6 pixels) while aligning the spectra along the wavelength axis. The model components were jointly fit starting with a single component and then adding components up to the ACWFB composite model for both the Gemini and the LJT spectra. PrepSpec determines the best-fitting model by accessing the Bayesian Information Criterion and reduced χ^2 (χ^2_ν, where ν stands for degrees of freedom) statistic. The goal of the fitting process is to use the fewest possible parameters to describe the data while penalizing the model for the number of parameters used. A good model yields $\chi^2_\nu \sim 1$. Figure 2.3 displays the final model (dark blue curve) passing through the black mean spectrum (panel *a*) and the model (dark grey curve) to the residual root-mean-square (RMSx) spectrum (panel *b*) for the 64 narrow-slit Gemini spectra. The RMS spectrum shows that the spectra are noisier at the bluer end.

Figure 2.4 shows the final model (panel *a*) along with the residuals (in the units of σ; panel *b*) in greyscale for the Gemini spectra. The best-fit model yielded a χ^2_ν value of 0.782, which indicates overfitting of the data, possibly indicating inaccurate error bars larger than the scatter in the data. The dark regions in the model highlight the prominent emission-line features of Hβ λ4861 and [O III] $\lambda\lambda$4960, 5008. The weak fluctuations blueward of ~4700 Å indicate more noise in that region as compared to the red end of the spectra. The residuals in greyscale display horizontal wiggles that are strongly evident in some spectra. We noted that the wiggles appear in the spectral regions replaced by simulated data to correct for residual features either from cosmic-ray correction or sky subtraction. The replacement with simulated data may have resulted in a lower performance of the model in those regions. Another probable reason for the wiggles is the use of a higher-order spline during flat-fielding in the spectral reduction process (refer Section 2.3.1 for details). However, we visually inspected all spectra processed through PrepSpec and observed no anomalous behaviour in the regions with wiggles. Therefore, the spectra were considered valid for further analysis.

PrepSpec modelling of LJT spectra yielded nearly even residuals with a χ^2_ν value of 0.791. The region redward of 6300 Å in LJT spectra comprises several blended narrow-line features, which resulted in a sub-optimal performance of the PrepSpec model. Therefore, we excluded the red side of the LJT spectra (λ > 6300 Å) during PrepSpec processing.

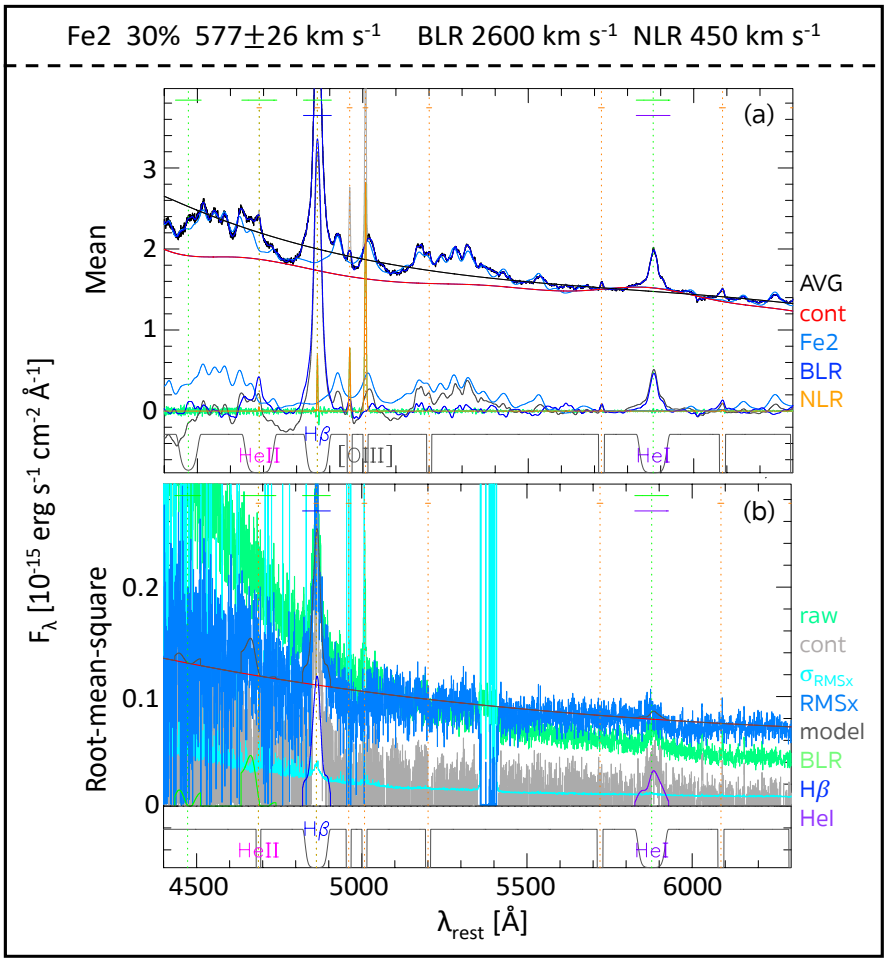

Figure 2.3: Mean (panel *a*) and root-mean-square (RMS; panel *b*) of 64 narrow-slit Mrk 142 Gemini spectra processed through `PrepSpec` showing model fits with individual components. In panel *a*, the composite model (dark blue curve), including the components shown at the bottom of the plot – average spectrum (AVG; black), continuum (cont; red), Fe II (Fe2; faint blue), broad-line region (BLR; dark blue), and narrow-line region (NLR; orange), is overlaid on the mean spectrum (black curve). The broad (narrow) emission lines are indicated with green (orange) dotted vertical lines as well as with green (orange) solid horizontal dashes. The broad lines of Hβ (blue label) and He I (purple label) are marked with solid horizontal dashes. In panel *b*, model (model; dark grey curve) fit to the residual RMS spectrum (RMSx; blue curve) includes the components: continuum (cont; red curve) and BLR (green curve at the bottom of the plot). The raw RMS spectrum is the upper green curve. The BLR component comprises the broad lines of Hβ (blue bump around ~4862 Å) and He I (purple bump around ~5877 Å) shown at the bottom of the plot. The broad He II emission feature at ~4687 Å (box-like feature in the model) is contaminated with Fe II and hence difficult to fit given the noise in the region. The deviation in the residual RMS spectrum ($\sigma_{\rm RMSx}$; cyan curve) shows large values in the region of the GMOS detector chip gap from ~5345 Å to ~5420 Å.

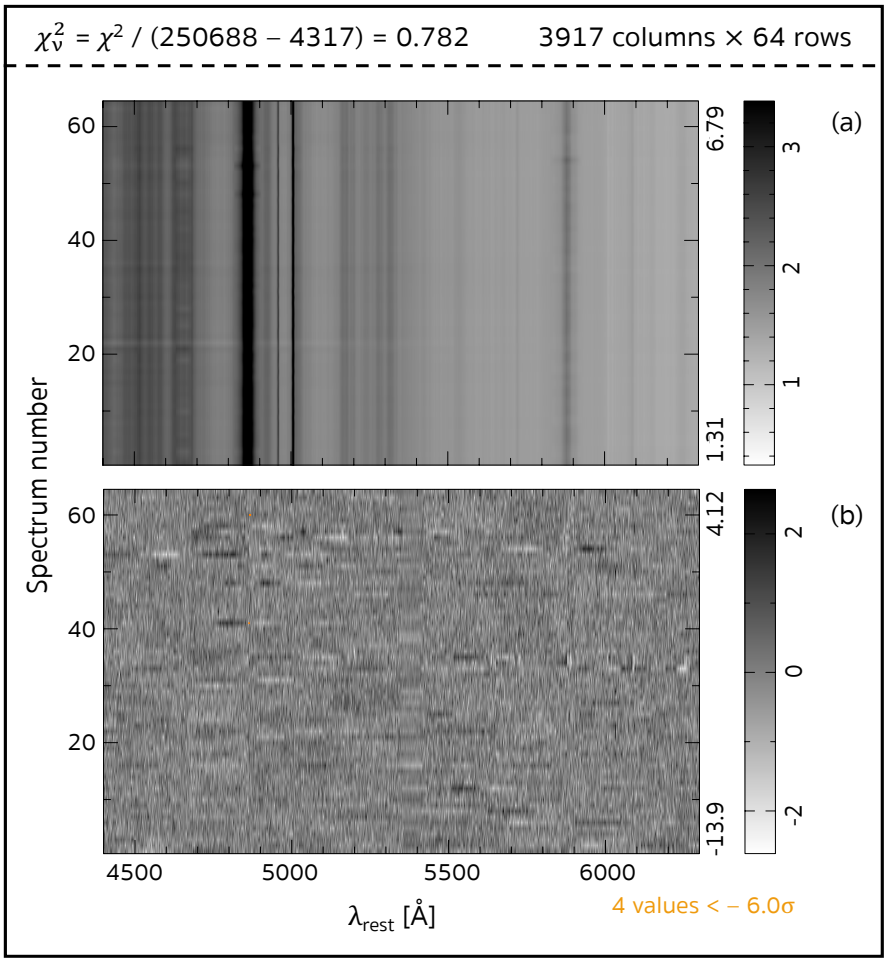

Figure 2.4: `PrepSpec` model including all components (panel *a*) and residuals (*data* − *model* in units of standard deviation, σ; panel *b*) with a reduced χ^2 (χ^2_ν) of 0.782 for 64 narrow-slit Mrk 142 spectra from Gemini. In panel *a*, dark regions indicate strong emission lines of Hβ and [O III], whereas the weaker He I lines and Fe II emission appears as less prominent features. In panel *b*, each row represents a single exposure spectrum (where multiple exposures at a given epoch are not yet combined). The horizontal wiggles strongly evident in some spectra are likely the result of either replacing values with simulated data in those regions or using a higher order function during flat-fielding (see text for more details). Four points where the values were less than 6σ are indicated with orange dots in the residuals plot. The smeared region from ~5345 Å to ~5420 Å is one of the chip gaps of the GMOS detector where simulated data was added during reduction.

2.4.2 Spectral Modelling in Sherpa

We modelled the continuum and emission lines in the Gemini and LJT spectra in Sherpa[12] (Freeman et al. 2001) v4.10.0 with a Python wrapper script. We first corrected the Gemini and LJT spectra for Galactic reddening using $E(B-V)^{[13]} = 0.015$ (Schlafly & Finkbeiner 2011). Averaging the two narrow-slit Gemini exposures from every night into a single spectrum per epoch (with exceptions for spectra from epochs 11, 25, and 28, where we only used single exposures) yielded a total of 33 Gemini spectra. Together with the 69 LJT spectra, we modelled a total of 102 Mrk 142 spectra.

We developed a composite model with a goal of performing a clean extraction of the Hβ and He I emission lines from the Gemini and LJT spectra. We included a power-law fit to the continuum, three Gaussians to model each of the Hβ, He I and He II emission lines, and a single Gaussian for each of the [O III] doublet lines. We adopted the I Zw 1 template model from Boroson & Green (1992) as a pseudo-continuum to trace the Fe II emission-line features. We also experimented with the Fe II template from Véron-Cetty et al. (2001). However, it failed to suitably trace the sharp Fe II features in Mrk 142. With the Boroson & Green (1992) Fe II template model, the fits yielded lower ($\chi_\nu{}^2$) values than with the Véron-Cetty et al. (2001) template. Following the procedure in Hu et al. (2015), we added single Gaussian profiles for each of the six coronal lines (Fe VII λ5160, Fe VI λ5177, Ca V λ5311, Fe VII λ5278, Fe VII λ5722, Fe VII λ6088; see Figure 2.2). In addition, we included the host-galaxy template with 11 Gyr at $z = 0.05$ from the 2013 updated version of Bruzual & Charlot (2003) galaxy templates. The host-galaxy template, affecting the redder part of the spectrum more than the bluer, contributed greatly in producing a good fit to the He I emission-line region. The fit in the Hβ region was less sensitive to host-galaxy emission. We referred to the Vanden Berk et al. (2001) rest wavelengths for setting the positions of all emission lines.

Gemini Spectral Analysis

Our goal of spectral fitting was to accurately estimate the Hβ, [O III], and He I profiles in the Gemini spectra. We aimed at finding a robust and flexible set of parameters that fit the structure in the spectra over all epochs. Figure 2.5 shows the composite model fit to a single-epoch Gemini spectrum.

We describe the fitting process as follows. The Gaussian used for each of the [O III] doublet lines traces the systemic narrow-line emission peaks. While fitting the Gemini spectra, the position, FWHM, and flux of the [O III] λ5008 emission line were freed. However, we fixed the position of the [O III] λ4960 line relative to the [O III] λ5008 line and the flux in the [O III] λ4960 line to a factor of 1/3 compared to the [O III] λ5008 flux. We chose Gaussians over Lorentzians to appropriately trace the narrower wings of the [O III] lines. We fixed the positions of the narrow components of Hβ, He I, and He II relative to the [O III] λ5008 line,

[12] Sherpa is a software application for modelling and fitting astronomical images and spectra. In this work, the Sherpa v4.10.0 application was used within Coronagraphic Imager with Adaptive Optics (CIAO) v4.10.0, the X-ray Data Analysis Software designed by the Chandra X-ray Center. For full documentation of CIAO-Sherpa, see https://cxc.harvard.edu/sherpa4.14/.

[13] $E(B-V)$ is the degree of reddening for the colour index $B-V$, where B is the bluer apparent magnitude (typically, the Blue colour in the optical) and V is the redder apparent magnitude (typically, the green colour referred to as the Visible colour in the optical).

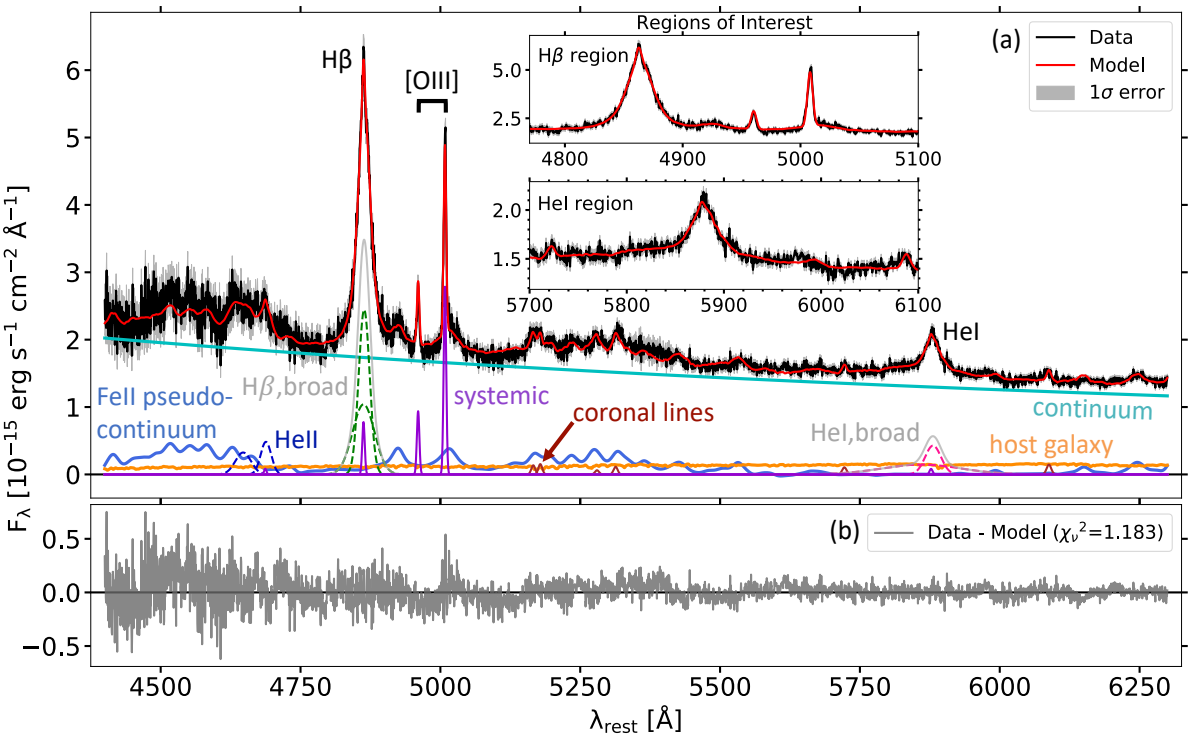

Figure 2.5: Composite model fit to epoch 24 of the Mrk 142 Gemini data displaying individual components of the model. Panel *a*: Composite model (red solid curve) fit to the data (black solid curve) from 4430 Å to 6300 Å is shown in the main panel, and the Hβ and He I *Regions of Interest* are shown in the *Inset* panels. The individual components of the model are displayed at the bottom of the panel: continuum (cyan solid curve); Fe II I Zw 1 template as a pseudo-continuum (faint blue solid curve); host-galaxy template (orange solid curve); He II broad components (blue dashed Gaussians); Hβ broad components (green dashed Gaussians); He I broad components (pink dashed Gaussians); narrow-line components of Hβ, He I, and [O III] (purple solid Gaussians); and high-ionization coronal lines (brown solid Gaussians). The total broad Hβ and He I profiles are also overplotted (grey solid curves). Panel *b*: Residuals of the model with $\chi_\nu^2 = 1.183$. The model shows larger residuals around the [O III] λ5008 line indicating a sub-optimal fit in that region. The noisier blue end of the spectrum affects the overall fit in that region, thus resulting in larger residuals compared to the red end of the spectrum.

and their widths equal to the [O III] λ5008 FWHM. The position and flux parameters of the two broad components of both Hβ and He I were freed. The width of only one of the Hβ Gaussians was allowed to vary while the second Gaussian was fixed at twice the width of the first. On the other hand, the widths of the He I broad components were fixed at factors of 1 and 6 of the FWHM of the flexible, broad Hβ component. We determined the above FWHM ratios for the broad Hβ and He I emission lines from the mean spectrum. The insets in Figure 2.5 show a closer view of the two *Regions of Interest* – Hβ and He I. A single broad component of He II

with position fixed relative to the flexible, broad Hβ component and width equal to the FWHM of the same component proved insufficient to trace the broader emission around ~4650 Å, indicating a plausible blueshifted broad component of He II. Adding another blueshifted Gaussian 1.5 times the width of the flexible, broad Hβ component with flux equal to that of the first broad He II component significantly improved the fit in that region. Table 2.3 lists the emission-line parameters along with their settings as used during spectral fitting.

Table 2.3: Emission-Line Fitting Parameters for Mrk 142 Spectra from the Gemini North Telescope (Gemini) and the Lijiang Telescope (LJT)

Line	Parameter	Fixed relative to line[a]	Ratio relative to the fixed line	
			Gemini	LJT
[O III] λ5008	Position	...	...	...
	FWHM	...	...	...
	Flux	...	...	...
[O III] λ4960	Position	[O III] λ5008	0.990	0.990
	FWHM	[O III] λ5008	1.000	1.000
	Flux	[O III] λ5008	0.333	0.333
Narrow Hβ λ4861	Position	[O III] λ5008	0.971	0.971
	FWHM	[O III] λ5008	1.000	1.000
	Flux	[O III] λ5008	...	0.293
Narrower broad Hβ λ4861	Position	...	...	...
	FWHM	...	...	...
	Flux	...	...	...
Broader broad Hβ λ4861	Position	...	...	...
	FWHM	Narrower broad Hβ λ4861	2.000	2.500
	Flux	...	...	...
Narrow He I λ5877	Position	[O III] λ5008	1.174	1.174
	FWHM	[O III] λ5008	1.000	1.000
	Flux	[O III] λ5008	...	0.034
Narrower broad He I λ5877	Position	...	...	...
	FWHM	Narrower broad Hβ λ4861	1.200	1.000
	Flux	...	...	...
Broader broad He I λ5877	Position	...	...	...
	FWHM	Narrower broad Hβ λ4861	6.000	6.000
	Flux	...	...	...
Narrow He II λ4687	Position	[O III] λ5008	0.936	0.936
	FWHM	[O III] λ5008	1.000	1.000
	Flux	...	...	...
Narrower broad He II λ4687	Position	Narrower broad Hβ λ4861	0.964	0.964
	FWHM	Narrower broad Hβ λ4861	1.000	1.000
	Flux	...	...	...

Continuation of Table 2.3				
Blueshifted broad He II λ4687	Position	Narrower broad Hβ λ4861	0.956	0.956
	FWHM	Narrower broad Hβ λ4861	1.500	1.500
	Flux	Narrower broad He II λ4687	1.000	1.000

[a] Parameter settings with no data indicate that the parameter was kept flexible during spectral fitting.

FWHM stands for full width at half maximum.

We followed the Fe II template fitting procedure described in Hu et al. (2015), where the Fe II emission is defined by a convolution of the Boroson & Green (1992) template with a Gaussian. We applied the Gaussian as a 1D Point Spread Function (PSF) with a fixed FWHM, and the amplitude of the convolved Fe II model was set as a flexible parameter while fitting. Although the Fe II model successfully traces the sharp Fe II features in most parts of the spectrum, it performs sub-optimally near the Fe II emission at the red wing of the [O III] λ5008 line thus resulting in larger residuals in that region. In contrast, the model overestimates the emission between the two [O III] lines due to the broader wing of Fe II from the template model.

Modelling individual coronal lines in the spectra considerably improved the fit in the Fe II emission region from ~5150 Å to ~5350 Å. In this region, the Fe coronal lines appeared to be slightly redshifted ($\leq$0.003) with respect to their rest wavelengths. We set the coronal-line widths to 1.5 times the [O III] λ5008 line width while their flux values were set to specific fractions of the [O III] λ5008 flux that were determined from the fit to the Gemini mean spectrum.

From spectral modelling, we derived, at each epoch, the total FWHM and flux values of the Hβ, He I, and [O III] lines. We measured the FWHM of the broad and total (including both the broad and the narrow components) Hβ and He I lines empirically by subtracting all other model components from the spectra including the narrow lines. To calculate the contribution from the broad-line and total (again, including both the broad- and the narrow-line) flux in the Hβ and He I emission profiles, we simply added the contribution from each of their components. Tables 2.4, 2.5, and 2.6 provide emission-line measurements for the Gemini spectra from 33 epochs. For epoch 11, the model failed to constrain the broad Hβ emission as the region blueward of the Hβ line appeared noisier compared to the other epochs. We therefore excluded epoch 11 from further analysis. Also, due to improper flux calibration at the location of the Hβ line in epoch 25, the line appeared unusually broader and brighter than at the other epochs. We therefore excluded the spectrum from epoch 25 as well.

Table 2.4: [O III] Emission-Line Measurements for Mrk 142 Gemini Spectra

Epoch	Position$_{[\mathrm{O\ III}]\lambda5008}$ [Å]	FWHM$_{[\mathrm{O\ III}]\lambda5008}$ [km s^{-1}]	$F_{[\mathrm{O\ III}]\lambda5008}$ [10^{-15} erg s^{-1} cm^{-2}]	χ^2_ν (see *Notes* below)
1	5008.21 ± 0.04	312.77 ± 5.14	15.68 ± 0.23	1.066
2	5008.19 ± 0.05	317.80 ± 8.51	15.80 ± 0.32	1.059
3	5008.12 ± 0.04	325.49 ± 5.91	16.14 ± 0.25	1.232
4	5008.19 ± 0.04	303.17 ± 9.17	15.67 ± 0.28	1.209
5	5008.18 ± 0.05	319.54 ± 4.94	16.16 ± 0.30	0.993

Continuation of Table 2.4

6	5008.20 ± 0.04	324.73 ± 3.24	16.05 ± 0.24	1.080
7	5008.23 ± 0.03	310.77 ± 3.92	15.52 ± 0.21	1.184
8	5008.15 ± 0.04	321.72 ± 4.85	16.08 ± 0.21	1.220
9	5008.15 ± 0.05	336.09 ± 6.75	16.15 ± 0.29	0.972
10	5008.11 ± 0.04	326.23 ± 4.81	16.03 ± 0.25	1.036
11	5008.11 ± 0.07	317.13 ± 9.46	15.64 ± 0.45	0.987
12	5008.16 ± 0.06	332.79 ± 10.17	16.28 ± 0.38	1.076
13	5008.19 ± 0.04	303.59 ± 6.02	15.59 ± 0.27	1.115
14	5008.16 ± 0.04	316.61 ± 5.41	15.81 ± 0.24	1.239
15	5008.20 ± 0.04	319.08 ± 3.98	15.87 ± 0.22	1.202
16	5008.19 ± 0.04	311.32 ± 5.13	15.64 ± 0.23	1.265
17	5008.22 ± 0.04	315.17 ± 4.08	15.95 ± 0.22	1.269
18	5008.14 ± 0.04	337.61 ± 5.78	16.13 ± 0.24	1.331
19	5008.22 ± 0.04	311.85 ± 1.83	15.80 ± 0.24	1.097
20	5008.21 ± 0.03	291.76 ± 5.87	15.54 ± 0.23	1.167
21	5008.23 ± 0.04	312.71 ± 5.63	15.99 ± 0.23	1.285
22	5008.18 ± 0.03	307.67 ± 5.65	15.83 ± 0.22	1.211
23	5008.20 ± 0.03	304.28 ± 3.88	15.60 ± 0.20	1.239
24	5008.15 ± 0.04	319.51 ± 3.44	15.85 ± 0.24	1.183
25	5008.20 ± 0.05	307.35 ± 5.21	15.94 ± 0.29	1.115
26	5008.20 ± 0.05	309.73 ± 7.36	15.89 ± 0.26	1.191
27	5008.21 ± 0.04	301.67 ± 5.34	15.54 ± 0.23	1.241
28	5008.34 ± 0.05	300.79 ± 2.18	15.29 ± 0.28	1.067
29	5008.18 ± 0.04	322.62 ± 7.23	16.12 ± 0.26	1.185
30	5008.24 ± 0.04	321.49 ± 4.08	15.94 ± 0.23	1.355
31	5008.27 ± 0.03	306.30 ± 5.01	15.71 ± 0.22	1.162
32	5008.25 ± 0.04	321.17 ± 5.83	16.04 ± 0.25	1.099
33	5008.22 ± 0.05	328.18 ± 4.30	16.42 ± 0.23	1.052

Notes: FWHM stands for full width at half maximum and F stands for flux. Reduced χ^2, $\chi^2_\nu = \chi^2/\nu = 3897$, where ν stands for degrees of freedom, gives the model statistic for individual epochs.

Table 2.5: Hβ Emission-Line Measurements for Mrk 142
Gemini Spectra

Epoch	FWHM$_{H\beta,b}$ [km s^{-1}]	$F_{H\beta,b}$ [10^{-15} erg s^{-1} cm^{-2}]	FWHM$_{H\beta,n}$ [km s^{-1}]	$F_{H\beta,n}$ [10^{-15} erg s^{-1} cm^{-2}]	FWHM$_{H\beta,t}$ [km s^{-1}]	$F_{H\beta,t}$ [10^{-15} erg s^{-1} cm^{-2}]
1	1777.60 ± 72.76	112.20 ± 2.37	312.80 ± 5.14	5.30 ± 0.41	1445.10 ± 52.09	117.50 ± 2.40
2	1682.00 ± 109.66	106.30 ± 4.27	317.80 ± 8.51	5.50 ± 0.56	1324.90 ± 83.77	111.80 ± 4.31
3	1703.30 ± 69.35	115.80 ± 5.06	325.50 ± 5.91	5.10 ± 0.45	1412.80 ± 73.87	120.90 ± 5.08
4	1746.00 ± 83.88	110.50 ± 2.69	303.20 ± 9.17	4.50 ± 0.40	1478.40 ± 67.23	115.00 ± 2.72
5	1555.20 ± 80.12	107.50 ± 3.35	319.50 ± 4.94	3.10 ± 0.56	1466.00 ± 96.50	110.60 ± 3.40
6	1830.70 ± 77.96	109.30 ± 3.65	324.70 ± 3.24	5.10 ± 0.46	1524.30 ± 80.74	114.40 ± 3.68
7	1797.50 ± 69.03	112.20 ± 2.16	310.80 ± 3.92	4.50 ± 0.38	1525.80 ± 56.96	116.70 ± 2.19
8	1697.30 ± 62.27	106.50 ± 2.33	321.70 ± 4.85	3.50 ± 0.38	1447.70 ± 62.23	110.00 ± 2.37
9	1499.40 ± 83.84	100.20 ± 3.15	336.10 ± 6.75	5.10 ± 0.57	1379.60 ± 58.58	105.40 ± 3.20
10	1593.50 ± 77.58	103.40 ± 2.72	326.20 ± 4.81	5.00 ± 0.45	1328.20 ± 55.38	108.40 ± 2.76
11[a]	1637.50 ± 132.49	104.30 ± 3.26	317.10 ± 9.46	5.70 ± 0.82	1235.20 ± 165.58	110.10 ± 3.36
12	1732.00 ± 120.89	101.50 ± 5.80	332.80 ± 10.17	5.90 ± 0.66	1322.50 ± 81.62	107.30 ± 5.84
13	1628.70 ± 88.37	101.30 ± 2.49	303.60 ± 6.02	3.70 ± 0.48	1354.70 ± 77.03	105.00 ± 2.54
14	1708.00 ± 69.07	109.10 ± 2.65	316.60 ± 5.41	4.20 ± 0.42	1384.70 ± 56.63	113.30 ± 2.68
15	1673.00 ± 104.18	108.80 ± 2.66	319.10 ± 3.98	4.90 ± 0.41	1341.70 ± 30.71	113.70 ± 2.69
16	1780.60 ± 76.14	103.20 ± 2.31	311.30 ± 5.12	4.40 ± 0.39	1412.80 ± 73.00	107.60 ± 2.34
17	1623.30 ± 65.39	108.40 ± 2.96	315.20 ± 4.08	3.80 ± 0.41	1402.90 ± 60.98	112.20 ± 2.98
18	1712.00 ± 72.56	105.60 ± 2.40	337.60 ± 5.78	4.60 ± 0.46	1477.90 ± 64.86	110.20 ± 2.44
19	1579.90 ± 91.48	106.10 ± 4.21	311.90 ± 1.83	6.10 ± 0.47	1348.80 ± 64.01	112.20 ± 4.23
20	1558.50 ± 62.95	115.20 ± 2.08	291.80 ± 5.87	3.40 ± 0.36	1473.50 ± 42.12	118.70 ± 2.11
21	1604.10 ± 43.52	112.60 ± 2.12	312.70 ± 5.63	3.60 ± 0.37	1446.20 ± 71.24	116.20 ± 2.15
22	1698.90 ± 62.32	109.30 ± 2.80	307.70 ± 5.65	4.40 ± 0.36	1442.20 ± 55.95	113.70 ± 2.82
23	1590.30 ± 57.23	108.30 ± 2.15	304.30 ± 3.88	3.70 ± 0.35	1416.60 ± 52.27	112.00 ± 2.18
24	1668.80 ± 77.18	110.90 ± 2.66	319.50 ± 3.44	4.30 ± 0.47	1391.90 ± 54.88	115.20 ± 2.70
25[b]	1672.70 ± 73.34	140.40 ± 3.64	307.30 ± 5.21	5.90 ± 0.67	1603.80 ± 83.52	146.30 ± 3.70

Continuation of Table 2.5

26	1655.60 ± 95.15	107.00 ± 2.60	309.70 ± 7.36	4.90 ± 0.43	1297.70 ± 50.57	111.90 ± 2.63
27	1649.30 ± 48.01	103.40 ± 3.92	301.70 ± 5.34	4.60 ± 0.42	1356.80 ± 59.85	108.00 ± 3.95
28	1678.60 ± 96.47	102.60 ± 3.24	300.80 ± 2.18	3.90 ± 0.60	1459.80 ± 148.40	106.50 ± 3.29
29	1713.40 ± 76.77	94.90 ± 3.05	322.60 ± 7.23	4.30 ± 0.38	1410.30 ± 66.80	99.20 ± 3.07
30	1754.70 ± 96.17	102.70 ± 3.74	321.50 ± 4.08	5.50 ± 0.46	1395.00 ± 92.30	108.20 ± 3.77
31	1816.20 ± 81.55	109.40 ± 4.30	306.30 ± 5.01	6.10 ± 0.38	1489.70 ± 96.81	115.50 ± 4.31
32	1682.50 ± 79.14	109.60 ± 2.33	321.20 ± 5.83	4.90 ± 0.42	1423.40 ± 47.55	114.50 ± 2.37
33	1699.90 ± 58.56	110.00 ± 4.96	328.20 ± 4.30	3.80 ± 0.49	1515.60 ± 78.31	113.80 ± 4.99

[a] Because the noisy region blueward of the Hβ emission line was unable to well constrain the broad, blue wing of Hβ, this epoch was excluded from further analysis.

[b] Due to a calibration issue at the location of the Hβ emission line, the Hβ profile appeared unusually broader and brighter than in other spectra. Therefore, this epoch was excluded from further analysis.

The second and the third columns providing full width at half maximum (FWHM) and flux (F) values, respectively, for the broad ('b') Hβ component include contributions from both the broad Gaussians defined for the line. The FWHM of the narrow ('n') Hβ is equal to the FWHM of the [O III] λ5008 (see Table 2.4, third column). The total ('t') FWHM and flux include contributions from both the broad and the narrow components ($t = b + n$).

Table 2.6: He I Emission-Line Measurements for Mrk 142
Gemini Spectra

Epoch	FWHM$_{\mathrm{He\ I},b}$ [km s^{-1}]	$F_{\mathrm{He\ I},b}$ [10^{-15} erg s^{-1} cm^{-2}]	FWHM$_{\mathrm{He\ I},n}$ [km s^{-1}]	$F_{\mathrm{He\ I},n}$ [10^{-15} erg s^{-1} cm^{-2}]	FWHM$_{\mathrm{He\ I},t}$ [km s^{-1}]	$F_{\mathrm{He\ I},t}$ [10^{-15} erg s^{-1} cm^{-2}]
1	47.50 ± 37.16	34.40 ± 0.84	312.80 ± 5.14	0.70 ± 0.12	47.50 ± 95.12	35.10 ± 0.85
2	53.10 ± 37.69	33.40 ± 0.99	317.80 ± 8.51	0.60 ± 0.16	53.10 ± 36.35	34.00 ± 1.01
3	90.90 ± 44.68	41.30 ± 0.93	325.50 ± 5.91	0.70 ± 0.14	90.90 ± 41.60	42.00 ± 0.94
4	36.60 ± 25.45	36.00 ± 0.89	303.20 ± 9.17	0.80 ± 0.12	36.60 ± 20.91	36.80 ± 0.90
5	335.90 ± 70.17	35.20 ± 1.09	319.50 ± 4.94	0.30 ± 0.17	335.90 ± 71.22	35.50 ± 1.10
6	46.40 ± 36.37	35.10 ± 0.89	324.70 ± 3.24	0.60 ± 0.14	46.40 ± 35.10	35.70 ± 0.90
7	136.00 ± 170.28	39.70 ± 0.76	310.80 ± 3.92	0.60 ± 0.12	1962.20 ± 312.77	40.30 ± 0.77
8	49.20 ± 65.25	39.10 ± 0.71	321.70 ± 4.85	0.50 ± 0.11	49.20 ± 59.32	39.60 ± 0.72
9	34.50 ± 43.78	33.10 ± 0.88	336.10 ± 6.75	0.70 ± 0.16	34.50 ± 46.77	33.70 ± 0.90
10	92.10 ± 53.24	36.30 ± 0.79	326.20 ± 4.81	0.70 ± 0.15	92.10 ± 52.57	37.00 ± 0.81
11[a]	153.60 ± 39.85	36.60 ± 1.41	317.10 ± 9.46	0.40 ± 0.23	153.60 ± 38.98	37.10 ± 1.43
12	92.00 ± 51.55	31.40 ± 1.29	332.80 ± 10.17	0.50 ± 0.17	92.00 ± 52.74	32.00 ± 1.30
13	1419.30 ± 90.06	35.90 ± 0.91	303.60 ± 6.02	0.00 ± 0.16	1419.30 ± 108.55	35.90 ± 0.93
14	83.00 ± 51.38	41.00 ± 0.82	316.60 ± 5.41	0.80 ± 0.12	83.00 ± 55.73	41.80 ± 0.83
15	66.90 ± 41.21	38.40 ± 0.77	319.10 ± 3.98	0.50 ± 0.12	66.90 ± 41.58	38.90 ± 0.78
16	152.80 ± 225.26	38.80 ± 0.82	311.30 ± 5.12	0.60 ± 0.12	1758.60 ± 497.15	39.40 ± 0.83
17	1825.50 ± 303.93	38.80 ± 0.86	315.20 ± 4.08	0.30 ± 0.15	1528.20 ± 415.45	39.10 ± 0.88
18	37.50 ± 32.33	37.20 ± 0.84	337.60 ± 5.78	0.40 ± 0.12	37.50 ± 181.48	37.60 ± 0.85
19	1828.60 ± 42.84	35.40 ± 0.90	311.90 ± 1.83	0.70 ± 0.14	1806.90 ± 41.89	36.10 ± 0.91
20	1862.20 ± 357.48	42.00 ± 0.72	291.80 ± 5.87	0.40 ± 0.11	1829.20 ± 631.89	42.40 ± 0.73
21	1798.60 ± 399.40	38.40 ± 0.84	312.70 ± 5.63	0.90 ± 0.13	1651.70 ± 647.54	39.30 ± 0.85
22	1870.20 ± 654.91	41.90 ± 0.79	307.70 ± 5.65	0.40 ± 0.12	1870.20 ± 682.49	42.20 ± 0.80
23	38.20 ± 189.58	40.20 ± 0.77	304.30 ± 3.88	0.50 ± 0.11	1873.70 ± 336.54	40.70 ± 0.77
24	55.00 ± 84.96	41.10 ± 0.87	319.50 ± 3.44	0.50 ± 0.14	55.00 ± 132.73	41.70 ± 0.88
25[b]	137.20 ± 43.01	38.30 ± 1.30	307.30 ± 5.21	0.60 ± 0.17	137.20 ± 45.89	38.90 ± 1.31

Continuation of Table 2.6

26	61.80 ± 53.92	36.90 ± 0.81	309.70 ± 7.36	0.50 ± 0.12	61.80 ± 110.20	37.40 ± 0.82
27	114.30 ± 180.23	38.70 ± 0.85	301.70 ± 5.34	0.50 ± 0.12	1935.50 ± 389.50	39.30 ± 0.86
28	81.90 ± 60.82	55.60 ± 1.08	300.80 ± 2.18	0.10 ± 0.20	81.90 ± 52.72	55.70 ± 1.10
29	181.40 ± 100.03	36.00 ± 0.80	322.60 ± 7.23	0.40 ± 0.12	181.40 ± 96.30	36.40 ± 0.81
30	34.50 ± 86.12	40.00 ± 0.96	321.50 ± 4.08	0.50 ± 0.14	34.50 ± 125.31	40.50 ± 0.97
31	66.50 ± 268.38	44.60 ± 0.89	306.30 ± 5.01	0.90 ± 0.12	66.50 ± 627.31	45.50 ± 0.90
32	294.50 ± 50.82	41.20 ± 0.89	321.20 ± 5.83	0.90 ± 0.13	1631.40 ± 160.94	42.10 ± 0.90
33	1537.10 ± 161.59	35.30 ± 0.90	328.20 ± 4.30	0.30 ± 0.14	1528.10 ± 267.64	35.60 ± 0.91

[a] Excluded from further analysis. See corresponding note in Table 2.5.

[b] Excluded from further analysis. See corresponding note in Table 2.5.

The second and the third columns providing full width at half maximum (FWHM) and flux (F) values, respectively, for the broad ('b') He I component include contributions from both the broad Gaussians defined for the line. The FWHM of the narrow ('n') He I is equal to the FWHM of the [O III] λ5008 (see Table 2.4, third column). The total ('t') FWHM and flux include contributions from both the broad and the narrow components ($t = b + n$).

LJT Spectral Analysis

We fit the 69 LJT spectra with the same goal of modelling the Hβ, [O III], and He I lines accurately. Figure 2.6 shows the fit to a single-epoch LJT spectrum.

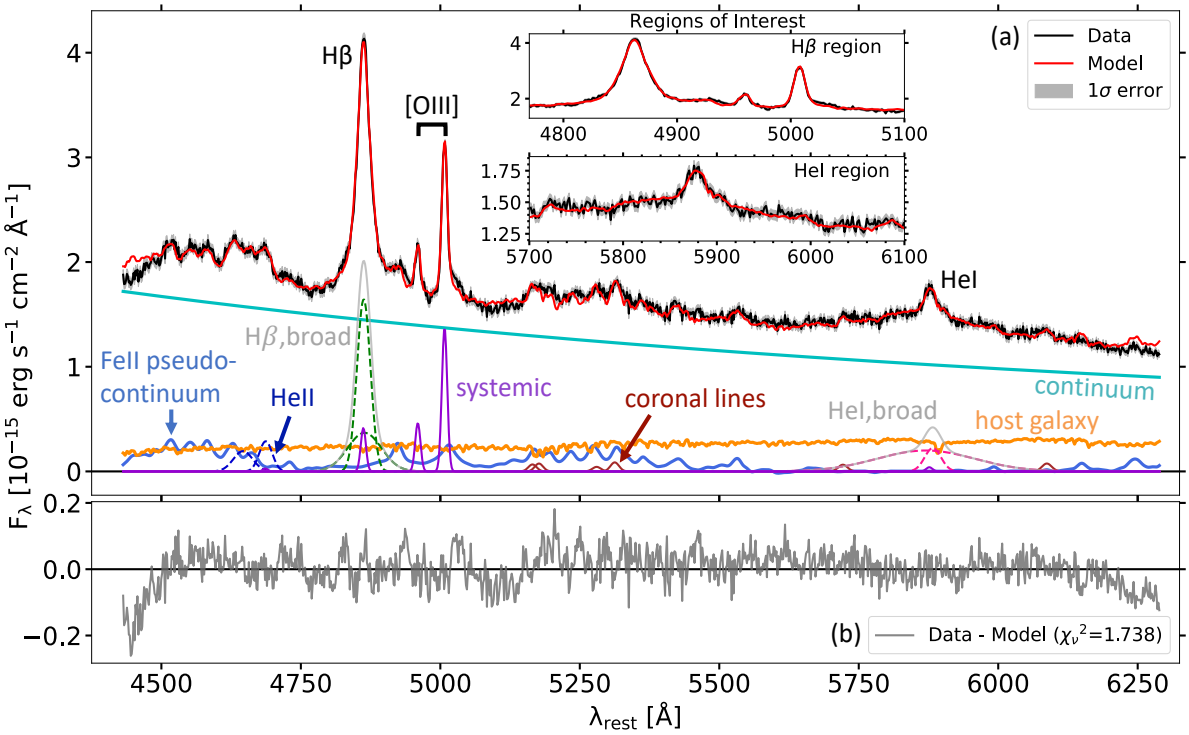

Figure 2.6: Composite model fit to epoch 24 of the Mrk 142 LJT data displaying individual components of the model. Panel *a*: See caption of Figure 2.5 for a description of the individual model components. The red side of the broad Hβ emission line shows contamination with the Fe II emission at ~4923 Å. Similarly, the [O III] λ5008 line shows considerable blending with the Fe II feature in its red wing, thus affecting a reliable measurement of the [O III] λ5008 line. Panel *b* shows the residuals of the model with χ_ν^2 = 1.711. The smaller residuals indicate an overall good fit to the spectrum. The model performance drops significantly at both the end of the spectrum although it does not impact measurements in the *Regions of Interest*.

We adopted the same model as for the Gemini spectra with small modifications to the ratios of certain fixed parameters. We determined the flux ratios for the coronal lines relative to the [O III] λ5008 line flux from the fit to the mean LJT spectrum. The width of the fixed broad Hβ Gaussian was fixed at a factor of 2.5 (instead of 2 for the Gemini spectra). A factor of 2 for this second Hβ Gaussian in LJT spectra was insufficient to trace the broad wing of Hβ, which also affected the fit to the blended Fe II feature at ~4923 Å. Therefore, a broader Hβ component was required to generate a good fit in that region. This indicates an interplay between the broad Hβ and Fe II line emission in the fitting process. Similarly, the [O III] λ5008 appears to be blended with the Fe II emission feature at its red wing. This is caused by the instrumental

broadening in LJT spectra that further resulted in wider [O III] FWHM measurements than typically expected for [O III] in NLS1 objects. To contain the effect of the "broader" [O III] FWHM measurements on the Hβ and He I line measurements, we fixed the narrow-line flux ratios of Hβ to [O III] λ5008 and He I to [O III] λ5008 from the Gemini spectral measurements (see Table 2.3). Tables 2.7, 2.8, and 2.9 provide emission-line measurements for the LJT spectra from 69 epochs.

Table 2.7: [O III] Emission-Line Measurements for Mrk 142
LJT Spectra

Epoch	Position$_{[\mathrm{O\ III}]\lambda5008}$ [Å]	FWHM$_{[\mathrm{O\ III}]\lambda5008}$ [km s^{-1}]	$F_{[\mathrm{O\ III}]\lambda5008}$ [10^{-15} erg s^{-1} cm^{-2}]	χ^2_ν (see *Notes* below)
1	5007.25 ± 0.09	718.53 ± 9.73	16.55 ± 0.24	2.265
2	5007.22 ± 0.13	754.17 ± 22.05	17.49 ± 0.44	1.446
3	5007.25 ± 0.13	741.00 ± 13.81	17.15 ± 0.30	2.001
4	5007.40 ± 0.12	787.83 ± 19.33	17.81 ± 0.39	2.033
5	5007.33 ± 0.10	716.88 ± 18.44	16.11 ± 0.36	2.069
6	5007.43 ± 0.13	740.35 ± 21.82	16.37 ± 0.42	1.705
7	5007.44 ± 0.16	880.35 ± 6.07	19.59 ± 0.37	1.601
8	5007.46 ± 0.06	691.28 ± 13.96	16.90 ± 0.31	2.557
9	5007.42 ± 0.10	679.82 ± 19.29	17.14 ± 0.35	1.680
10	5007.51 ± 0.17	707.68 ± 27.43	17.42 ± 0.59	1.283
11	5007.43 ± 0.14	742.40 ± ⋯	17.64 ± 0.32	1.513
12	5007.26 ± 0.09	713.60 ± 10.97	16.74 ± 0.26	2.186
13	5007.41 ± 0.20	716.25 ± 27.24	17.18 ± 0.60	1.513
14	5007.49 ± 0.12	757.80 ± 13.08	16.82 ± 0.32	1.671
15	5007.57 ± 0.14	737.32 ± 22.10	16.85 ± 0.42	1.416
16	5007.53 ± 0.10	682.41 ± 16.94	17.45 ± 0.33	1.658
17	5007.44 ± 0.10	682.02 ± 2.45	15.73 ± 0.24	1.985
18	5007.46 ± 0.15	736.23 ± 27.94	16.30 ± 0.46	1.202
19	5007.65 ± 0.14	752.66 ± 15.02	16.61 ± 0.29	1.926
20	5007.45 ± 0.15	727.33 ± 28.68	17.24 ± 0.58	1.242
21	5007.53 ± 0.14	758.33 ± 17.43	17.13 ± 0.42	1.398
22	5007.67 ± 0.17	802.28 ± 16.85	17.09 ± 0.42	1.469
23	5007.16 ± 0.23	772.50 ± 26.92	17.68 ± 0.71	1.213
24	5007.56 ± 0.10	674.68 ± 17.76	16.48 ± 0.31	1.738
25	5007.57 ± 0.11	700.33 ± 26.48	16.94 ± 0.38	1.658
26	5007.55 ± 0.11	733.35 ± 14.99	17.14 ± 0.32	1.767
27	5007.45 ± 0.09	680.14 ± 4.21	16.81 ± 0.26	2.025
28	5007.66 ± 0.14	801.55 ± 6.43	16.87 ± 0.28	1.449
29	5007.48 ± 0.10	785.48 ± 16.20	18.65 ± 0.34	1.959
30	5007.60 ± 0.14	742.64 ± 22.47	17.69 ± 0.47	1.337
31	5007.46 ± 0.10	707.32 ± 11.59	16.08 ± 0.26	2.248
32	5007.38 ± 0.08	699.42 ± 5.78	16.28 ± 0.36	1.323
33	5007.48 ± 0.13	684.96 ± 17.23	16.51 ± 0.38	1.797

Continuation of Table 2.7

34	5007.52 ± 0.11	683.06 ± 17.40	17.06 ± 0.35	1.759
35	5007.38 ± 0.11	776.64 ± 15.97	16.75 ± 0.30	2.821
36	5007.39 ± 0.06	681.62 ± 2.73	16.55 ± 0.15	4.364
37	5007.44 ± 0.09	682.09 ± 0.55	16.45 ± 0.24	2.127
38	5007.66 ± 0.13	810.86 ± 9.59	17.35 ± 0.39	1.465
39	5007.65 ± 0.24	719.85 ± 49.39	17.23 ± 1.00	2.021
40	5007.63 ± 0.12	719.57 ± 16.43	16.87 ± 0.36	1.714
41	5007.56 ± 0.08	728.84 ± 9.74	16.93 ± 0.22	4.650
42	5007.61 ± 0.09	688.18 ± 2.65	16.94 ± 0.20	3.737
43	5007.41 ± 0.14	713.02 ± 27.17	17.17 ± 0.54	1.522
44	5007.48 ± 0.16	712.60 ± 45.56	17.41 ± 0.93	1.633
45	5007.51 ± 0.13	745.88 ± 18.33	18.28 ± 0.39	1.527
46	5007.47 ± 0.10	731.28 ± 14.52	16.85 ± 0.29	1.979
47	5007.57 ± 0.22	744.07 ± 36.91	16.54 ± 0.72	1.045
48	5007.60 ± 0.12	685.57 ± 26.97	16.06 ± 0.45	2.259
49	5008.33 ± 0.21	857.08 ± 30.62	18.79 ± 0.56	2.061
50	5007.51 ± 0.09	691.27 ± 31.07	17.12 ± 0.48	3.209
51	5007.76 ± 0.08	726.03 ± 11.10	16.70 ± 0.24	3.277
52	5007.64 ± 0.12	686.30 ± 31.57	16.14 ± 0.50	1.615
53	5007.44 ± 0.11	707.77 ± 19.38	17.05 ± 0.39	1.821
54	5007.64 ± 0.11	679.58 ± 15.91	16.61 ± 0.37	1.592
55[a]	5007.50 ± 0.23	670.27 ± 26.30	14.49 ± 0.58	1.966
56	5007.40 ± 0.12	646.52 ± 31.81	15.84 ± 0.42	1.529
57	5007.39 ± 0.08	634.18 ± 1.41	16.06 ± 0.22	2.551
58	5007.55 ± 0.08	711.23 ± 8.50	17.44 ± 0.21	3.541
59	5007.62 ± 0.08	724.57 ± 12.47	17.69 ± 0.25	3.370
60	5007.57 ± 0.16	726.35 ± 21.79	17.52 ± 0.49	1.485
61	5007.39 ± 0.14	668.86 ± 27.44	17.21 ± 0.60	1.500
62	5007.60 ± 0.13	750.29 ± 14.14	18.55 ± 0.29	2.576
63	5007.68 ± 0.09	659.36 ± 14.10	16.40 ± 0.30	2.021
64	5007.32 ± 0.08	660.46 ± 11.08	16.44 ± 0.25	3.388
65	5007.70 ± 0.08	727.58 ± 12.06	17.44 ± 0.25	3.456
66	5007.55 ± 0.09	681.18 ± 12.68	17.10 ± 0.29	2.271
67	5007.63 ± 0.10	709.48 ± 14.44	17.00 ± 0.32	2.030
68	5007.70 ± 0.10	756.87 ± 3.52	17.44 ± 0.31	1.733
69	5007.59 ± 0.17	752.31 ± 25.47	17.25 ± 0.37	1.777

[a] This spectrum appeared very noisy likely due to some disturbance in the field of view at the time of observation. Therefore, we excluded this epoch from further analysis.

Notes: FWHM stands for full width at half maximum and F stands for flux. Reduced χ^2, $\chi^2_\nu = \chi^2/\nu = 1071$, where ν stands for degrees of freedom, gives the model statistic for individual epochs.

Table 2.8: Hβ Emission-Line Measurements for Mrk 142
LJT Spectra

Epoch	FWHM$_{H\beta,b}$ [km s^{-1}]	$F_{H\beta,b}$ [10^{-15} erg s^{-1} cm^{-2}]	FWHM$_{H\beta,n}$ [km s^{-1}]	$F_{H\beta,n}$ [10^{-15} erg s^{-1} cm^{-2}]	FWHM$_{H\beta,t}$ [km s^{-1}]	$F_{H\beta,t}$ [10^{-15} erg s^{-1} cm^{-2}]
1	1912.30 ± 52.05	83.50 ± 1.52	718.50 ± 9.73	4.80 ± 0.07	1660.30 ± 42.52	88.30 ± 1.52
2	1933.60 ± 73.49	82.70 ± 3.48	754.20 ± 22.05	5.10 ± 0.13	1702.10 ± 46.69	87.80 ± 3.48
3	1951.90 ± 38.49	83.30 ± 1.58	741.00 ± 13.81	5.00 ± 0.09	1748.30 ± 48.65	88.30 ± 1.58
4	1902.00 ± 52.64	84.90 ± 2.81	787.80 ± 19.33	5.20 ± 0.11	1700.90 ± 69.61	90.10 ± 2.82
5	1881.30 ± 46.94	80.30 ± 3.83	716.90 ± 18.44	4.70 ± 0.10	1706.90 ± 46.00	85.00 ± 3.83
6	1958.90 ± 85.17	82.20 ± 3.13	740.40 ± 21.82	4.80 ± 0.12	1708.40 ± 47.94	87.00 ± 3.13
7	2055.10 ± 86.83	82.60 ± 2.27	880.40 ± 6.07	5.70 ± 0.11	1750.10 ± 69.51	88.30 ± 2.27
8	1956.40 ± 54.49	81.30 ± 2.43	691.30 ± 13.96	5.00 ± 0.09	1804.80 ± 71.19	86.30 ± 2.43
9	1884.50 ± 63.48	78.30 ± 1.54	679.80 ± 19.29	5.00 ± 0.10	1618.90 ± 33.14	83.40 ± 1.55
10	1988.90 ± 85.31	85.20 ± 4.72	707.70 ± 27.43	5.10 ± 0.17	1742.50 ± 82.81	90.30 ± 4.72
11	1985.60 ± 102.52	78.20 ± 4.90	742.40 ± ⋯	5.20 ± 0.09	1647.50 ± 54.19	83.30 ± 4.90
12	1924.10 ± 44.77	82.10 ± 1.77	713.60 ± 10.97	4.90 ± 0.07	1703.40 ± 46.42	87.00 ± 1.77
13	1981.80 ± 87.56	84.80 ± 7.04	716.20 ± 27.24	5.00 ± 0.18	1848.70 ± 48.55	89.80 ± 7.05
14	2041.40 ± 64.72	80.20 ± 1.52	757.80 ± 13.08	4.90 ± 0.10	1779.80 ± 58.27	85.10 ± 1.52
15	2005.00 ± 57.21	78.50 ± 4.29	737.30 ± 22.10	4.90 ± 0.12	1684.60 ± 77.71	83.40 ± 4.29
16	2018.00 ± 83.47	82.30 ± 1.46	682.40 ± 16.94	5.10 ± 0.10	1630.70 ± 61.75	87.40 ± 1.47
17	1928.40 ± 64.59	81.80 ± 1.90	682.00 ± 2.45	4.60 ± 0.07	1702.30 ± 41.47	86.40 ± 1.90
18	1904.70 ± 79.53	82.90 ± 4.63	736.20 ± 27.94	4.80 ± 0.14	1678.90 ± 55.17	87.70 ± 4.63
19	2024.50 ± 63.95	83.00 ± 2.20	752.70 ± 15.02	4.90 ± 0.09	1782.50 ± 52.61	87.90 ± 2.20
20	1961.60 ± 91.94	81.30 ± 4.05	727.30 ± 28.68	5.10 ± 0.17	1658.00 ± 70.42	86.40 ± 4.05
21	1999.60 ± 68.62	77.60 ± 1.98	758.30 ± 17.43	5.00 ± 0.12	1696.10 ± 92.13	82.70 ± 1.98
22	1878.30 ± 92.12	76.60 ± 2.21	802.30 ± 16.85	5.00 ± 0.12	1685.10 ± 55.59	81.60 ± 2.22
23	1904.30 ± 60.58	77.10 ± 12.98	772.50 ± 26.92	5.20 ± 0.21	1755.80 ± 59.69	82.30 ± 12.99
24	1933.90 ± 44.35	77.70 ± 1.51	674.70 ± 17.76	4.80 ± 0.09	1653.50 ± 57.44	82.60 ± 1.51
25	1885.50 ± 73.40	76.80 ± 2.50	700.30 ± 26.48	5.00 ± 0.11	1647.80 ± 61.90	81.80 ± 2.50

Continuation of Table 2.8

26	2037.40 ± 49.58	78.90 ± 1.76	733.40 ± 14.99	5.00 ± 0.09	1816.40 ± 70.18	83.90 ± 1.76
27	1968.50 ± 76.64	79.70 ± 1.60	680.10 ± 4.21	4.90 ± 0.08	1735.10 ± 41.13	84.60 ± 1.60
28	1976.40 ± 77.05	76.70 ± 2.00	801.50 ± 6.43	4.90 ± 0.08	1764.50 ± 58.56	81.70 ± 2.00
29	1984.70 ± 45.75	78.00 ± 3.01	785.50 ± 16.20	5.50 ± 0.10	1742.40 ± 47.10	83.40 ± 3.01
30	1862.10 ± 89.44	75.40 ± 2.67	742.60 ± 22.47	5.20 ± 0.14	1698.60 ± 62.10	80.60 ± 2.67
31	2007.50 ± 39.14	80.20 ± 1.91	707.30 ± 11.59	4.70 ± 0.07	1744.60 ± 42.44	84.90 ± 1.92
32	2058.50 ± 96.40	81.30 ± 2.34	699.40 ± 5.78	4.80 ± 0.11	1741.80 ± 63.26	86.00 ± 2.35
33	1912.20 ± 56.62	82.90 ± 2.06	685.00 ± 17.23	4.80 ± 0.11	1688.60 ± 73.41	87.70 ± 2.07
34	1936.60 ± 39.84	84.70 ± 2.89	683.10 ± 17.40	5.00 ± 0.10	1726.30 ± 50.12	89.70 ± 2.89
35	1964.30 ± 29.09	81.90 ± 1.24	776.60 ± 15.97	4.90 ± 0.09	1730.30 ± 67.57	86.90 ± 1.24
36	1919.80 ± 32.65	84.60 ± 0.99	681.60 ± 2.73	4.80 ± 0.04	1702.90 ± 29.63	89.50 ± 0.99
37	1895.70 ± 76.09	85.50 ± 1.69	682.10 ± 0.55	4.80 ± 0.07	1654.30 ± 34.38	90.30 ± 1.69
38	1922.20 ± 72.29	84.50 ± 1.73	810.90 ± 9.59	5.10 ± 0.11	1709.00 ± 50.86	89.60 ± 1.73
39	1869.00 ± 69.04	85.10 ± 21.50	719.80 ± 49.39	5.00 ± 0.29	1655.90 ± 33.83	90.10 ± 21.50
40	1911.90 ± 50.71	87.10 ± 3.94	719.60 ± 16.43	4.90 ± 0.11	1670.90 ± 68.93	92.10 ± 3.94
41	1866.90 ± 45.29	88.70 ± 0.66	728.80 ± 9.74	5.00 ± 0.06	1641.70 ± 31.32	93.60 ± 0.66
42	1933.90 ± 47.99	87.30 ± 1.95	688.20 ± 2.65	5.00 ± 0.06	1682.90 ± 45.65	92.20 ± 1.95
43	1836.00 ± 74.08	91.00 ± 6.75	713.00 ± 27.17	5.00 ± 0.16	1700.70 ± 34.60	96.00 ± 6.75
44	1919.70 ± 58.92	87.20 ± 8.90	712.60 ± 45.56	5.10 ± 0.27	1686.70 ± 45.15	92.30 ± 8.91
45	1888.80 ± 66.52	86.50 ± 3.03	745.90 ± 18.33	5.40 ± 0.12	1676.10 ± 57.53	91.80 ± 3.03
46	1943.30 ± 46.47	85.20 ± 2.83	731.30 ± 14.52	4.90 ± 0.09	1663.20 ± 43.23	90.10 ± 2.83
47	1809.70 ± 133.31	80.00 ± 4.84	744.10 ± 36.91	4.80 ± 0.21	1606.90 ± 79.10	84.90 ± 4.84
48	1937.90 ± 54.89	82.20 ± 3.18	685.60 ± 26.96	4.70 ± 0.13	1700.60 ± 62.51	86.90 ± 3.18
49	2129.40 ± 115.06	80.40 ± 2.71	857.10 ± 30.62	5.50 ± 0.17	1702.50 ± 127.83	85.90 ± 2.71
50	2033.00 ± 39.57	87.90 ± 1.88	691.30 ± 31.07	5.00 ± 0.14	1773.30 ± 45.34	92.90 ± 1.88
51	1996.80 ± 36.64	85.70 ± 1.79	726.00 ± 11.10	4.90 ± 0.07	1749.80 ± 40.48	90.60 ± 1.80
52	1921.20 ± 51.06	81.70 ± 2.57	686.30 ± 31.57	4.70 ± 0.15	1665.20 ± 56.37	86.50 ± 2.58
53	1857.60 ± 43.01	81.60 ± 1.93	707.80 ± 19.38	5.00 ± 0.12	1667.70 ± 48.77	86.60 ± 1.93
54	1846.80 ± 71.96	80.30 ± 3.59	679.60 ± 15.91	4.90 ± 0.11	1627.90 ± 53.02	85.10 ± 3.59
55[a]	2051.10 ± 101.02	98.80 ± 3.24	670.30 ± 26.30	4.20 ± 0.17	1837.80 ± 91.10	103.00 ± 3.25

Continuation of Table 2.8

56	1900.90 ± 60.18	84.40 ± 3.27	646.50 ± 31.81	4.60 ± 0.12	1657.30 ± 35.32	89.10 ± 3.27
57	1855.20 ± 32.16	84.30 ± 1.50	634.20 ± 1.41	4.70 ± 0.06	1673.20 ± 36.47	89.00 ± 1.50
58	1874.00 ± 45.85	85.10 ± 1.06	711.20 ± 8.50	5.10 ± 0.06	1648.30 ± 35.92	90.30 ± 1.06
59	1880.60 ± 33.60	83.10 ± 1.16	724.60 ± 12.47	5.20 ± 0.07	1683.70 ± 33.69	88.30 ± 1.17
60	1831.50 ± 79.49	82.80 ± 4.33	726.30 ± 21.79	5.10 ± 0.14	1674.80 ± 49.65	87.90 ± 4.33
61	1802.10 ± 72.00	79.50 ± 7.29	668.90 ± 27.44	5.00 ± 0.17	1536.40 ± 60.57	84.50 ± 7.30
62	1943.20 ± 57.88	78.10 ± 2.86	750.30 ± 14.14	5.40 ± 0.09	1724.30 ± 43.09	83.60 ± 2.86
63	1934.50 ± 51.49	79.90 ± 2.27	659.40 ± 14.10	4.80 ± 0.09	1639.30 ± 39.42	84.70 ± 2.27
64	1852.70 ± 36.96	77.70 ± 1.71	660.50 ± 11.08	4.80 ± 0.07	1653.40 ± 37.04	82.50 ± 1.71
65	1893.10 ± 33.46	81.00 ± 1.12	727.60 ± 12.06	5.10 ± 0.07	1682.80 ± 46.75	86.20 ± 1.12
66	1930.50 ± 47.79	82.60 ± 1.45	681.20 ± 12.69	5.00 ± 0.09	1706.10 ± 32.90	87.60 ± 1.46
67	1877.50 ± 35.22	83.70 ± 2.16	709.50 ± 14.44	5.00 ± 0.09	1695.80 ± 56.16	88.70 ± 2.16
68	1838.90 ± 47.88	81.50 ± 2.43	756.90 ± 3.52	5.10 ± 0.09	1651.80 ± 43.06	86.60 ± 2.43
69	1893.90 ± 67.36	81.30 ± 3.04	752.30 ± 25.47	5.10 ± 0.11	1696.20 ± 35.67	86.30 ± 3.05

Excluded from further analysis. See note *a* in Table 2.7.

The second and the third columns providing full width at half maximum (FWHM) and flux (F) values, respectively, for the broad ('b') Hβ component include contributions from both the broad Gaussians defined for the line. The FWHM of the narrow ('n') Hβ is equal to the FWHM of the [O III] λ5008 (see Table 2.7, third column). The total ('t') FWHM and flux include contributions from both the broad and the narrow components ($t = b + n$).

Table 2.9: He I Emission-Line Measurements for Mrk 142
LJT Spectra

Epoch	FWHM$_{\mathrm{He\ I},b}$ [km s^{-1}]	$F_{\mathrm{He\ I},b}$ [10^{-15} erg s^{-1} cm^{-2}]	FWHM$_{\mathrm{He\ I},n}$ [km s^{-1}]	$F_{\mathrm{He\ I},n}$ [10^{-15} erg s^{-1} cm^{-2}]	FWHM$_{\mathrm{He\ I},t}$ [km s^{-1}]	$F_{\mathrm{He\ I},t}$ [10^{-15} erg s^{-1} cm^{-2}]
1	3321.90 ± 340.09	56.50 ± 1.28	718.50 ± 9.73	0.60 ± 0.01	3233.30 ± 310.70	57.00 ± 1.28
2	4215.70 ± 487.44	54.00 ± 1.93	754.20 ± 22.05	0.60 ± 0.01	3719.60 ± 432.81	54.60 ± 1.93
3	2677.20 ± 393.19	53.40 ± 1.49	741.00 ± 13.81	0.60 ± 0.01	2640.80 ± 335.95	54.00 ± 1.49
4	3526.50 ± 460.40	51.20 ± 1.61	787.80 ± 19.33	0.60 ± 0.01	3472.20 ± 439.97	51.80 ± 1.61
5	3672.30 ± 430.27	50.70 ± 1.55	716.90 ± 18.44	0.50 ± 0.01	2955.20 ± 380.12	51.20 ± 1.55
6	4021.40 ± 559.61	53.00 ± 1.70	740.40 ± 21.82	0.60 ± 0.01	3358.50 ± 509.57	53.60 ± 1.70
7	2801.00 ± 413.54	56.60 ± 1.93	880.40 ± 6.07	0.70 ± 0.01	2652.40 ± 370.69	57.30 ± 1.93
8	2393.00 ± 429.12	59.90 ± 1.77	691.30 ± 13.96	0.60 ± 0.01	2390.50 ± 356.89	60.50 ± 1.77
9	3007.50 ± 395.37	51.50 ± 1.48	679.80 ± 19.29	0.60 ± 0.01	3002.90 ± 377.58	52.10 ± 1.48
10	3440.80 ± 567.86	57.70 ± 2.40	707.70 ± 27.43	0.60 ± 0.02	3384.80 ± 534.77	58.30 ± 2.40
11	3742.60 ± 464.54	50.20 ± 2.05	742.40 ± ⋯	0.60 ± 0.01	3336.60 ± 414.10	50.80 ± 2.05
12	3707.10 ± 394.25	52.60 ± 1.27	713.60 ± 10.97	0.60 ± 0.01	3234.30 ± 349.07	53.10 ± 1.27
13	2031.80 ± 523.51	58.00 ± 3.71	716.20 ± 27.24	0.60 ± 0.02	2020.40 ± 440.68	58.60 ± 3.71
14	4636.30 ± 499.22	54.80 ± 1.67	757.80 ± 13.08	0.60 ± 0.01	3448.20 ± 477.32	55.30 ± 1.67
15	3570.60 ± 482.89	51.30 ± 2.10	737.30 ± 22.10	0.60 ± 0.01	3392.20 ± 451.91	51.90 ± 2.10
16	3777.30 ± 455.33	52.60 ± 1.58	682.40 ± 16.94	0.60 ± 0.01	2817.50 ± 387.51	53.20 ± 1.58
17	3086.90 ± 433.25	55.40 ± 1.48	682.00 ± 2.45	0.50 ± 0.01	3061.80 ± 378.12	55.90 ± 1.48
18	2644.90 ± 473.69	49.80 ± 2.21	736.20 ± 27.94	0.60 ± 0.02	2584.70 ± 432.55	50.40 ± 2.21
19	3681.00 ± 401.39	54.90 ± 1.46	752.70 ± 15.02	0.60 ± 0.01	3607.10 ± 366.87	55.40 ± 1.46
20	3500.60 ± 533.53	52.30 ± 2.19	727.30 ± 28.68	0.60 ± 0.02	3260.90 ± 504.05	52.90 ± 2.19
21	2511.80 ± 515.08	45.00 ± 1.95	758.30 ± 17.43	0.60 ± 0.01	2479.60 ± 447.60	45.60 ± 1.95
22	4378.20 ± 683.05	57.80 ± 2.05	802.30 ± 16.85	0.60 ± 0.01	3636.50 ± 586.59	58.40 ± 2.05
23	3628.50 ± 556.65	53.80 ± 3.67	772.50 ± 26.92	0.60 ± 0.02	3230.90 ± 523.56	54.40 ± 3.67
24	3526.30 ± 399.28	52.00 ± 1.43	674.70 ± 17.76	0.60 ± 0.01	3148.90 ± 367.20	52.60 ± 1.43
25	3227.40 ± 518.74	51.50 ± 1.66	700.30 ± 26.48	0.60 ± 0.01	3101.60 ± 485.38	52.10 ± 1.66

Continuation of Table 2.9

26	3575.80 ± 504.17	53.00 ± 1.59	733.40 ± 14.99	0.60 ± 0.01	3365.30 ± 459.45	53.50 ± 1.59
27	4302.90 ± 565.67	53.10 ± 1.39	680.10 ± 4.21	0.60 ± 0.01	4133.00 ± 484.86	53.60 ± 1.39
28	3591.50 ± 602.08	52.10 ± 1.71	801.50 ± 6.43	0.60 ± 0.01	3578.90 ± 529.44	52.60 ± 1.71
29	3724.10 ± 551.95	49.40 ± 1.45	785.50 ± 16.20	0.60 ± 0.01	3287.10 ± 540.93	50.00 ± 1.45
30	2501.40 ± 565.49	53.20 ± 2.11	742.60 ± 22.47	0.60 ± 0.02	2342.70 ± 479.92	53.80 ± 2.11
31	4400.20 ± 518.68	50.70 ± 1.36	707.30 ± 11.59	0.50 ± 0.01	4224.90 ± 445.09	51.30 ± 1.36
32	3186.80 ± 487.63	57.90 ± 1.95	699.40 ± 5.78	0.60 ± 0.01	3123.50 ± 437.13	58.40 ± 1.95
33	3456.90 ± 555.83	58.80 ± 1.82	685.00 ± 17.23	0.60 ± 0.01	3362.20 ± 519.98	59.30 ± 1.82
34	2880.20 ± 373.95	57.80 ± 1.85	683.10 ± 17.40	0.60 ± 0.01	2793.50 ± 302.62	58.40 ± 1.85
35	3257.80 ± 410.04	55.00 ± 1.34	776.60 ± 15.97	0.60 ± 0.01	3217.70 ± 374.73	55.60 ± 1.34
36	3778.50 ± 482.23	55.30 ± 0.95	681.60 ± 2.73	0.60 ± 0.01	3648.90 ± 431.31	55.80 ± 0.95
37	3369.40 ± 351.55	57.00 ± 1.42	682.10 ± 0.55	0.60 ± 0.01	3007.60 ± 302.49	57.50 ± 1.42
38	3024.40 ± 428.89	52.60 ± 1.96	810.90 ± 9.59	0.60 ± 0.01	3009.10 ± 400.53	53.20 ± 1.96
39	2901.40 ± 389.87	53.00 ± 4.09	719.80 ± 49.39	0.60 ± 0.03	2809.20 ± 349.70	53.50 ± 4.09
40	3125.00 ± 489.74	57.30 ± 1.85	719.60 ± 16.43	0.60 ± 0.01	3069.50 ± 431.89	57.90 ± 1.85
41	4761.30 ± 506.69	57.80 ± 1.03	728.80 ± 9.74	0.60 ± 0.01	3452.40 ± 380.24	58.40 ± 1.03
42	3699.50 ± 399.22	61.10 ± 1.21	688.20 ± 2.65	0.60 ± 0.01	3664.30 ± 382.17	61.70 ± 1.21
43	2720.70 ± 318.24	56.20 ± 2.42	713.00 ± 27.17	0.60 ± 0.02	2658.10 ± 296.64	56.80 ± 2.42
44	3220.80 ± 447.63	51.50 ± 2.37	712.60 ± 45.56	0.60 ± 0.03	3184.70 ± 440.37	52.10 ± 2.37
45	3481.80 ± 491.90	53.90 ± 2.03	745.90 ± 18.33	0.60 ± 0.01	3422.10 ± 444.64	54.50 ± 2.03
46	3367.30 ± 428.49	50.90 ± 1.39	731.30 ± 14.52	0.60 ± 0.01	3317.70 ± 417.84	51.50 ± 1.39
47	3618.30 ± 841.69	54.10 ± 3.18	744.10 ± 36.91	0.60 ± 0.02	3612.20 ± 762.87	54.60 ± 3.18
48	2302.30 ± 454.56	51.50 ± 1.72	685.60 ± 26.96	0.50 ± 0.01	2300.20 ± 404.61	52.00 ± 1.72
49	3621.50 ± 1008.02	56.90 ± 2.65	857.10 ± 30.62	0.60 ± 0.02	3598.70 ± 876.47	57.60 ± 2.65
50	3405.90 ± 461.62	55.30 ± 1.41	691.30 ± 31.07	0.60 ± 0.02	2868.40 ± 423.12	55.90 ± 1.41
51	2974.10 ± 380.00	50.90 ± 1.12	726.00 ± 11.10	0.60 ± 0.01	2512.20 ± 286.88	51.40 ± 1.12
52	3095.00 ± 465.57	49.00 ± 1.59	686.30 ± 31.57	0.50 ± 0.02	3061.60 ± 412.09	49.60 ± 1.59
53	3560.40 ± 386.81	55.20 ± 1.51	707.80 ± 19.38	0.60 ± 0.01	2853.20 ± 361.40	55.80 ± 1.51
54	4011.00 ± 529.26	54.90 ± 1.85	679.60 ± 15.91	0.60 ± 0.01	3867.00 ± 475.32	55.40 ± 1.85
55[a]	1713.80 ± 519.99	56.20 ± 2.93	670.30 ± 26.30	0.50 ± 0.02	1708.40 ± 510.68	56.60 ± 2.93

Continuation of Table 2.9

56	3026.10 ± 343.12	50.50 ± 1.69	646.50 ± 31.81	0.50 ± 0.01	2986.70 ± 363.23	51.00 ± 1.69
57	3362.40 ± 424.72	49.00 ± 1.20	634.20 ± 1.41	0.50 ± 0.01	2803.20 ± 397.62	49.60 ± 1.20
58	3533.50 ± 224.93	52.50 ± 1.09	711.20 ± 8.50	0.60 ± 0.01	3401.80 ± 203.52	53.10 ± 1.09
59	4223.20 ± 565.36	51.40 ± 1.09	724.60 ± 12.47	0.60 ± 0.01	2775.30 ± 415.60	52.00 ± 1.09
60	2515.60 ± 545.45	50.30 ± 2.37	726.30 ± 21.79	0.60 ± 0.02	2515.50 ± 480.20	50.80 ± 2.37
61	3274.40 ± 521.19	50.40 ± 2.23	668.90 ± 27.44	0.60 ± 0.02	3129.00 ± 497.58	51.00 ± 2.23
62	3352.30 ± 421.63	51.90 ± 1.68	750.30 ± 14.14	0.60 ± 0.01	3337.00 ± 419.84	52.50 ± 1.68
63	3756.60 ± 487.99	53.00 ± 1.36	659.40 ± 14.10	0.60 ± 0.01	3257.40 ± 447.67	53.60 ± 1.36
64	4128.00 ± 1067.59	49.80 ± 1.18	660.50 ± 11.08	0.60 ± 0.01	3030.40 ± 761.33	50.30 ± 1.18
65	4321.00 ± 452.31	57.70 ± 1.18	727.60 ± 12.06	0.60 ± 0.01	3535.20 ± 420.12	58.30 ± 1.18
66	5321.00 ± 693.68	57.00 ± 1.44	681.20 ± 12.69	0.60 ± 0.01	3285.40 ± 608.54	57.60 ± 1.44
67	3695.60 ± 507.40	56.90 ± 1.48	709.50 ± 14.44	0.60 ± 0.01	3549.70 ± 504.09	57.50 ± 1.48
68	3375.90 ± 481.92	52.80 ± 1.67	756.90 ± 3.52	0.60 ± 0.01	2925.40 ± 432.97	53.40 ± 1.67
69	3431.70 ± 465.23	53.30 ± 1.73	752.30 ± 25.47	0.60 ± 0.01	2660.20 ± 385.87	53.90 ± 1.73

Excluded from further analysis. See note *a* in Table 2.7.

The second and the third columns providing full width at half maximum (FWHM) and flux (F) values, respectively, for the broad ('b') He I component include contributions from both the broad Gaussians defined for the line. The FWHM of the narrow ('n') He I is equal to the FWHM of the [O III] λ5008 (see Table 2.7, third column). The total ('t') FWHM and flux include contributions from both the broad and the narrow components ($t = b + n$).

2.5 Light Curve Analysis

We used the Mrk 142 Gemini and LJT spectral measurements to generate light curves for the broad Hβ and He I emission-line profiles. We obtained the total broad-line light curves by integrating the flux under the two broad components (see green dashed Gaussians for Hβ and pink dashed Gaussians for He I in Figures 2.5 and 2.6) for the two emission lines.

We scaled the broad Hβ light curve from Gemini to the broad Hβ light curve from LJT to generate an inter-calibrated light curve. The Hβ light curves from Gemini and LJT were offset by ~25% from each other although they displayed similar fluctuations in their patterns. The offset can be attributed to various factors – different seeing conditions at Gemini and LJT or even the difference in the calibrations from the two telescopes. Because we are interested in measuring a time shift in the pattern with reference to the continuum variations, scaling and combining the light curves is valid for our purpose. Figure 2.7 shows the scaled broad Hβ light curve plotted with the original Gemini and LJT light curves. We then inter-calibrated the original Hβ light curve from LJT and the scaled Hβ light curve from Gemini with `PyROA` (see Section 2.5.1) to use the combined light curve to determine the time lag between the continuum and emission-line variability.

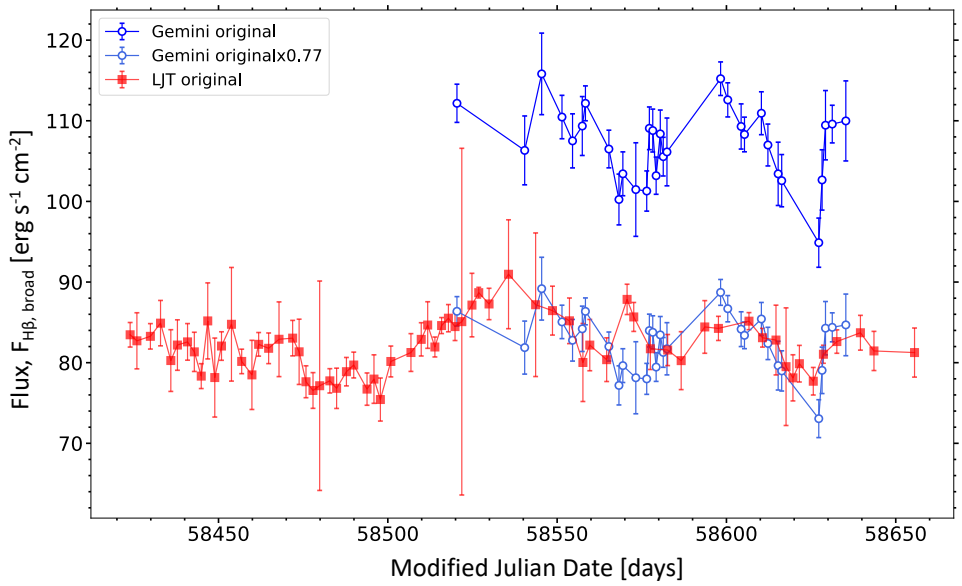

Figure 2.7: Broad Hβ light curve from Gemini (dark blue open circles) scaled down (faint blue open circles) to the broad Hβ light curve from LJT (red solid squares). The scaling factor of 0.77 was determined such that the Gemini data points are distributed evenly above and below the LJT light curve. The two light curves show similar behaviour except at Modified Julian Date ~58540, where the LJT light curve increases in flux while the Gemini light curve appears fainter.

2.5.1 Cross Correlation Time Lags

We cross-correlated the broad Hβ Gemini+LJT inter-calibrated light curve with the *UVW2* light curve from *Swift* to measure the reverberation lag of the BLR response to the continuum variability from the accretion disk, which is at smaller size scales than the BLR. Following Cackett et al. (2020), we chose the *UVW2* because we aim to measure the response of Hβ line-emitting gas to the UV continuum and the *UVW2* was the shortest wavelength available from the photometric monitoring of Mrk 142. During cross-correlation, we also included the LCO/g, the inter-calibrated 5100 Å continuum from Gemini and LJT data, and the LJT broad Hβ light curves to use maximum available information for a reliable measurement of the variability pattern.

We employed `Python`-based Running Optimal Average (`PyROA`; Donnan et al. 2021) to calculate cross-correlation time lags. `PyROA`[14] uses a running optimal average (ROA) calculated with a window function (defined by a Gaussian by default) of a certain width to estimate light-curve behaviour. The width of the window function controls the flexibility of the model in deriving the driving light curve – a narrower window function traces the fluctuating pattern of a highly variable light curve more appropriately than a wider window, which behaves more rigidly. The code uses priors to initiate the modelling process, and the performance of the model is evaluated using Bayesian Information Criterion. `PyROA` offers a robust treatment for outliers with an extra variance parameter and a standard deviation threshold. The extra variance adds in quadrature to the nominal uncertainties of the input light curves, and the threshold set by the user allows further inflation of the uncertainties to mitigate the influence of large outliers. Figure 2.8 shows the cross-correlation results with reference to the *Swift*/*UVW2* band.

In addition to the Hβ time lag for the Gemini+LJT inter-calibrated light curve ($8.58^{+0.76}_{-0.75}$ days), `PyROA` provided lag measurements for other input light curves ($0.87^{+0.11}_{-0.11}$ days for LCO/g, $0.76^{+0.26}_{-0.28}$ days for Gemini+LJT/5100 Å, and $8.05^{+0.81}_{-0.79}$ days for LJT/Hβ) with reference to the *Swift*/*UVW2* band. With respect to the shorter-wavelength *UVW2* emission, we expect to measure positive lags for the longer-wavelength emission in the g-band, at 5100 Å, and for the Hβ emission line. We thus modelled the distribution of time lags as a Log-Gaussian function that imposes positive lags with reference to *UVW2*, whose lag is fixed at 0.00 days (see Figure 2.8). In addition to measuring the time shift in the light-curve pattern, the width of the Log-Gaussian model also accounts for the amount of blurring applied to the reference light curve (here, *UVW2*) to match the response in the echo light curves. This becomes important for BLR RM, where the emission-line variations, emerging farther away from the central engine and from a more spatially extended structure (size scale $\sim$1 parsec) than the accretion disk, are smoother compared to the continuum variations closer to the centre. In `PyROA`, the width of the time-lag distribution quantifies the blurring determined for each of the echo light curves: $0.31^{+0.20}_{-0.20}$ days for LCO/g, $0.88^{+0.67}_{-0.49}$ days for Gemini+LJT/5100 Å, $4.99^{+1.17}_{-0.93}$ days for LJT/Hβ), and $5.52^{+1.13}_{-0.93}$ days for Gemini+LJT/Hβ.

[14] See `PyROA` code and documentation at `https://github.com/FergusDonnan/PyROA`.

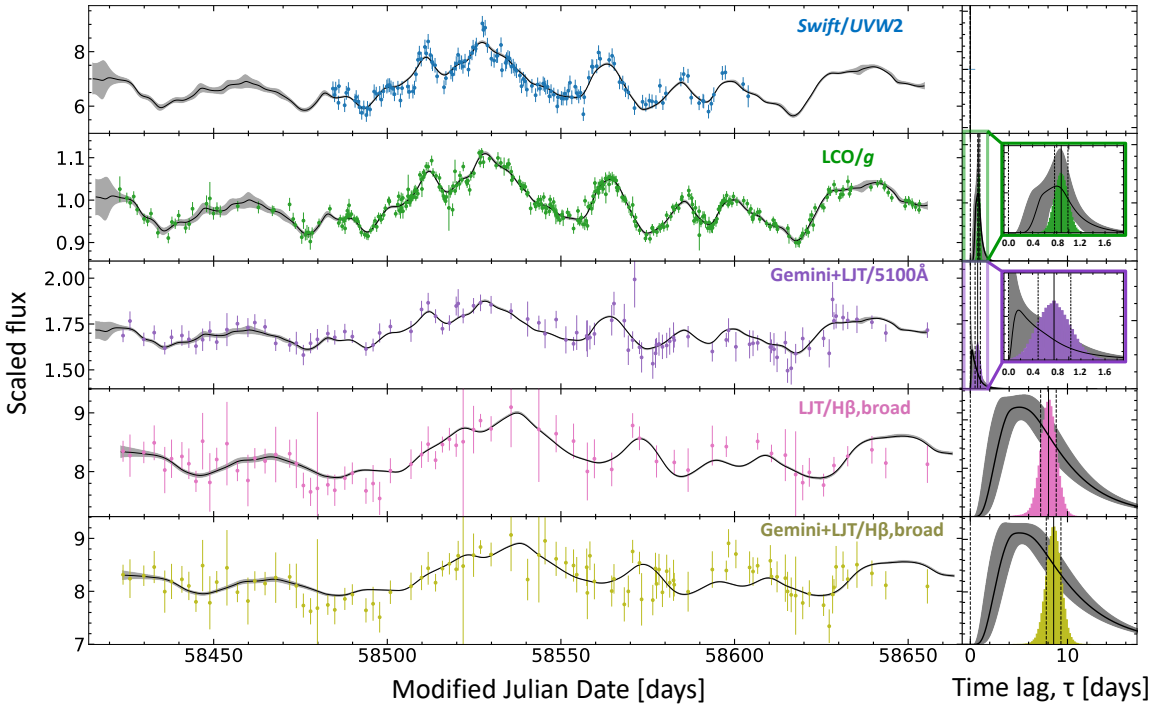

Figure 2.8: Time-lag measurements with reference to the *Swift*/*UVW2* band (top row) with lag distributions modelled as Log-Gaussians. *Left*: Top three panels show continuum light curves – *Swift*/*UVW2* (blue), LCO/*g* (green), and inter-calibrated Gemini+LJT/5100 Å – in units of 10^{-15} erg s^{-1} cm^{-2} Å^{-1}. Bottom two panels show the broad Hβ light curves – LJT only (pink) and Gemini+LJT inter-calibrated (olive) – in units of 10^{-14} erg s^{-1} cm^{-2} Å^{-1}. *Right*: Time-lag distributions (coloured histograms for the median lag and grey shaded estimates for the Log-Gaussian lag) of the light curves on the left with reference to the *Swift*/*UVW2* band, which has a fixed lag of 0.00 days. Insets in the second and the third panels show a close view of the time lag distributions for LCO/*g* and Gemini+LJT/5100 Å light curves, respectively. For each of the echo light curves, the black solid vertical lines mark the lag measurements, given by the median lag of the Log-Gaussian lag distribution, and the black dashed vertical lines (on either sides of the solid lines) mark the corresponding uncertainty.

2.5.2 He I Light Curves

The peculiar, asymmetrical shape of the He I line – narrow-line emission and a broad, asymmetrical component (modelled by a Gaussian 6 times the width of the broad Hβ line in our spectra fitting procedure) – is clearly evident in the high S/N Gemini mean spectrum. The asymmetry in the broad component due to the stronger blueshifted emission feature likely indicates a wind component in the broad-line region. Leighly (2004) performed CLOUDY simulations to model 10 high- and low-ionization emission lines observed in NLS1s. She suggests that the blueshifted emission evident in the high-ionization lines in NLS1s arises from a wind moving towards us. Interestingly, the plausible broad, blueshifted component for He II in the spectral model may also be a result of such a wind emission. Further analysis of the He II line is needed to draw firm inferences in this regard. In addition to the blueshifted wind, Leighly (2004) found that the high-ionization Lyα was dominated by emission in the accretion-disk atmosphere or at the low-velocity base of the broad-line wind. The very broad, flattened emission feature in He I may be indicative of a disk wind feature as noted for Lyα. Furthermore, Leighly (2004) derived a small covering fraction for the BLR. They argue that in an object with a small black hole mass, as in the case of Mrk 142 (which has a black hole mass, $M_\bullet = 3.89 \times 10^6\ M_\odot$, where $M_\odot$ is the mass of our Sun), the small covering fraction can result from an emission-line region closer to the plane of the disk. A flattened distribution for the disk emission is a possible explanation for the structure observed in the He I line in Mrk 142.

Although the LJT RMS spectrum shows a weak variable feature for He I, the variability is not usefully quantifiable given the timescale and S/N of our current Gemini+LJT spectroscopic campaigns. Figure 2.9 displays the individual and total broad-line components of He I emission from both the Gemini and the LJT observations. The offset observed in the narrower broad component is similar to that observed in the broad Hβ, where the light curve from Gemini appears at higher flux values than the LJT light curve. Interestingly, the broader broad component is brighter in LJT than in Gemini likely resulting from the blueshifted disk wind component broadened due to the wider slit used for LJT data.

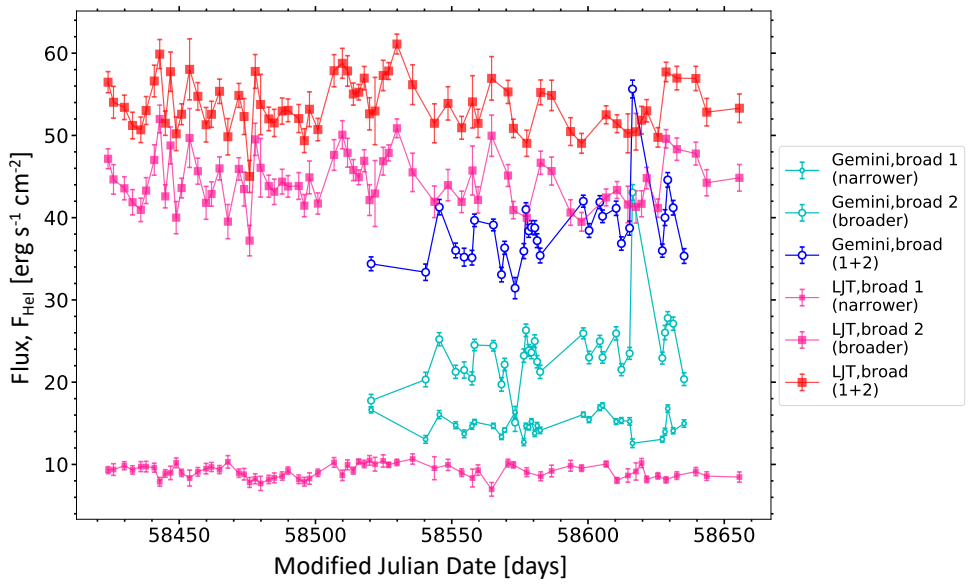

Figure 2.9: He I light curves highlighting the contributions from the individual broad components (labelled 1 and 2) to the total broad components from the Gemini (open circles) and LJT (solid boxes) data. Smaller (larger) size of the markers represents narrower (broader) components. It is interesting to note that the broader He I light curve from the LJT spectra is brighter than the broader He I component from the Gemini spectra likely due to the blue wing of He I (traced primarily by the broader component) in the LJT data affected by instrumental broadening.

2.6 Results and Discussion

We present the first results on the lag of the broad Hβ line with respect to the UV continuum in Mrk 142 from optical spectroscopic observations from Gemini+LJT with simultaneous monitoring in the photometric *Swift*/*UVW2* and LCO/*g* bands.

We applied a spectral model with same number of components but different parameter settings to the Gemini and LJT spectra to derive Hβ and He I light curves. We noted that a narrow+two broad Gaussians sufficiently traced both the Hβ and the He I lines, where the widths and positions of the narrow components were tied to the [O III] λ5008 line. However, we employed fixed narrow-line flux ratios $F_{\mathrm{H}\beta}/F_{[\mathrm{O\ III}]\ \lambda5008}$ and $F_{\mathrm{He\ I}}/F_{[\mathrm{O\ III}]\ \lambda5008}$ for the LJT spectral model (determined from flexible flux ratios for the Gemini spectra) due to the instrumental broadening in the LJT spectra affecting emission-line measurements. Although the LJT RMS spectrum shows a weak feature at the He I location, `PrepSpec` modelling and light-curve analysis suggested that there is no adequate variability in the line that is measurable with the current Gemini+LJT data. However, we acknowledge that the He I emission line shows a peculiar profile evident from the high S/N of the Gemini spectra. The broader Gaussian used for the line indicates stronger blueshifted emission than the redshifted side of the line. Also, the He II line specifically required a broad, blueshifted component to accurately trace the

emission in that region. Followed by spectral analysis, we empirically measured the FWHM values as well as calculated the narrow- and broad-line flux values of the Hβ and He I lines to obtain their light curves.

Applying `PyROA`, we performed cross-correlation analysis with continuum (*Swift*/*UVW2*, LCO/g, and Gemini+LJT/5100 Å) and broad Hβ light curves (LJT and Gemini+LJT inter-calibrated) with a goal of determining reverberation time lag for the Gemini+LJT inter-calibrated Hβ light curve. `PyROA` provided an improvement in quantifying the uncertainties compared to previous studies. Most early RM studies have extensively applied the Interpolated Cross-Correlation Function (ICCF; Gaskell & Sparke 1986; Gaskell & Peterson 1987) for time-lag measurements which makes it a good comparison standard. However, ICCF struggles with non-uniformly sampled data, which is true for our Gemini+LJT campaigns similar to most other studies, and uses linear interpolation to estimate the light-curve behaviour in the regions with data gaps. Consequently, the uncertainties reported with ICCF-based measurements are typically overestimated. In this context, Just Another Vehicle for Estimating Lags In Nuclei (`JAVELIN`; Zu et al. 2011, 2013) has been shown to perform better. For instance, Edelson et al. (2019) reported uncertainties from ICCF to be twice as large as those from JAVELIN. JAVELIN uses damped random walk (DRW) to estimate the light-curve pattern in the regions where data are not available. DRW closely characterizes the variability observed in AGN, plausibly leading to smaller uncertainties in the final lag measurements. However, JAVELIN requires a good estimation of uncertainties in data. For sub-optimally calibrated uncertainties, JAVELIN can sometimes fail to deliver reliable lag measurements (Donnan et al. 2021). Here, `PyROA` offers an improvement. The ROA along with a robust error treatment in `PyROA` not only prevents the outlier points from disrupting the estimation of the driving light curve but also applies a valid algorithm for resolving data gaps.

We measured a time lag of $8.58^{+0.76}_{-0.75}$ days for the Gemini+LJT inter-calibrated Hβ emission with reference to the *UVW2* continuum. We also obtained a lag of 0.76 ± 0.28 days for the 5100 Å continuum with reference to the *UVW2* emission that yields an optical lag of 7.82 ± 0.81 days for the Hβ emission line. From here, we report a black hole mass of $\log(M_\bullet/M_\odot) = 6.63 \pm 0.05$ derived using Equation 2.1,

$$M_\bullet = \frac{f\ c\ \tau_{\mathrm{H}\beta}\ \Delta V^2_{\mathrm{FWHM,\,H}\beta}}{G} \tag{2.1}$$

where c is the speed of light, $\tau_{\mathrm{H}\beta}$ is the time lag of the Hβ line, $\Delta V_{\mathrm{FWHM,\,H}\beta}$ is the Hβ velocity width in terms of the FWHM of the line profile, G is the universal gravitational constant, and f is the dimensionless scale factor. We used an f value of 1 following previous work by Du et al. (2014) and Wang et al. (2014a). We note that there is high uncertainty in this value of f. We further measured mean luminosities of $\log L_{\mathrm{UVW2}} = 43.832 \pm 0.001$, $\log L_{5100} = 43.643 \pm 0.002$, and $\log L_{\mathrm{H}\beta} = 41.621 \pm 0.002$.

Our results agree with previously published measurements of Mrk 142 (Du et al. 2015). From the previous SEAMBH campaign over several months, Du et al. (2015) reported a time lag of $7.9^{+1.2}_{-1.1}$ days for Hβ with reference to 5100 Å. We measured an optical lag of 7.82 ± 0.81 days for Hβ in agreement with the Du et al. (2015) value within uncertainties. Furthermore, the derived black hole mass for Mrk 142 in this work, $\log(M_\bullet/M_\odot) = 6.63 \pm 0.05$, agrees with the value reported by Du et al. (2015), $6.59^{+0.07}_{-0.07}$, within uncertainty limits. In deriving the black hole mass from Equation 2.1, we used the mean Hβ FWHM of 1680.34 ± 14.29 km s^{-1}

from the Gemini spectra. Here, we chose the Gemini spectra due to their higher resolution providing a more reliable measurement of the narrower Hβ broad-line profile than the LJT spectra. For the L_{5100} and $L_{\mathrm{H}\beta}$ measurements, we adopted the mean flux value from our Gemini+LJT inter-calibrated light curves as their respective Gemini light curves alone were insufficient to provide a reliable flux scale due to the shorter observing timescale. Table 2.6 summarizes the measured quantities in this work and shows their comparison with the Du et al. (2015) values.

Table 2.10: Summary of Mrk 142 Measurements

Measured Quantity	This Work	Du et al. (2015)
$\tau^{*}_{\mathrm{UVW2\text{-}to\text{-}H}\beta}$	$8.58^{+0.76}_{-0.75}$ days	···
$\tau_{5100\ \text{Å-to-H}\beta}$	7.82 ± 0.81 days	$7.9^{+1.2}_{-1.1}$ days
$\log(M_{\bullet}/M_{\odot})$	6.63 ± 0.05	$6.59^{+0.07}_{-0.07}$
$\log L_{\mathrm{UVW2}}{}^{*}$	43.832 ± 0.001	···
$\log L_{5100}$	43.643 ± 0.002	43.56 ± 0.06
$\log L_{\mathrm{H}\beta}$	41.621 ± 0.002	43.56 ± 0.06

* New measurements

To visualize our results in the broader context of reverberation-mapped AGN, we placed the measured size of the Hβ line-emitting region on various *R–L* scaling relations. Comparisons are discussed below.

Figure 2.10 shows the $R_{\mathrm{H}\beta}$–L_{5100} (panel *a*) and $R_{\mathrm{H}\beta}$–$L_{\mathrm{H}\beta}$ (panel *b*) relations with the red star representing the Mrk 142 measurements from this work. In agreement with the findings from previous SEAMBH campaigns (black circles in Figure 2.10; see references in the figure caption), the red Mrk 142 star appears to depart from the general trend observed for all other RM objects (green circles, panel *a* and grey circles, panel *b*; see the entire reference list in the figure caption). This reiterates the characteristic of super-Eddington AGN exhibiting smaller BLR sizes in contrast to the sub-Eddington population at the same luminosities (Du et al. 2016b). Du et al. (2015) tested this deviation of high accretion-rate AGN from the $R_{\mathrm{H}\beta}$–L_{5100} relationship. Studying the differences in the BLR sizes for AGN with low ($\dot{M}/\dot{M}_{\mathrm{Edd}} < 3$) and high ($\dot{M}/\dot{M}_{\mathrm{Edd}} \geq 3$) mass-accretion rates, Du et al. (2015) inferred that $\dot{M}$ influences the size scales observed in super-Eddington AGN while such a correlation is absent in the low mass-accretion rate objects.

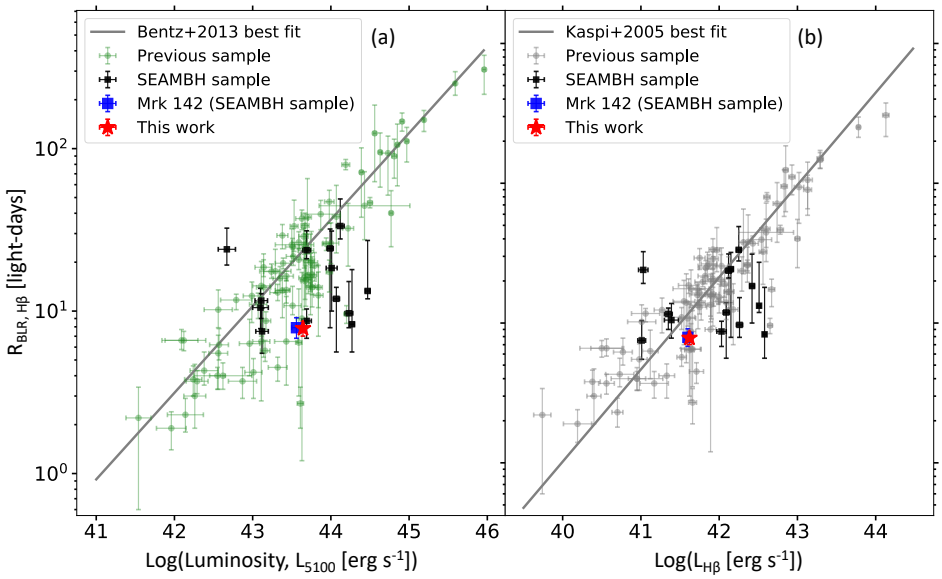

Figure 2.10: Radius-luminosity (R–L) scaling relations for Hβ in the optical including results from this work (red star). Panel *a*: $R_{\mathrm{H}\beta}$–L_{5100} relation showing Mrk 142 from this work close to the Du et al. (2015) measurement (blue square). Panel *b*: $R_{\mathrm{H}\beta}$–$L_{\mathrm{H}\beta}$ relation showing Mrk 142 from this work overlapping with the measured value in Du et al. (2015). The SEAMBH objects (black squares; Du et al. 2014; Wang et al. 2014b; Hu et al. 2015; Du et al. 2015) appear on the lower right of the grey solid lines, which represent the best-fit R–L relations from Bentz et al. (2013) with L_{5100} (panel *a*) and Kaspi et al. (2005) with $L_{\mathrm{H}\beta}$ (panel *b*), indicating a smaller size for the broad-line region in highly accreting AGN compared to the more typical, sub-Eddington AGN mapped in previous studies (green circles, panel *a* and grey circles, panel *b*; Stirpe et al. 1994; Santos-Lleó et al. 1997; Collier et al. 1998; Dietrich et al. 1998; Peterson et al. 1998; Kaspi et al. 2000; Santos-Lleó et al. 2001; Kaspi et al. 2005; Bentz et al. 2006; Collin et al. 2006; Denney et al. 2006; Bentz et al. 2007, 2009a,b; Denney et al. 2010; Dietrich et al. 2012; Grier et al. 2012; Barth et al. 2013; Bentz et al. 2013, 2014; Pei et al. 2014; Peterson et al. 2014, 2002, and references therein) at same luminosities.

Figure 2.11 shows the $R_{\mathrm{H}\beta}$–L_{5100} and $R_{\mathrm{H}\beta}$–L_{1350} scaling relations for NGC 5548 over time with optical lag measurements for Hβ and luminosities at 5100 Å and 1350 Å (L_{1350}) from Eser et al. (2015). Again, the red star in both panels represents the Mrk 142 point from this work. Eser et al. (2015) formulated a conversion from L_{5100} to L_{1350} for NGC 5548 (see their Equation 4) from all RM campaigns of the object from 1988 to 2008 (Peterson et al. 2002; Bentz et al. 2007, 2009b; Denney et al. 2010). We applied that conversion to calculate L_{1350} for NGC 5548 and generated the $R_{\mathrm{H}\beta}$–L_{UV} plot (Figure 2.11, panel *b*). Here, the luminosity for Mrk 142 is the luminosity in the L_{UVW2} value at the effective wavelength of 1928 Å as against L_{1350} for NGC 5548. The shift in the position of Mrk 142 from panel *a* to *b*, closer to the R–L scaling relation in UV, indicates that the UV emission is a better proxy for the ionizing continuum than the 5100 Å optical emission. If UV emission (here, in the *UVW2* band) is closer to the driving continuum, this will affect the black hole mass of Mrk 142 derived

from the 5100 Å to Hβ time lag. Recently, Cackett et al. (2020) performed the accretion-disk RM analysis for Mrk 142 with data from *Swift*, LCO, and other ground-based observatories, simultaneous to the Gemini+LJT data taken as a part of the same broader RM campaign. Cackett et al. (2020) pointed that if the *UVW2* band represents the driving continuum, then the black hole mass derived from the Hβ optical lag is underestimated by ∼10%. We used the *UVW2* to Hβ time lag result from this work to calculate the black hole mass in Mrk 142. We obtained a mass of $\log(M_\bullet/M_\odot) = 6.67 \pm 0.04$ based on the *UVW2* to Hβ time lag. This value is ∼10% greater than the black hole mass derived by assuming 5100 Å as the driving continuum band, and thus verifies the estimated discrepancy by Cackett et al. (2020). However, this discrepancy would be as high as ∼40% if X-ray, instead of UV, were the driving continuum (Cackett et al. 2020). A robust Hβ lag measurement with reference to the X-ray continuum will help understand how X-ray plays a role in driving the continuum variability in Mrk 142.

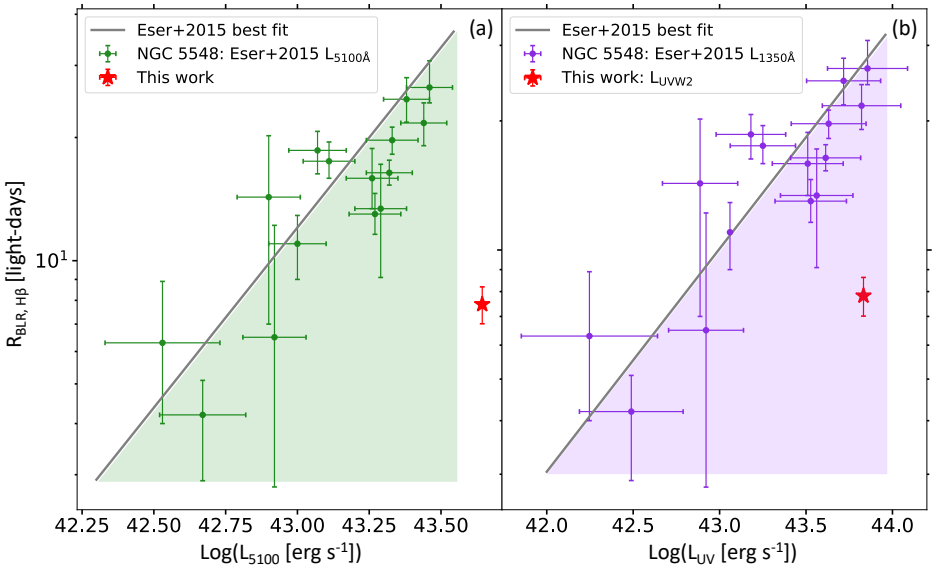

Figure 2.11: Multi-epoch NGC 5548 radius-luminosity (*R*–*L*) scaling relations for Hβ in the optical and UV including luminosities from Eser et al. (2015) and results from this work (red star). Panel *a*: NGC 5548 $R_{\mathrm{H}\beta}$–L_{5100} relation (green circles) on which Mrk 142 from this work is located to the right at higher luminosities. This follows the similar deviation from the entire RM sample that is observed in Figure 2.10, panel *a*. Panel *b*: $R_{\mathrm{H}\beta}$–L_{UV} relation with 1350 Å luminosity values for NGC 5548 and *UVW2* luminosity (effective wavelength of 1928 Å) for Mrk 142 from this work. From its position to the far right of the Eser et al. (2015) best-fit *R*–*L* relation (grey solid line) with L_{5100} in panel *a*, Mrk 142 has moved closer to the Eser et al. (2015) best-fit *R*–*L* relation in the UV in panel *b*, suggesting the UV as a better proxy for the driving continuum than the optical. In general, the offset of the SEAMBHs may reflect different spectral energy distribution.

2.7 Summary

We performed BLR RM analysis of Mrk 142 with medium- and low-resolution optical spectra from Gemini and LJT, simultaneous to the *Swift* and LCO photometric campaigns reported by Cackett et al. (2020) to measure the UV lag for Hβ emission line. With `PrepSpec` analysis, we corrected calibration discrepancies for both the Gemini and the LJT spectra individually. From spectral modelling in `Sherpa`, we measured FWHM and fluxes for [O III] $\lambda\lambda$4960, 5008; Hβ λ4861; and He I λ5877 emission lines. To combine the 5100 Å and Hβ light curves from Gemini and LJT, we inter-calibrated the respective light curves from the two telescopes in `PyROA`. Applying `PyROA` for time-lag analysis, we measured a UV time lag for Hβ and further derived refined black hole masses. Placing our results on various *R*–*L* scaling relations, we verified that our results are consistent with previously published values for Mrk 142. We summarize our main findings below.

1. `PyROA`, using Bayesian Information Criterion to evaluate model performance along with a rigorous treatment of uncertainties, provided a robust method for measuring cross-correlation time lags. This project is one of the early works employing `PyROA` technique for measuring RM time lags with real data. In this process, the longer timescale of LJT spectra nicely complemented the gaps in the Gemini observations.

2. We measured, for the first time, a UV time lag of $8.58^{+0.76}_{-0.75}$ days for Hβ in Mrk 142, with simultaneous photometry in the *Swift*/*UVW2* band and optical spectroscopy with Gemini and LJT. Assuming the UV continuum as the primary driver of the observed variability, we derived a black hole mass of $\log(M_\bullet/M_\odot) = 6.67 \pm 0.04$.

3. We obtained a 5100 Å to Hβ time lag of 7.82 ± 0.81 days, consistent with the measured value from previous SEAMBH campaigns (Du et al. 2015). From this lag measurement, we also derived a black hole mass for Mrk 142 of $\log(M_\bullet/M_\odot) = 6.63 \pm 0.05$, again in agreement to the mass reported by Du et al. (2015).

4. We placed the 5100 Å to Hβ time lag with measured $L_{\rm UVW2}$ on the $R_{\rm H\beta}$–L_{1350} relation for NGC 5548 (Eser et al. 2015). Mrk 142 falls closer to the $R_{\rm H\beta}$–L_{1350} scaling relation than the $R_{\rm H\beta}$–L_{5100} relation indicating that the *UVW2* band is closer to the "true" driving continuum as opposed to 5100 Å band.

In addition, we also recorded supplementary results. Our spectral analysis indicated blueshifted, broad components for the He I and He II emission lines suggestive of wind components in these higher-ionization lines. Such disk+wind components have been previously observed for high-ionization lines from emission-line simulations of NLS1s (Leighly 2004). We intend to study these lines in further detail in our future work. Furthermore, BLR RM analysis with the concurrent X-ray data available from *Swift* can better inform our understanding of the measured Hβ time lags with respect to the UV continuum. We aim to explore this in our future study.

Chapter 3

Revisiting Emission-Line Measurement Methods for Narrow-Line Active Galactic Nuclei

This work will be submitted as an article to the Publications of the Astronomical Society of the Pacific.

3.1 Introduction

Observing gaps in multi-epoch astronomical data are commonplace. Sparsely sampled ground-based observations are mainly a result of weather conditions and pressure from other programs (for queue observatories). Data gaps can impact the programs requiring frequent visits to the sky, e.g., time-series observations. One way to work around data gaps is by performing simultaneous observations with different telescopes. However, using data from various observatories together in a meaningful way can be challenging because of the need for sufficient cross-calibration.

Combining spectroscopic observations from different facilities needs a careful consideration of various factors (e.g., exposure time, seeing, spectral resolution, etc.) affecting the data. When employing multiple telescopes to observe the same spectral region for a given data set, the instrument specifications used with different facilities may not be identical. As an example, if the data from two telescopes were taken with different slit widths, their spectral resolutions may not match. The wider the slit, the lower the spectral resolution (depending on the grating used). Instrumental broadening in lower-resolution spectra causes line features to appear broader than the true value or sometimes blended with neighbouring lines. This broadening effect can result in inaccurate measurements of the physical parameters, e.g., full width at half maximum (FWHM) and flux (F) of an emission line. However, the severity of the effect may be different for different studies. For objects showing narrow-line profiles considerably narrower than the typical AGN population, e.g., Narrow-Line Seyfert 1 galaxies (NLS1s) accreting at super-Eddington rates, accounting for instrumental broadening effects while performing line measurements becomes more critical.

Historically, reverberation-mapping (RM; Blandford & McKee 1982; Peterson 1993) stud-

ies have focused mainly on low-redshift AGN ($z < 0.3$) that typically follow sub-Eddington accretion (e.g., Stirpe et al. 1994; Santos-Lleó et al. 1997; Collier et al. 1998; Dietrich et al. 1998; Kaspi et al. 2000; Bentz et al. 2006) as against the more atypical super-Eddington objects (accreting well above the Eddington limit). RM is a power technique that takes advantage of the variability in AGN over several timescales (from several days to weeks and years; e.g, Peterson et al. 1982) – BLR response on larger scales to the continuum variations from the accretion disk, with a positive time lag – and provides a way to convert the time lag into a spatial distance, the size of the BLR. The BLR size along with the FWHM of an emission line is used to obtain black hole masses in AGN. Applying the RM technique successfully to measure AGN black hole masses thus requires accurate measurements of the emission-line widths. A majority of the low-redshift AGN exhibit broad emission lines (e.g., Hβ, Hα, C IV, etc.) with FWHM $\geq$ 2000 km s^{-1} in their spectra. Recent efforts by the Super-Eddington Accreting Massive Black Holes (SEAMBH) collaboration (Du et al. 2014; Wang et al. 2014b; Hu et al. 2015; Du et al. 2015, 2016a,b, 2018) have successfully identified ~25 highly accreting AGN to date. SEAMBH objects show spectral features containing narrower Hβ broad lines (FWHM$_{\rm H\beta} \lesssim$ 2000 km s^{-1}), weak [O III] and strong optical Fe II emission lines that appear as a bumpy pseudo-continuum, similar to other NLS1s (Osterbrock & Pogge 1987; Boroson & Green 1992; Boller et al. 1996; Véron-Cetty et al. 2001). As we branch out to studying different categories of AGN, and given the importance of accurate line measurements for RM analysis, we must carefully reconsider: (1) *How does spectral resolution influence the shapes of emission lines in our data?*; and (2) *Are the current methods of measuring emission-line properties sufficient or are they limited in any way to achieving our desired science goals?*

The aim of this chapter is to address the above two questions with the optical spectra of the super-Eddington AGN, Markarian 142 (Mrk 142), taken with the Gemini North Telescope (Gemini) and the Lijiang Telescope (LJT). As a part of the broader RM campaign (P.I.: E. Cackett), we performed overlapping photometric and spectroscopic observations of Mrk 142 with telescope facilities worldwide. The goal of the campaign is to study the structure of the accretion disk and the BLR simultaneously, for the first time, in a super-Eddington AGN. Because the spectral observations of Mrk 142 with Gemini suffered with gaps due to unfavourable weather, we complemented those data with simultaneous observations from LJT. With the Gemini+LJT data, we measured, for the first time, an ultraviolet (UV) continuum to Hβ lag for the object (see Chapter 2). The Gemini and LJT spectra were taken with the same grating but different slit widths – 0.75″ for Gemini and 2.5″ for LJT; therefore, their spectral resolutions differed – ~270 km s^{-1} for Gemini and ~500 km s^{-1} (Hu et al. 2015) for LJT . Here, the challenge was to accurately measure the emission lines for spectra at considerably different spectral resolutions for a narrow-line object. In this chapter, we discuss how to address this challenge with our spectral-fitting procedure. Further, we provide recommendations of the best strategies for performing accurate emission-line measurements in narrow-line AGN.

This chapter is organized as follows. Section 3.2 details the process of preparing the data for correlation analysis and the correlations between the Gemini and LJT spectral measurements. Section 3.3 outlines the results. We further discuss the results in Section 3.4 along with our recommendations. Finally, Section 3.5 summarizes our findings.

3.2 Methodology

We pre-processed the Gemini and LJT calibrated spectra independently through `PrepSpec`[1] (developer: K. Horne) to correct for any relative deviations from their calibrations. We then modelled the continuum and emission lines in the spectra in `Sherpa`[2] (Freeman et al. 2001) v4.10.0 with a `Python` wrapper script to examine the correlations between the Gemini and LJT spectral measurements.

3.2.1 `PrepSpec` Pre-processing

`PrepSpec` corrects for differences in relative wavelength and flux calibrations of the spectra by modelling their continuum, emission lines, and absorption lines. However, `PrepSpec` requires that spectra have no gaps and extremely large flux values. To prepare the Gemini spectra for `PrepSpec`, we applied the following corrections: (1) replaced detector gaps, and residual features from cosmic-ray correction and sky subtraction with interpolated and simulated data; (2) recovered the flat spectral regions with zero flux values (resulting from the position angle of the slit non-parallel to the parallactic angle) and bumpy regions (resulting from the calibration process) by using a high signal-to-noise (S/N) mean spectrum as the reference spectrum; and (3) recovered slit losses (resulting from the 0.75″ narrow slit used for observations) using 5.00″ wide-slit spectra taken on the same nights (see Chapter 2, Section 2.3.1 for a detailed description of the corrections). We developed multiple scripts in `Python` v3.6.5 to perform the above corrections. All `Python` scripts will be made publicly available on `GitHub` (Khatu et al., in prep.). Appendix B includes a brief summary of the `GitHub` repository. The LJT spectra had no gaps and hence were directly processed through `PrepSpec` after calibration. Appendix C provides the user manual for `PrepSpec` including a detailed tutorial on the application of `PrepSpec` to the Mrk 142 Gemini data set.

3.2.2 Gemini/LJT Correlation Analysis

We investigated correlations between the Mrk 142 Gemini and LJT emission-line measurements to study the effect of low spectral resolution on the measured FWHM values. To fit the Hβ λ4861 and He I λ5877 regions of interest, we initially followed a standard approach. We set the FWHM, flux, and position of the [O III] λ5008 line to vary during the fit, and fixed the FWHMs and positions of the narrow components in Hβ and He I relative to the [O III] λ5008 line. We kept the Hβ and He I narrow-line fluxes as free parameters. Further, we used two Gaussians to model the broad Hβ and He I emission lines. We fixed the FWHM of the broader broad Hβ component and allowed the width of the narrower broad component to be a free parameter. For the He I line, we fixed the FWHMs of both its broad components with respect to the FWHM of the flexible, narrower broad Hβ component. We applied the Boroson & Green (1992) template to fit the Fe II pseudo-continuum and the Bruzual & Charlot (2003) host

[1] See Appendix C for documentation of `PrepSpec` and the current version of the software.

[2] `Sherpa` is a software application for modelling and fitting astronomical images and spectra. In this work, the `Sherpa` v4.10.0 application was used within Coronagraphic Imager with Adaptive Optics (`CIAO`) v4.10.0, the X-ray Data Analysis Software designed by the Chandra X-ray Center. For full documentation of `CIAO-Sherpa`, see `https://cxc.harvard.edu/sherpa4.14/`.

galaxy template with 11 Gyr[3] at $z = 0.05$ to correct for the effect of host-galaxy emission. This approach worked well for the Gemini spectra. However, the LJT Hβ FWHM measurements were broader than expected, indicating that the fitting approach failed for the LJT spectra. Figures 3.1 and 3.2 show model fits to a single-epoch spectrum from Gemini and LJT, respectively.

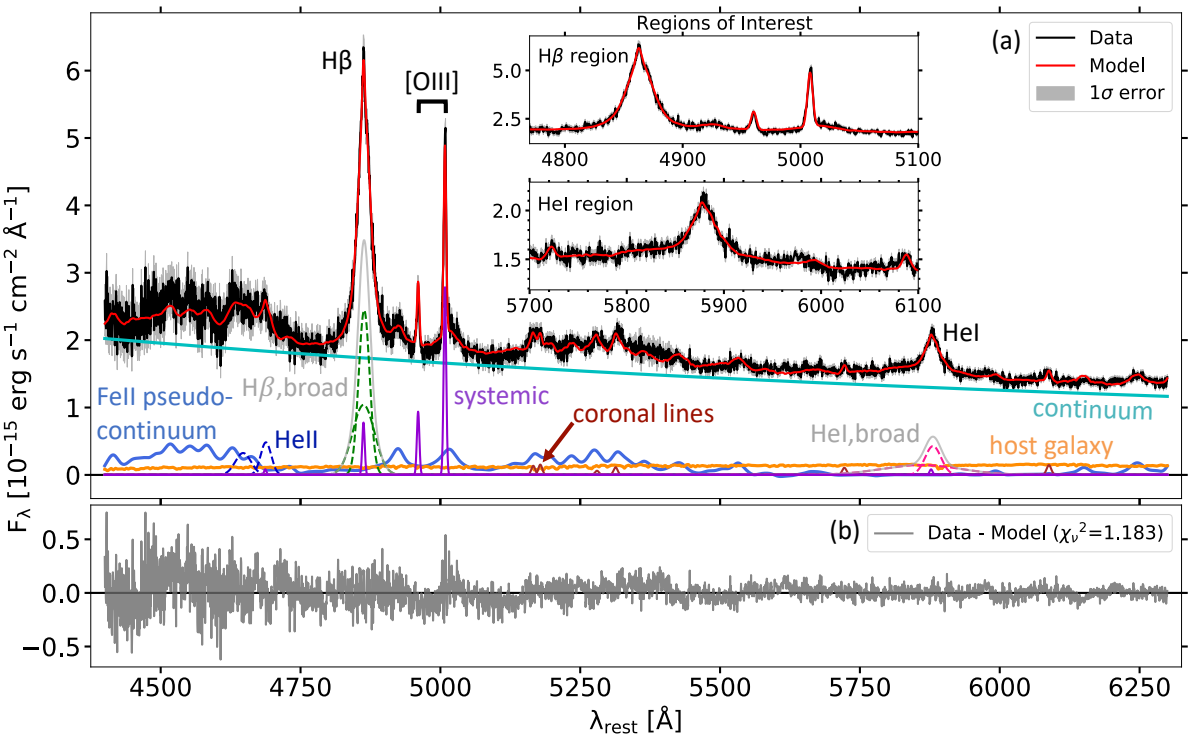

Figure 3.1: Composite model fit to epoch 24 of the Mrk 142 Gemini data displaying individual components of the model. Panel *a*: Composite model (red solid curve) fit to the data (black solid curve) from 4430 Å to 6300 Å is shown in the main panel, and the Hβ and He I *Regions of Interest* are shown in the *Inset* panels. The individual components of the model are displayed at the bottom of the panel: continuum (cyan solid curve); Fe II I Zw 1 template as a pseudo-continuum (faint blue solid curve); host-galaxy template (orange solid curve); He II broad components (blue dashed Gaussians); Hβ broad components (green dashed Gaussians); He I broad components (pink dashed Gaussians); narrow-line components of Hβ, He I, and [O III] (purple solid Gaussians); and high-ionization coronal lines (brown solid Gaussians). The total broad Hβ and He I profiles are also overplotted (grey solid curves). Panel *b*: Residuals of the model with reduced $\chi^2, \chi_\nu{}^2 = 1.183$. The model shows larger residuals around the [O III] λ5008 line indicating a sub-optimal fit in that region. The noisier blue end of the spectrum affects the overall fit in that region, thus resulting in larger residuals compared to the red end of the spectrum.

[3] 1 Gyr = 10^9 years

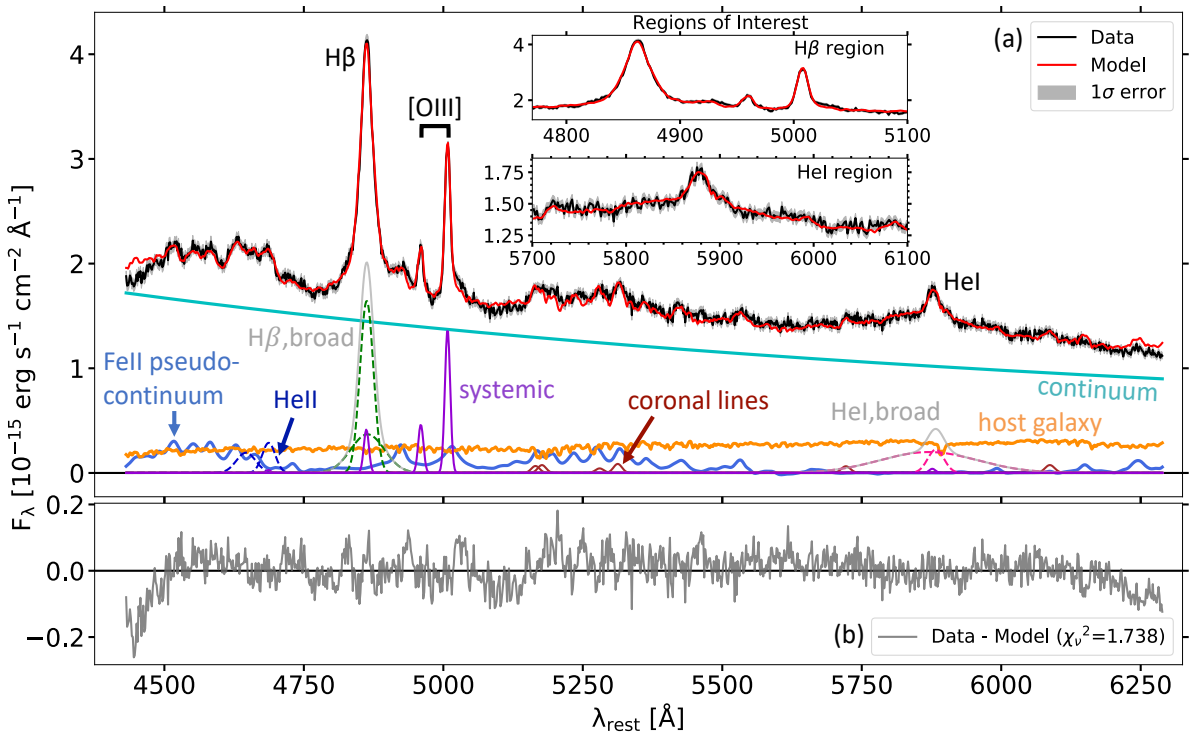

Figure 3.2: Composite model fit to epoch 24 of the Mrk 142 LJT data displaying individual components of the model. See caption of Figure 3.1 for a description of the individual model components in Panel *a*. The red side of the broad Hβ emission line shows contamination with the Fe II emission at ~4923 Å. Similarly, the [O III] λ5008 line shows considerable blending with the Fe II feature in its red wing, thus affecting a reliable measurement of the [O III] λ5008 line. Panel *b* shows the residuals of the model with $\chi_\nu^2 = 1.711$. The smaller residuals indicate an overall good fit to the spectrum. The model performance drops significantly at both the end of the spectrum although it does not impact measurements in the *Regions of Interest*.

Due to low resolution of the LJT spectrum, emission-line features appear smeared as compared to the Gemini spectrum. In Hβ, the sharper peak of the narrow component evident in the Gemini spectrum is not clearly distinguishable in the LJT spectrum. The Fe II emission-line component on the red side of Hβ also appears to contaminate the broader Hβ component. Similarly, the red wing of the [O III] λ5008 line appears to be blended with the Fe II emission on its red side. The possible contamination with Fe II emission due to lower spectral resolution of the LJT spectra results in a broad FWHM for the [O III] λ5008 line. Further, at the instrumental resolution of the LJT spectrograph, the [O III] lines with FWHM $\sim$ 320 km s^{-1} (as measured from the higher-resolution Gemini spectra) are unresolved. The unresolved [O III] lines in the LJT spectra further complicate the measurements of their widths.

The Problem – Posed: Why do the broad* Hβ *FWHMs from the Gemini and LJT spectra not match?

We found that the FWHM values of the broad Hβ and the [O III] λ5008 lines in the Gemini and LJT spectra did not agree with each other. Figure 3.3 displays the differences in the measured FWHMs of the two lines. Considering the difference in the resolutions of the Gemini ($\sim$270 km s^{-1}) and LJT ($\sim$500 km s^{-1}) spectra, we expect the FWHM values from LJT to have $\sim$420 km s^{-1} broader effective width (here, defined as the width of the Gaussian kernel required to smooth the higher-resolution Gemini spectrum to the lower-resolution LJT spectrum, and given by $\sqrt{500^2 - 270^2}$ for Gaussian profiles) than the Gemini FWHM values. However, the unresolved [O III] line (Figure 3.3, panel *a*) has $\sim$680 km s^{-1} broader effective widths than the [O III] FWHMs measured for the Gemini spectra. The LJT Hβ broad line shows a much greater effect, $\sim$1450 km s^{-1} broader effective widths than those measured from the Gemini spectra. The broad He I FWHM measurements were affected in the same way as Hβ. This implies that there are multiple factors influencing the FWHM measurements in the LJT spectra, likely resulting from instrumental broadening.

To identify the possible reason(s) for the observed discrepancies in the FWHM measurements, we considered the narrow-line fluxes in the Hβ and [O III] λ5008 lines that we allowed to vary during spectral fitting. Figure 3.4 displays the correlation between the measured fluxes for the two lines. For the LJT spectra, the fluxes in the narrow Hβ line (red open squares) are correlated to the [O III] $\lambda\lambda$4960, 5008 line fluxes ($r_{\rm Spearman} \sim 0.5$) with a large scatter in the measured values from both lines. However, the fluxes for narrow lines, originating in the narrow-line region of AGN, are not expected to vary relative to the continuum variations over the timescale of a reverberation-mapping campaign. The constancy of the narrow-line fluxes is attributed to the narrow-line region being farther away from the central source (supermassive black hole + accretion disk) than the broad-line region, which receives the continuum variations. The correlation observed between the LJT narrow Hβ and [O III] λ5008 line fluxes is absent in the Gemini flux values (blue open circles; $r_{\rm Spearman} \sim 0.1$), which are also more constrained than the LJT measurements.

The Culprit – Pronounced: A "broader"* [O III] λ5008 *FWHM leads to a broader broad* Hβ *FWHM in the LJT spectra.

Integrating the observations from Figures 3.3 and 3.4, we concluded that the "broader" (than expected) [O III] λ5008 line in the LJT spectra causes the correlation and scatter observed in the Hβ narrow-line fluxes, consequently leading to the "broader" broad Hβ FWHMs in the LJT spectra as compared to the narrower broad Hβ in the Gemini spectra. The lower spectral resolution of the LJT spectra smears the narrow-line profile of the [O III] λ5008 line causing it to appear broader than usual (see Figure 3.2). This effect is amplified in the case of Mrk 142 as it is a NLS1 with narrower and weaker [O III] lines compared to the more typical broad-line objects (with narrow-line widths of several hundred km s^{-1}). Also, the likely contamination from the Fe II emission at the red wing of [O III] λ5008 (see Figure 3.2) further complicates the picture. The net result is a "broader" FWHM measured for the [O III] line. We interpret this result to mean the following:
Because the width of the narrow Hβ *component is set equal to width of the* [O III] *line, a*

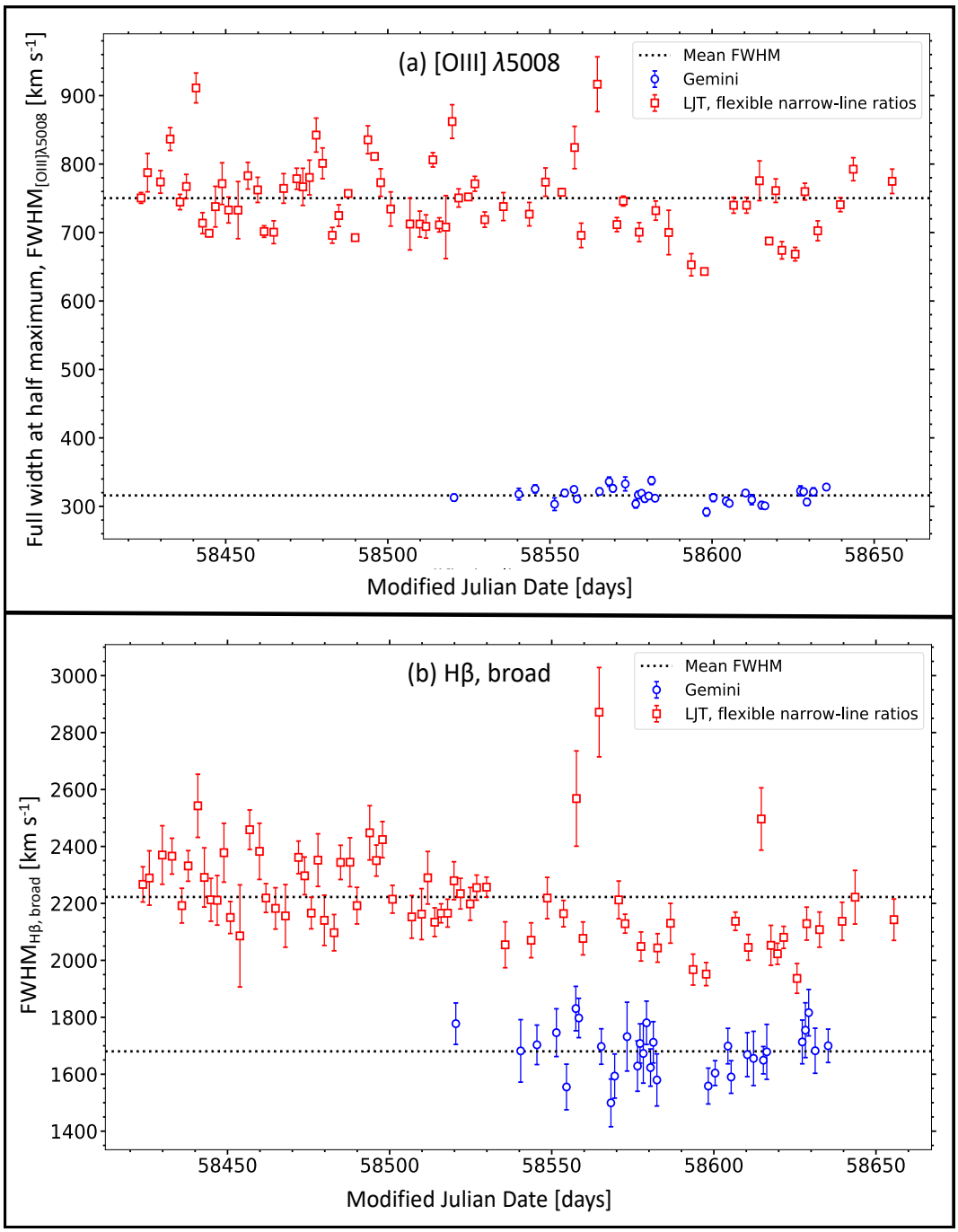

Figure 3.3: Differences in the full width at half maximum (FWHM) values measured from the Gemini (blue open circles) and LJT (red open circles) spectra for [O III] λ5008 (panel *a*) and broad Hβ (panel *b*), indicating that the LJT measurements have a broader effective width (see text for the definition) than the expected value of ~420 km s^{-1}. The fitting procedure for both the Gemini and the LJT spectra incorporated flexible narrow-line ratio of Hβ to [O III] λ5008.

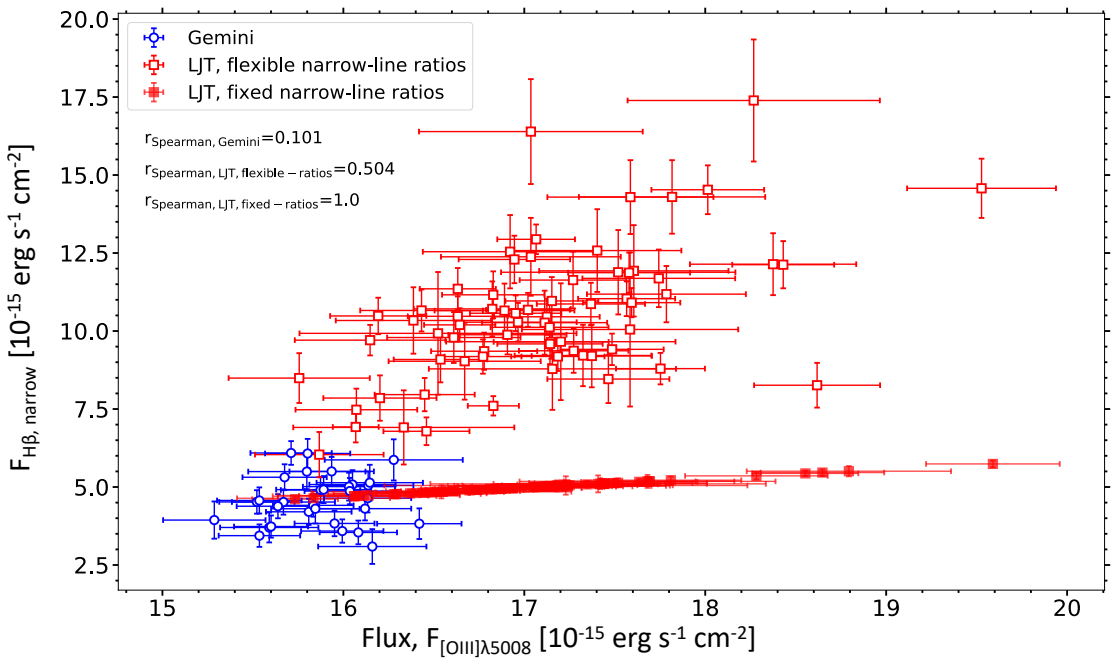

Figure 3.4: Correlations between the narrow Hβ line flux and the [O III] λ5008 line flux from the Gemini (blue circles) and LJT (red squares) spectra. Open symbols represent measurements with flexible narrow-line flux ratios of $F_{\mathrm{H}\beta}/F_{[\mathrm{O\ III}]\ \lambda5008}$ and $F_{\mathrm{He\ I}}/F_{[\mathrm{O\ III}]\ \lambda5008}$, whereas filled symbols (for LJT only) represent measurements with fixed narrow-line flux ratios. For fitting the LJT spectra, we fixed the above narrow-line flux ratios determined from the Gemini spectra fitting process (0.293 for Hβ to [O III] λ5008 and 0.034 for He I to [O III] λ5008) as the resolved [O III] λ5008 line in the Gemini spectra provided reliable measurements of the narrow-line flux ratios. The weak positive correlation for the LJT measurements with flexible narrow-line ratios indicates that the "broader" [O III] λ5008 line results in an excess narrow-line flux for the narrow Hβ component.

"broader" [O III] *leads to a "broader" narrow* Hβ *in the LJT spectra. The "broader" narrow* Hβ *collects more flux leaving less flux for the broad* Hβ *components, which are kept flexible in the model. The more the flux in the narrow* Hβ *line, the lower the peak flux of the broad* Hβ *(after subtracting the narrow component), resulting into a "broader" broad* Hβ *FWHM.*

The Solution – Proposed: Tie the flux in narrow Hβ ***relative to the flux in*** [O III] λ5008**.**

To contain the effect of the "broader" [O III] λ5008 line on the broad Hβ FWHM measurements in the LJT spectra, we fixed the narrow-line fluxes as well as the widths of Hβ and He I relative to the [O III] flux from the Gemini spectral measurements. At the resolution of the Gemini spectra (~270 km s^{-1}), the [O III] λ5008 line is just resolved. Thus, the FWHM measurements for the [O III] line in the Gemini spectra are more reliable than the LJT values. We therefore applied the narrow-line flux ratios, $F_{\mathrm{H}\beta}/F_{[\mathrm{O\ III}]\ \lambda5008}$ = 0.293 and $F_{\mathrm{He\ I}}/F_{[\mathrm{O\ III}]\ \lambda5008}$ = 0.034, from the Gemini spectra to the Hβ and He I lines in the LJT spectra.

Tying the LJT narrow-line flux ratios confined the flux measured for the Hβ narrow component. Figure 3.4 displays the fixed Hβ narrow-line fluxes from the LJT spectra (red filled squares) as highly correlated ($r_{\rm Spearman}$ = 1.0) to the LJT [O III] λ5008 fluxes. The large scatter in the narrow Hβ line fluxes from flexible line ratios for the LJT spectra (red open squares) has considerably reduced after adopting fixed narrow-line ratios. This reduction in scatter signifies that the Hβ narrow-line fluxes in the LJT spectra are now well constrained.
The applied flux ratios along with fixed widths for the narrow lines helped constrain the narrow Hβ *flux. With a fixed width and constrained flux of the narrow* Hβ *component, the "excess" flux is directed back to the broad components. The more the broad* Hβ *flux, the higher the peak flux measured for the broad* Hβ*, resulting into a narrower broad* Hβ *FWHM.*

3.3 Results

We studied the effect of the LJT spectral resolution (~500 km s^{-1}) on the measured Hβ FWHMs by correlating the emission-line measurements in the Mrk 142 Gemini and LJT spectra. We identified that the "broader" FWHM measurements of the unresolved [O III] λ5008 line in the LJT spectra lead to an overestimation of the Hβ narrow-line fluxes by a factor of two, ultimately resulting in Hβ FWHM values with ~1450 km s^{-1} broader effective width than the Hβ FWHM values from the Gemini spectra. To correct for this effect, we adapted our spectra fitting procedure for the LJT spectra by fixing the narrow-line ratios of Hβ and He I with respect to the [O III] λ5008 line based on our spectral measurements for the Gemini spectra containing resolved [O III] lines. We present our results below.

Applying narrow-line flux ratios for fitting the lower-resolution LJT spectra significantly reduces the scatter in the narrow-line fluxes of the Hβ and He I broad lines. Figure 3.5 displays the fluxes of the narrow component in Hβ (panel *a*) and He I (panel *b*) before and after applying the flux ratios for the LJT spectra. Before fixing the narrow-line fluxes, the higher Hβ to [O III] λ5008 and He I to [O III] λ5008 flux ratios for the lower-resolution LJT spectra result from the "excess" flux gathered under the narrow Hβ and He I lines owing to the narrow Hβ and He I line widths set equal to the width of the "broader" [O III] λ5008 line. After fixing the narrow-line flux ratios, the Hβ and He I line measurements are more consistent, with values similar to the narrow-line fluxes from the Gemini data. The higher resolution of the Gemini spectra, providing resolved [O III] lines, allowed precise measurements of [O III] line widths and fluxes, thus resulting in the smaller scatter in the Hβ and He I narrow-line fluxes. In addition, we expect the narrow-line fluxes to be constant over the length of our campaign. However, the Hβ and He I narrow-line fluxes from the LJT spectra are unreliable when the narrow-line ratios are free parameters due to the large uncertainties and scatter in the measured values. The constant Hβ and He I narrow-line flux is clearly evident after fixing the narrow-line ratios for the LJT spectra.

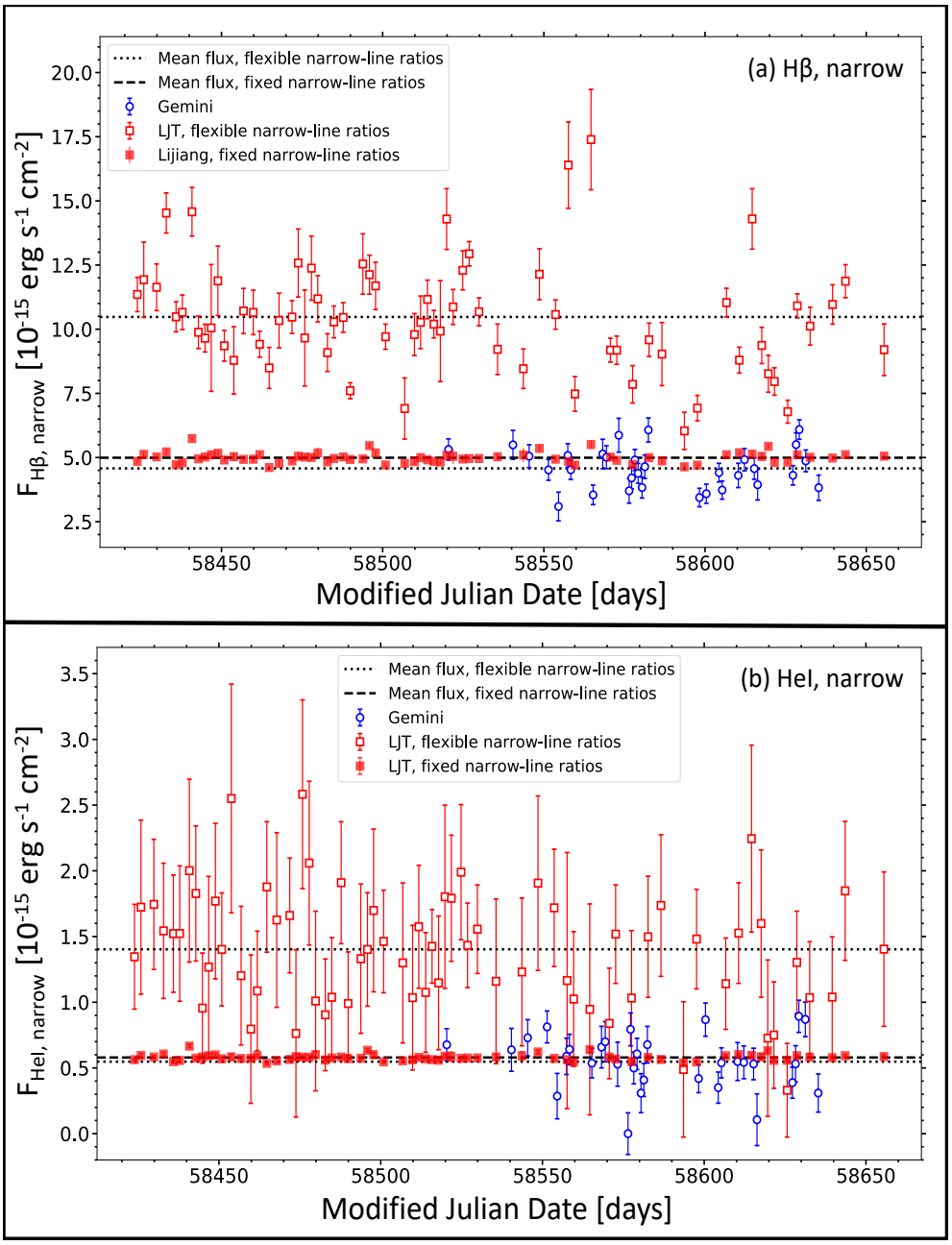

Figure 3.5: Narrow Hβ (panel *a*) and He I (panel *b*) light curves measured from the Gemini (blue circles) and LJT (red squares) spectra fit with flexible (open symbols) and fixed (filled symbols) narrow-line flux ratios. Fixing the Hβ and He I narrow-line flux ratios of 0.293 and 0.034, respectively, relative to the [O III] λ5008 line flux considerably reduced the scatter in the LJT measurements as well as resulted in lower uncertainties. With fixed narrow-line flux ratios, the new fluxes for the narrow Hβ and He I lines from the LJT spectra are closer to the Gemini measurements.

We found that the constrained Hβ narrow-line fluxes in the LJT spectra yield narrower FWHMs for the Hβ broad component, and Figure 3.6 displays this result. Flexible narrow-

line flux ratios in the LJT spectra result in a large scatter in the broad Hβ FWHMs (red open squares) with a mean value of $\sim$2220 km s^{-1}. After fixing the narrow-line flux ratios, the constrained narrow-line flux in Hβ re-allocates the "excess" flux to the broad components. As a result of the higher broad-line peak flux, the half-maximum point increases, thus measuring a narrower Hβ broad-line profile. Figure 3.7 explicitly shows the dependence of the measured Hβ FWHM on the peak flux of the line. With flexible narrow-line ratios for the lower-resolution LJT spectra, the measured broad Hβ FWHMs are strongly negatively correlated ($r_{\rm Spearman}$ = -0.789) with the peak fluxes of the line. This correlation is weaker ($r_{\rm Spearman}$ = -0.449) with the fixed narrow-line flux ratios for the LJT spectra and also similar to the correlation observed for the Gemini spectra ($r_{\rm Spearman}$ = -0.487). The remaining dependence of the broad Hβ FWHM on its peak flux can be attributed to the contamination in the Hβ line from the nearby Fe II emission (also discussed below). The new measurements of the broad Hβ FWHM, obtained after fixing the narrow-line flux ratios for the LJT spectra, have a mean of $\sim$1930 km s^{-1}, $\sim$54% closer to the Gemini Hβ mean FWHM. The new broad Hβ FWHM values also show a scatter of $\sim$340 km s^{-1}, similar to the scatter in the Gemini Hβ FWHM values (see Figure 3.6).

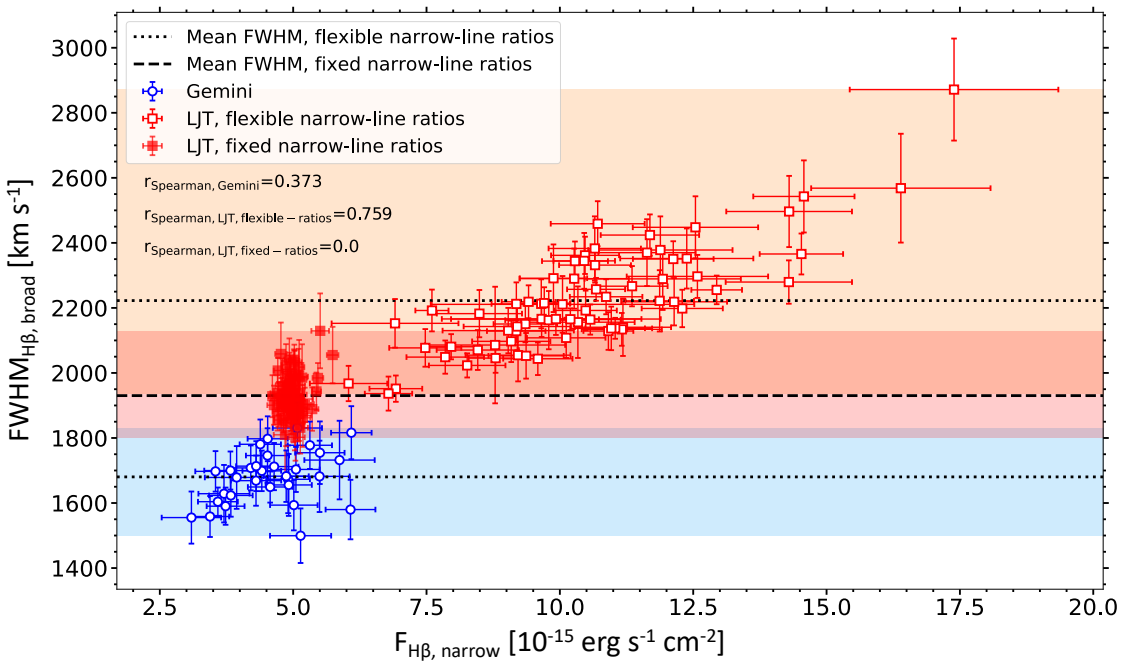

Figure 3.6: Correlations between the broad Hβ full width at half maximum (FWHM) and the narrow Hβ flux from the Gemini (blue circles) and LJT (red squares) spectra fit with flexible (open symbols) and fixed (filled symbols) narrow-line flux ratios. The scatter in the LJT Hβ FWHM measurements with flexible narrow-line ratios (orange shaded region) is considerably reduced (red shaded region) after fixing the narrow-line ratios. Fixed ratios nullified the strong correlation that is evident in the LJT measurements with flexible ratios.

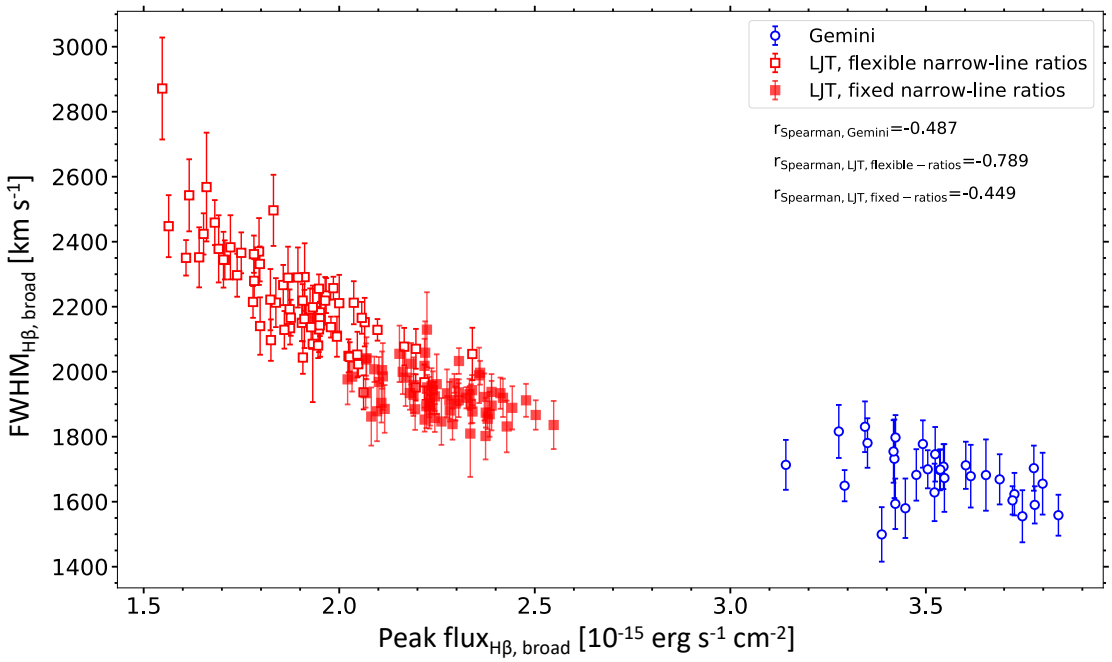

Figure 3.7: Dependence of the full width at half maximum (FWHM) on the peak flux for the broad Hβ line from the Gemini (blue circles) and LJT (red squares) spectra fit with flexible (open symbols) and fixed (filled symbols) narrow-line flux ratios. The strong negative correlation in the LJT measurements with flexible narrow-line flux ratios is considerably reduced after fixing the narrow-line flux ratios. The remaining weaker correlation and the offset between the LJT and Gemini measurements can be attributed to the contamination from the Fe II emission in the broad Hβ line.

We also examined the correlation between the strength of Fe II ($R_{\rm Fe\ II}$, defined as the ratio of equivalent width of Fe II in the 4434–4684 Å region to that of broad Hβ) and the FWHM of broad Hβ, shown in Figure 3.8. The $R_{\rm Fe\ II}$–FWHM$_{\rm H\beta,broad}$ correlation reiterates the issue of the broader Hβ FWHM measurements in a different context. The LJT Hβ FWHM values with flexible narrow-line ratios (red open squares) are weakly correlated to $R_{\rm Fe\ II}$. This correlation vanishes after fixing the narrow-line flux ratio of Hβ to [O III] λ5008. The new broad Hβ measurements (red filled squares) are closer to the values measured from the Gemini spectra; however, an offset is still present. At the low spectral resolution of the LJT spectra, the Fe II emission around the Hβ line likely contaminates the Hβ broad-line emission (see Figure 3.2). The remainder offset noted above can likely be a result of the potential Fe II contamination with the broad Hβ line in the LJT spectra. Therefore, understanding any interplay between the two lines is crucial. In addition, we note that the $R_{\rm Fe\ II}$ measurements from the LJT spectra are smaller as compared to those from the Gemini spectra, likely due to the lower resolution of the LJT data.

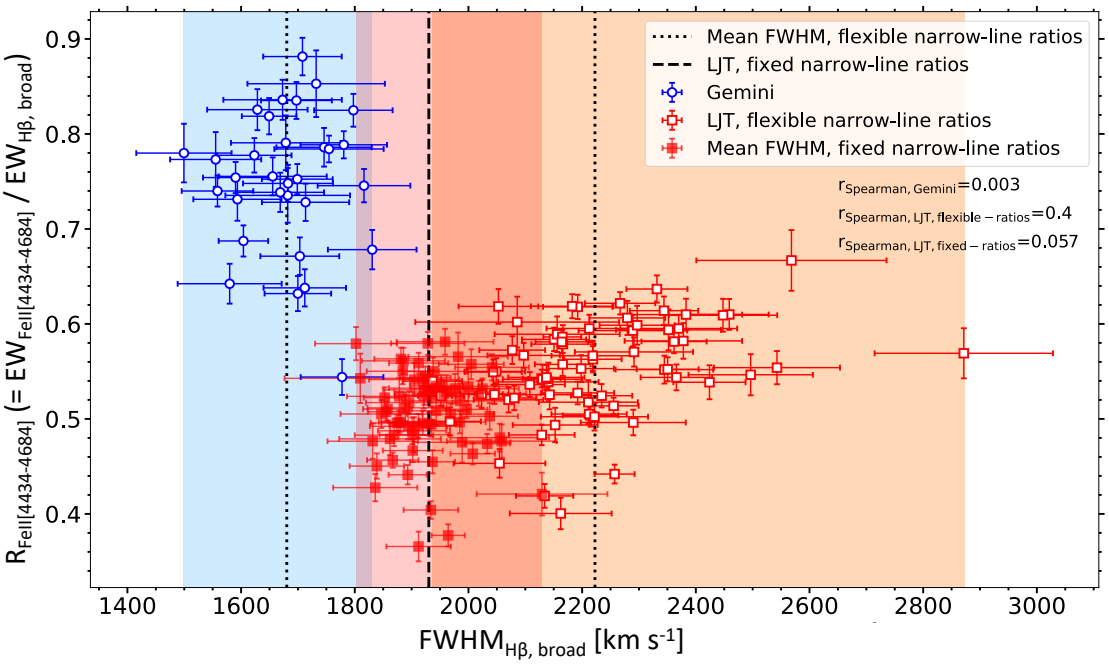

Figure 3.8: Correlations between the strength of Fe II (ratio of equivalent width of Fe II in the [4434–4684 Å] region to that of broad Hβ) and the full width at half maximum (FWHM) of the broad Hβ from the Gemini (blue circles) and LJT (red squares) spectra fit with flexible (open symbols) and fixed (filled symbols) narrow-line flux ratios. Fixing the narrow-line flux ratios moved the mean Hβ FWHM from the LJT data closer to the mean of the Gemini Hβ FWHM measurements. There is an unexplained offset between the Gemini and the new LJT measurements likely due to the Fe II emission contaminating the broad Hβ line in the LJT spectra.

3.4 Discussion

We correlated emission-line measurements from Mrk 142 spectra taken with Gemini and LJT at different resolutions (~270 km s^{-1} for the former and ~500 km s^{-1} for the latter) to study the discrepancies observed in the measured FWHM values of broad Hβ. Given the NLS1 nature of Mrk 142, its broad Hβ profile is narrower as compared to the more typical broad-line Seyfert 1s, and therefore challenging to accurately measure in lower-resolution spectra. Accurate measurements of the narrow-line fluxes are critical to measure broad emission-line widths, which in turn are used to derive the black hole masses in AGN.

Our adopted method of measuring the broad Hβ FWHM decreased the FWHM values measured from the LJT spectra significantly, thus bringing them closer to the Gemini measurements as well as reducing the scatter in the measured values. The smaller scatter in the Hβ FWHMs from the LJT spectra was an improvement by a factor of ~2.6 as compared to the measurements with flexible narrow-line ratios. Although we significantly improved our measurements from the LJT spectra, the new Hβ FWHM values do not exactly match with those from the Gemini spectra. There is an offset of ~250 km s^{-1} between the mean FWHM values from the two data

sets that is perhaps a consequence of the Fe II emission contaminating the broad, red wing of Hβ. At lower resolution, the strong Fe II lines in the LJT spectra are smeared as compared to the sharper features in the Gemini spectra (see Figures 3.1 and 3.2), resulting in weaker Fe II measured from the LJT spectra (see Figure 3.8). Therefore, there likely exists cross-talk between the two broad lines affecting the measurements of both the Fe II emission and the broad Hβ wings.

We also caution that our method does not affect the [O III] line measurements from the LJT spectra although it restores the broad-line flux measured for the Hβ line. Figure 3.9 makes this explicit. The [O III] fluxes measured from the LJT spectra are approximately the same (red filled squares) before fixing the narrow-line flux ratios (see in Figure 3.9, panel *a*). The [O III] fluxes remain unchanged because the [O III] λ5008 flux was freed during spectral fitting. In contrast, an increase in flux is clearly seen in the broad Hβ light curve (red filled squares in Figure 3.9, panel *b*). Fixing the narrow-line flux ratios resulted in an increase of $\lesssim$10% in the Hβ broad-line flux in the LJT spectra – a difference that is greater than or similar to the Hβ flux uncertainties in a majority of the LJT epochs.

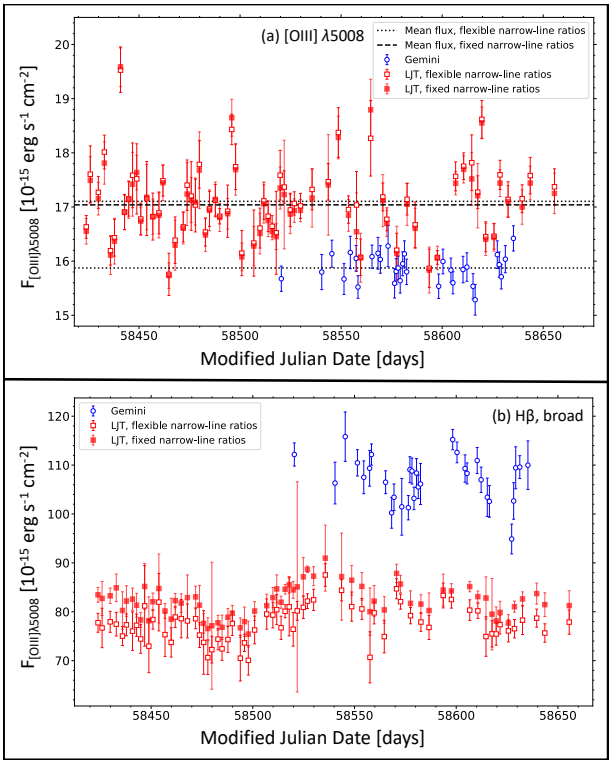

Figure 3.9: [O III] λ5008 (panel *a*) and broad Hβ (panel *b*) light curves from the Gemini (blue circles) and LJT (red squares) spectra fit with flexible (open symbols) and fixed (filled symbols) narrow-line flux ratios. Because the [O III] λ5008 line flux is kept flexible even while fitting with fixed narrow-line flux ratios, the measured fluxes before and after fixing narrow-line ratios are similar for the [O III] line. However, there is $\sim$10% increase in the the broad Hβ flux from the LJT spectra fit with fixed narrow-line ratios.

3.4.1 Comparison to Previous Studies

We compared our methodology to the techniques used in previous studies. In a previous SEAMBH monitoring campaign with LJT, Mrk 142 spectra were taken with the same instrument settings as used for the data set in this work (Du et al. 2014; Hu et al. 2015). Hu et al. (2015) describe the spectra fitting technique adopted for measuring Hβ FWHM from the previous campaign. They followed a two-step process: (1) Assuming no narrow-line contribution in the Hβ emission and given that the narrow lines do not vary at the short variability timescales of the broad-line gas, they modelled the Hβ profile with a Gauss-Hermite function. (2) They modelled the Hβ narrow line with a Gaussian whose width was set equal to that of the [O III] λ5008 line and its position fixed relative to the [O III] line. They ran their fits in two cycles – first, assuming 10% of the [O III] λ5008 flux for the narrow Hβ component, and the value of the broad Hβ FWHM was used from this run; and second, assuming 20% narrow-line flux, and the uncertainty on the FWHM measurement was used from this run in addition to the uncertainty from the Gauss-Hermite fit for the line. While the calibration of the uncertainties on the measured Hβ FWHMs from the two-cycle fits and Gauss-Hermite fits appears sufficient, the flux ratio of the Hβ to [O III] narrow lines is somewhat arbitrarily defined. As the narrow-line flux ratios can be different for different objects, using arbitrary ratios or even the same ratios for different objects can result in a systematic overestimation or underestimation of the broad Hβ FWHM values. With the opportunity of using Mrk 142 spectra at two different resolutions, we applied the more reliable narrow-line flux ratios determined from the higher-resolution and high S/N Gemini spectra to the lower-resolution LJT spectra for the Hβ FWHM measurements from the latter.

Past studies discuss the use of different line-width measures for reliable black hole mass estimates. Peterson et al. (2004) conducted a time-series analysis of 35 AGN to test the effectiveness of different line width measures for calculating black hole masses. They conclude that the line dispersion ($\sigma_{\rm line}$; or the root-mean-square [RMS] width calculated from the second moment of a line profile) is a more robust measure of the variable line profile than FWHM, especially in objects with strong narrow lines. However, Bian et al. (2008) argue that $\sigma_{\rm line}$ strongly depends on the contribution from the wings of broad lines. They analyzed 329 NLS1s from the Sloan Digital Sky Survey catalog to determine their black hole masses using $\sigma_{\rm line}$. They infer that in the cases where the Hβ broad profile is defined by two broad components (as for Mrk 142 spectra in this work), the black hole mass measurements using $\sigma_{\rm line}$ are about 0.5 dex larger than those obtained from FWHM measurements.

In another study, Collin et al. (2006) characterized the broad Hβ emission-line profiles of all reverberation-mapped AGN to then based on the ratio of FWHM/$\sigma_{\rm line}$[4], separating the AGN with narrower broad Hβ profiles (FWHM/$\sigma_{\rm line}$ $<$ 2.35) from those with broader Hβ (FWHM/$\sigma_{\rm line}$ $>$ 2.35). In their analysis of the virial product ($VP = M_\bullet/f$, where f is scale factor) with FWHM and $\sigma_{\rm line}$ from both mean and RMS spectra, they showed: (1) although $\sigma_{\rm line}$ yields consistent results for scale factors from both the mean and the RMS spectra for objects with narrower as well as broader broad Hβ profiles, $\sigma_{\rm line}$ from the mean spectrum is on average ~20% broader in the mean than the RMS spectra; and (2) for the narrower broad Hβ population (including NLS1s), although the scale factors from FWHM are larger by a factor

[4]The nature of a broad-line profile determines the relationship between the FWHM and $\sigma_{\rm line}$, where FWHM/$\sigma_{\rm line}$ = 2.35 for a Gaussian profile.

of ∼3 from both mean and RMS spectra, FWHM is only ∼10% broader in the mean than the RMS spectra. It is worth noting from the above discussions that both the FWHM and the $\sigma_{\rm line}$ are typically measured to be broader in the mean than the RMS spectra.

3.4.2 Recommendations for Line-Width Measurements in Narrow-Line AGN

The discrepancies highlighted by previous studies emphasize that accurately measuring broad-line widths in narrow-line objects, e.g., NLS1s, is not straightforward. As demonstrated in this work, the flux leak from the broad-line to the narrow-line components can significantly affect the measured FWHM of the broad lines, e.g., Hβ, in NLS1s. The flux leak from Fe II around Hβ can also affect the Hβ FWHM measurements. A consistent watch on how the quality of the data and measurement methods influence each other is essential. Hβ, surrounded by Fe II emission in the optical and the [O III] $\lambda\lambda$4960, 5008 lines, is challenging to measure; however, it is accessible to most of the ground-based observatories over a considerably wide redshift range and therefore prominently used for RM studies. Based on our analysis in this work, we provide recommendations on measuring emission-line widths in narrow-line AGN. Figure 3.10 shows the decision-making tree for line-width measurements.

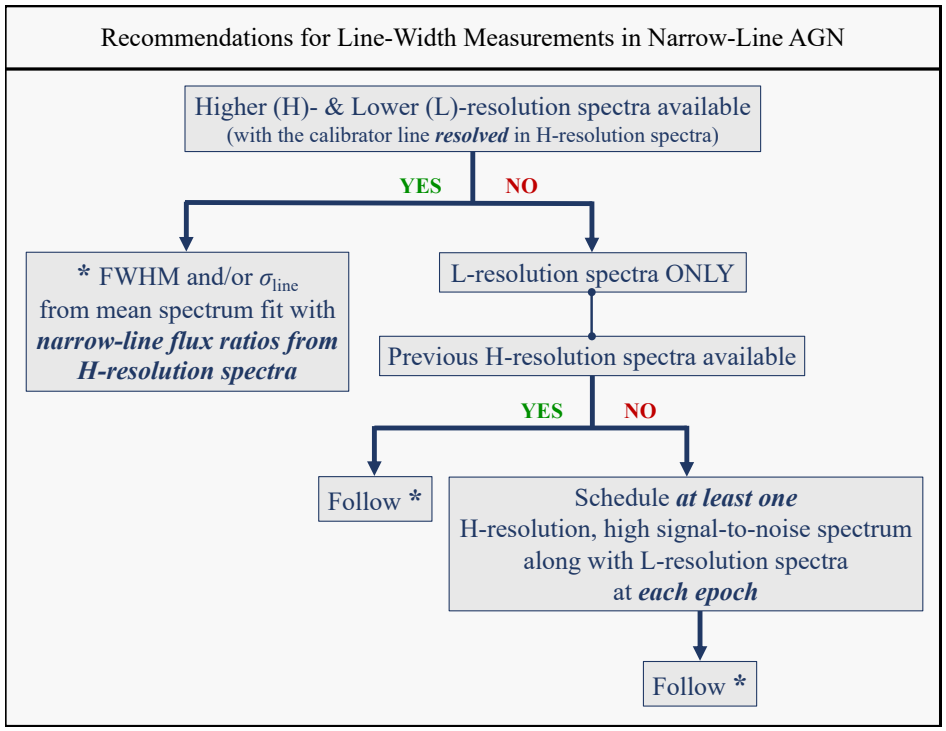

Figure 3.10: Recommendations for measuring line widths in narrow-line AGN. It is highly recommended to use both higher- and lower-resolution spectra for line-profile measurements in narrow-line objects with the calibrator narrow line (such as [O III] λ5008 for broad Hβ line measurements) *completely resolved* in the higher-resolution observations. The decision-making tree suggests the way forward depending on the availability of data.

We strongly recommend both higher- and lower-resolution observations for RM analysis of narrow-line AGN. In RM, the nearest neighbouring narrow line is typically used for relative flux calibration of the broad lines of interest, e.g., [O III] λ5008 is used as a calibrator line for measuring Hβ. Therefore, a *completely resolved* calibrator line is essential. We regard this as the primary requirement for accurately measuring the broad-line widths in narrow-line AGN. Then, while measuring line profiles, applying narrow-line flux ratios (relative to the calibrator line) determined from the higher-resolution spectra will allow more accurate measurements of line widths with the mean spectra. If only lower-resolution spectra are available, we recommend using higher-resolution spectra from archival observations to determine the appropriate narrow-line flux ratios. If no archival higher-resolution spectra exist, we highly recommend scheduling *at least one* higher-resolution spectrum along with lower-resolution spectra at *each epoch*. RM analysis of narrow-line AGN will benefit extensively with simultaneous higher- and lower-resolution observations.

3.5 Summary

We performed a detailed correlation analysis of the spectral measurements from the Mrk 142 data taken with Gemini at higher resolution ($\sim$270 km s^{-1}) and LJT at lower resolution ($\sim$500 km s^{-1}) to understand the effect of different spectral resolutions on the measured physical properties of emission lines. The FWHMs measured for the broad Hβ from the Gemini and LJT spectra did not overlap. Through our analysis, we identified that the "broader", unresolved [O III] λ5008 in the LJT spectra affected the Hβ FWHM measurements during spectral fitting. We corrected for the LJT Hβ FWHM values by fixing the narrow-line flux ratio of Hβ to the [O III] λ5008 line flux as determined from the Gemini spectral fits. Adopting this procedure, the mean Hβ FWHM reduced from $\sim$2220 km s^{-1} to $\sim$1930 km s^{-1}, an improvement of $\sim$54% in the mean value. We summarize our main results below.

1. In Mrk 142, lower-resolution spectra with an unresolved [O III] λ5008 line, a fixed width (equal to the [O III] line width) but flexible line flux for the narrow Hβ caused a flux leak from the broad to the narrow component, resulting in a lower peak flux for the broad-line profile and therefore a broader broad Hβ FWHM as compared to the higher-resolution spectra with a resolved [O III] λ5008 line.

2. Fixing the narrow-line flux ratio of Hβ to [O III] λ5008 while measuring the Hβ broad-line profile in the LJT spectra nullified the correlation of the broad Hβ FWHM with the [O III] λ5008 flux as well as reduced the scatter in the FWHM values by a factor of 2.6, equal to the scatter in the Hβ FWHMs measured from the Gemini spectra. Consequently, the mean of the Hβ FWHM values decreased by $\sim$54% or an effective width of $\sim$1000 km s^{-1}. The remaining offset is likely from Fe II.

3. Considering the impact of a *resolved* [O III] λ5008 on the Hβ FWHM measurements, we strongly recommend using both higher- and lower-resolution spectra for measuring line profiles in narrow-line AGN.

We leveraged the access to both the Gemini and the LJT spectra of Mrk 142 for RM analysis – while the LJT observations expanded the time baseline and filled the gaps in Gemini

observations, the Gemini spectra at higher resolution allowed more precise Hβ line measurements from the LJT spectra. We emphasize that measuring broad-line profiles in objects with narrower broad lines than the typical AGN population is not straightforward. Branching out to diverse populations for RM studies perhaps needs a revisit to emission-line measurement methods.

Chapter 4

Designing Large-Scale Variability Surveys of Active Galactic Nuclei

4.1 Introduction

Active galactic nuclei (AGN) are highly energetic systems located at the centres of massive galaxies. In growing AGN, the inflow of gas through an accretion disk onto the central supermassive black hole (SMBH) releases tremendous amounts of energy, part of which is observed over a wide range of energies from the X-ray to radio wavelengths (λ). Such massive, growing AGN systems are common at high redshifts, but are rare in the local Universe. Therefore, it is important to consider one of the key questions – *How do SMBHs grow over cosmic time?*

Characterizing black hole masses of a diverse population of AGN at a range of redshifts and luminosities is essential for constraining the history of SMBH growth over cosmic time. The "gold standard" for measuring black hole masses is reverberation mapping (RM). RM (Peterson et al. 2014) is a powerful technique for probing the detailed structure and kinematics of the inner regions of AGN. X-ray/ultraviolet (UV) radiation from the central accretion disk photoionizes the gas located in the broad-line region (BLR) giving rise to correlated continuum and BLR light curves with a positive time offset. RM allows measuring the time lag between two correlated light curves that is equal to the light travel time from the accretion disk to the BLR gas (with a correction for observer orientation) which is then translated to a distance measurement, the size of the BLR (Peterson 1993). Time lag combined with the velocity (obtained from the velocity widths of emission lines in AGN spectra) of the BLR gas can be used to calculate black hole masses (Peterson 2006) for AGN.

RM has been successfully applied to ~250 AGN to date, and the sample size continues to increase. The data required for RM are continuum photometry and emission-line spectroscopy. Bentz & Katz (2015) compiled black hole masses measured with the RM technique for ~40 low-redshift AGN ($z \lesssim 0.3$) primarily using the Hβ λ4861 line. The Super-Eddington Accreting Massive Black Holes (SEAMBH) campaign performing photometric and spectroscopic observations over the past seven years of high accretion-rate AGN have studied ~25 AGN, 17 of which are new targets (e.g., Du et al. 2014; Wang et al. 2014b; Hu et al. 2015; Du et al. 2015, 2016b, 2018). The Sloan Digital Sky Survey Reverberation-Mapping (SDSS-RM) program, from its four years of photometric and spectroscopic monitoring, has measured sig-

nificant time lags for ∼120 quasars (the most luminous AGN) at redshifts $0.3 < z < 2.8$ with Hβ, Hα λ6565, Mg II λ2799, and C IV λ1549 (Shen et al. 2015, 2016; Grier et al. 2017, 2019; Homayouni et al. 2020). The SDSS-RM results contributed significantly to the previous black hole mass measurements at intermediate and higher redshifts, and for more luminous AGN during the epoch of peak AGN growth.

Although the size of the overall AGN RM sample is growing with new and wide-field campaigns, the number of reverberation-mapped AGN in different redshift regimes is quite low, and there are discrepancies in the calibration of black hole mass measurements due to different emission lines used at different redshifts. Traditionally, Hβ λ4861 has been predominantly used to obtain black hole masses in AGN at low redshifts. Efforts with SDSS-RM pushed the redshift limit for Hβ-based time lag measurements to $0.3 < z < 0.8$ (Grier et al. 2017). Grier et al. (2019) published black hole masses from C IV lags for 48 AGN with $1.4 < z < 2.8$, which is a factor of 2.5 greater than in the previous C IV-based RM measurements (e.g., Kaspi et al. 2007; Trevese et al. 2014; Lira et al. 2018). However, the Hβ and C IV lines originate in different parts of the BLR; the high-ionization C IV line is generated much closer to the accretion disk. There is a discrepancy between the black hole mass-host galaxy velocity dispersion ($M_\bullet$–σ_*) relation with Hβ at low redshifts and the $M_\bullet$–σ_* relation with C IV at high redshifts (Ferrarese & Merritt 2000). In addition, Denney et al. (2016) investigated the differences in AGN properties measured from C IV emission lines for single-epoch data (signal-to-noise [S/N] ∼ 5) and coadded spectra (S/N ∼ 10) for 482 quasars at $z > 1.46$. They noted that the systematic offsets in the measured quasar properties increased with decreasing S/N of the data. For other lines such as Mg II λ2799 and Lyα λ1215, the radius-luminosity (R–L) relationships are poorly calibrated. An issue with the Mg II line is that it does not show strong variations like the C IV or Balmer lines. Hence, measuring reliable lags with Mg II requires data with high S/N. The Lyα line has strong blue absorption and is inaccessible for optical surveys from the ground until they probe high redshift objects, which again require sufficient S/N for significant time-lag measurements. An important point to note is that AGN at different redshifts occupy completely different regions of parameter space given their luminosity, the shape of their ionizing SED, and the properties of their host galaxies. Therefore, it is crucial to obtain more high-quality data with consistent emission lines at intermediate and high redshifts to accurately measure reverberation-mapped black hole masses for AGN in a uniform luminosity-redshift (L–z) parameter space.

Applying the RM technique successfully to an extensive sample requires strategic planning with a targeted observational campaign. The science outcomes of an RM campaign heavily depend on its design specifications. For instance, measuring short lags on the order of several days requires a shorter cadence (∼2–3 days at the least) as compared to lags on the order of months that can be retrieved by longer cadences of weeks. As seen from previous studies, reliable lag measurements for high-redshift AGN with higher luminosities need higher S/N, due to lower fractional variability, than those for AGN at low redshifts. Therefore, optimizing various observational parameters of a survey is essential to maximize its science return. Survey optimization requires a full-featured survey simulation pipeline capable of generating and analyzing mock data while experimenting with the observable parameters.

In this chapter, we illustrate the use of an AGN Survey Simulation Pipeline (currently under development) for planning large-scale AGN RM surveys with the *Cosmological Advanced*

Survey Telescope for Optical and ultraviolet Research (CASTOR[1]; Côté et al. 2019). CASTOR is a Canadian flagship UV mission proposed to the Canadian Space Agency (CSA) that aims to perform photometric and spectroscopic (with both grism[2] and slit spectrograph) surveys in three UV/optical bands from 1350–5550Å (P.I.: Patrick Côté). One of the key science goals of the mission is to study the growth of SMBHs. Considering this mission goal, we are developing an AGN Survey Simulation Pipeline (hereafter, AGN Survey Simulation) to optimize the design of AGN variability surveys in order to measure black hole masses in a statistically significant AGN sample spanning a wide redshift-luminosity space. We aim to: (1) measure black hole masses for 1000+ AGN from low to high redshifts ($0 < z < 2.5$) with grism spectroscopy, and (2) calibrate black hole mass measurements with UV lines to those with optical lines. The objective of the AGN Survey Simulation is to determine the optimum observing specifications of CASTOR required to achieve our desired science goals.

This chapter is structured as follows. Section 4.2 describes the AGN survey simulation design, highlighting the various factors to be considered while designing RM surveys. Section 4.3 presents representations of the AGN Survey Simulation deliverables. In Section 4.4, we discuss the significance of the AGN Survey Simulation for planning large-scale RM surveys, compare the capabilities of CASTOR to RM studies conducted to date, and state the limitations of the simulation pipeline. Section 4.5 states the concluding remarks including directions for the future. Throughout this work, we use the standard cosmology for a flat Universe with H_0[3] = 70 km s^{-1} Mpc^{-1}, Ω_Λ[4] = 0.7, and Ω_M[5] = 0.3 (Hinshaw et al. 2013).

4.2 AGN Survey Simulation Pipeline

To optimize large-scale AGN RM campaigns for measuring black hole masses in 1000+ AGN, we are designing an end-to-end pipeline – the AGN Survey Simulation. The simulation design broadly consists of three sets of modules: first, simulating the behaviour of AGN; second, simulating the photometric and spectroscopic (grism for the RM survey) instruments on CASTOR; and third, performing cross-correlation analysis with the simulated data to measure time lags and derive black hole masses. All modules perform distinct functions and work in collaboration to obtain the end results. Throughout the design flow, the outputs from preceding modules are supplied as inputs to the succeeding modules. Figure 4.1 shows the AGN Survey Simulation flowchart explaining its structural design.

We briefly describe the individual modules (with their *development status*) below.

1. AGN Simulated Sample (*ready*) – Module A ::
   This module generates a simulated sample of AGN in the parameter space of luminosity and redshift (L–z). The simulated sample is drawn from the source density of AGN

[1]For more information about CASTOR, visit `https://www.castormission.org/`.

[2]Grism is an instrument setup containing a grating placed on a prism (grating + prism = grism) such that all the light falling on the prism is dispersed by the grating, thus providing the spectra of everything in the field of view of a telescope. Because a grism setup does not use a slit, grism spectroscopy is also referred to as slitless spectroscopy.

[3]H_0: Hubble constant

[4]Ω_Λ: Density of dark energy

[5]Ω_M: Mass density (including ordinary mass and dark matter)

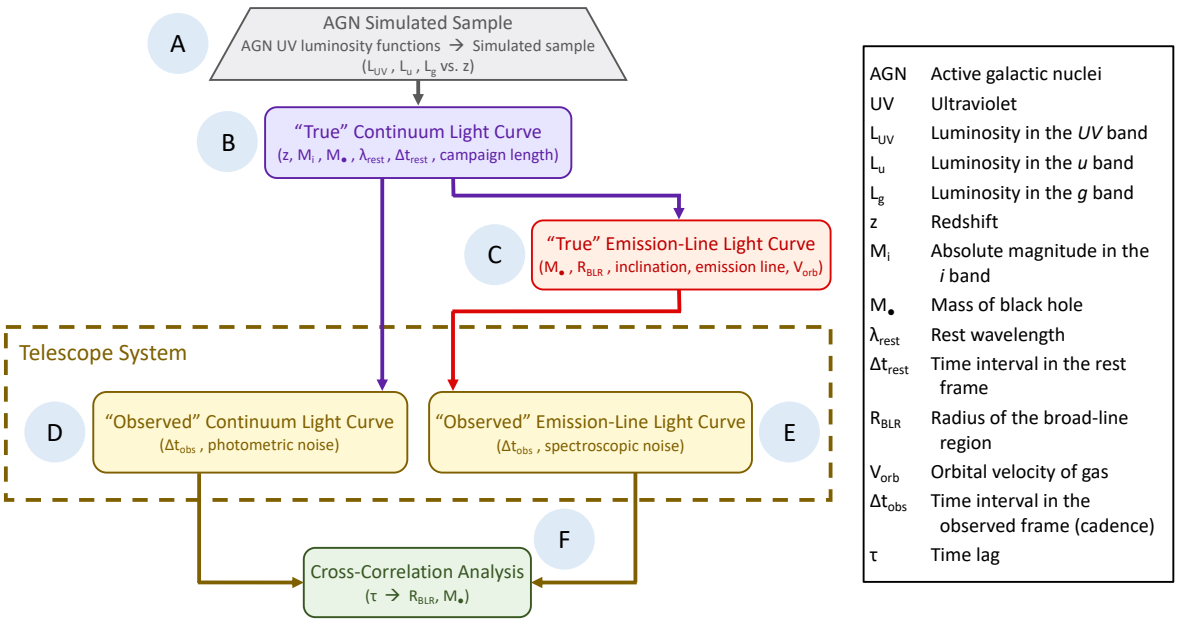

Figure 4.1: AGN Survey Simulation design showing the broader sets of modules (labelled from A–F). Module A generates the simulated sample using AGN ultraviolet luminosity functions (Kulkarni et al. 2019). Module B selects a sub-sample from the simulated sample and generates continuum light curves using the damped random walk (DRW; Kelly et al. 2009) and long-term variability parameters (MacLeod et al. 2010). Module C (under development) simulates emission-line response to the continuum variations for the sub-sample. Modules D and E (where E is under development) simulate the light curves in the frame of the observer by considering cadence, campaign length, and signal-to-noise of the data. Finally, module F (under development) measures time lags and calculates black hole mass by cross-correlating the input "observed" light curves.

(number per square degree [deg^2] on the sky) obtained by integrating over the UV luminosity function given by Equation 4.1, the empirical luminosity function in Kulkarni et al. (2019) (see their Equation 7), as follows:

$$\phi(M) = \frac{\phi_*}{10^{0.4\ (\alpha+1)\ (M-M_*)} + 10^{0.4\ (\beta+1)\ (M-M_*)}}\ [\mathrm{cMpc^{-3}\ mag^{-1}}] \tag{4.1}$$

where ϕ_*, the luminosity function amplitude; M_*, the break magnitude of the broken power law; α, the bright-end slope; and β, the faint-end slope are free parameters of the model. The luminosity function, ϕ as a function of absolute magnitude M, is given in the units of per comoving volume (comoving Megaparsec[3][6] [cMpc^3]) per magnitude (mag). The observed source density is computed with a limiting apparent magnitude and/or a limiting absolute magnitude with the specified cosmology.

[6] 1 Megaparsec (Mpc) $\approx 3 \times 10^{24}$ cm

2. "True" Continuum Light Curve (*ready*) – Module B ::
This module generates "true" observed continuum light curves in the three CASTOR bandpasses – *UV* (1500 Å–3000 Å), *u* (3000 Å–4000 Å), and *g* (4000 Å–5000 Å) – with variability defined by the damped random walk model (DRW; Kelly et al. 2009). The "true" signifies that the simulated light curves are as they originate at the location of the AGN system with a fixed cadence over a given monitoring duration (or length) of a campaign. The DRW model requires two long-term variability parameters – variability amplitude (Δm_∞) representing root-mean-square (RMS) variability on long-term timescales; and characteristic timescale ($\tau_{\rm damping}$) representing the long-term damping timescale for AGN variability – calculated as a function of the black hole mass, absolute magnitude in the *i*-band, rest-frame wavelength, and redshift (MacLeod et al. 2010).

3. "True" Emission-Line Light Curve (*under development*) – Module C ::
This module is being developed to generate "true" emission-line light curves for lines of interest (Lyα, C IV, and Mg II for the AGN legacy survey) by modelling different transfer functions for the BLR. Modelling a transfer function requires assuming a geometry for the BLR – $M_\bullet$, radius ($R_{\rm BLR}$), inclination angle, and velocity structure (e.g., BLR gas in virial motions given by $R_{\rm BLR} \propto V_{\rm orb}^{-2}$, where $V_{\rm orb}$ is the orbital velocity of the gas).

4. "Observed" Continuum Light Curve (*ready*) – Module D :: This module generates "observed" (in the rest-frame of the observer) continuum light curves in the three CASTOR bandpasses (see above) given the desired exposure time and type of cadence. It takes into account the observational noise using existing estimates of CASTOR performance in different bandpasses for which S/N tables were provided by Patrick Côté. Various cadence types – regular (observations at fixed intervals), variable (observations with fixed intervals varying over the campaign length), and random (number of random observations over the campaign length) – are considered to allow flexibility in planning surveys.

5. "Observed" Emission-Line Light Curve (*under development*) – Module E ::
This module is being developed to generate "observed" emission-line light curves in the same way as the "observed" continuum light curves, with spectroscopic noise and different cadence setups. Currently, there is limited information available on the grism performance. Further development in this regard is expected in the near future as part of the ongoing Phase 0 study.

6. Cross-Correlation Analysis (*under development*) – Module F ::
This module performs cross-correlation analysis between different continuum light curves for measuring continuum time lags or continuum and emission-line light curves for measuring emission-line lags. It currently employs two different methods for time-lag measurements: Interpolated Cross-Correlation Function (ICCF; Gaskell & Sparke 1986; Gaskell & Peterson 1987) and Python-based Running Optimal Average (`PyROA`; Donnan et al. 2021).

4.2.1 Colour Correction

Colour correction, also known as K-correction (K), accounts for the difference in the brightness of a source from its emitted rest-frame bandpass to an observed bandpass. The structure of an AGN spectrum, and the shifting and stretching of a spectrum from cosmological redshifting[7] lead the K-correction to be highly structured. To compute AGN source densities as a part of the "AGN Simulated Sample" module, we incorporated the $K_{1450,\mathrm{UV}}$ from the 1450 Å band to the observed, *UV* band using Equation 4.2, the definition of K-correction from Hogg et al. (2002) (see their Equation 12), as follows:

$$K_{QR} = -2.5 \times \log_{10}\left[\frac{1}{[1+z]} \frac{\int \mathrm{d}\lambda_{\mathrm{obs}}\, \lambda_{\mathrm{obs}}\, F_\lambda(\lambda_{\mathrm{obs}})\, R(\lambda_{\mathrm{obs}}) \int \mathrm{d}\lambda_{\mathrm{emit}}\, \lambda_{\mathrm{emit}}\, G^Q_\lambda(\lambda_{\mathrm{emit}})\, Q(\lambda_{\mathrm{emit}})}{\int \mathrm{d}\lambda_{\mathrm{obs}}\, \lambda_{\mathrm{obs}}\, G^R_\lambda(\lambda_{\mathrm{obs}})\, R(\lambda_{\mathrm{obs}}) \int \mathrm{d}\lambda_{\mathrm{emit}}\, \lambda_{\mathrm{emit}}\, F_\lambda([1+z]\lambda_{\mathrm{emit}})\, Q(\lambda_{\mathrm{emit}})}\right] \quad (4.2)$$

where G^Q_λ and G^R_λ are the zero-point definitions of the Q and R filters, respectively; $Q(\lambda_{\mathrm{emit}})$ and $R(\lambda_{\mathrm{obs}})$ are the filter response functions in the emitted (emit) and observed (obs) bandpasses, respectively; F_λ is the flux density (flux per unit wavelength); and z is the redshift. The filter function for the *UV* band was provided by Patrick Côté. For the 1450 Å band, we assumed a square wave filter function with a 100 Å wide window around the effective wavelength of 1450 Å and a constant transmission efficiency at 50%. We adopted the $K_{1450,\mathrm{UV}}$ derived with the Shang et al. (2011) composite as the reference spectrum. We also compared the $K_{1450,\mathrm{UV}}$ with the Shang et al. (2011) composite to that with Vanden Berk et al. (2001) as shown in Figure 4.2.

$K_{1450,\mathrm{UV}}$ with the Vanden Berk et al. (2001) composite suffers due to strong absorption in the Lyα forest. At very low redshifts $0 < z < 0.25$, the $K_{1450,\mathrm{UV}}$ is roughly the same. However, the values with the Vanden Berk et al. (2001) composite start rising from $z \sim 0.4$, when the Lyα forest enters the *UV* bandpass. After this point, the strong absorption in the Lyα forest (grey shaded region marked in Figure 4.2, *Inset* panel) causes the $K_{1450,\mathrm{UV}}$ with the Vanden Berk et al. (2001) composite to rise more steeply than that with the Shang et al. (2011) composite, where there is negligible absorption. Given that CASTOR AGN surveys will target the low to high redshifts of $0 < z < 2.5$, the $K_{1450,\mathrm{UV}}$ with the Shang et al. (2011) composite that is unaffected at shorter wavelengths from the Lyα absorption is desirable. In general, $K_{1450,\mathrm{UV}}$ evolves from negative values at lower redshifts to positive at higher redshifts as AGN are brighter at shorter (or bluer) wavelengths than at longer (or redder) wavelengths.

[7] Cosmological redshifting is a phenomenon in which the rest wavelengths of light appear to shift to the longer (or redder) wavelengths for a distance observer due to the expansion of the Universe.

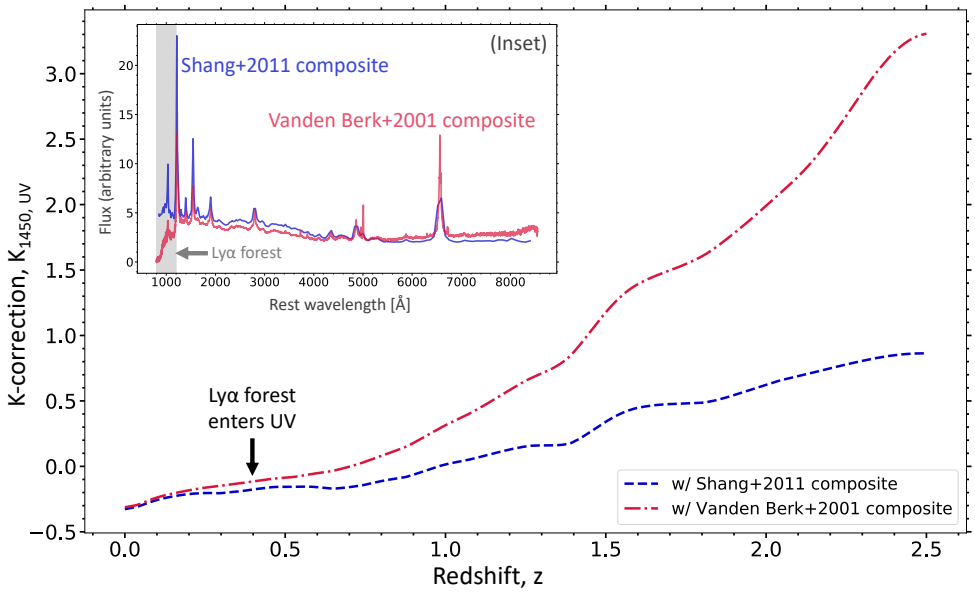

Figure 4.2: Comparison between K-correction ($K_{1450,\mathrm{UV}}$) over the range of redshifts, $0 \leq z \leq 2.5$, derived for the 1450 Å band (with a 100 Å wide bandpass at 50% transmission) when targets are observed in the CASTOR *UV* band (2260 Å) using the Shang et al. (2011) (blue dashed line) and Vanden Berk et al. (2001) (red dashed-dotted line) composites. *Inset*: Shang et al. (2011) (blue solid curve) and Vanden Berk et al. (2001) (red solid curve) composite spectra. The grey shaded patch marks the Lyα forest region, where the Vanden Berk et al. (2001) spectrum shows a significant drop in flux because it is generated from high-redshift quasars observed from the ground, whereas the Shang et al. (2011) spectrum is made from low-redshift AGN. Thus, the Shang et al. (2011) composite has smaller $K_{1450,\mathrm{UV}}$ owing to the less Lyα absorption.

4.2.2 Factors Under Consideration for CASTOR AGN RM Surveys

AGN surveys with CASTOR will benefit from the multiple advantages in the UV that make this regime ideal for RM campaigns.

1. The UV AGN continuum directly tracks the ionizing light that dominates the BLR energetics, whereas typical ground-based RM campaigns are only able to use the optical continuum luminosity as a proxy for the UV.

2. AGN are more variable in the UV than in the optical, and so successfully correlating continuum and emission-line light curves is more feasible.

3. The UV continuum variability timescale is shorter than in the optical (MacLeod et al. 2010).

4. High-ionization UV emission lines are generated closer to the central continuum and therefore have shorter time lags (Kaspi et al. 2005; Denney et al. 2013).

5. RM campaigns in the UV can have shorter monitoring durations than those in the optical (due to #3 and 4).

Monitoring the short variability timescales for UV emission at lower redshifts as well as accounting for delayed time lags at higher redshifts requires a good balance between cadence and campaign length. Shorter cadence or densely spaced observations are desirable to detect AGN variability on shorter timescales on the order of a few days. If observations are sparsely distributed (longer cadence), interpolating between observations while measuring time lags increases the uncertainties. This further results in more uncertain black hole mass measurements. Equally important is the length of an RM survey – a sufficiently long campaign is required to capture the time dilated from cosmological redshifting for high-redshift AGN. Time takes longer to travel from objects far away and is stretched due to the expanding Universe – an effect called cosmological time dilation – which results in longer observed time lags for AGN at higher redshifts. Therefore, while deciding the cadence as well as campaign length, incorporating the time dilation effect is essential. Press (1978) suggests a campaign length thrice as long as the longest time lag to be measured. Cadence and campaign length impact the efficiency of the program in a significant way.

The slitless (grism) spectroscopy mode offered by CASTOR is particularly useful to survey a large number of AGN. Because a grism covers the entire field of view (FOV) of a telescope, grism images capture more objects on the sky, thus providing a significantly large sample. Because CASTOR will be sensitive to faint objects at relatively high redshifts, RM surveys can span a wide L–z parameter space. Figure 4.3, panel *a* shows the key emission lines accessible in the observed frame within the three CASTOR bandpasses. However, the grism will operate in only the two channels in the ultraviolet – *UV* and *u*. This limits the highest redshift that RM surveys can probe to ~2.3, when the Lyα line exits the *u* band, and the Lyα forest impacts the emission-line detection significantly. While Lyα and C IV are accessible over a wide redshift range, Mg II will be limited to the low-redshift regime $0 < z \lesssim 0.4$. Redshift ranges in which multiple emission lines are accessible are particularly interesting for probing multi-scale BLR. AGN with reverberation-mapped black hole masses are currently limited in the intermediate-

and high-redshift regimes, where CASTOR has an opportunity to vastly expand the sample. The wide parameter space in redshift covers a broad swath of cosmic time and hence is critical to understand black hole growth over astronomical timescales.

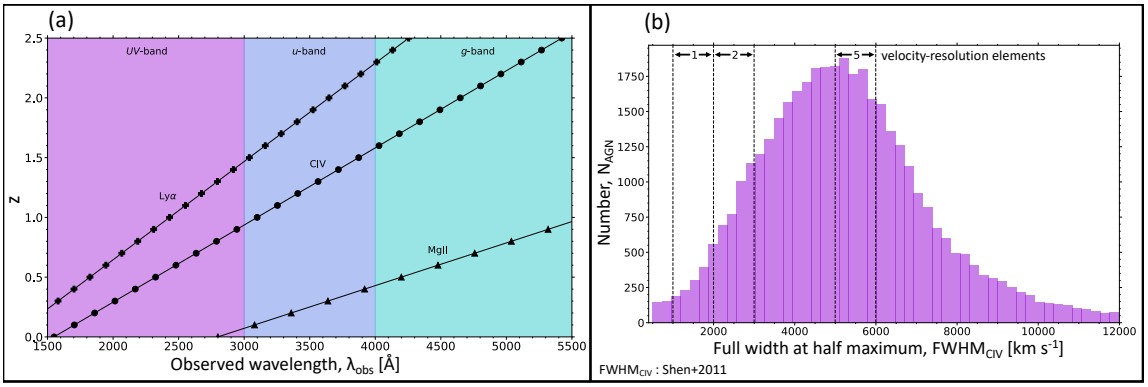

Figure 4.3: Panel *a*: Observed wavelengths of the broad emission lines, Lyα λ1215 (line with pluses), C IV λ1549 (line with circles), and Mg II λ2799 (line with triangles), in the redshift space $0 \leq z < 2.5$. The three bands of the *Cosmological Advanced Survey Telescope for Optical and ultraviolet Research* (CASTOR) – *UV* (purple shaded region), *u* (blue shaded region), and *g* (cyan shaded region), are colour-coded in the z–$\lambda_{\rm obs}$ parameter space. Because the CASTOR grism operation is limited to the *UV* and *u* bands, reverberation-mapping surveys can probe up to redshifts ~2.3. Panel *b*: Distribution of the full width at half maximum (FWHM) values of the C IV line from Shen et al. (2011). The dashed vertical lines mark the boundaries of the regions giving 1, 2, and 5 velocity-resolution elements across the C IV FWHMs.

The lines of interest drive the resolution requirement of the grism. The required spectral resolution of the data is set such that the emission lines appear resolved. A resolved line profile is necessary to reliably measure the full width at half maximum (FWHM) of the line. Reliable FWHM measurements are critical because the measurement uncertainties on FWHMs directly translate to increased uncertainties in the derived black hole masses. To reliably identify and measure emission lines for RM, a line must have at least *three* velocity resolution elements across it. For the C IV line, this sets the minimum resolution requirement of the grism to ~300 and ~400 in the *UV* and *u* bands, respectively. Figure 4.3, panel *b* shows the distribution of C IV FWHM values measured for AGN in the Sloan Digital Sky Survey catalog (Shen et al. 2011). The numbers at the top of the dashed vertical lines indicate the number of resolution elements that can be achieved for the corresponding FWHM. With the minimum resolution requirement for the CASTOR grism, we will be able to resolve the C IV line for ~85% of the objects.

Employing the AGN survey simulation will allow optimization of the survey parameters to ultimately provide ideal campaign length, cadence, S/N, spectral resolution, survey area, and depth for planning RM campaigns.

4.3 Applications of the AGN Survey Simulation

The AGN Survey Simulation can be employed to estimate observational parameters required for designing goal-oriented variability campaigns. A few examples of questions that the AGN Survey Simulation can answer are described below.

1. How many CASTOR fields do we need to detect 500 AGN at S/N of 10 in the *UV* band? For this purpose, we first need to identify the apparent *UV* magnitude ($m_{\rm UV}$) that can be reached at an S/N of 10 in a given exposure time. Using this limiting magnitude in module A can provide a source density distribution of AGN. Considering the CASTOR FOV of 0.25 deg^2, we can calculate the number of fields required for the survey.

2. What cadence do we need to detect C IV variability of ~20% in a given L–z space? To answer this, we first need to simulate a realistic sample in the given L–z space with module A. For this simulated sample, module C will produce C IV emission-line light curves in the rest-frame of the AGN. Module E can then be used to optimize the observing cadence (and other parameters) with the specified variability detection threshold of 20%.

3. With a survey flux limit of $m_{\rm UV} < 23.0$, for how many objects can we derive black hole masses with a 3σ significance given a set of observing parameters (exposure time, cadence, and campaign length)? Simulating the AGN sample with the specified apparent limit, we need to run the entire pipeline and assess the significance of the black hole mass measurements.

Thus, the AGN Survey Simulation will offer a reliable way of estimating the observational parameters required to achieve desired science goals. Here, we present some examples of the AGN Survey Simulation deliverables.

Figure 4.4 shows luminosity and redshift distributions of the simulated sample with apparent and absolute magnitude limits of $m_{\rm UV} = 24$ and $M_{\rm UV} = -21$, respectively. We generated this simulated sample with module A in a survey area of 5 deg^2. With both the apparent and absolute magnitude limits (purple circles; panel *c*), many low-luminosity AGN are excluded which reduces the sample size from 800 (for objects with only the apparent magnitude limit; black circles, panel *c*) to 520. The luminosity distribution for the sample with both magnitude limits (purple; panel *b*) ends at $\log L_{\rm UV}[{\rm erg\ s^{-1}}] \sim 43.9$ (where $L_{\rm UV}$ is the luminosity in the *UV* band), while the distribution for the sample with only the apparent flux limit (grey; panel *b*) stretches to lower luminosities. AGN at high redshifts are typically more luminous than those at low redshifts. Therefore, setting the absolute flux limit selects the high-redshift AGN (purple; panel *a*) and ignores the less luminous AGN at low redshifts (grey; panel *a*).

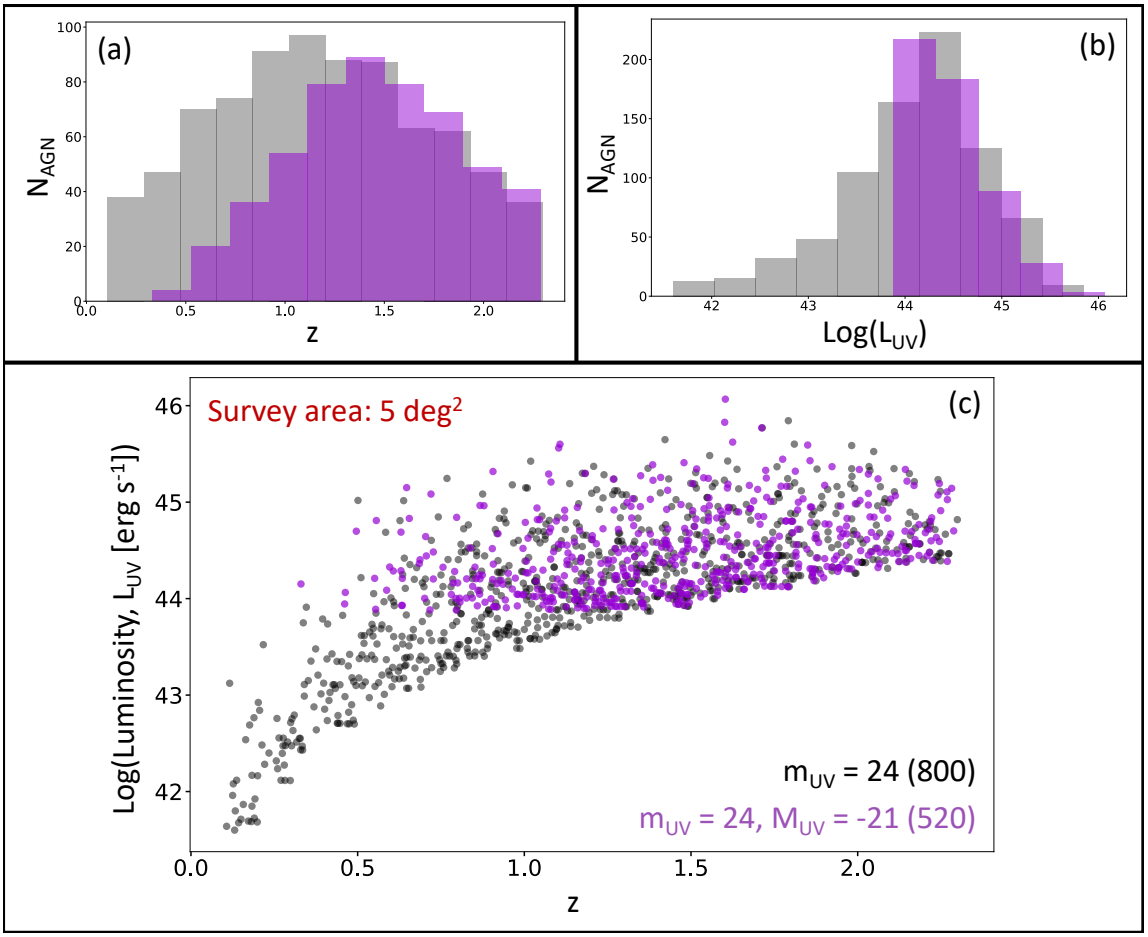

Figure 4.4: Redshift (z; panel *a*) and *UV*-band luminosity ($L_{\rm UV}$; panel *b*) distributions of the simulated sample (panel *c*) with only an apparent magnitude limit of $m_{\rm UV} = 24$ (black) as well as with both the apparent and absolute *UV*-band magnitude limits of 24 and -21, respectively (purple). The sample was simulated in a survey area of 5 square degree (deg^2). The distributions illustrate that we select more luminous AGN at higher redshifts by applying the absolute magnitude limit, and therefore the cadence and campaign duration should be adjusted accordingly.

Figure 4.5 presents an example of how campaign length depends on the redshifts and luminosities to be probed with different emission lines. C IV is accessible with the CASTOR grism till redshift $\lesssim$1.6 (marked with a solid vertical line; see panel *a*). However, time dilation becomes significant at higher redshifts that expands time lags in the observed frame. Therefore, campaign length increases with the targeted redshift. More luminous AGN are larger systems; hence, we expect longer lags in more luminous systems. Thus, longer campaigns are required to detect longer C IV lags. We used Equation 4.3, the *R*–*L* relation for C IV derived by Grier et al. (2019) (see their Equation 2), to estimate time lags at different luminosities.

$$\log \frac{R_{\rm BLR}}{\text{(light-days)}} = 0.92 \pm 0.08 \; + \; 0.52 \pm 0.04 \; \times \; \log \frac{\lambda L_{\lambda}\,[1350\ \text{Å}]}{10^{44}\ \text{erg s}^{-1}} \; + \; 0.11 \pm 0.04 \qquad (4.3)$$

where $R_{\rm BLR}$ is the radius (or size) of C IV ionization front in the BLR and λL_λ [1350 Å] is the luminosity at 1350 Å. As there does not exist a well-calibrated R–L relation for Mg II λ2799, we assumed the Hβ R–L derived by Kaspi et al. (2005), given by Equation 4.4 (see their Equation 2), to approximate the Mg II time lags.

$$\frac{R_{\rm BLR}}{(10\ \text{light-days})} = 2.23 \pm 0.21 \times \left[\frac{\lambda L_\lambda\,[5100\ \text{Å}]}{10^{44}\ \text{erg s}^{-1}}\right]^{0.69\pm0.05} \tag{4.4}$$

where $R_{\rm BLR}$ now marks the radius (or size) of Mg II ionization front in the BLR and λL_λ [5100 Å] is the luminosity at 5100 Å.We set the campaign length to be at least thrice as long as the time lag expected in the observed frame (Press 1978; Horne et al. 2004).

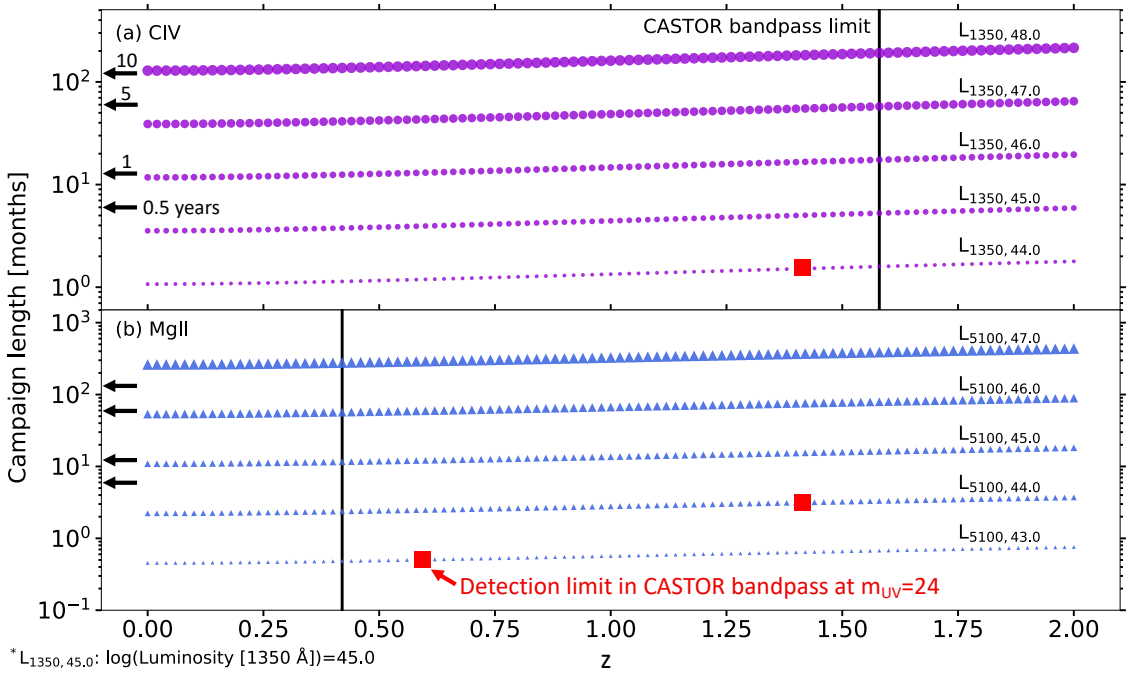

Figure 4.5: Illustration of the dependence of campaign length on redshifts (z) and luminosities (L expressed in the form of logarithmic values) for the C IV λ1549 (purple circles; panel *a*) and Mg II λ2799 (blue triangles; panel *b*) lines. Vertical lines in both panels mark the redshift limits when each line is lost in the CASTOR bandpass. Red boxes show the detection limits at an apparent magnitude of 24 in the *UV* band. Smaller (larger) symbols correspond to lower (higher) luminosities. As an example of the luminosity notation, $\log L_{1350,\,45.0}$ corresponds to the luminosity of $10^{45.0}$ erg s^{-1} at 1350 Å.

Figure 4.6 shows the amount of variability that can be detected at different cadences. We used the DRW model (Kelly et al. 2009) as implemented by MacLeod et al. (2010) with Equation 4.5 to derive the magnitude of observed variability ($\Delta m_{\rm obs}$) as a function of observed cadence ($\Delta t_{\rm obs}$) at rest wavelengths of 1350 Å (panel *a*) and 2200 Å (panel *b*).

$$\Delta m_{\rm obs}(\Delta t_{\rm obs}) = \Delta m_\infty\ (1 - e^{-|\Delta t_{\rm obs}|/\tau_{\rm damping}})^{1/2} \tag{4.5}$$

where Δm_∞, the amplitude of long-term variability, and $\tau_{\rm damping}$, the damping timescale of the observed variability, are the two model parameters. We used 1350 Å and 2200 Å as the nearest continuum points to represent variability in the C IV and Mg II lines, respectively. More luminous AGN vary on longer timescales. Therefore, to detect stronger variability (at least ~20%) in higher-luminosity AGN, we need longer cadences in general. For example, Mg II at a luminosity of $\log L_{\rm UV}[{\rm erg\ s^{-1}}] = 43.5$ shows ~20% variability in ~15 days; however, at $\log L_{\rm UV}[{\rm erg\ s^{-1}}] = 44.5$, it varies by the same amount in ~70 days. The more energetic continuum at 1350 Å shows stronger variability on shorter timescales than the 2200 Å continuum.

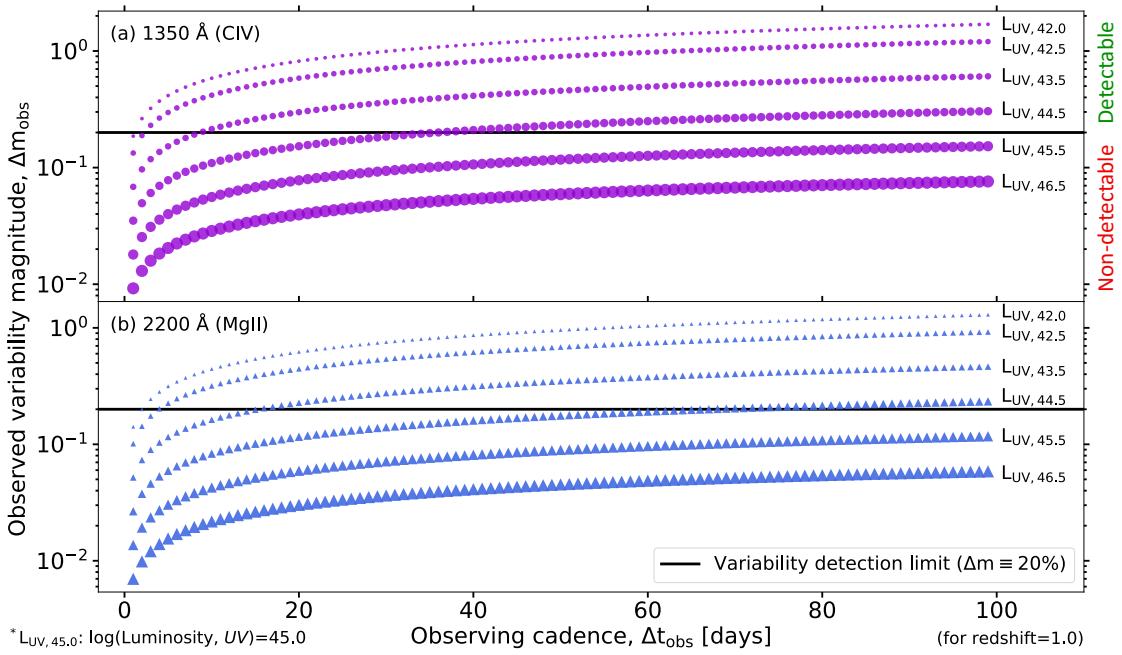

Figure 4.6: Illustration of the variability magnitude that can be detected with different cadences for the 1350 Å continuum (for C IV λ1549; purple circles, panel *a*) and 2200 Å continuum (for Mg II λ2799; blue triangles, panel *b*). Horizontal lines in both panels mark the detection limit at a variability of ~20%; below the lines, AGN are not expected to have detectable variability. As an example of the luminosity notation, $\log L_{\rm UV,\ 45.0}$ corresponds to the luminosity of $10^{45.0}$ erg s^{-1} in the *UV* band.

The above illustrations show that the interplay between various observational parameters can be non-trivial, especially with higher-redshift or higher-luminosity systems. The AGN Survey Simulation will provide a systematic way of incorporating the interdependence of various observational parameters while designing large-scale RM campaigns.

4.4 Discussion

We are constructing the AGN Survey Simulation to optimize AGN variability surveys with CASTOR. Our goal with the AGN Survey Simulation is to optimally design large-scale RM

surveys to obtain black hole masses in more than a thousand AGN as well as to determine design requirements for the CASTOR Phase 0 study. Several factors such as the emission lines to be probed, cadence of the photometric and spectroscopic observations, FOV, S/N, resolution, etc. need to be closely considered to be able to perform reliable measurements of time lags from light curves. In Section 4.3, we illustrated how the AGN Survey Simulation can be used to optimize these factors. Optimizing large-scale survey design is essential to maximize their science returns.

The illustrations presented in Figures 4.5 and 4.6 clearly state two important points: (1) Longer campaigns are required to span a wide L–z space; and (2) A variable cadence throughout the campaign can optimally capture variability on different timescales as expected for a range of rest-frame bandpasses, redshifts, and luminosities found in a survey field. Shorter campaigns, e.g., six months long, are sufficient to detect variability in only low-luminosity objects, e.g., $\log L_{\rm UV}[\rm erg\ s^{-1}] \sim 43.0$, at low redshifts. To target high-redshift objects at higher luminosities, we need longer RM campaigns. As an example, to perform RM with the C IV line in objects at the luminosities of $\log L_{\rm UV}[\rm erg\ s^{-1}] \sim 45.0$ at intermediate redshifts $1 < z < 1.5$, we need a campaign of ∼5 years. Coupled with the campaign length, the cadence is critical to be able to detect variability at different luminosities. While a shorter cadence is desirable in general, AGN at higher luminosities do not vary on shorter timescales. As we probe higher-redshift and higher-luminosity AGN, the cadence of the observations needs to be adjusted to capture that longer-timescale variability. Thus, an optimal RM campaign can be designed as starting at shorter cadences targeting low-redshift objects at lower luminosities and gradually switching to longer cadences to cover more high-redshift, higher-luminosity objects. Referring to the simulated AGN with only the apparent flux limit in Figure 4.4 (black circles; panel *c*), such an optimal campaign will start surveying from the bottom left to the upper right in the $L_{\rm UV}$–z space.

4.4.1 Context of Previous Studies

At present, the AGN sample from all previous studies does not uniformly span the L–z space. A majority of the low-redshift (and thus low-luminosity) AGN have been studied with Hβ, which is readily accessible for low-redshift objects with ground-based facilities. More recently, SDSS-RM has made considerable progress in detecting significant lags in ∼100 AGN at intermediate and high redshifts with the Hβ, Mg II, and C IV lines (Shen et al. 2016; Grier et al. 2017, 2019; Homayouni et al. 2020). However, optical campaigns with ground-based facilities cannot probe the redshift space uniformly with different emission lines. The more energetic UV region closer to the ionizing continuum in AGN is inaccessible to telescopes on the ground until the lines are shifted to the optical part of the spectrum at higher redshifts ($z > 0.25$ for the Mg II λ2799 line and $z \sim 1.88$ for Lyα). However, S/N also becomes an important consideration at high redshifts. Denney et al. (2013) discuss how low S/N of the AGN spectra at high redshifts affects the C IV line more than the Balmer lines. CASTOR will offer a collective solution to all the above issues. With its spectroscopic (grism for RM surveys) capabilities in two different UV bands, having the advantage of low sky background in the UV, and having control over cadence because of being in space, CASTOR will be able to survey a large number of AGN in a wide L–z parameter space compared to all previous studies. Figure 4.7 shows the L–z parameter space spanned by CASTOR in comparison with previous studies.

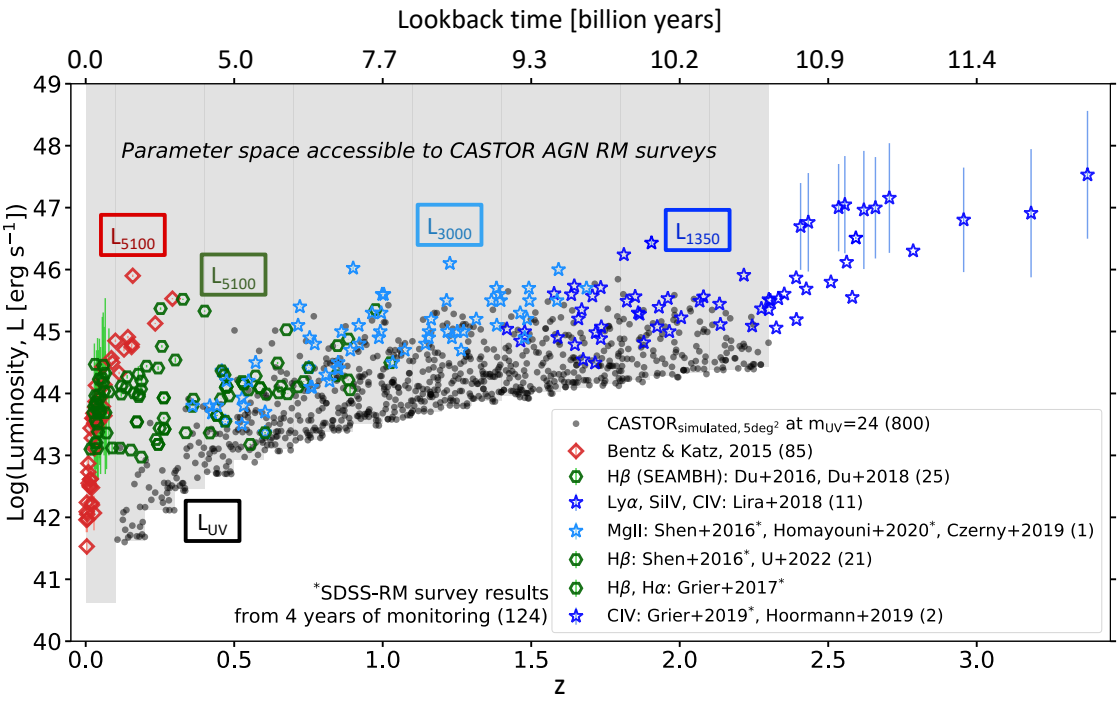

Figure 4.7: Luminosity-redshift (L–z) parameter space accessible to AGN RM surveys with CASTOR (grey shaded region) as compared to previous studies (various coloured symbols; Bentz & Katz 2015; Czerny et al. 2019; Du et al. 2016b, 2018; Grier et al. 2017, 2019; Homayouni et al. 2020; Hoormann et al. 2019; Lira et al. 2018; Shen et al. 2016; U et al. 2022). CASTOR simulated sample in a survey area of 5 square degree (deg^2) with an apparent magnitude limit of $m_{\rm UV}$ = 24 is shown for illustration. The rest-frame bandpass of the luminosities for different samples is specified in coloured boxes (corresponding to the sample colours). With UV coverage from space and the use of grism for RM surveys, CASTOR can simultaneously probe a significantly larger sample in a wide L–z space.

The primary goal of the AGN RM surveys with CASTOR is to determine black hole masses with the UV lines, Lyα λ1215, C IV λ1549, and Mg II λ2799 for over 1000 AGN with redshifts $0 \leq z \lesssim 2.3$. This sample would increase the number of directly measured black hole masses for AGN by a factor of ~5 over a wide range in redshift as compared to all previous studies. The secondary goal is to calibrate the black hole mass measurements with UV lines such as C IV (accessible with CASTOR) to previously measured black hole masses with optical lines such as Hβ, for low-redshift AGN. The R–L relationships established by previous RM studies can then be calibrated to more accurately estimate black hole masses from single-epoch spectra of other AGN. However, Denney (2012) highlights that the single-epoch black hole mass measurements for high-redshift AGN with the C IV line are systematically biased as compared to the masses determined using optical lines such as Hβ for their low-redshift counterparts. With the CASTOR AGN RM surveys, we can compare the single-epoch black hole masses measured with C IV to the existing measurements with Hβ for low-redshift AGN. Furthermore, we can directly compare the C IV single-epoch and RM masses for a large sample. The calibration

of the ($M_\bullet$–σ_*) relation for both C IV and Hβ in the case of low-redshift AGN will help us in understanding the discrepancies in black hole mass measurements and develop the appropriate calibrations to determine black hole masses for single-epoch AGN spectra.

4.4.2 Limitations of the AGN Survey Simulation

Although the AGN Survey Simulation follows a generic pipeline design, there are certain limitations to it similar to any simulation design. We briefly outline those limitations below.

1. To simulate the variability in an emission line (e.g., C IV λ1549), the AGN Survey Simulation uses the continuum wavelength closest to that line (i.e., 1350 Å; see Figure 4.6). However, the BLR has more complicated geometry and kinematics. Therefore, the "true" variability in the line likely differs from the closest continuum variability. Modelling the BLR is essential to accurately simulate the emission-line variability in AGN.

2. Because the sensitivity of the CASTOR grism is not currently established, the response of the *Space Telescope Imaging Spectrograph* on the *Hubble Space Telescope* is used to simulate the response of the CASTOR grism. The specifications of the CASTOR grism will be developed as part of the ongoing Phase 0 study after which the sensitivity of the grism would be available for the AGN Survey Simulation.

3. For estimating the K-correction in Module A, a fiducial filter response resembling a square wave function is used for the 1450 Å continuum bandpass. Therefore, the corrections generated are not accurate as there does not exist a real filter function for the 1450 Å bandpass. However, the corrections can be improved by using a smoother filter function such as a Gaussian (as against the sharper square wave), which would provide smoother inflections through an AGN spectrum rich in features.

4.5 Summary

We introduced the AGN Survey Simulation – an end-to-end survey simulation pipeline – that is being developed to optimize AGN variability surveys. The AGN Survey Simulation comprises various sets of modules that (1) simulate the "true" AGN behaviour to generate "true" continuum and emission-line light curves, (2) simulate the telescope system to generate "observed" continuum and emission-line light curves, and (3) perform cross-correlation analysis to derive black hole masses. The goal of designing this kind of survey simulation is to optimally plan large-scale variability surveys, e.g., for RM studies, such that we can maximize their science outcomes. We presented illustrations of how AGN RM surveys can be optimized for CASTOR, which will perform photometric and spectroscopic observations in the UV. AGN RM surveys with CASTOR will benefit from (1) shorter variability timescales of AGN in the UV, (2) the UV emission lines being closer to the ionizing continuum in AGN, (3) low sky background in the UV, and (4) no constraints due to weather because the telescope will be in space. Our illustrations highlight the following main points.

1. With a survey designed with an apparent flux limit, more high-redshift and high-luminosity AGN are probed, excluding the low-luminosity population at low redshifts. While the

less luminous AGN are difficult to observe, in order to survey the L–z parameter space uniformly, the flux limits need to carefully chosen.

2. Shorter RM campaigns target low-luminosity objects at low redshifts. Longer campaigns are needed to survey high-redshift or high-luminosity AGN.

3. Shorter cadences (on the order of a few days) are required to detect variability (at ∼20%) in low-luminosity AGN. For high-luminosity AGN, longer cadences (on the order of weeks or months) are essential. RM campaign design should incorporate varying cadences to span a wide range in redshifts and luminosities.

Implementing the AGN Survey Simulation for RM surveys with CASTOR, we aim to considerably increase the current sample size in a wide L–z space as compared to all previous studies. Furthermore, black hole mass measurements with UV lines such as C IV will allow cross-calibration with previous measurements of Hβ-based black hole masses in low-redshift AGN. Both the above goals will significantly contribute to RM science while improving our understanding of the growth of supermassive black holes over time.

Further developments for the AGN Survey Simulation are underway. In the current phase of the CASTOR science development study that started in February 2022, we plan to develop the telescope modules significantly. An improvement that is in progress is using simulated galaxy + AGN images for CASTOR to mock the performance of both the photometric and grism modules. Additionally, as the technical team progresses with the grism design specifications, we aim to incorporate those specifications in the grism module of the pipeline. Looking forward, the benefits of the AGN Survey Simulation are not limited to the scientific value that the CASTOR AGN RM surveys will offer. We are following a generic design for the AGN Survey Simulation that can be adapted to optimize variability surveys with different facilities.

Chapter 5

Conclusions

Active galactic nuclei (AGN) are growing supermassive black holes located at the centres of massive galaxies. Matter orbiting close to the central black hole accretes onto the black hole through a disk of ionized gas called the accretion disk. This mechanism releases tremendous amounts of energy in the form of electromagnetic radiation that can drive energetic outflows in these systems (Weymann et al. 1991). The photons from the central source (supermassive black hole + accretion disk) ionize the nearby gas generating high- and low-ionization emission lines that are observed in the spectra of AGN. Broad emission lines (several thousands of km s^{-1}) are a result of both thermal motions and the Doppler broadening effect. In the AGN system, broad emission lines originate in the broad-line region (BLR) at the base of UV line-driven outflows.

AGN are variable sources. The continuum varies on several timescales (days to weeks or months; e.g, Peterson et al. 1982). The powerful technique of reverberation mapping (RM) takes advantage of this variability in AGN to derive their size scales (e.g., Blandford & McKee 1982; Peterson 1993). A change in the ionizing continuum propagates radially outward, and gas in the BLR responds to the change with a positive time lag. The BLR absorbs the more energetic ionizing photons in X-ray/ultraviolet (UV) and re-radiates in the less energetic UV/optical, resulting in correlated continuum and emission-line light curves. RM allows translating the time lag between the continuum variation and emission-line response to a distance scale that is equal to the size of the BLR (e.g., Peterson et al. 2014). Because AGN remain unresolved through telescopes, we rely on the RM technique to study AGN systems.

Through RM, we can derive black hole masses in AGN, and further establish useful scaling relationships. Assuming virial motions of the gas around the central black hole, we can calculate the black hole mass ($M_\bullet$) given the distance of the gas from the central source and the velocities of the gas orbiting the black hole. The distance from the central source is simply the radius (or size) of the BLR (R) obtained by applying the RM technique. Typically, the full width at half maximum (FWHM) of the broad emission lines such as Hβ λ4861 or C IV λ1549 from AGN spectra is used as a measure for the velocities of the gas in the BLR gas ($\Delta V_{\rm FWHM}$). Thus, $M_\bullet \equiv f\ R\ \Delta V^2_{\rm FWHM}/G$, where G is the gravitational constant and f is a dimensionless factor that incorporates underlying assumptions about the geometry, kinematics, and orientation of the BLR. There exists a huge uncertainty in the f factor (see Section 1.7). Accurate and precise measurements of the line widths is therefore essential for a robust calibration of the mean f factor from large AGN samples. With the sizes and black hole masses in AGN, we can derive scaling relationships. One such relation is the R–L relation, showing how the size of

the BLR depends on the luminosity of the AGN, L (e.g., Kaspi et al. 2005; Bentz et al. 2009a, 2013). Here, L is the luminosity of the continuum closest to the measured emission line, e.g., luminosity at the rest-frame wavelength of 1350 Å is considered if the C IV line is measured. Another example is the correlation between $M_\bullet$ and the FWHM measured for various broad emission lines in AGN (Pancoast et al. 2014). Well calibrated scaling relations are beneficial to obtain more black hole masses from single-epoch AGN.

The success of an RM campaign depends on several factors including the observing cadence, spectral resolution, accurate spectrophotometry, signal-to-noise (S/N), and length of the campaign (described in detail in Section 1.8). To derive reliable time-lag and black hole mass measurements using RM, we need high quality data. Higher cadence is required to appropriately trace the behaviour of the continuum and emission lines varying on different timescales. Similarly, an RM campaign should be long enough to capture the variability of the emission lines under consideration. Further, a clean measurement of the emission-line profile requires medium- to high- spectral resolution such that the narrow emission lines are resolved. Lower spectral resolution can affect reliable measurements of FWHM of emission lines, thus increasing the uncertainty in the measured black hole masses. Accurate spectrophotometry is another critical requirement to measure small variations in the continuum and emission lines. For the same reason, high S/N is also important. Noisy data makes it difficult to measure weaker variability in certain lines, e.g., Mg II λ2799. High S/N becomes even more important as we probe AGN at high redshifts (z). It is not straightforward to combine all the above RM requirements, and therefore for successful RM campaigns, a systematic way of designing large-scale surveys is essential.

Despite decades of research, several questions about AGN still remain unanswered. One of the issues that we highlighted in Chapter 1 is the structure of accretion-disk and BLR in super-Eddington AGN that remains poorly understood. Super-Eddington AGN that likely evolved at high redshifts (z = 1–3) accrete well above the Eddington limit. At high accretion rates, the radiation pressure is expected to dominate inflating the inner regions of the accretion disk (e.g., Abramowicz et al. 1988). Many theoretical studies have thus proposed a "slim"-disk model for high accretion-rate AGN in contrast to a thin disk in their sub-Eddington counterparts (e.g., Abramowicz et al. 1988). However, not much observational research has been conducted on these highly accreting AGN. Since the past several years, the Super-Eddington Accreting Massive Black Holes (SEAMBH) collaboration has studied ∼25 super-Eddington objects (Du et al. 2014; Wang et al. 2014b; Hu et al. 2015; Du et al. 2015, 2016b, 2018). Empirically, their spectral characteristics are similar to those of Narrow-Line Seyfert 1 galaxies (NLS1s) with narrower broad Hβ profiles ($\Delta V_{\rm FWHM} \lesssim 2000$ km s^{-1}), weak [O III] $\lambda\lambda$4960, 5008 lines, and strong Fe II emission lines (e.g., Osterbrock & Pogge 1987; Boroson & Green 1992; Boller et al. 1996; Véron-Cetty et al. 2001). Super-Eddington AGN show smaller BLR sizes measured with Hβ as compared to other AGN at same luminosities (Du et al. 2016b). Past studies have attributed the smaller BLRs to the shrinking of the Hβ ionization front due to self-shadowing effects in the inner regions of the assumed slim disk (Wang et al. 2014a). However, more high-quality data and a larger sample are needed to better understand the structure of the accretion disk and its effects on the BLR. We studied one of the most promising SEAMBH candidates, Markarian 142 (Mrk 142) in Chapter 2. We cover a brief summary of Chapter 2 below.

5.1 Summary of Chapter 2

We used concurrent observations, for the first time, of the continuum (in UV and optical) and BLR (in optical) in a super-Eddington AGN – Mrk 142 (RA[1] = 156.380327°, Dec[2] = 51.676352°; $z = 0.045$) – with four different telescopes to measure, again for the first time, a time lag relative to the UV continuum for the object. It is important to measure time lags with reference to the UV continuum as the UV likely traces the ionizing continuum more closely than the optical. We used continuum data from (1) the *Neil Gehrels Swift Observatory* (*Swift*) in the *UVW2* band (centred at 1928 Å) that were taken from January 1 through April 30, 2019; and (2) the Las Cumbres Observatory (LCO) in the g band (centred at 4770 Å). E. Cackett provided the continuum light curves. Simultaneous to the *Swift* and LCO observations, optical spectra were taken with (1) the Gemini North Telescope (Gemini) with a narrow slit of 0.75″ (resolution of ∼270 km s^{-1}) at 33 epochs, and (2) the Lijiang Telescope (LJT) with a wide slit of 2.5″ (resolution of ∼500 km s^{-1}; Hu et al. 2015) at 69 epochs. We used the LJT spectra to complement the shorter observing period with Gemini. The Gemini spectra were reduced and calibrated using the Gemini Image Reduction and Analysis Facility (Gemini `IRAF`) software, while the calibrated LJT spectra were provided by C. Hu. We corrected the Gemini and LJT spectra for relative flux calibration with `PrepSpec` modelling (developer: K. Horne; see Appendix B for an introduction to `PrepSpec`). In `Sherpa`, we modelled the continuum and emission lines (including Hβ λ4861, [O III] $\lambda\lambda$4960, 5008, He I, and He II λ4687) with a goal of performing a clean measurement of the Hβ and He I broad lines. We used Hβ to further derive time lags and black hole mass in Mrk 142. Although the He I line showed a peculiar shape in the high S/N Gemini mean spectrum, the timescale of the Gemini+LJT campaigns was insufficient to capture the variability in the He I line; therefore, we excluded it from further analysis.

We employed the Python-based Running Optimal Average (`PyROA`; Donnan et al. 2021) technique to determine time lags in Mrk 142. As compared to the traditional Interpolated Cross-Correlation Function (ICCF; Gaskell & Sparke 1986; Gaskell & Peterson 1987) and Just Another Vehicle for Estimating Lags In Nuclei (`JAVELIN`; Zu et al. 2011, 2013), `PyROA` provides robust treatment for outliers. With `PyROA`, we measured a UV time lag of $8.58^{+0.76}_{-0.75}$ days for the Hβ line, and derived a black hole mass of $\log(M_\bullet/M_\odot) = 6.67 \pm 0.04$. From the Gemini and LJT spectral measurements, we first generated inter-calibrated light curves for the 5100 Å continuum and Hβ emission line. With `PyROA`, we then measured time lags for the LCO/g band, inter-calibrated 5100 Å continuum, LJT Hβ, and Gemini+LJT inter-calibrated Hβ light curves with reference to the *UVW2* continuum. From the measured time lags, we obtained a 5100 Å to Hβ lag of 7.82 ± 0.81 days, and consequently a black hole mass of $\log(M_\bullet/M_\odot) = 6.63 \pm 0.05$, both in agreement to the values published by Du et al. (2015). Our measured Hβ time lags fall close to $R_{\mathrm{H}\beta}$–L_{1350} relation for NGC 5548 (Eser et al. 2015), indicating that in Mrk 142 the UV is likely closer to the ionizing continuum than the optical. However, further analysis is required to verify this.

As we expand the application of RM to diverse populations of AGN, we must carefully consider how the quality of the data and our measurement techniques influence measured entities.

[1]RA: Right Ascension
[2]Dec: Declination

Traditionally, RM has been used to derive black hole masses in a majority of the low-redshift AGN accreting within the sub-Eddington limit (e.g., Stirpe et al. 1994; Santos-Lleó et al. 1997; Collier et al. 1998; Dietrich et al. 1998; Kaspi et al. 2000; Bentz et al. 2006; Denney et al. 2010; Grier et al. 2012). A high fraction of these reverberation-mapped AGN show broad emission lines ($\Delta V_{\rm FWHM} > 4000$ km s^{-1}) unlike the super-Eddington AGN with narrower line profiles (see above). In this context, achieving high spectral resolution and high S/N for the data become more essential to accurately measure emission-line profiles, and subsequently the black hole masses. In Section 1.7, we discussed in detail about how difficult it is to constrain black hole mass measurements – while there is high uncertainty in the f factor, part of the reason is the line width measurements. High spectral resolution ($\sim$100 km s^{-1}) is required to resolve the narrow lines in the spectra. Referring to the discussion of narrow lines in Section 1.3, they originate in the narrow-line region that is farther away from the central source in AGN. As a result, the narrow lines do not witness the continuum variations and are therefore regarded constant at the timescales of RM campaigns. RM studies use narrow lines for relative flux calibration, and hence it is necessary that we obtain a good handle on the flux measured in these lines. At low resolution, instrumental broadening can severely damage the emission-line profiles with effects like blending with neighbouring line features. Low S/N can make the line measurements even more challenging. In such cases, testing the effects on the quality of data on measured quantities as well as revisiting our measurement methods is critical. In Chapter 3, we focused on this issue and demonstrated how low spectral resolution affect measurements of narrower broad emission lines used for RM analysis. A brief summary of Chapter 3 is given below.

5.2 Summary of Chapter 3

We performed an in-depth correlation analysis of emission-line properties of the Hβ, He I, and [O III] λ5008 lines in the Mrk 142 spectra taken with the Gemini and LJT telescopes to investigate the discrepancy in the Hβ FWHM measurements from the Gemini and LJT spectra. The Gemini and LJT spectra were taken with different grating/slit configurations that resulted in different resolutions for the two data sets, $\sim$270 km s^{-1} for Gemini and $\sim$500 km s^{-1} for LJT (Hu et al. 2015). We first modelled the emission lines with flexible narrow-line ratios, i.e., the narrow-line fluxes of Hβ and He I were allowed to vary during spectral fitting while their FWHMs and positions were fixed relative to the [O III] λ5008 line. This setup yielded a mean Hβ FWHM of $\sim$1680 km s^{-1} for the Gemini spectra but as high as $\sim$2220 km s^{-1} the LJT spectra, giving an offset of $\sim$1450 km s^{-1} in effective FWHM ($\sqrt{2220^2 - 1680^2}$). This is much higher than the difference in the effective width observed between the FWHM of the [O III] λ5008 line ($\sim$680 km s^{-1}). We found a positive correlation between the narrow Hβ and the [O III] λ5008 fluxes from the LJT spectra, suggesting that more narrow Hβ flux was measured for more flux in [O III] λ5008. However, at the low resolution of the LJT spectra, the [O III] λ5008 line was not only affected by instrumental broadening but also unresolved. With a "broader" [O III] line and the FWHM of the narrow Hβ set equal to the [O III] FWHM, excess narrow-line flux was measured for the narrow Hβ resulting in a broader (than expected) FWHM for the broad Hβ.

For LJT spectral modelling, fixing the narrow-line fluxes of Hβ and He I relative to the

[O III] λ5008 line flux as determined from the Gemini spectral measurements constrained the narrow-line flux in Hβ. The excess flux was then redirected to the broad Hβ components, rising the broad-line peak flux and thus yielding narrower broad Hβ FWHM. Adopting narrow-line flux ratios determined from higher-resolution Gemini spectra for fitting the lower-resolution LJT spectra pushed the mean Hβ FWHM from LJT spectra ~54% closer to the Gemini Hβ FWHM measurement. The remaining offset likely results from blending of the Hβ broad-line profile with the Fe II emission in the surrounding region. Although the Fe II emission in Mrk 142 is stronger as compared to the typical broad-line Seyferts, the low spectral resolution of LJT smears the sharp features. Therefore, separating the broad Hβ and Fe II emission becomes difficult. Considering the significant improvement in the measured Hβ after fixing the narrow-line flux ratios for the broad lines in Mrk 142, we provided recommendations on measuring emission lines in narrow-line AGN. For performing RM studies of narrow-line objects, e.g., NLS1s, we strongly recommend taking a higher-resolution spectrum (with resolved calibrator line, e.g., [O III]) at high S/N along with lower-resolution data to accurately measure narrower broad-line profiles.

From the beginning through this point, it is clear that RM studies of AGN rely heavily on the quality of data available. In Section 1.8, we discussed the observational requirements of RM campaigns in detail. Table 1.1 provides a quick summary of all RM campaigns till date. Over the years, RM studies have considered various types of AGN starting from the less luminous Seyferts at low redshifts (Osterbrock et al. 1978; Osterbrock 1978; Peterson et al. 1982; Clavel et al. 1991; Peterson et al. 1991; Dietrich et al. 1993; Maoz et al. 1993; Romanishin et al. 1995) to the more luminous quasars at high redshifts (Maoz 1990; Maoz et al. 1991; Netzer et al. 1990; Maoz et al. 1991; Kaspi et al. 2007; Lira et al. 2018; Czerny et al. 2019; Hoormann et al. 2019). The Sloan Digital Sky Survey Reverberation Mapping (SDSS-RM) Project took several steps further by surveying 849 AGN at redshifts $0.1 < z < 4.5$ and a limiting apparent magnitude of $m_i < 21.7$ in a 7 square degree (deg^2) field (Shen et al. 2015). Since the first SDSS-RM results from a six-month campaign, they have reported significant time-lag measurements with various emission lines such as Hβ, Hα, C IV, and Mg II in ~120 AGN up to $z < 2.9$ (Shen et al. 2016; Grier et al. 2017, 2019; Homayouni et al. 2020). However, different redshift regimes are probed with different emission lines, e.g., Hβ is used to study the low-redshift population while C IV is typically used for high-redshift AGN. It is important to note that the different emission lines mark different ionization fronts in the BLR. Past studies have identified discrepancies between black hole mass measurements derived from Hβ at low redshifts and C IV at high redshifts (e.g., Denney 2012). To calibrate the scaling relations at different redshifts against each other, a large and uniform AGN sample in a wide redshift range is required. To plan such large-scale surveys, RM campaigns need to be optimized to maximize their science return. In Chapter 4, we illustrated how the AGN Survey Simulation (currently under development) can be used to optimize large-scale variability surveys with the *Cosmological Advanced Survey Telescope for Optical and ultraviolet Research* (CASTOR; Côté et al. 2019). We provide a brief summary of Chapter 4 below.

5.3 Summary of Chapter 4

We are designing an end-to-end survey simulation pipeline – the AGN Survey Simulation – to optimize large-scale variability surveys with next-generation telescope facilities. We presented the use of such a survey simulation for CASTOR. CASTOR is a Canadian flagship UV mission proposed to the Canadian Space Agency. It aims to perform photometric and spectroscopic surveys in three bands – *UV* (1500 Å–3000 Å), *u* (3000 Å–4000 Å), and *g* (4000 Å–5000 Å). A key science goal of CASTOR is to study the growth in supermassive black holes. To understand how supermassive black holes grow over time, we need to probe a wide range of the luminosity-redshift parameter space (*L*–*z*). The primary goal of AGN RM surveys with CASTOR is to derive black holes masses in more than a thousand AGN in a wide *L*–*z* space, and thus the need for the AGN Survey Simulation. The preliminary simulation design broadly comprises of different sets of modules that (1) simulate the AGN system behaviour, generating the "true" continuum and emission-line light curves; (2) simulate the telescope photometric and spectroscopic modules, generating the observed continuum and emission-line light curves, and (3) perform cross-correlation analysis to ultimately derive black hole masses. The goal is to input a set of observational parameters that will be optimized by the simulation pipeline for a given mock sample of AGN, thus providing optimal parameters for an RM survey.

We presented illustrations of the AGN Survey Simulation deliverables – how length of RM campaigns will depend on the luminosities and redshifts probed, and how cadence will depend on the observed variability in AGN at different luminosities. For campaign length, we inferred that longer campaigns are required in general to survey high-redshift, high-luminosity AGN as compared to the low-redshift, low-luminosity population. For cadence, shorter cadences (more frequent observations) are required to detect sufficient variability in low-luminosity AGN, while longer cadences can detect variability in high-luminosity objects that vary on longer timescales. Given the goal of probing a wide *L*–*z* space with CASTOR AGN RM surveys, a single cadence is likely not sufficient – variable cadence throughout the campaign may be optimal. The AGN Survey Simulation can basically be employed to derive such survey specifications while considering various observing constraints. We also discussed limitations of the simulation pipeline considering the functions performed by each of the modules and the inputs supplied to the modules. One of the primary roadblocks for the AGN Survey Simulation is the design of the CASTOR grism, which is still under development. With more inputs on the grism specifications from CASTOR industry partners, we aim to further develop the spectroscopy module in the simulation design. Planned developments to the AGN Survey Simulation are underway, and we hope to make significant progress during the current phase of CASTOR science development study.

5.4 Overall Summary

In a nutshell, RM is a powerful tool to study the structure and kinematics in AGN that are otherwise unresolved through telescopes. In Chapter 2, we first applied RM to determine a UV time lag in a super-Eddington AGN, Mrk 142, for the first time, with simultaneous monitoring of the continuum and the BLR. Chapter 2 allowed us to penetrate into (1) the intricate details of the available data at two different spectral resolutions, and (2) the rigorous process of RM

analysis, to perform an in-depth study of a special case AGN. In Chapter 3, we addressed how low spectral resolution can affect FWHM measurements of narrower broad emission-line profiles – a point that is critical to consider in order to obtain reliable black hole masses through RM. Chapter 3 enabled us to explore the challenge we faced in Chapter 2, from working with spectra at different resolutions, for a specific class of AGN. Capitalizing on the knowledge of RM and its requirements from Chapters 2 and 3, we illustrated in Chapter 4 how the AGN Survey Simulation can be used to optimize AGN RM surveys with CASTOR. RM has been successfully applied to ~250 AGN to date, and the size and quality of data continue to improve. Looking towards the future, the AGN Survey Simulation can bear promising results for large-scale AGN variability surveys with next-generation telescope facilities.

In this thesis, we started on a *micro* scale – focusing on a specific AGN, moved to a *medium* scale – discussing emission-line measurements for a class of AGN, and progressed towards the *macro* – introducing how AGN RM science can grow in the future.

Bibliography

Abazajian, K. N., Adelman-McCarthy, J. K., Agüeros, M. A., et al. 2009, The Seventh Data Release of the Sloan Digital Sky Survey, *ApJS*, 182, 543

Abramowicz, M. A., Czerny, B., Lasota, J. P., & Szuszkiewicz, E. 1988, Slim Accretion Disks, *ApJ*, 332, 646

Baldwin, J., Ferland, G., Korista, K., & Verner, D. 1995, Locally Optimally Emitting Clouds and the Origin of Quasar Emission Lines, *ApJL*, 455, L119

Barth, A. J., Pancoast, A., Bennert, V. N., et al. 2013, The Lick AGN Monitoring Project 2011: Fe II Reverberation from the Outer Broad-line Region, *ApJ*, 769, 128

Barvainis, R. 1990, On the optical-to-far-infrared spectral energy distributions of radio-quiet quasars, *ApJ*, 353, 419

Begelman, M. C. 2002, Super-Eddington Fluxes from Thin Accretion Disks?, *ApJL*, 568, L97

Bentz, M. C., & Katz, S. 2015, The AGN Black Hole Mass Database, *PASP*, 127, 67

Bentz, M. C., Peterson, B. M., Netzer, H., Pogge, R. W., & Vestergaard, M. 2009a, The Radius-Luminosity Relationship for Active Galactic Nuclei: The Effect of Host-Galaxy Starlight on Luminosity Measurements. II. The Full Sample of Reverberation-Mapped AGNs, *ApJ*, 697, 160

Bentz, M. C., Denney, K. D., Cackett, E. M., et al. 2006, A Reverberation-based Mass for the Central Black Hole in NGC 4151, *ApJ*, 651, 775

—. 2007, NGC 5548 in a Low-Luminosity State: Implications for the Broad-Line Region, *ApJ*, 662, 205

Bentz, M. C., Walsh, J. L., Barth, A. J., et al. 2009b, The Lick AGN Monitoring Project: Broad-line Region Radii and Black Hole Masses from Reverberation Mapping of Hβ, *ApJ*, 705, 199

Bentz, M. C., Horne, K., Barth, A. J., et al. 2010a, The Lick AGN Monitoring Project: Velocity-delay Maps from the Maximum-entropy Method for Arp 151, *ApJL*, 720, L46

Bentz, M. C., Walsh, J. L., Barth, A. J., et al. 2010b, The Lick AGN Monitoring Project: Reverberation Mapping of Optical Hydrogen and Helium Recombination Lines, *ApJ*, 716, 993

Bentz, M. C., Denney, K. D., Grier, C. J., et al. 2013, The Low-luminosity End of the Radius-Luminosity Relationship for Active Galactic Nuclei, *ApJ*, 767, 149

Bentz, M. C., Horenstein, D., Bazhaw, C., et al. 2014, The Mass of the Central Black Hole in the Nearby Seyfert Galaxy NGC 5273, *ApJ*, 796, 8

Bian, W.-H., Hu, C., Gu, Q.-S., & Wang, J.-M. 2008, A note on black hole masses estimated by the second moment in narrow-line Seyfert 1 Galaxies, *MNRAS*, 390, 752

Blandford, R. D., & McKee, C. F. 1982, Reverberation mapping of the emission line regions of Seyfert galaxies and quasars, *ApJ*, 255, 419

Boksenberg, A., Snijders, M. A. J., Wilson, R., et al. 1978, IUE observations of extragalactic objects, *Nature*, 275, 404

Boller, T., Brandt, W. N., & Fink, H. 1996, Soft X-ray properties of narrow-line Seyfert 1 galaxies., *A&A*, 305, 53

Boroson, T. A., & Green, R. F. 1992, The Emission-Line Properties of Low-Redshift Quasi-stellar Objects, *ApJS*, 80, 109

Brandt, W. N., & Alexander, D. M. 2010, Supermassive black-hole growth over cosmic time: Active galaxy demography, physics, and ecology from Chandra surveys, Proceedings of the National Academy of Science, 107, 7184

Bruzual, G., & Charlot, S. 2003, Stellar population synthesis at the resolution of 2003, *MNRAS*, 344, 1000

Cackett, E. M., Bentz, M. C., & Kara, E. 2021, Reverberation mapping of active galactic nuclei: From X-ray corona to dusty torus, iScience, 24, 102557. https://www.sciencedirect.com/science/article/pii/S2589004221005253

Cackett, E. M., Horne, K., & Winkler, H. 2007, Testing thermal reprocessing in active galactic nuclei accretion discs, *MNRAS*, 380, 669

Cackett, E. M., Gelbord, J., Li, Y.-R., et al. 2020, Supermassive Black Holes with High Accretion Rates in Active Galactic Nuclei. XI. Accretion Disk Reverberation Mapping of Mrk 142, *ApJ*, 896, 1

Charlton, J., & Churchill, C. 2000, Quasistellar Objects: Intervening Absorption Lines, ed. P. Murdin, doi:10.1888/0333750888/2366

Chiu, H.-Y. 1964, Gravitational collapse, Physics Today, 17, 21. http://dx.doi.org/10.1063/1.3051610

Clavel, J., Reichert, G. A., Alloin, D., et al. 1991, Steps toward determination of the size and structure of the broad-line region in active galactic nuclei. I - an 8 month campaign of monitoring NGC 5548 with IUE, *ApJ*, 366, 64

Collier, S., & Peterson, B. M. 2001, Characteristic Ultraviolet/Optical Timescales in Active Galactic Nuclei, *ApJ*, 555, 775

Collier, S. J., Horne, K., Kaspi, S., et al. 1998, Steps toward Determination of the Size and Structure of the Broad-Line Region in Active Galactic Nuclei. XIV. Intensive Optical Spectrophotometric Observations of NGC 7469, *ApJ*, 500, 162

Collin, S., Kawaguchi, T., Peterson, B. M., & Vestergaard, M. 2006, Systematic effects in measurement of black hole masses by emission-line reverberation of active galactic nuclei: Eddington ratio and inclination, *A&A*, 456, 75

Côté, P., Abraham, B., Balogh, M., et al. 2019, CASTOR: A Flagship Canadian Space Telescope, Zenodo, white paper identifier W018, doi:10.5281/zenodo.3758463. `https://doi.org/10.5281/zenodo.3758463`

Czerny, B., Olejak, A., Rałowski, M., et al. 2019, Time Delay Measurement of Mg II Line in CTS C30.10 with SALT, *ApJ*, 880, 46

Dalla Bontà, E., Peterson, B. M., Bentz, M. C., et al. 2020, The Sloan Digital Sky Survey Reverberation Mapping Project: Estimating Masses of Black Holes in Quasars with Single-epoch Spectroscopy, *ApJ*, 903, 112

De Rosa, G., Peterson, B. M., Ely, J., et al. 2015, Space Telescope and Optical Reverberation Mapping Project.I. Ultraviolet Observations of the Seyfert 1 Galaxy NGC 5548 with the Cosmic Origins Spectrograph on Hubble Space Telescope, *ApJ*, 806, 128

Denney, K. D. 2012, Are Outflows Biasing Single-epoch C IV Black Hole Mass Estimates?, *ApJ*, 759, 44

Denney, K. D., Pogge, R. W., Assef, R. J., et al. 2013, C IV Line-width Anomalies: The Perils of Low Signal-to-noise Spectra, *ApJ*, 775, 60

Denney, K. D., Bentz, M. C., Peterson, B. M., et al. 2006, The Mass of the Black Hole in the Seyfert 1 Galaxy NGC 4593 from Reverberation Mapping, *ApJ*, 653, 152

Denney, K. D., Peterson, B. M., Pogge, R. W., et al. 2010, Reverberation Mapping Measurements of Black Hole Masses in Six Local Seyfert Galaxies, *ApJ*, 721, 715

Denney, K. D., Horne, K., Shen, Y., et al. 2016, The Sloan Digital Sky Survey Reverberation Mapping Project: An Investigation of Biases in C IV Emission Line Properties, *ApJS*, 224, 14

Dietrich, M., Kollatschny, W., Peterson, B. M., et al. 1993, Steps toward determination of the size and structure of the broad-line region in active galactic nuclei. IV - Intensity variations of the optical emission lines of NGC 5548, *ApJ*, 408, 416

Dietrich, M., Peterson, B. M., Albrecht, P., et al. 1998, Steps toward Determination of the Size and Structure of the Broad-Line Region in Active Galactic Nuclei. XII. Ground-based Monitoring of 3C 390.3, *ApJS*, 115, 185

Dietrich, M., Peterson, B. M., Grier, C. J., et al. 2012, Optical Monitoring of the Broad-line Radio Galaxy 3C 390.3, *ApJ*, 757, 53

Donnan, F. R., Horne, K., & Hernández Santisteban, J. V. 2021, Bayesian analysis of quasar light curves with a running optimal average: new time delay measurements of COSMOGRAIL gravitationally lensed quasars, *MNRAS*, 508, 5449

Du, P., Hu, C., Lu, K.-X., et al. 2014, Supermassive Black Holes with High Accretion Rates in Active Galactic Nuclei. I. First Results from a New Reverberation Mapping Campaign, *ApJ*, 782, 45

—. 2015, Supermassive Black Holes with High Accretion Rates in Active Galactic Nuclei. IV. Hβ Time Lags and Implications for Super-Eddington Accretion, *ApJ*, 806, 22

Du, P., Lu, K.-X., Hu, C., et al. 2016a, Supermassive Black Holes with High Accretion Rates in Active Galactic Nuclei. VI. Velocity-resolved Reverberation Mapping of the Hβ Line, *ApJ*, 820, 27

Du, P., Lu, K.-X., Zhang, Z.-X., et al. 2016b, Supermassive Black Holes with High Accretion Rates in Active Galactic Nuclei. V. A New Size-Luminosity Scaling Relation for the Broad-line Region, *ApJ*, 825, 126

Du, P., Zhang, Z.-X., Wang, K., et al. 2018, Supermassive Black Holes with High Accretion Rates in Active Galactic Nuclei. IX. 10 New Observations of Reverberation Mapping and Shortened Hβ Lags, *ApJ*, 856, 6

Edelson, R., Gelbord, J. M., Horne, K., et al. 2015, Space Telescope and Optical Reverberation Mapping Project. II. Swift and HST Reverberation Mapping of the Accretion Disk of NGC 5548, *ApJ*, 806, 129

Edelson, R., Gelbord, J., Cackett, E., et al. 2019, The First Swift Intensive AGN Accretion Disk Reverberation Mapping Survey, *ApJ*, 870, 123

Elvis, M., Wilkes, B. J., McDowell, J. C., et al. 1994, Atlas of quasar energy distributions, *ApJS*, 95, 1

Eser, E. K., Vestergaard, M., Peterson, B. M., Denney, K. D., & Bentz, M. C. 2015, ON THE SCATTER IN THE RADIUS-LUMINOSITY RELATIONSHIP FOR ACTIVE GALACTIC NUCLEI, The Astrophysical Journal, 801, 8. https://doi.org/10.1088/0004-637x/801/1/8

Fausnaugh, M. M., Denney, K. D., Barth, A. J., et al. 2016, Space Telescope and Optical Reverberation Mapping Project. III. Optical Continuum Emission and Broadband Time Delays in NGC 5548, *ApJ*, 821, 56

Ferrarese, L., & Ford, H. 2005, Supermassive Black Holes in Galactic Nuclei: Past, Present and Future Research, *SSRv*, 116, 523

Ferrarese, L., & Merritt, D. 2000, A Fundamental Relation between Supermassive Black Holes and Their Host Galaxies, *ApJL*, 539, L9

Ferrarese, L., Pogge, R. W., Peterson, B. M., et al. 2001, Supermassive Black Holes in Active Galactic Nuclei. I. The Consistency of Black Hole Masses in Quiescent and Active Galaxies, *ApJL*, 555, L79

Fonseca Alvarez, G., Trump, J. R., Homayouni, Y., et al. 2020, The Sloan Digital Sky Survey Reverberation Mapping Project: The Hβ Radius-Luminosity Relation, *ApJ*, 899, 73

Freeman, P., Doe, S., & Siemiginowska, A. 2001, in Society of Photo-Optical Instrumentation Engineers (SPIE) Conference Series, Vol. 4477, Astronomical Data Analysis, ed. J.-L. Starck & F. D. Murtagh, 76–87

Gallagher, S. C., & Everett, J. E. 2007, in Astronomical Society of the Pacific Conference Series, Vol. 373, The Central Engine of Active Galactic Nuclei, ed. L. C. Ho & J.-W. Wang, 305

Gaskell, C. M., & Peterson, B. M. 1987, The Accuracy of Cross-Correlation Estimates of Quasar Emission-Line Region Sizes, *ApJS*, 65, 1

Gaskell, C. M., & Sparke, L. S. 1986, Line Variations in Quasars and Seyfert Galaxies, *ApJ*, 305, 175

Goad, M. R., Korista, K. T., De Rosa, G., et al. 2016, Space Telescope and Optical Reverberation Mapping Project. IV. Anomalous Behavior of the Broad Ultraviolet Emission Lines in NGC 5548, *ApJ*, 824, 11

Grier, C. J., Peterson, B. M., Pogge, R. W., et al. 2012, Reverberation Mapping Results for Five Seyfert 1 Galaxies, *ApJ*, 755, 60

Grier, C. J., Peterson, B. M., Horne, K., et al. 2013a, The Structure of the Broad-line Region in Active Galactic Nuclei. I. Reconstructed Velocity-delay Maps, *ApJ*, 764, 47

Grier, C. J., Martini, P., Watson, L. C., et al. 2013b, Stellar Velocity Dispersion Measurements in High-luminosity Quasar Hosts and Implications for the AGN Black Hole Mass Scale, *ApJ*, 773, 90

Grier, C. J., Trump, J. R., Shen, Y., et al. 2017, The Sloan Digital Sky Survey Reverberation Mapping Project: Hα and Hβ Reverberation Measurements from First-year Spectroscopy and Photometry, *ApJ*, 851, 21

Grier, C. J., Shen, Y., Horne, K., et al. 2019, The Sloan Digital Sky Survey Reverberation Mapping Project: Initial C IV Lag Results from Four Years of Data, *ApJ*, 887, 38

Hinshaw, G., Larson, D., Komatsu, E., et al. 2013, Nine-year Wilkinson Microwave Anisotropy Probe (WMAP) Observations: Cosmological Parameter Results, *ApJS*, 208, 19

Hogg, D. W., Baldry, I. K., Blanton, M. R., & Eisenstein, D. J. 2002, The K correction, arXiv e-prints, astro

Homayouni, Y., Trump, J. R., Grier, C. J., et al. 2019, The Sloan Digital Sky Survey Reverberation Mapping Project: Accretion Disk Sizes from Continuum Lags, *ApJ*, 880, 126

—. 2020, The Sloan Digital Sky Survey Reverberation Mapping Project: Mg II Lag Results from Four Years of Monitoring, *ApJ*, 901, 55

Homayouni, Y., Sturm, M. R., Trump, J. R., et al. 2022, The Sloan Digital Sky Survey Reverberation Mapping Project: UV-Optical Accretion Disk Measurements with the Hubble Space Telescope, *ApJ*, 926, 225

Hönig, S. F., & Kishimoto, M. 2017, Dusty Winds in Active Galactic Nuclei: Reconciling Observations with Models, *ApJL*, 838, L20

Hook, I. M., Jørgensen, I., Allington-Smith, J. R., et al. 2004, The Gemini-North Multi-Object Spectrograph: Performance in Imaging, Long-Slit, and Multi-Object Spectroscopic Modes, *PASP*, 116, 425

Hoormann, J. K., Martini, P., Davis, T. M., et al. 2019, C IV black hole mass measurements with the Australian Dark Energy Survey (OzDES), *MNRAS*, 487, 3650

Horne, K. 1999, in Astronomical Society of the Pacific Conference Series, Vol. 162, Quasars and Cosmology, ed. G. Ferland & J. Baldwin, 189

Horne, K., Peterson, B. M., Collier, S. J., & Netzer, H. 2004, Observational Requirements for High-Fidelity Reverberation Mapping, *PASP*, 116, 465

Horne, K., Welsh, W. F., & Peterson, B. M. 1991, Echo mapping of broad H-beta emission in NGC 5548, *ApJL*, 367, L5

Horne, K., De Rosa, G., Peterson, B. M., et al. 2021, Space Telescope and Optical Reverberation Mapping Project. IX. Velocity-Delay Maps for Broad Emission Lines in NGC 5548, *ApJ*, 907, 76

Hu, C., Du, P., Lu, K.-X., et al. 2015, Supermassive Black Holes with High Accretion Rates in Active Galactic Nuclei. III. Detection of Fe II Reverberation in Nine Narrow-line Seyfert 1 Galaxies, *ApJ*, 804, 138

Jackson, N., O'Brien, P. T., Goad, M., et al. 1992, Monitoring of active galactic nuclei. I - The quasars 1302 - 102 and 1217 + 023, *A&A*, 262, 17

Jaroszyński, M., Abramowicz, M. A., & Paczynski, B. 1980, Supercritical accretion disks around black holes, *AcA*, 30, 1

Just, D. W., Brandt, W. N., Shemmer, O., et al. 2007, The X-Ray Properties of the Most Luminous Quasars from the Sloan Digital Sky Survey, *ApJ*, 665, 1004

Kaspi, S., Brandt, W. N., Maoz, D., et al. 2007, Reverberation Mapping of High-Luminosity Quasars: First Results, *ApJ*, 659, 997

Kaspi, S., Maoz, D., Netzer, H., et al. 2005, The Relationship between Luminosity and Broad-Line Region Size in Active Galactic Nuclei, *ApJ*, 629, 61

Kaspi, S., & Netzer, H. 1999, Modeling Variable Emission Lines in Active Galactic Nuclei: Method and Application to NGC 5548, *ApJ*, 524, 71

Kaspi, S., Smith, P. S., Netzer, H., et al. 2000, Reverberation Measurements for 17 Quasars and the Size-Mass-Luminosity Relations in Active Galactic Nuclei, *ApJ*, 533, 631

Keck, M. L., Brenneman, L. W., Ballantyne, D. R., et al. 2015, NuSTAR and Suzaku X-ray Spectroscopy of NGC 4151: Evidence for Reflection from the Inner Accretion Disk, *ApJ*, 806, 149

Kelly, B. C., Bechtold, J., & Siemiginowska, A. 2009, Are the Variations in Quasar Optical Flux Driven by Thermal Fluctuations?, *ApJ*, 698, 895

Krolik, J. H. 1999, Active galactic nuclei : from the central black hole to the galactic environment

Krolik, J. H., Horne, K., Kallman, T. R., et al. 1991, Ultraviolet variability of NGC 5548 - Dynamics of the continuum production region and geometry of the broad-line region, *ApJ*, 371, 541

Kulkarni, G., Worseck, G., & Hennawi, J. F. 2019, Evolution of the AGN UV luminosity function from redshift 7.5, *MNRAS*, 488, 1035

Leighly, K. M. 2004, Hubble Space Telescope STIS Ultraviolet Spectral Evidence of Outflow in Extreme Narrow-Line Seyfert 1 Galaxies. II. Modeling and Interpretation, *ApJ*, 611, 125

Li, J., Shen, Y., Horne, K., et al. 2017, The Sloan Digital Sky Survey Reverberation Mapping Project: Composite Lags at z $\leq$ 1, *ApJ*, 846, 79

Lira, P., Kaspi, S., Netzer, H., et al. 2018, Reverberation Mapping of Luminous Quasars at High z, *ApJ*, 865, 56

Longair, M. S. 1994, High energy astrophysics. Volume 2. Stars, the Galaxy and the interstellar medium.

MacLeod, C. L., Ivezić, Ž., Kochanek, C. S., et al. 2010, Modeling the Time Variability of SDSS Stripe 82 Quasars as a Damped Random Walk, *ApJ*, 721, 1014

Magorrian, J., Tremaine, S., Richstone, D., et al. 1998, The Demography of Massive Dark Objects in Galaxy Centers, *AJ*, 115, 2285

Maoz, D. 1990, PhD thesis, Tel-Aviv Univ. (Israel).

Maoz, D., Netzer, H., Mazeh, T., et al. 1991, High-rate active galaxy monitoring at the Wise Observatory. III - The broad-line region of NGC 4151, *ApJ*, 367, 493

Maoz, D., Netzer, H., Peterson, B. M., et al. 1993, Variations of the ultraviolet Fe II and Balmer continuum emission in the Seyfert galaxy NGC 5548, *ApJ*, 404, 576

Mathur, S., Gupta, A., Page, K., et al. 2017, Space Telescope and Optical Reverberation Mapping Project. VII. Understanding the Ultraviolet Anomaly in NGC 5548 with X-Ray Spectroscopy, *ApJ*, 846, 55

Murray, N., Chiang, J., Grossman, S. A., & Voit, G. M. 1995, Accretion Disk Winds from Active Galactic Nuclei, *ApJ*, 451, 498

Netzer, H. 2013, The Physics and Evolution of Active Galactic Nuclei

Netzer, H., Maoz, D., Laor, A., et al. 1990, High-rate spectroscopic active galactic nucleus monitoring at the Wise Observatory. II - NGC 5548, *ApJ*, 353, 108

Osterbrock, D. E. 1978, Optical emission-line spectra of Seyfert galaxies and radio galaxies., Lick Observatory Bulletin, 774, 1

Osterbrock, D. E., Grandi, S. A., & Cohen, R. D. 1978, Spectra of Suspected Seyfert Galaxies, *PASP*, 90

Osterbrock, D. E., & Pogge, R. W. 1987, Optical Spectra of Narrow Emission Line Palomar-Green Galaxies, *ApJ*, 323, 108

Pancoast, A., Brewer, B. J., Treu, T., et al. 2014, Modelling reverberation mapping data - II. Dynamical modelling of the Lick AGN Monitoring Project 2008 data set, *MNRAS*, 445, 3073

Park, D., Woo, J.-H., Treu, T., et al. 2012, The Lick AGN Monitoring Project: Recalibrating Single-epoch Virial Black Hole Mass Estimates, *ApJ*, 747, 30

Pei, L., Barth, A. J., Aldering, G. S., et al. 2014, Reverberation Mapping of the KEPLER Field AGN KA1858+4850, *ApJ*, 795, 38

Pei, L., Fausnaugh, M. M., Barth, A. J., et al. 2017, Space Telescope and Optical Reverberation Mapping Project. V. Optical Spectroscopic Campaign and Emission-line Analysis for NGC 5548, *ApJ*, 837, 131

Penston, M. V. 1991, in Variability of Active Galactic Nuclei, ed. H. R. Miller & P. J. Wiita, 343

Penston, M. V., Boksenberg, A., Bromage, G. E., et al. 1981, Detailed observations of NGC 4151 with IUE. I - Low dispersion data up to 1979 January, *MNRAS*, 196, 857

Perola, G. C., Boksenberg, A., Bromage, G. E., et al. 1982, Detailed observations of NGC 4151 with IUE. II - Variability of the continuum from 1978 February to 1980 May, including X-ray and optical observations, *MNRAS*, 200, 293

Peterson, B. M. 1993, Reverberation mapping of active galactic nuclei, *PASP*, 105, 247

—. 1997, An Introduction to Active Galactic Nuclei

Peterson, B. M. 2006, in Astronomical Society of the Pacific Conference Series, Vol. 360, AGN Variability from X-Rays to Radio Waves, ed. C. M. Gaskell, I. M. McHardy, B. M. Peterson, & S. G. Sergeev, 191

—. 2009, Active galactic nuclei in the ultraviolet, *Ap&SS*, 320, 69

—. 2014, Measuring the Masses of Supermassive Black Holes, *SSRv*, 183, 253

Peterson, B. M., Foltz, C. B., Byard, P. L., & Wagner, R. M. 1982, Variability of the emission-line spectra and optical continua of Seyfert galaxies. I, *ApJS*, 49, 469

Peterson, B. M., & Horne, K. 2004, Echo mapping of active galactic nuclei, Astronomische Nachrichten, 325, 248

Peterson, B. M., Wanders, I., Bertram, R., et al. 1998, Optical Continuum and Emission-Line Variability of Seyfert 1 Galaxies, *ApJ*, 501, 82

Peterson, B. M., Balonek, T. J., Barker, E. S., et al. 1991, Steps toward determination of the size and structure of the broad-line region in active galactic nuclei. II - an intensive study of NGC 5548 at optical wavelengths, *ApJ*, 368, 119

Peterson, B. M., Berlind, P., Bertram, R., et al. 2002, Steps toward Determination of the Size and Structure of the Broad-Line Region in Active Galactic Nuclei. XVI. A 13 Year Study of Spectral Variability in NGC 5548, *ApJ*, 581, 197

Peterson, B. M., Ferrarese, L., Gilbert, K. M., et al. 2004, Central Masses and Broad-Line Region Sizes of Active Galactic Nuclei. II. A Homogeneous Analysis of a Large Reverberation-Mapping Database, *ApJ*, 613, 682

Peterson, B. M., Grier, C. J., Horne, K., et al. 2014, Reverberation Mapping of the Seyfert 1 Galaxy NGC 7469, *ApJ*, 795, 149

Planck Collaboration, Ade, P. A. R., Aghanim, N., et al. 2014, Planck 2013 results. XVI. Cosmological parameters, A&A, 571, A16. https://doi.org/10.1051/0004-6361/201321591

Polidan, R. S., & Peterson, B. M. 2001, in Astronomical Society of the Pacific Conference Series, Vol. 224, Probing the Physics of Active Galactic Nuclei, ed. B. M. Peterson, R. W. Pogge, & R. S. Polidan, 479

Press, W. H. 1978, Flicker noises in astronomy and elsewhere, Comments on Astrophysics, 7, 103

Proga, D., Stone, J. M., & Kallman, T. R. 2000, Dynamics of Line-driven Disk Winds in Active Galactic Nuclei, *ApJ*, 543, 686

Richards, G. T., Lacy, M., Storrie-Lombardi, L. J., et al. 2006, Spectral Energy Distributions and Multiwavelength Selection of Type 1 Quasars, *ApJS*, 166, 470

Romanishin, W., Balonek, T. J., Ciardullo, R., et al. 1995, The Galaxy Component and Nuclear Flux Measurements of NGC 5548 from Direct Imaging, *ApJ*, 455, 516

Santos-Lleó, M., Chatzichristou, E., de Oliveira, C. M., et al. 1997, Steps toward Determination of the Size and Structure of the Broad-Line Region in Active Galactic Nuclei. X. Variability of Fairall 9 from Optical Data, *ApJS*, 112, 271

Santos-Lleó, M., Clavel, J., Schulz, B., et al. 2001, Monitoring of the optical and 2.5-11.7 mu m spectrum and mid-IR imaging of the Seyfert 1 galaxy Mrk 279 with ISO, *A&A*, 369, 57

Schlafly, E. F., & Finkbeiner, D. P. 2011, Measuring Reddening with Sloan Digital Sky Survey Stellar Spectra and Recalibrating SFD, *ApJ*, 737, 103

Schmidt, M. 1963, 3C 273 : A Star-Like Object with Large Red-Shift, *Nature*, 197, 1040

—. 1969, Quasistellar Objects, *ARA&A*, 7, 527

Seyfert, C. K. 1943, Nuclear Emission in Spiral Nebulae., *ApJ*, 97, 28

Shakura, N. I., & Sunyaev, R. A. 1973, Black holes in binary systems. Observational appearance., *A&A*, 24, 337

Shang, Z., Brotherton, M. S., Wills, B. J., et al. 2011, The Next Generation Atlas of Quasar Spectral Energy Distributions from Radio to X-Rays, *ApJS*, 196, 2

Shen, X., Hopkins, P. F., Faucher-Giguère, C.-A., et al. 2020, The bolometric quasar luminosity function at z = 0-7, *MNRAS*, 495, 3252

Shen, Y., Richards, G. T., Strauss, M. A., et al. 2011, A CATALOG OF QUASAR PROPERTIES FROM SLOAN DIGITAL SKY SURVEY DATA RELEASE 7, The Astrophysical Journal Supplement Series, 194, 45. https://doi.org/10.1088/0067-0049/194/2/45

Shen, Y., Brandt, W. N., Dawson, K. S., et al. 2015, The Sloan Digital Sky Survey Reverberation Mapping Project: Technical Overview, *ApJS*, 216, 4

Shen, Y., Horne, K., Grier, C. J., et al. 2016, The Sloan Digital Sky Survey Reverberation Mapping Project: First Broad-line Hβ and Mg II Lags at z $\gtrsim$ 0.3 from Six-month Spectroscopy, *ApJ*, 818, 30

Siebenmorgen, R., Haas, M., Kruegel, E., & Schulz, B. 2005, Discovery of 10 Mu.m silicate emission in quasars. - Evidence of the AGN unification scheme., Astronomische Nachrichten, 326, 556

Silk, J., & Rees, M. J. 1998, Quasars and galaxy formation, *A&A*, 331, L1

Stirpe, G. M., Winge, C., Altieri, B., et al. 1994, Steps toward Determination of the Size and Structure of the Broad-Line Region in Active Galactic Nuclei. VI. Variability of NGC 3783 from Ground-based Data, *ApJ*, 425, 609

Sun, M., Trump, J. R., Shen, Y., et al. 2015, The Sloan Digital Sky Survey Reverberation Mapping Project: Ensemble Spectroscopic Variability of Quasar Broad Emission Lines, *ApJ*, 811, 42

Tananbaum, H., Avni, Y., Branduardi, G., et al. 1979, X-ray studies of quasars with the Einstein Observatory., *ApJL*, 234, L9

Trèvese, D., Kron, R. G., & Bunone, A. 2001, Continuum Variability of Active Galactic Nuclei in the Optical-Ultraviolet Range, *ApJ*, 551, 103

Trevese, D., Perna, M., Vagnetti, F., Saturni, F. G., & Dadina, M. 2014, C IV and C III] Reverberation Mapping of the Luminous Quasar PG 1247+267, *ApJ*, 795, 164

U, V., Barth, A. J., Vogler, H. A., et al. 2022, The Lick AGN Monitoring Project 2016: Velocity-resolved Hβ Lags in Luminous Seyfert Galaxies, *ApJ*, 925, 52

Ulrich, M. H., Boksenberg, A., Bromage, G. E., et al. 1984, Detailed observations of NGC 4151 with IUE. III - Variability of the strong emission lines from 1978 February to 1980 May, *MNRAS*, 206, 221

Vanden Berk, D. E., Richards, G. T., Bauer, A., et al. 2001, Composite Quasar Spectra from the Sloan Digital Sky Survey, *AJ*, 122, 549

Véron-Cetty, M. P., Véron, P., & Gonçalves, A. C. 2001, A spectrophotometric atlas of Narrow-Line Seyfert 1 galaxies, *A&A*, 372, 730

Wanders, I., van Groningen, E., Alloin, D., et al. 1993, Spectroscopic monitoring of active galactic nuclei. II - The Seyfert-1 galaxy NGC 3516, *A&A*, 269, 39

Wang, C.-J., Bai, J.-M., Fan, Y.-F., et al. 2019, Lijiang 2.4-meter Telescope and its instruments, Research in Astronomy and Astrophysics, 19, 149. https://doi.org/10.1088/1674-4527/19/10/149

Wang, F., Yang, J., Fan, X., et al. 2021, A Luminous Quasar at Redshift 7.642, The Astrophysical Journal Letters, 907, L1. https://doi.org/10.3847/2041-8213/abd8c6

Wang, J.-M., Qiu, J., Du, P., & Ho, L. C. 2014a, Self-shadowing Effects of Slim Accretion Disks in Active Galactic Nuclei: The Diverse Appearance of the Broad-line Region, *ApJ*, 797, 65

Wang, J.-M., Du, P., Hu, C., et al. 2014b, Supermassive Black Holes with High Accretion Rates in Active Galactic Nuclei. II. The Most Luminous Standard Candles in the Universe, *ApJ*, 793, 108

Weymann, R. J., Morris, S. L., Foltz, C. B., & Hewett, P. C. 1991, Comparisons of the emission-line and continuum properties of broad absorption line and normal quasi-stellar objects, *ApJ*, 373, 23

White, R. J., & Peterson, B. M. 1994, Comments on cross-correlation methodology in variability studies of active galactic nuclei, *PASP*, 106, 879

Wilson, A. S., & Colbert, E. J. M. 1995, The difference between radio-loud and radio-quiet active galaxies, *ApJ*, 438, 62

Zu, Y., Kochanek, C. S., Kozłowski, S., & Udalski, A. 2013, Is Quasar Optical Variability a Damped Random Walk?, *ApJ*, 765, 106

Zu, Y., Kochanek, C. S., & Peterson, B. M. 2011, An Alternative Approach to Measuring Reverberation Lags in Active Galactic Nuclei, *ApJ*, 735, 80

Appendix A

Gemini Spectral Reduction - Special Cases

This section describes the the special cases from the spectral reduction of the Mrk 142 Gemini Spectra that were either treated differently or discarded due to calibration issues.

- Epoch 11 narrow-slit standard star spectra: The extracted spectrum from exposure 1 appeared to drop in flux and flatten shorter than (blueward of) ~4740 Å, whereas the exposure 2 spectrum was flat on both ends. While it was possible to recover the flat region of exposure 1 spectrum spectrum, the one from exposure 2 was not suitable for further analysis and hence was discarded. Because the shape of the spectrum blueward of ~4740 Å was not evident from the exposure 2 spectrum, we recovered the region from ~4520 Å to ~4740 Å with reference to the mean wide-slit standard star spectrum (used as the reference to correct for slit losses). Consequently, only the region longer than (redward of) ~4740 Å was corrected for slit losses with the spline fitting procedure. The former and the latter were then concatenated to obtain *only one* slitloss-corrected spectrum for epoch 11 from exposure 1. Note that the standard star spectrum from exposure 1 was later used to calibrate the narrow-slit science spectrum from exposure 2.

- Epoch 11, exposure 1 wide-slit standard star spectrum: Two bumps with bad data were recovered redward of ~5900 Å with reference to the spectrum from exposure 2. However, the recoverey is not reliable as the two spectra had slightly different count levels.

- Discarded wide-slit standard star spectra: The wide-slit standard star spectra from exposures 1, 1, and 2 of epochs 21, 22, and 25, respectively, showed bump-like features, which could not be recovered as the standard star spectra from the other exposure of the same epochs had different count levels. Therefore, the epochs/exposures listed here were discarded.

- Correction of affected pixels or recovery of bump-like regions on or close to the emission lines of interest: A few science spectra showed bumpy features on or close to the emission lines of interest, He I λ5877 and Hβ λ4861. We attempted to recover the "true" shape of such regions with reference to the other exposure taken with the same slit on the same night. In most cases, the two exposures had similar count levels. However, spectral measurements from the recovered spectra with different count levels are less reliable and must be considered carefully. Following is the list of the specific cases.

Epoch 13, exposure 2 narrow-slit spectrum: A large, downward bump with bad data from ~5545 Å till the red wing of the He I emission line was recovered with reference to the exposure 1 spectrum. Spectra from both exposures had similar count levels.

Epoch 16 narrow-slit spectra: Spectra from both exposures showed partially overlapping bump-like features in the region blueward of the Hβ emission line. Because neither of the exposures could be used to recover the shape of the spectrum in the affected region, we recovered the shapes of both the spectra with reference to the mean mean wide-slit science spectrum (used as the reference to correct for slit losses). In the exposure 2 spectrum, the recovery extended till the blue wing of Hβ. Spectra from both exposures had similar count levels.

Epoch 21, exposure 2 narrow-slit spectrum: The bumpy region from ~4325 Å to ~4740 Å was recovered with reference to exposure 1 with similar count levels. The recovered region extended till the tail end of the blue wing of Hβ.

Epoch 27, exposure 1 narrow-slit spectrum: A small bumpy region from till the blue wing of Hβ was recovered with reference to exposure 2 with similar count levels.

Epoch 28, exposure 1 narrow-slit spectrum: A 17-pixel wide region residual from sky subtraction on the blue wing of Hβ was replaced by simulated data values after linear interpolation in that region. However, this correction was affecting Hβ line measurements and hence was excluded from the analysis.

Epoch 30 narrow-slit spectra: Spectra from both exposures showed overlapping bump-like features in the region from ~4370 Å to ~4685 Å that were recovered with reference to the mean wide-slit science spectrum. In the exposure 1 spectrum, another bumpy feature from the red wing of the [O III] emission line at ~5008 Å was recovered with reference to the exposure 2 spectrum with similar count levels.

Epoch 3, exposure 1 wide-slit spectrum: A bumpy feature on the blue wing of the He I line was recovered with reference to the exposure 2 spectrum, where both spectra had similar count levels. This is one of the brighter wide-slit spectra. However, it was not used to generate the mean wide-slit spectrum for slitloss correction.

Epoch 11, exposure 1 wide-slit spectrum: A spike, possibly residual of sky subtraction, on the blue side of the [O III] peak at ~5008 Å was replaced by simulated data after linear interpolation in the affected region.

Epoch 14, exposure 2 wide-slit spectrum: A huge bump-like feature with bad data was replaced by simulated data after linear interpolation till the blue wing of Hβ.

Epoch 24, exposure 2 wide-slit spectrum: A huge bump with bad data extended from the region blueward of the He I line till the red end of the line. This affected region was recovered with reference to the exposure 1 spectrum, which was at slightly lower count levels than the exposure 2 spectrum.

Epoch 32, exposure 2 wide-slit spectrum: A bump-like feature from blueward region of the He I line till the blue side of the He I peak was recovered with reference to the exposure 1 spectrum. Spectra from both exposures had similar count levels.

- Epoch 25, exposure 2 narrow-slit science spectrum: The region on the blue side of He I λ5877 emission line shows a large bumpy feature with bad data. Because the region redward of ~5320 Å has lower count levels overall as compared to the spectrum from exposure 1, the affected region in spectrum 2 was not recovered. Therefore, this exposure was discarded.

- Epoch 22, exposure 2 wide-slit science spectrum: The red end of the spectrum from ~6320 Å to ~6400 Å was recovered with reference to the spectrum from exposure 1. However, the exposure 2 spectrum had slightly higher count levels than exposure 1.

Appendix B

Preparing Data for PrepSpec – GitHub Repository

This section describes the GitHub repository containing the Python v3.6.5 scripts developed to perform corrections to one-dimensional spectra required before modelling the spectra with PrepSpec. Because PrepSpec is not designed to handle spikes in data (e.g., due to cosmic rays) and gap regions (e.g., detector gaps in the Mrk 142 Gemini data), we need to remove such features prior to processing the spectra through PrepSpec. The GitHub repository, which will be made publicly available (Khatu et al., in prep.), contains the following scripts.

- selectSpectralRegion.py: Selects a region of the spectra specified by shorter (blue) and longer (red) wavelength bounds or lower and upper pixel bounds.
- recoverCurveShapes.py: Recovers the region of the spectra specified by blue and red wavelength bounds or lower and upper pixel bounds by estimating the shape of reference spectra.
- correctAffectedPixels.py: Corrects undesirable artefacts in pixel regions specified by the user for each spectrum by either replacing the affected pixels with median values or linearly interpolating in the affected regions and replacing interpolated values with simulated data assuming Gaussian distribution of errors. This script runs interactively with user inputs required for all spectra.
- correctSlitlosses.py: Corrects flux losses in narrow-slit spectra using wide-slit reference spectra taken on the same night. This script requires the Image Reduction and Analysis Facility with Python wrapper (PyRAF) environment for execution of the curfit task non-interactively. The interactive mode of curfit may not work on all systems as is therefore turned off.

The above four scripts read their inputs from a configuration file – a text file containing input parameters organized in separate sections for each of the scripts. The user can simply modify parameters in the configuration file to execute the scripts for different data sets without having to interact with the code in the scripts. The default parameter settings in the configuration file are applicable for the example data set of Mrk 142 Gemini spectra used in this work.

The example spectra will also be made available in the remote repository. Inputs and outputs for all scripts will be described in the repository.

To use the scripts with the example spectra, simply download the repository and run the scripts in a Python environment except the script for slitloss correction which needs a PyRAF environment. To run the scripts with other data, modify the parameters in the configuration file as required for the new data set.

Appendix C

PrepSpec User Manual

C.1 Introduction

PrepSpec[1] (developer: K. Horne) is a spectral analysis software that fits the continuum and emission lines in the input spectra with a composite model through an iterative process while correcting for any relative deviations in the calibrated wavelength and flux scales of the spectra. It outputs the model fits and the aligned spectra after correcting for the discrepancies in the relative wavelength and flux scales. Processing spectra through PrepSpec becomes important while analyzing variability in the light output from astronomical objects. An example of such a program is reverberation-mapping (RM) study of active galactic nuclei (AGN), where velocity line profiles of specific emission lines are measured from spectral data to determine changes in flux over a period of time. Measuring subtle changes in fluxes requires the spectra to be free of variations from relative differences in calibration processes, as much as possible.

In this manual, we use the long-slit, optical spectra of Markarian 142 (Mrk 142), a super-Eddington AGN in the local universe (redshift, $z = 0.045$), taken with the Gemini Multi-Object Spectrograph (GMOS) on the Gemini North Telescope (Gemini). The target was observed in two different configurations – B600 grating and two slits, 0.75″ (narrow slit) and 5.00″ (wide slit) – along with the comparison star (calibration star) in the same slit for accurate spectrophotometric calibration. In the long-slit mode, two chip gaps of the GMOS detector appear in the spectra. Data were collected from February through June 2019 for 33 epochs with two exposures in each configuration every night. The original purpose of the Mrk 142 Gemini campaign was to perform velocity-resolved reverberation mapping to probe the structure of the broad-line region (BLR) in a super-Eddington AGN system and hence the need for the narrow-slit data. However, due to insufficient data, we revised the aim to only determining an ultraviolet (UV) time lag for Hβ λ4861 emission with concurrent photometric observations in the UV. The wide-slit data were used to correct for potential slit losses from the narrow slit. To achieve the science goal of the campaign, we processed the narrow-slit spectra through PrepSpec to obtain accurate flux measurements for the target. In what follows, we demonstrate the use of PrepSpec for the Mrk 142 RM data set (hereafter, "this work" or "example data set").

PrepSpec comes with several dependencies. The code is written in FORTRAN and hence

[1]Find current version of PrepSpec at PrepSpec link.

needs a FORTRAN compiler (gfortran, ifort, gcc, g77, or ifort). The recommended one is ifort as it compiles faster than the others and has the advantage of using -parallel switch that allows tuning the code on multiple cores with less efforts. PrepSpec uses PGPLOT for graphing purposes.

The following input files are required for PrepSpec in the same directory as the code.

1. Wavelength- and flux-calibrated one-dimensional (1D) spectra files: ASCII files of calibrated spectra, with three columns – wavelength [Å], flux density, 1σ (where, σ is the standard deviation) error bars on flux density.

2. Timing file: ASCII file with two columns – filenames of the input spectra, Heliocentric Julian Date[2] (HJD). In this work, HJD values were calculated with the HJD calculator developed by the British Astronomical Association.

C.2 Installation

PrepSpec package contains the following four files.

1. *prepspec.for*: This is the main program that contains PrepSpec routines.

2. *misc.for*: This program contains all sub-routines that are used by *prepspec.for*.

3. *prepspec.exe*: This programs contains the executable file to run PrepSpec.

4. *prepspec.com*: This program contains commands that compile and link the code to generate the *prepspec.exe* file. It is required to generate a new *prepspec.com* file if the default one made available with the code is incompatible with the system. To generate *prepspec.exe*, in a Terminal window, change directory to the location of the software on the system and run `source prepspec.com`.

C.3 Preparing Your Data for PrepSpec

To prepare data for PrepSpec, the user must bear in mind the following points.

1. Input spectra are wavelength and flux calibrated: PrepSpec is specially designed to correct for shifts in wavelength and flux scales of calibrated spectra. Therefore, the input spectra must be wavelength and flux calibrated to approximately close wavelength and flux scales. Significant differences in wavelength solutions or flux levels likely indicate calibration issues that must be resolved before supplying spectra to PrepSpec. Similarly, no flux or saturated values (e.g., due to cosmic-ray hits or bad pixels) result in outliers in spectra and affect the modelling process in PrepSpec. Such outliers can be typically removed by using sigma-clipping algorithms during spectral reduction. Accurate spectrophotometric calibration is desirable for the input spectra and can be achieved

[2]Heliocentric Julian Date is the Julian Date of a given observation calculated by regarding that the observation was done from the centre of the Sun and is typically calculated by a computer.

by capturing a given calibration standard star in the same slit as the target. Target and calibration star in the same slit also allows optimal correction of slit losses if spectra were taken with narrow slits (see discussion on slitloss correction for Mrk 142 example spectra in this section).

2. Input spectra have no gap regions: One caveat is that PrepSpec is not currently designed to handle gaps in spectra. Therefore, chip gaps or regions with no data cause issues during modelling in PrepSpec. The GMOS detector gaps in the example data set were replaced by median or simulated flux values (see discussion on simulated data below) before supplying them to PrepSpec. We recognize that replacement with simulated data is not ideal as it introduces information that is not original to the data. However, using simulated data was the only possible fix to the chip gaps in the Mrk 142 spectra. An appropriate solution to this type of data-gap issue is to take spectra with slightly different central wavelengths at the time of observations.

3. The more the number of input spectra, the more the information available to PrepSpec for modelling: A large number of input spectra implies that PrepSpec has access to information in the spectra in great details. Details about the spectra are crucial during the modelling stage. If good spectra from multiple exposures are combined or discarded, information is lost or *blurred* which limits the software from modelling the data optimally. Therefore, providing as many spectra as possible to PrepSpec is important.

To illustrate the data preparation process, we describe below the key steps we followed in preparing the Mrk 142 (wavelength-calibrated and extracted 1D) spectra for PrepSpec.

1. Correcting for GMOS chip gaps, and residuals from cosmic-ray correction and sky subtraction:
   In the spectra showing strong/sharp residuals from cosmic-ray correction or sky subtraction, we replaced the values of the affected pixels either with median values from the neighbouring region or with simulated data. For a region of <5 pixels, we used the local median values. For a region of ≥ 5 pixels, we first applied linear interpolation in the region and then simulated data values assuming a Gaussian distribution of points with standard deviation equal to the noise in the interpolated values. Finally, we assigned the simulated data an uncertainty twice as high as the noise from interpolation. We used larger uncertainties for corrected regions so that they will be weighed lesser than the good data values in further analysis.

2. Recovering distorted regions in the spectra:
   For a few spectra, we noticed bump-like features – "distorted" regions – that affected the shape of the spectra in those regions. We applied a recovery algorithm to achieve the original shape of the spectra in the distorted regions. Since we had taken two exposures every night, we used the other, good spectrum of a particular night with similar count levels – the reference spectrum – to recover the spectrum containing the distorted regions. We employed a low-order cubic-spline to estimate the shape of the reference spectra in the distorted regions and scaled those regions of the affected spectra to the estimated shape. For the nights when the spectra from the two exposures had slightly different

count levels, we used the mean wide-slit target spectrum as the reference spectrum (also used as the reference spectrum for slitloss-correction – see below).

3. Correcting for (wavelength-dependent) slit losses:
Narrow slits, used to achieve higher resolution for the data, end up blocking some of the light from the source. Therefore, narrow-slit spectra are typically supplemented with wide-slit spectra to be able to correct for any flux losses from the narrow slits (referred to as "slit losses"). For Mrk 142, we used the wide-slit observations to correct for slit losses due to the narrow slit. We applied this correction to both the calibration star and the target spectra as follows:

   (a) We selected some of the brightest wide-slit calibration star spectra from our data set and generated a mean wide-slit calibration star spectrum – the reference calibration star spectrum.

   (b) We calculated one-to-one ratios of the reference calibration star spectrum to the narrow-slit calibration star spectra at each epoch. We then fit a cubic-spline of order 2 to the ratios to obtain a sensitivity curve across the spectrum. The user can also try using binned ratios (ratios of binned spectra) as long as the sensitivity function is able to reasonably estimate the wavelength dependence of the slit losses. For the example data set, one-to-one ratios provided a better estimation of the slit losses than binned ratios; hence, we used the former. One should expect higher (lower) slit losses on the shorter-wavelength or bluer (longer-wavelength or redder) end of the spectra due to scattering. The order of the sensitivity function should be low as we aim to fit only the overall behaviour of the slit losses.

   (c) We scaled up the calibration star spectra at each epoch by dividing the spectra with the sensitivity curves determined for the respective epochs.

   (d) We repeated steps (a), (b), and (c) for the target spectra.

At this point, we performed flux calibration and proceeded to analyze the Mrk 142 data with `PrepSpec`.

C.4 Get Set... Go...!

To get going with `PrepSpec`, simply type `prepspec.exe` on the command line to start working with `PrepSpec`. In some cases, the system needs the full path to the *prepspec.exe* file to start running `PrepSpec`.

C.4.1 Preparing `PrepSpec` for Your Data

`PrepSpec` can be run interactively or through a set of commands organized in a shell script. For beginners, the interactive way is recommended first to get an idea of how the code works. Figure C.1 shows the terminal display after `PrepSpec` is launched. The initial steps to prepare the software for modelling variations in the spectra are outlined below.

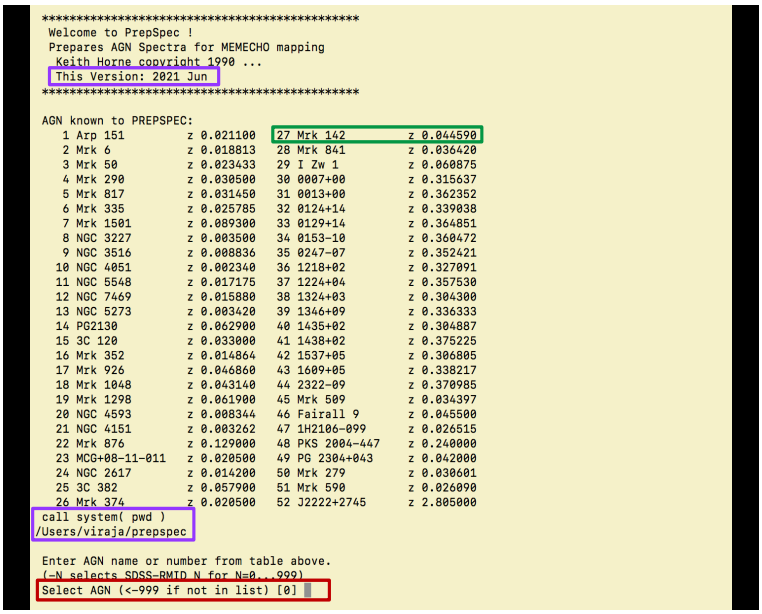

Figure C.1: Terminal display after `PrepSpec` is launched highlighting useful information (reference information enclosed in purple boxes, information required to proceed in green boxes, and the next step at the command prompt in red boxes) for the user. The copyright and version details are shown at the top left followed by a list of 52 known AGN. The working directory is printed below the list where outputs will be saved (if outputs are written to files). The first command prompt is at the bottom of the figure. The user may enter an AGN number from the known AGN list or simply enter any number *less than* -999 if the AGN is not in the list.

1. Select the appropriate number corresponding to the target AGN from the list that appears after launching `PrepSpec` (see Figure C.1). If the target AGN is not in the list of known AGN, type a number *less than* -999. The example data set is of Mrk 142. Therefore, we selected "27" at the command prompt (enclosed in a red box at the bottom of Figure C.1).

2. Enter the name of the AGN at the next command prompt. Figure C.2 highlights this with the first purple box. If an AGN was selected from the list, its name appears in square brackets at the prompt. Simply type <`return`> to accept the prompted name.

3. At this point, the software searches for a redshift file beginning with the name "redshift*" (see Figure C.2) in the working directory. If a redshift file is not found, a command prompt appears to enter the redshift of the selected AGN. If the selected AGN is from the available database, the redshift is known and appears in square brackets at the prompt. Enter a new value to overwrite the known one or type <`return`> to accept the known value. The example Mrk 142 spectra are in rest-frame wavelengths. Hence, we entered a redshift of "0.0" (or simply "0"!).

4. The software then searches for a *Timing* file with an extension ending in ".*jd" in the working directory. For the example data, there exists one timing file named "mrk142_075.hjd" in the working directory as displayed in Figure C.2 with a green box. We typed <`return`>

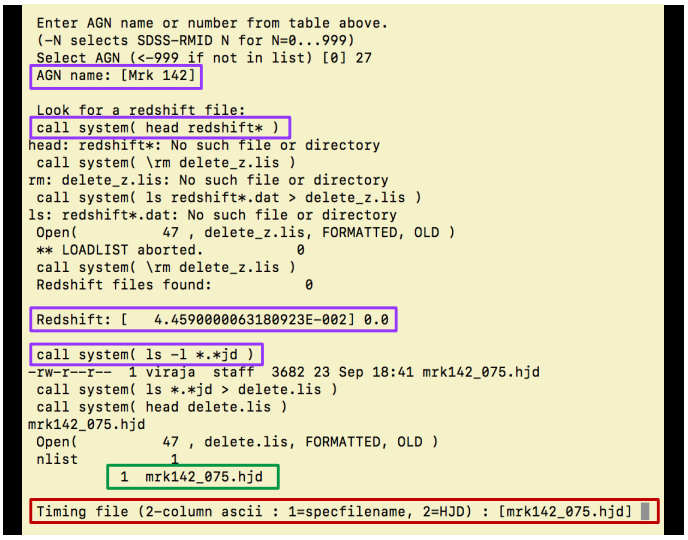

Figure C.2: Terminal display after an AGN number is selected in PrepSpec. The annotated text follows the same colour coding as Figure C.1. The software requires the name of the AGN (at the top of the figure) and then its redshift. The user is required to enter a redshift filename or the redshift value for the selected AGN. PrepSpec needs a *Timing* file (see text for details) containing information about the spectra to be loaded. The software found one such file in its search "mrk142_075.hjd". The user may enter a file from the search results or another file available in the directory that contains the required information.

to accept the existing timing file for the example data set. The user may type another filename to overwrite the filename option that appears in square brackets at the prompt. Providing the timing file will load the input spectra in PrepSpec. Figures C.3 and C.4 display the terminal output after the 64 Mrk 142 spectra are loaded.

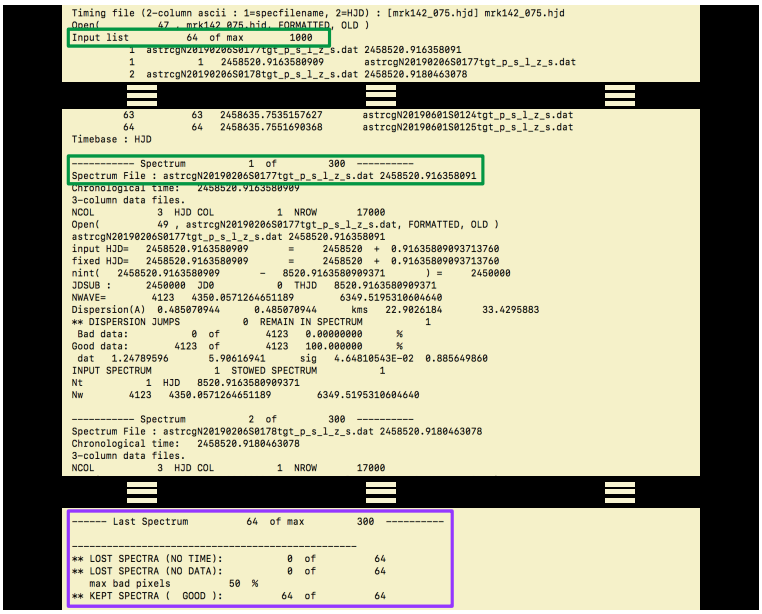

Figure C.3: Terminal display when spectra are being loaded in `PrepSpec`. The annotated text follows the same colour coding as Figure C.1. The software detected 64 input spectra that are loaded in the order in which they appear in the *Timing* file. Spectra with no data are lost by `PrepSpec`. The number of lost and retained spectra appears at the end of the loading process.

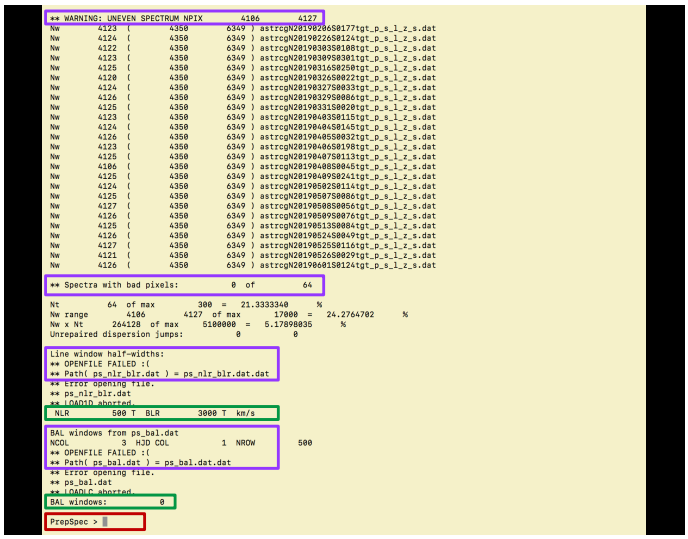

Figure C.4: Terminal display after loading spectra in `PrepSpec`. The annotated text follows the same colour coding as Figure C.1. The software shows a message about uneven total number of pixels of the spectra, but no bad pixels are detected. The software searches for two files, "ps_nlr_blr.dat" and "ps_bal.dat", containing velocity ranges affected by broad-absorption lines (BALs) in the spectra (see text for more details). However, BAL windows are not required if the input spectra are devoid of absorption. The software safely proceeds with assuming no BAL windows for the spectra (highlighted with a green box at the bottom of the figure).

By default, the software also searches for two other files containing the half-widths of typical broad absorption-line (BAL) windows in AGN. The BAL windows inform the model the velocity ranges that are affected by absorption so that they are weighed lower than the rest of the spectrum during model fitting. If the files are not found, a warning message appears. However, these inputs are not required if the input spectra are devoid of absorption similar to the Mrk 142 example spectra. Figure C.4 shows that PrepSpec did not find the files "ps_nlr_blr.dat" and "ps_bal.dat" for the example data set. In our example case, the warning message there can be safely ignored.

5. Type H or <return> at this point to view a list of parameters with current settings and a list of commands available to proceed in PrepSpec. The output is displayed in Figure C.5 with a few commonly used options enclosed in purple boxes.

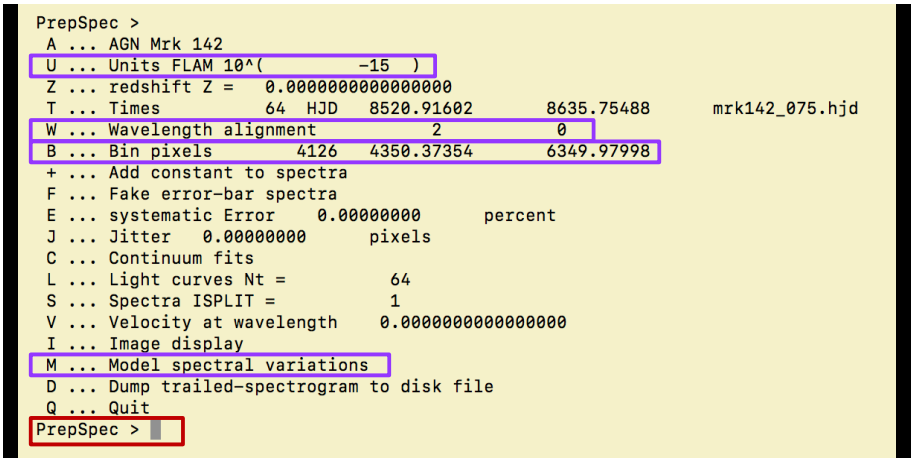

Figure C.5: Terminal display showing available options to start processing spectra in PrepSpec. The annotated text follows the same colour coding as Figure C.1. Commonly used options are highlighted in the figure – option "U" allows setting appropriate flux units, "W" allows aligning spectra along the wavelength axis, and "B" allows binning of spectra (see text for more details). The user can enter the modelling mode with option "M".

6. Type U to set appropriate units for flux. The options here are "FLAM" (flux density per unit wavelength given by erg s^{-1} cm^{-2} $Å^{-1}$) or "MJY" (milliJanskys). A dex value must be specified for scaling the axis (default is 0). We set the units to FLAM with a dex of -15 for the example data.

7. Type W to calculate the pixel shifts (to the nearest pixel) along the wavelength axis with reference to the [O III] λ5008 line. This corrects for any shifts in the dispersion solutions of the calibrated input spectra suggesting whether or not there is a need to tweak the wavelength jitter in the modelling process. Figure C.6 shows small pixel shifts (<7 pixels) for the Mrk 142 example spectra.

8. Type B to apply a different binning for the spectra. The user is required to specify whether to use Observed (specified by "O") or Rest ("R") wavelengths for the binning and the

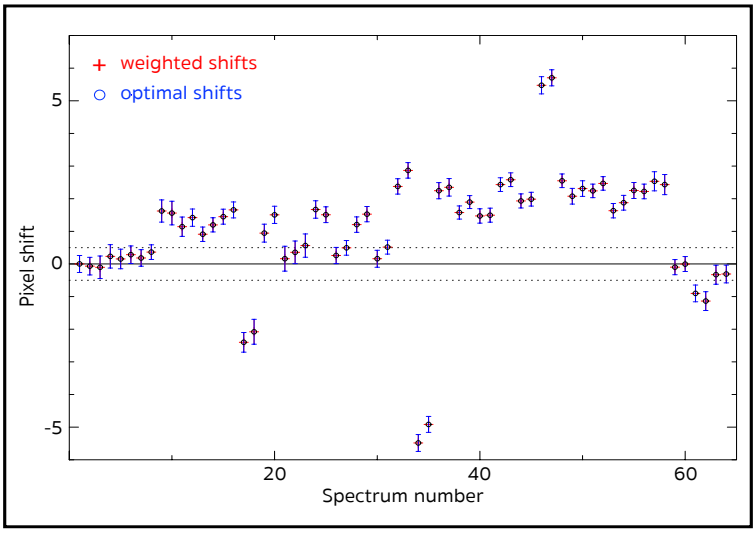

Figure C.6: Pixel shifts for the 64 Mrk 142 example spectra during wavelength alignment in `PrepSpec`. The shifts are calculated to the nearest pixel using the [O III] λ5008 narrow line as the reference line.

new wavelength range and pixel binning. The user may consider binning the data for high-resolution spectra if the high resolution is not required for further analysis. The user may also consider binning if a specific range of the full spectrum is needed for analysis. We discarded the ends of the Mrk 142 spectra as the calibration toward the ends is not reliable. Moreover, there is greater noise in the data toward the blue end than the rest of the spectrum. Because the blue end of the spectrum is beyond the region of interest for the Mrk 142 data analysis, we only used the region from 4430 Å to 6300 Å. We retained the bin size of 1 from the original spectra.

9. At this stage, `PrepSpec` is ready to enter the modelling mode. Type `M` to do so. The output will display some pre-defined quantities for analysis and finally display a list of options that the user can set before beginning the modelling process. Typing `<return>` anytime also lists all available options for the user. Figure C.7 shows the terminal output when we enter the modelling mode. The green boxes show some of the preset parameters in this mode. Various broad lines can be set to variable with the "L" option. This is done by assigning a negative expansion factor for specific lines. We defined the Hβ and He I λ5877 lines for the example data set to be variable as we are interested in measuring their velocity profiles from the spectra. Thus, the two broad lines appear as "VarBLR" components in Figure C.6. If the expansion factor of a line is set to 0, the line is excluded from the final model. Type "K" to adjust the velocity widths of broad and narrow lines. We used the preset values for the example data set. Typing "H" allows to display HJD on light-curve plots instead of the spectrum number. This can be useful if the user plans to write out the output at the end of the modelling process. Note that the average spectrum for the example data shows a contribution from Fe II which will be fit during iterative modelling. `PrepSpec` assumes the I Zwicky 1 template model (Véron-Cetty et al. 2001)

to model the Fe II component while fitting the spectra.

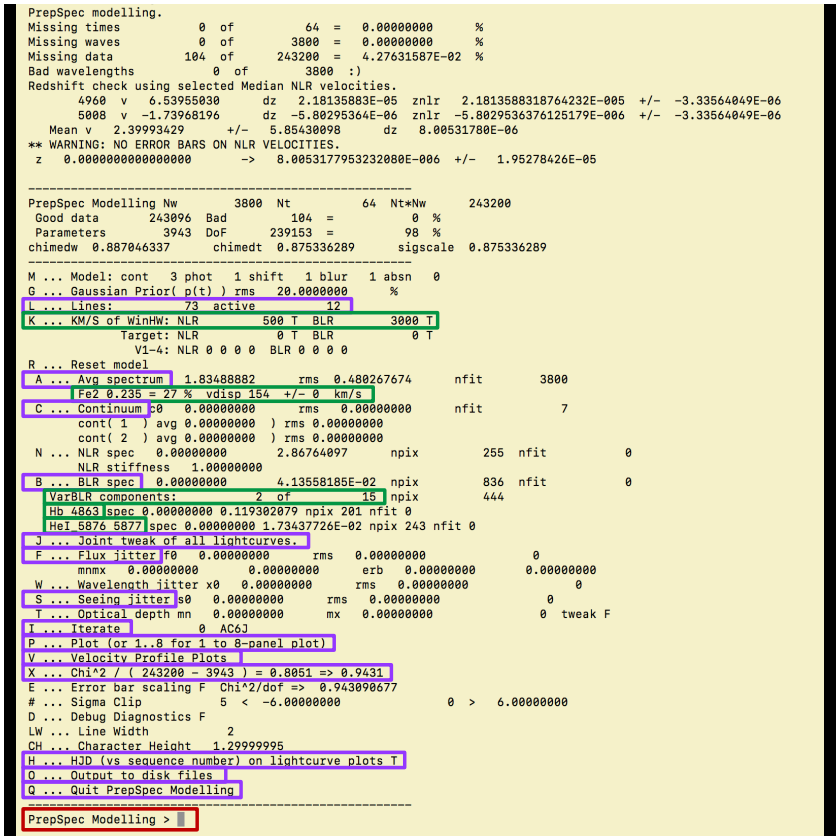

Figure C.7: Terminal display showing available options in the modelling mode in PrepSpec. The annotated text follows the same colour coding as Figure C.1. The software allows the user to set several parameters for processing the input data set. Some commonly used options are highlighted with purple boxes (see text for details). For Mrk 142 example spectra, the software has already estimated the contribution from Fe II emission (specified below the "A ... Avg spectrum" option in the figure). Furthermore, the Hβ and He I lines of interest are set as variable for the model fitting process.

C.4.2 Modelling Spectral Variations

The iterative process for modelling spectral variations in PrepSpec takes into account contributions from various components. The model components that can be fit include:

- Average spectrum (specified by "A"): Mean of the input spectra.
- Continuum: Variations in the continuum emission from the accretion disk modelled as a polynomial defined by $\log \lambda$ with time-dependent coefficients
- Flux jitter: Time-dependent photometric corrections, defined by a scale factor and a lower order polynomial as a function of wavelength, to minimize the scatter of narrow emission-line fluxes relative to their median.

- Broad-line variations: Variability in the broad emission-line features defined as splines. The breadth of the features is computed from the number of nodes of the piece-wise cubic spline needed to trace the broad profiles.

- Narrow-line variations: The modelled broad-line profiles are subtracted from the data values to obtain the narrow-line features, which are then estimated with spline functions.

- Wavelength jitter: Inter-spectra deviations in the calibrated wavelengths estimated to the fraction of a pixel by aligning the spectra with respect to the [O III] λ5008 line. The deviations are measured by scaling the the first derivative of the wavelength with the data. If spectra do not show large pixel shifts during initial wavelength alignment, this component can be excluded from the final model.

- Seeing: Corrects for any changes in the line widths due to changes in the seeing conditions from one epoch to the next. The correction is estimated from the second derivative of the model and defined by a constant or a lower order polynomial as a function of wavelength.

Each of the model components can be fit either individually or jointly, specified by "J" at the end of a given composite model. For instance, "ACJ" performs joint fitting of the average and continuum together, or "FWJ" jointly fits the flux and wavelength deviations for the input spectra. The best practice is to start with one component, typically, the average spectrum and then add additional components to the model. Each time a new component is added, the model takes ~10–30 iterations to re-fit the data. In theory, the sequence of the fit components does not matter as long as the global minimum of the badness-of-fit function is attained. However, if the fit encounters a local minimum, the fit can keep oscillating in the region and may never be able to converge.

`PrepSpec` determines the best-fitting model by accessing the Bayesian Information Criterion (BIC) and reduced χ^2 (χ^2_ν) statistic for every model. The BIC method involves maximizing the likelihood function[3] of a given model while balancing the function with both, the number of data points (N) and the number of parameters (P) used to define the model. BIC is given by $\chi^2 + \mathrm{P} \ln \mathrm{N}$ and uses Occam penalty for complex models. Thus, the goal is to use the fewest possible parameters to appropriately describe the data while penalizing the model for the number of parameters used. `PrepSpec` further computes ΔBIC as the difference between the BIC values of the current and previous models. The smaller the change in BIC, the closer the current model is to the best fit. The relative probability is also calculated for comparing models with different number of parameters, and a rise in the relative probability is desirable till it reaches a constant value, indicating that the model is not evolving any further. A good model yields $\chi^2_\nu \sim 1$. A χ^2_ν smaller (larger) than the expected value of 1 implies over-fitting (under-fitting) or large (small) variance in the errors. In the `PrepSpec` modelling mode, the performance of the models can be visually inspected by typing "X", which displays the BIC and χ^2 plots in-between iterations. Initially, fitting data interactively helps gain an understanding of which

[3]Likelihood function signifies how likely can a model, defined with a set of parameters, describe the given data. When the probability of the model describing the data is the maximum, we refer to it as the maximum likelihood function.

model works reasonably well for a given data set. We cover below the interactive modelling procedure for the Mrk 142 Gemini spectra.

For our example data set, we began by entering "I" for iteration. The user must provide the model at the first command prompt and the number of iterations at the next prompt every time they start the iteration process. We first performed 10 iterations with component "A" and visualized the model performance by typing "X". The software asks for the selection of a plotting device, and here, the user can select either "X" (again!) to visualize the relative probability plots in a PGPLOT window or "C" to save the plots as a PostScript (PS) file in the working directory. During the iteration process, it is more convenient and advisable to visualize the plots for inspection in the PGPLOT window rather than saving and opening a PS file after every series of iterations. If the model shows convergence (both the ΔBIC and the χ^2 (χ^2_ν) equal to zero), the user can proceed to adding a second component to the model. If there were no convergence, the user must perform more iterations with the same model until the model converges. For the Mrk 142 data, the model converged after 10 iterations with "A", and hence we proceeded to perform 10 iterations with the "ACJ" composite. Recollect that "ACJ" allows the joint fitting of the average spectrum and continuum to the input spectra. After the "ACJ" model convergence with 5 more iterations, we performed 20 iterations with "ACWJ". The user may choose to do only 10 iterations depending on the behaviour of their data. To gauge the optimum number of iterations with additional components to the model requires several runs through the entire modelling process. We performed 15 more iterations with "ACWJ" after which the model converged. We then performed 25 iterations with "ACWFJ" and finally 50 iterations with "ACWFBJ". The final model yielded a χ^2_ν of 0.780, which indicates overfitting of the data, possibly indicating inaccurate error bars larger than the scatter in the data. Figure C.8 shows χ^2 and BIC plots evaluating the performance of the model. The middle panel indicates relative probability of the model risen to a constant value suggesting no further evolution in the model. We excluded fitting the seeing component to the example spectra as we found that tweaking the seeing did not improve the model performance.

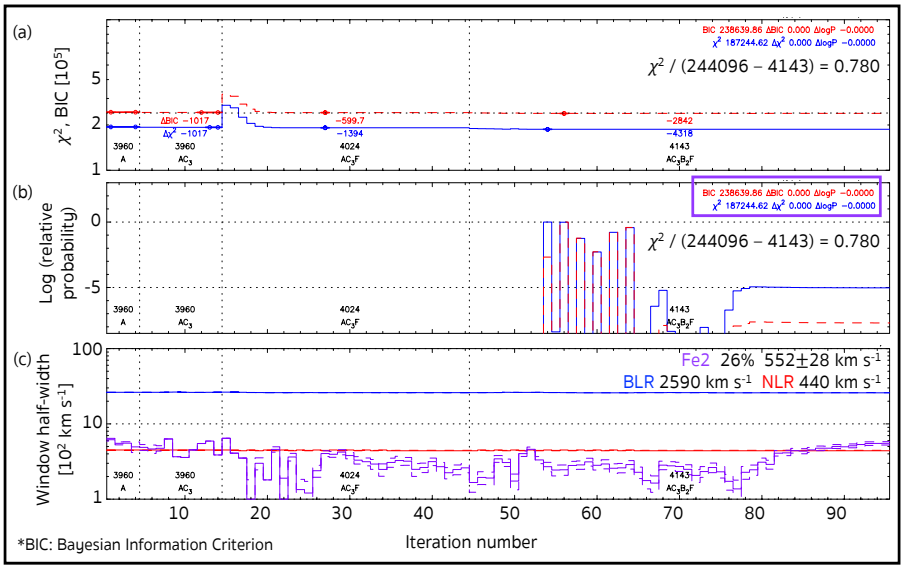

Figure C.8: χ^2 and Bayesian Information Criterion (BIC) plots indicating the performance of the `PrepSpec` model through the 95 iterations during the modelling stage. Panel *a* shows the evolution in χ^2 (blue solid curve) and BIC (red dashed curve) through the iterations, whereas panel *b* shows logarithm of the relative probability of change in χ^2 (blue solid curve) and BIC (red dashed curve) as the model progresses. In panel *b*, the change in relative probability ($\Delta \log P$) of 0 (purple box) indicates that the model has converged yielding a reduced χ^2 (χ^2_ν) of 0.780, and there will be no further evolution in the model. Panel *c* shows the velocity half-widths of the Fe II emission (purple dashed curve) and the emission lines in the broad-line region (BLR; blue solid curve) and the narrow-line region (NLR; red solid curve).

Figure C.9 displays the final model (panel *a*) and residuals (in the units of σ; panel *b*) in greyscale. Typing "1" followed by a specific letter – "G" for greyscale model and "E" for residuals in the units of σ – in the modelling mode allows the user to display or save a single plot. The greyscale model appears turbulent in the region The region blueward of ~4700 Å likely due to large variance in the region. The model is stable from the Hβ to the red end of the spectrum. The greyscale residuals for the Mrk 142 data show horizontal wiggles (dark or bright but not grey regions) prominently evident in some spectra. With visual inspection, we identified that the regions with wiggles were replaced before flux calibration by simulated data to correct for residuals from cosmic-ray correction or sky subtraction. The replacement with simulated data may have affected the performance of the model in the concerned regions. Another possible reason for such horizontal wiggles is when a higher order function is used during data reduction. In the Mrk 142 spectral reduction procedure, we used a higher order spline during flat-fielding to avoid discontinuities in the calibrated spectra across detector gaps. However, we observed no anomalous behaviour in the regions with wiggles when we performed a visual inspection of the spectra processed through `PrepSpec`.

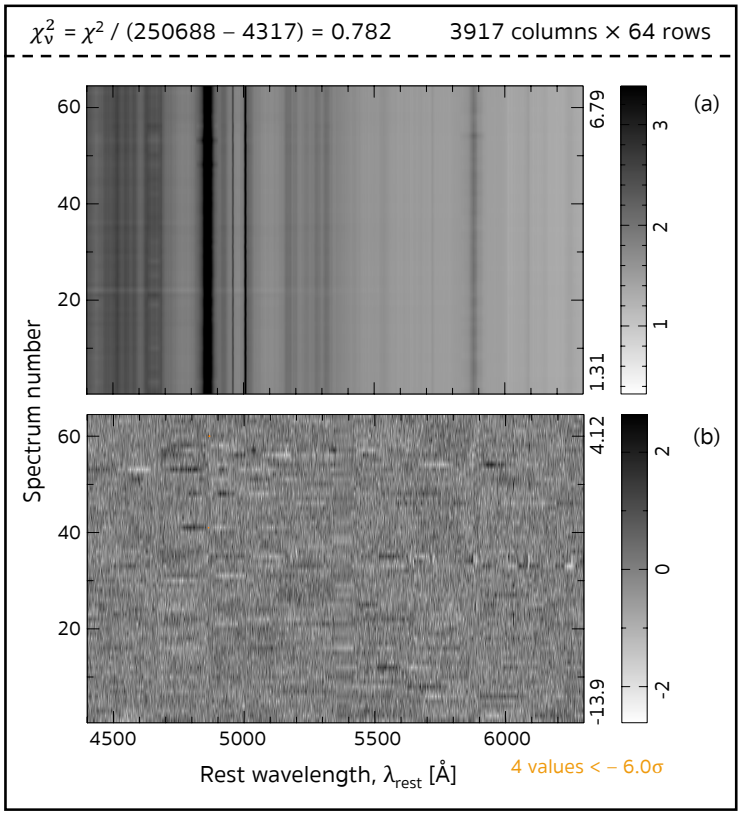

Figure C.9: PrepSpec model including all components (panel *a*) and residuals (*data* – *model* in units of standard deviation, σ; panel *b*) with a reduced χ^2 (χ^2_ν) of 0.782 for 64 narrow-slit Mrk 142 spectra. In panel *a*, dark regions indicate strong emission lines of Hβ and [O III], whereas the weaker He I lines and Fe II emission appears as less prominent features. In panel *b*, each row represents a single exposure spectrum (where multiple exposures at a given epoch are not yet combined). The horizontal wiggles strongly evident in some spectra are likely the result of either replacing values with simulated data in those regions or using a higher order function during flat-fielding (see text for more details). Four points where the values were less than 6σ are indicated with orange dots in the residuals plot. The smeared region from ~5345 Å to ~5420 Å is one of the chip gaps of the GMOS detector where simulated data was added during reduction.

Figure C.10 shows the mean (panel *a*) and root-mean-square (RMS; panel *b*) spectra displayed by typing "1" followed by "M" (for the mean) and "B" (for the RMS), respectively. The composite model for the mean spectrum shows overplotted continuum emission from the accretion disk and the Fe II pseudo continuum. The Fe II model fits less optimally indicating that a better template is required to carefully trace the sharp Fe II features in the spectra. Probably, using another Fe II template or tweaking individual lines in the existing template will result in better performance by the Fe II component. The adjusted BLR and NLR windows are indicated at the top of both the mean and the RMS plots, 2600 km s^{-1} and 450 km s^{-1} respectively. The model fit to the RMS spectrum nicely traces the Hβ and He I emission features. However, the

contamination of He II λ4687 with Fe II emission in the region makes it difficult to estimate the shape of the He II line. The residual RMS (RMSx) approaching to zero from ~5340 Å to ~5420 Å is indicative of the detector chip gap.

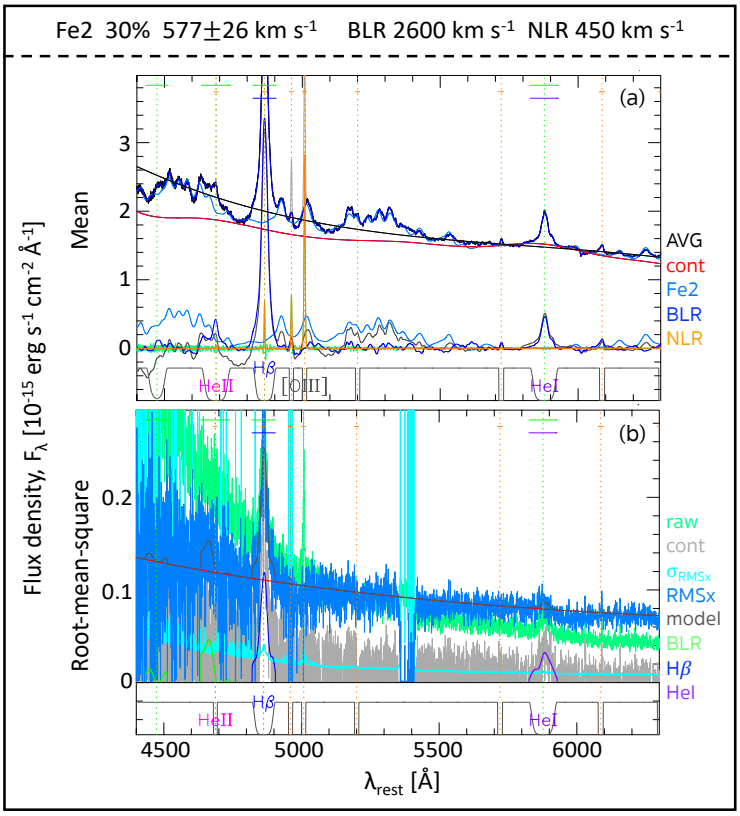

Figure C.10: Mean (panel *a*) and root-mean-square (RMS; panel *b*) of 64 narrow-slit Mrk 142 Gemini spectra processed through `PrepSpec` showing model fits with individual components. In panel *a*, the composite model (dark blue curve), including the components shown at the bottom of the plot – average spectrum (AVG; black), continuum (cont; red), Fe II (Fe2; faint blue), broad-line region (BLR; dark blue), and narrow-line region (NLR; orange), is overlaid on the mean spectrum (black curve). The broad (narrow) emission lines are indicated with green (orange) dotted vertical lines as well as with green (orange) solid horizontal dashes. The broad lines of Hβ (blue label) and He I (purple label) are marked with solid horizontal dashes. In panel *b*, model (model; dark grey curve) fit to the residual RMS spectrum (RMSx; blue curve) includes the components: continuum (cont; red curve) and BLR (green curve at the bottom of the plot). The raw RMS spectrum is the upper green curve. The BLR component comprises the broad lines of Hβ (blue bump around ~4862 Å) and He I (purple bump around ~5877 Å) shown at the bottom of the plot. The broad He II emission feature at ~4687 Å (box-like feature in the model) is contaminated with Fe II and hence difficult to fit given the noise in the region. The deviation in the residual RMS spectrum ($\sigma_{\rm RMSx}$; cyan curve) shows large values in the region of the GMOS detector chip gap from ~5345 Å to ~5420 Å.

In the modelling mode, `PrepSpec` also allows the user to output several other plots and

data. The user can display or save to file the velocity profile plots of both the narrow and the broad lines as well as the variable broad lines by typing "V". The user can also output data in the output mode "O", including data for the tweaked spectra (with and without the narrow lines), the mean and RMS spectra, continuum light curves, BLR light curves (for the specified variable lines), and the line velocity profiles.

C.5 Troubleshooting

With the limited time that I spent with `PrepSpec`, I dealt with the following issues, some of which are very commonly encountered by users.

1. While preparing the *prepspec.exe* file for your specific machine, you may need certain compiler switches in the *prepspec.com* file to be turned OFF or ON based on your operating system and version. For my Mac operating system version 10.12.6, I included the `-m64` switch (in addition to the default ones) to indicate that it was a 64-bit operating system.

2. The syntax to define aliases is different for different operating systems and must be accordingly set to successfully compile the code. By default, the *prepspec.com* file contains aliases for the `FORTRAN` compilers `g77`, `gfortran`, and `ifort`. However, if any of the compilers is not installed on your local machine, then the user may remove the specific command for the alias.

3. Specifying an incorrect path to a certain location is one of the most common errors during programming. Thus, the appropriate path to the `PGPLOT` directory is required to successfully compile `PrepSpec`.

4. While loading the *Timing* file, complete names of the spectra files with their extension (e.g., ".dat" or ".txt") must be specified. If file extensions are not included, the software reports a failure to load the data. One or more spectra can be ignored by including an "!" at the beginning of the specific row in the *Timing* file.

5. The spectral data provided to `PrepSpec` must be in ascending order of wavelengths. If the wavelengths are in random or descending order, the software attempts to predict the values where they are not in increasing order based on the values before and after that point. The predicted values can create abnormalities in the data that are undesirable.

Curriculum Vitae

Name:	VIRAJA KHATU

Post-Secondary Education and Degrees:	Doctor of Philosophy, Astronomy (Planetary Science and Exploration) *The University of Western Ontario* 2017 - 2022 (Expected Graduation Date: October 2022) Master of Science, Astronomy *The University of Western Ontario* 2015 - 2017 Honours Bachelor of Science, Astronomical Sciences *University of Toronto Mississauga* 2011 - 2015
Awards and Fellowships:	New Technologies for Canadian Observatories (NTCO) Fellowship *FLIR Integrated Imaging Solutions Inc.* *Gemini North Observatory* 2019 - 2022 Western Summer Student Internship *The University of Western Ontario* 2020 Ontario Graduate Scholarship *The University of Western Ontario* 2018 - 2019 Robert and Ruth Lumsden Graduate Fellowship *The University of Western Ontario* 2019 Dunlap Institute Summer School Travel Scholarship

Awards and Fellowships (cont'd):

University of Toronto
2018

La Serena School for Data Science Travel Scholarship
Association of Universities for Research in Astronomy (AURA)
2017

Public Service Alliance of Canada (PSAC) 610 Academic Achievement Scholarship
The University of Western Ontario
2017

Summer Undergraduate Research Program Fellowship
University of Toronto
2014

Related Work and Volunteer Experience:

Member of High Energy Astrophysics and Gravitational Waves Team
Space Exploration Topical Teams Initiative
Canadian Space Agency (CSA)
Present

Teaching Assistant
The University of Western Ontario
2015 - 2021

Facilitator
AstroComm2021 Workshop (virtual)
Centre for Research in Astrophysics of Québec (CRAQ)
2021

NTCO Intern
FLIR Integrated Imaging Solutions Inc.
2021

Education and Public Outreach Representative
Graduate Student Committee
Education and Public Outreach Committee
Canadian Astronomical Society (CASCA)
2020 - 2021

Visiting Student
Wayne State University
2019

NTCO Intern

Related Work and Volunteer Experience (cont'd):

Gemini North Observatory
2019

Organizing Committee Representative for Astronomy Science Rendezvous
The University of Western Ontario
2018 - 2019

Telescope Operator
Science Rendezvous
The University of Western Ontario
2017 - 2019

Volunteer Visitor
National Research Council Canada's Herzberg Astronomy and Astrophysics Research Centre
2018

Speaker, Telescope Operator, and Crowd Manager
The Hume Cronyn Memorial Observatory
The University of Western Ontario
2016 - 2018

Activity Facilitator
Space Explorers Summer Academy
The University of Western Ontario
2018

Activity Coordinator
Space Explorers Summer Camp
The University of Western Ontario
2018

Member of Local Organizing Committee
Great Lakes Quasar Symposium
The University of Western Ontario
2016

Activity Facilitator
Astronomy Teachers' Workshop
York University
2015

Event Coordinator
Astronomy & Space Exploration Society Symposium

Related Work and Volunteer Experience (cont'd):

University of Toronto
2015

Planetarium Operator and Presenter
AstroTours and AstroKeynote Events
University of Toronto
2014 - 2015

Research Supervision and Mentorship:

Optimizing Active Galactic Nuclei Variability Surveys for the *Cosmological Advanced Survey Telescope for Optical and ultraviolet Research (CASTOR)* (research project)
The University of Western Ontario
First-year Summer Student, Medical Sciences – 1 (Present)
Fourth-year Thesis Students, Computer Science – 2 (2020 - 2021)

Improving Methods of Black Hole Classification (Advanced Placement course project)
Harbour View High School
Grade 12 Student – 1 (2020 - 2021)

Spectral Reduction for a Highly Accreting Active Galactic Nucleus, Markarian 142 (research project)
The University of Western Ontario
Second-year Summer Student, Physics – 1 (2019)

Conference Presentations:

"Tracing Gas Flows in a Highly Accreting Active Galactic Nucleus, Markarian 142" (poster)
Gemini Science Meeting (hybrid)
Gemini Observatory
2022

"Designing Large-scale Active Galactic Nuclei Variability Surveys" (poster)
NTCO Annual General Meeting (hybrid)
Université de Montréal
2022

"How To Design Large-scale Active Galactic Nuclei Variability Surveys" (poster)
Canadian Space Exploration Workshop (virtual)
CSA
2022

"Probing Structure of Gas Flows in a Highly Accreting Active Galactic Nucleus, Markarian 142" (oral)

Conference Presentations (cont'd):

CASCA Annual General Meeting (virtual)
University of Waterloo
2022

"Mapping Gas Motions in a Highly Accreting Active Galactic Nucleus Markarian 142" (oral)
Zooming In on Compact Objects 2021 (virtual)
Wayne State University
2021

"Probing the Structure of a Highly Accreting Active Galactic Nucleus, Markarian 142" (poster)
CASCA Annual General Meeting (virtual)
National Research Council Canada's Herzberg Astronomy and Astrophysics Research Centre
2021

"Mapping the Structure of a Highly Accreting Active Galactic Nucleus, Markarian 142" (poster)
Space Day (virtual)
The University of Western Ontario
2021

"Probing the Inner Structure of the High-Accretion Rate Active Galactic Nucleus, Markarian 142" (poster)
NTCO Annual General Meeting (virtual)
University of Victoria
2020

"Tracing Accretion Flow in the Highly Accreting Active Galactic Nucleus, Markarian 142" (poster)
CASCA Annual General Meeting (virtual)
2020

"Experiencing Gemini...*from the perspectives of a user and an intern*" (oral)
NTCO Annual General Meeting
Dominion Radio Astrophysical Observatory
2019

"GNIRS Cross-dispersion Python-based Pipeline (GNIRS-Pype)" (poster)
NTCO Annual General Meeting
Dominion Radio Astrophysical Observatory
2019

Conference Presentations (cont'd):

"Weighing 1000 Supermassive Black Holes with CASTOR" (oral)
Mapping Central Regions of Active Galactic Nuclei
Institute of High Energy Physics
2019

"Weighing a 1000 Supermassive Black Holes!" (poster)
Space Day
The University of Western Ontario
2019

"Mapping the Inner Parsec of Quasars" (oral)
Massively Multiplexed Spectroscopy with Maunakea Spectroscopic Explorer
2019

"How do Supermassive Black Holes Grow? - Active Galactic Nuclei Reverberation-Mapping Experiment with the *Cosmological Advanced Survey Telescope for Optical and ultraviolet Research* (CASTOR)" (poster)
NTCO Annual General Meeting
Université Laval
2018

"How can we probe the Physics of Energetic Quasar Outflows?" (poster)
Fallona Family Interdisciplinary Showcase
The University of Western Ontario
2018

"How can we probe the Physics of Energetic Quasar Outflows?" (poster)
Space Day
The University of Western Ontario
2018

"How can we probe the Physics of Energetic Quasar Outflows?" (poster)
Women in Planetary Science and Exploration
University of Toronto
2018

"X-ray Insights into Mini Low-Ionization Broad Absorption Line Quasars" (poster)
AGN Winds on the Georgia Coast

Conference Presentations (cont'd):

Georgia State University
2017

"Rare He I* Transition traces Thick Gas Outflows in Quasars" (poster)
Fallona Family Interdisciplinary Showcase
The University of Western Ontario
2017

"Extremely High Velocity Outflows in Low-Redshift Active Galactic Nuclei" (poster)
Great Lakes Quasar Symposium
The University of Western Ontario
2016

"Investigating the rare He I* transition in the optical spectra of mini-broad absorption line quasars" (poster)
Great Lakes Quasar Symposium
The University of Western Ontario
2016

Research Training:

James Webb Space Telescope (JWST) Spectral Analysis (virtual)
Space Telescope Science Institute (STScI)
2021

JWST Near Infra-Red Spectrograph Data Processing and Analysis in the Multi-Object Spectroscopy Mode (virtual)
STScI
2021

Rubin Observatory Project and Community Workshop (virtual)
Vera C. Rubin Observatory
2020

Atacama Large Millimeter Array (ALMA) Proposal Writing Workshop (virtual)
University of Toronto
2020

JWST Proposal Training Workshop
The University of Western Ontario
2020

Next Level Python
University of Victoria
2018

Research Training (cont'd):

Introduction to Astronomical Instrumentation
University of Toronto
2018

Large Scale Astrophysics: galaxies and beyond (summer school)
CRAQ, McGill University
2018

La Serena School for Data Science
AURA
2017

Compute Ontario Summer School on Scientific and High Performance Computing
SciNet, University of Toronto
2017

Data Carpentry Workshop
SHARCNET, The University of Western Ontario
2016

Observing at the Mayall 4-m Telescope
Kitt Peak National Observatory
2015

Educational Training:

Space Educators Institute (virtual)
The University of Western Ontario
2020

Fostering a Problem-Solving Mindset in Your STEM Students
Centre for Teaching and Learning (CTL), The University of Western Ontario
2020

Preparing Your Teaching Dossier
CTL, The University of Western Ontario
2019

Teaching Mentor Program
CTL, The University of Western Ontario
2017

Advanced Teaching Program
CTL, The University of Western Ontario

Educational Training (cont'd):

2017

Leading Minds-On Labs
CTL, The University of Western Ontario
2017

Winter Conference on Teaching
CTL, The University of Western Ontario
2017

Leading Effective Tutorials
CTL, The University of Western Ontario
2017

Threshold Concepts: Teaching Troublesome Knowledge in the Disciplines
CTL, The University of Western Ontario
2016

Fall Perspectives on Teaching
CTL, The University of Western Ontario
2016

Winter Conference on Teaching
CTL, The University of Western Ontario
2016

Graduate Student Conference on Teaching
CTL, The University of Western Ontario
2015

Professional Development:

GradWRITE Seminar Series (virtual)
Writing Support Centre, The University of Western Ontario
2020

Equity, Diversity, and Allyship (virtual)
NTCO Annual General Meeting
2020

Leadership and Teamwork (virtual)
NTCO Annual General Meeting
2020

Science Communication Tools (virtual)
CASCA Annual General Meeting

Professional Development (cont'd):

2020

Well-being and Mindfulness from a Scientific Point of View (virtual)
CASCA Annual General Meeting
2020

Science Communication Workshop
The University of Western Ontario
2020

Goal Setting and Time Management
NTCO Annual General Meeting
2019

Using Social Media as a Tool for Teaching and Connecting
The University of Western Ontario
2019

Create Your Career and Get the Job....Keep the Job and Continue to Triumph
NTCO Annual General Meeting
2018

Essentials of Productive Teams
Mitacs, The University of Western Ontario
2018

Doctoral Leadership Forum
School of Graduate and Postdoctoral Studies (SGPS), The University of Western Ontario
2018

Improving Presentation Skills: Preparing for the Inevitable
CTL, The University of Western Ontario
2016

So You Think You're a Fraud? Overcoming Impostor Syndrome
CTL, The University of Western Ontario
2015

Memberships:

Early Career Research Professional
The International Society for Optics and Photonics (SPIE)
Present

Memberships (cont'd):

Student Representative
Program Committee, NTCO
2021 - Present

Student Member
CASCA
2015 - Present

Volunteer Member of Orientation and Social Committee
Society of Graduate Students (SOGS), The University of Western Ontario
2015 - 2016

Publications:

Rodríguez Hidalgo, P., Khatri, A. M., Hall, P. B., Haas, S., Quintero, C., **Khatu, V.**, et al. 2020. Survey of Extremely High-velocity Outflows in Sloan Digital Sky Survey Quasars. Astrophysical Journal, 896, 151.

Cackett, E. M., Gelbord, J., Li, Y.-R. Li, Horne, K., Wang, J.-M., Barth, A. J., Bai, J.-M., Bian, W.-H., Carroll, R. W., Du, P., Edelson, R., Goad, M. R., Ho, L. C., Hu, C., **Khatu, V. C.**, et al. 2020. Supermassive black holes with high accretion rates in active galactic nuclei. XI. Accretion disk reverberation mapping of Mrk 142. Astrophysical Journal, 896, 1.

Côté, P., Abraham, R., Balogh, M., Capak, P., Carlberg, R., Cowan, N., Djazovski, O., Drissen. L., Drout, M., Dupuis, J., Evans, C., Fantin, N., Ferrarese, L., Fraser, W., Gallagher, S., Girard, T., Gleisinger, R., Grandmont, F., Hall, P., Hellmich, M., Hardy, T., Harrison, P., Hložek, R., Haggard, D., Hénault-Brunet, V., Hutchings, J., **Khatu, V.**, et al. 2019. CASTOR: A Flagship Canadian Space Telescope. Canadian Long Range Plan for Astronomy and Astrophysics White Papers, 2020. (ID:18).

Woods, T. E., Alexandroff, R. M., Ellison, S. L., Ferrarese, L., Gallagher, S., Gallo, L., Haggard, D., Hall, P., Hlavacek-Larrondo, J., **Khatu, V. C.**, et al. 2019. Revealing the Origins and Cosmic Evolution of Supermassive Black Holes. Canadian Long Range Plan for Astronomy and Astrophysics White Papers, 2020. (ID: 34).

Hall, P., Balogh, M., Barmby, P., Blakeslee, J., Bovy, J., Bradley, C., Bridges, T., Cami, J., Chapman, Chateauneuf, F., Cowan, N., Côté, P., Damjanov, I., Drout, M. Eadie, G., Ellison, S., Ferrarese, L., Fraser, W., Gaensler, B., Gallagher, Haggard, D., Hénault-Brunet, V., Herwig, F., Hill, A., Hlavacek-Larrondo, J., Hudson, M., Johnson, M., **Khatu, V.**, et al. 2019. The Maunakea Spectroscopic Explorer. Canadian Long Range Plan for Astronomy and Astrophysics White Papers, 2020. (ID: 30).

Lester, J., **Khatu, V**., and Neilson, H. Indicators of Stellar Mass in the Photometric *H*-band.

2017. Publications of the Astronomical Society of the Pacific, 129, 024201.

Percy, J. R. and **Khatu, V**. 2014. Amplitude Variations in Pulsating Red Supergiants. Journal of the AAVSO, 42, 1.